

**Micro-geodynamics of the Karakoram Fault Zone, Ladakh,
NW Himalaya**

David Wallis

Submitted in accordance with the requirements for the degree of
Doctor of Philosophy

The University of Leeds

School of Earth and Environment

April, 2014

The candidate confirms that the work submitted is his/her own, except where work which has formed part of jointly-authored publications has been included. The contribution of the candidate and the other authors to this work has been explicitly indicated below. The candidate confirms that appropriate credit has been given within the thesis where reference has been made to the work of others.

Chapters 3 and 4 are based respectively on the following jointly-authored publications.

Wallis, D. et al. 2013. Fault weakening across the frictional-viscous transition zone, Karakoram Fault Zone, NW Himalaya. *Tectonics*, **32**(5), pp.1227-1246, doi: 10.1002/tect.20076..

Wallis, D. et al. 2014a. Evolution of the Eastern Karakoram Metamorphic Complex, Ladakh, NW India, and its relationship to magmatism and regional tectonics. *Tectonophysics*, **626**, pp.41-52, doi: 10.1016/j.tecto.2014.03.023.

All work included within the thesis is directly attributable to the candidate.

This copy has been supplied on the understanding that it is copyright material and that no quotation from the thesis may be published without proper acknowledgement.

The right of David Wallis to be identified as Author of this work has been asserted by him in accordance with the Copyright, Designs and Patents Act 1988.

© 2014 The University of Leeds and David Wallis

Acknowledgements

I am indebted to Richard Phillips and Geoff Lloyd for their enthusiastic and invaluable support, training, encouragement and mentoring throughout my time at Leeds, and for providing the opportunity to conduct this research, which has been both exciting and greatly enjoyable.

I would like to express particular thanks to Richard, Andy Parsons and Hannah Watkins, all of whom endured considerable trials and tribulations during our time in the Karakoram. Thanks also to Fida Hussein Mitoo of the New Royal Guest House in Leh, and the many other people of Leh, Nubra and Tangtse, without whom my fieldwork in Ladakh would not have been possible.

I am grateful to Richard Walshaw and Eric Condliffe for their patient support, training and assistance with use of the scanning electron microscope and electron microprobe. Thanks also to Geoff and Harri Wyn-Williams for their introductions to the nuances of sample preparation.

Thanks to the alumni and present occupants of office 8.152 for providing support, friendship and welcome distraction in equal measure.

Lastly, thank you to my family and close friends for unwaivering support and encouragement throughout my studies and travels.

Abstract

Microgeodynamics relates grain-scale deformation microstructures to macroscopic tectonic processes. Here the microgeodynamic approach combines optical and electron microscopy, including electron backscattered diffraction (EBSD), with field geology, geothermobarometry and microphysical modelling to study fault rocks deformed within a major continental strike-slip fault to quantify changes in fault zone structure and rheology with crustal depth. The overall thesis rationale therefore is to test existing fault models against an exhumed example of a continental strike-slip fault zone, namely the central Karakoram Fault Zone (KFZ), NW India. This approach establishes changes in deformation processes with depth in the upper- to mid-crust and suggests that a range of fault weakening mechanisms have reduced fault rock shear strengths, typified by friction coefficients of 0.3-0.4. Metamorphic petrology and geothermobarometry are used to place the KFZ in the context of regional tectono-metamorphic evolution. It is shown using diagnostic microstructures and pressure-temperature-time paths that the fault initiated after peak metamorphism (677-736°C, 875-1059 MPa) and subsequent migmatization (688±44°C, 522±91 MPa) and leucogranite emplacement (448±100 MPa). Retrograde phyllonites formed during later strike-slip deformation are investigated in detail using EBSD, geothermometry and microphysical modelling. The phyllonites formed at 351±34°C and had low shear strength (<30 MPa) during frictional-viscous flow. EBSD is also used to derive a novel strain proxy based on quartz crystal preferred orientation *intensity*. Application of this method distinguishes deformation distributions in transects across the KFZ. Deformation intensity varies from <0.2 in essentially undeformed domains to 1.6 within shear zone strands formed at 500-550°C and c. 15 km depth. Evaluation of the history of the KFZ suggests that whilst it plays a relatively minor role in accommodating India-Asia collision, it can nevertheless be used as an analogue for major continental strike-slip fault zone structure.

Table of Contents

Acknowledgements.....	iii
Abstract.....	iv
Table of Contents	v
List of Tables	x
List of Figures	xi
1. Microgeodynamics of Strike-Slip Faults: Overview and Rationale	1
Abstract	1
1.1 Introduction	1
1.2 Strike-Slip Fault Zones: Tectonic and Seismogenic Significance.....	4
1.3 Models of Fault Zone Structure and Deformation Processes	8
1.4 Rationale for Investigating the Microgeodynamics of the Karakoram Fault Zone	12
2. Structural and Geological Framework of the Central Karakoram Fault Zone	15
Abstract.....	15
2.1 Suitability of the Karakoram Fault Zone for Study of Strike-slip Fault Properties, Processes and Evolution.....	16
2.2 Geological and Kinematic Setting of the Karakoram Fault Zone.....	18
2.3 Geological Units	22
2.3.1 Eastern Karakoram Metamorphic Complex.....	22
2.3.2 Eastern Karakoram Granitoids	26
2.3.3 Ladakh Terrane Granitoids.....	29
2.3.4 Ladakh Terrane Volcanics.....	30
2.3.5 Shyok Suture Zone.....	31
2.4 Structural Architecture of the Central Karakoram Fault Zone.....	32
2.4.1 Nubra strand	32
2.4.2 Arganglas strand	34
2.4.3 Pangong strand.....	34
2.4.4 Tangtse strand	37
2.4.5 New Observations: The Taruk Fault Strand	37
2.5 Age of the Karakoram Fault Zone	42

2.6 Geological Offsets Across the Karakoram Fault Zone.....	44
2.7 Geological, Quaternary and Present-Day Slip-rate Estimates.....	44
2.8. Summary	46
3. Fault weakening across the frictional-viscous transition zone, Karakoram Fault Zone, NW Himalaya	47
Abstract	47
3.1 Introduction.....	48
3.2 Deformation Mechanisms Within the Karakoram Fault Zone	52
3.2.1 Deformation on the Nubra Fault Strand.....	52
3.2.1.1 Deformation Microstructures within the Nubra Formation	52
3.2.1.2 Deformation Microstructures within Nubra Formation Phyllonites.....	56
3.2.1.3 Deformation Microstructures within the Nubra- Siachen Leucogranite.....	57
3.2.1.4 Tourmaline±quartz Veins on the Nubra Fault Strand.....	59
3.2.1.5 Hydrothermal Springs along the Nubra Fault Strand.....	59
3.2.2 Interpretation of Deformation Mechanisms within the Nubra Fault Strand	60
3.2.3 Deformation on the Tangtse Fault Strand	63
3.2.3.1 Deformation Microstructures within the Tangtse Strand EKMC	63
3.2.3.2 Deformation Microstructures within the Tangtse- Darbuk Leucogranite.....	65
3.2.4 Interpretation of Deformation Mechanisms within the Tangtse Fault Strand.....	66
3.2.5 Deformation on the Arganglas Fault Strand	69
3.2.6 Interpretation of Deformation Mechanisms within the Arganglas Fault Strand.....	71
3.3 Discussion: Fault Weakening Mechanisms and Their Tectonic Significance	72
3.3.1 Weakening Mechanisms on the Nubra Fault Strand	72
3.3.2 Weakening Mechanisms on the Tangtse Fault Strand	75
3.3.3 Weakening Mechanisms on the Arganglas Fault Strand....	76
3.3.4 The Pangong Fault Strand	76
3.3.5 Hydraulic Characteristics of the Nubra Fault Strand.....	77
3.3.6 Seismogenic potential of the KFZ.....	78

3.3.7 Frictional heating on the KFZ	80
3.3.8 Fault Weakening and Implications for Continental Lithospheric Strength	81
3.4. Conclusions.....	82
4. Evolution of the Eastern Karakoram Metamorphic Complex, Ladakh, NW India, and its relationship to magmatism and regional tectonics	83
Abstract.....	83
4.1 Introduction	84
4.2 Mineralogy and microstructure	87
4.3 Data collection and geothermobarometers.....	93
4.3.1 Amphibole-plagioclase thermobarometry.....	93
4.3.2 Ti-in-biotite geothermometry	95
4.4 Geothermobarometry Results	98
4.4.1 Amphibole-plagioclase chemistry and P-T estimates.....	98
4.4.2 Biotite chemistry and temperature estimates	100
4.5 Metamorphism and deformation of the Eastern Karakoram Metamorphic Complex	101
4.5.1 The Pangong Transpressional Zone	101
4.5.2 The Pangong Metamorphic Complex.....	103
4.5.3 The Nubra Formation	105
4.5.4 The Saser Formation.....	106
4.6 Crustal evolution of the eastern Karakoram: relationship between metamorphism and strike-slip faulting	106
4.7 Conclusions.....	108
5. Low Effective Fault Strength due to Frictional-Viscous Flow in Phyllonites, Karakoram Fault Zone, NW India.....	110
Abstract.....	110
5.1 Introduction	110
5.2. Structural Setting of the Karakoram Fault Zone Phyllonites	113
5.3. Phyllonite Deformation Microstructures and Crystal Fabrics.....	116
5.4 Interpretation of Phyllonite Deformation Mechanisms	121
5.5 Chlorite Geothermometry	122
5.5.1 Chlorite Compositions	122
5.5.2 Chlorite Geothermometry	122
5.6 Frictional-Viscous Flow Modelling	126
5.6.1 Microphysical Modelling of Frictional-Viscous Flow in the KFZ Phyllonites.....	126

5.6.2 Effective Shear Strength of the KFZ Phyllonites.....	129
5.7 Discussion: Deformation-Metamorphism-Fluid Interactions and Impacts on Fault Zone Rheology.....	131
5.8 Conclusions.....	134
6. Quantifying strain distribution in crustal shear zones	135
Abstract.....	135
6.1 Introduction.....	136
6.2 Characterising Quartz Deformation Within The Karakoram Fault Zone	138
6.2.1 The Role of Quartz in the Deformed Eastern Karakoram Granitoids	138
6.2.2 Optical Microstructure of Deformed Quartz	139
6.2.3 Electron Backscattered Diffraction Characterisation of Deformed Quartz.....	140
6.2.3.1 Quartz Slip System Activity and CPO.....	140
6.2.3.2 EBSD Data Acquisition.....	142
6.3 Quartz Crystal Preferred Orientation as a Strain Proxy.....	155
6.3.1 Controls on CPO development.....	155
6.3.2 Quantifying Quartz CPO strength.....	159
6.4 Ductile Strain Distribution Within the Karakoram Fault Zone.....	165
6.4.1 Strain Distribution Across Miocene Intrusions	165
6.4.2 Strain Distribution Across the Karakoram Fault Zone.....	166
6.5 Constraints on the Depth of Deformation	169
6.6 Discussion	173
6.6.1 Implications for the Age, Thermal Regime and Strain Rate of the KFZ Shear Zone	173
6.6.1.1 Age of the KFZ	173
6.6.1.2 Strain Rate Within the KFZ Shear Zone	175
6.6.1.3 Thermal Regime During KFZ Deformation	177
6.6.2 Relationship to Other Faults and Implications for Fault Modelling.....	178
6.6.2.1 Comparison to Other Faults	178
6.6.2.2 Implications for Fault Modelling	182
6.7 Conclusions.....	183
7. The structure, strength and significance of continental strike- slip faults	185
Abstract.....	185
7.1 Introduction.....	186

7.2	Characterising the Karakoram Fault Zone and its role in the India-Asia collision zone.....	186
7.3	Fault zone structure and strain accommodation.....	192
7.3.1	Structure and strength of the Karakoram Fault Zone	192
7.3.2	Implications for the structure and deformation processes of large scale strike-slip faults.....	200
7.3.2.1	Implications for the structure of strike-slip faults in the Tibetan plateau.....	200
7.3.2.2	Implications for the behaviour of seismogenic strike-slip faults	205
7.3.2.3	Summary.....	212
8.	Conclusions and Future Work	213
8.1	Conclusions.....	213
8.1.1	Architecture of the Central Karakoram Fault Zone	213
8.1.2	Rheology of the Central Karakoram Fault Zone	214
8.1.3	Evolution of the Karakoram Fault Zone	215
8.2	Future Work	216
8.2.1	Calibration of Crystal Preferred Orientation Strain Profiles	216
8.2.2	Petrofabric-Derived Seismic Modelling of Strike-Slip Fault Zones	216
8.2.3	Characterisation of Deformation Mechanisms by Misorientation and Schmid Factor Analyses	217
	List of References	218
	List of Abbreviations.....	259
	Appendix A Summary of Electron Microprobe Compositional Data ..	262
A.1	Summary of Amphibole Compositional Data	262
A.2	Summary of Plagioclase Compositional Data	264
A.3	Summary of Biotite Compositional Data	265
A.4	Summary of Chlorite Compositional Data	266

List of Tables

Table 4.1 Sample locations and representative chemical compositions of minerals used for amphibole-plagioclase geothermobarometry.	94
Table 4.2 Sample locations and representative chemical compositions of minerals used for Ti-in-biotite geothermometry.	96
Table 4.3 Amphibole-plagioclase thermobarometry and Ti-in-biotite thermometry results and estimated geothermal gradients.	99
Table 5.1 Summary of fault zones where frictional-viscous flow has been inferred or where reported microstructures are highly suggestive of such deformation.....	113
Table 5.2 Representative chlorite compositional analyses as oxide wt.% and cations per 28 oxygen formula unit.	124
Table 5.3 Comparison between the compositions of chlorites (28 oxygen basis) from the Karakoram Fault Zone phyllonite and those in the calibration datasets of various chlorite geothermometers.	125
Table 5.4 Values used for frictional-viscous flow modelling of the Karakoram Fault Zone phyllonite, where derived independently from the original model of Niemeijer and Spiers (2005).	129
Table 6.1 Sample details for EBSD study.	144
Table 6.2 Examples of samples showing CPO characteristics described in Section 6.2.3.3.	154
Table 6.3 Summary of eigenvalue-based CPO strength parameters.	159
Table 6.4 Reference fault strands, profile distances, normalised quartz (c)-axes eigenvalues and the I, C, 1-R and pfJ values used to construct Figures 5.10 and 5.11.	162

List of Figures

Figure 1.1 Schematic generalised strike-slip fault zone model of Scholz (1988).	9
Figure 1.2 Generalised strike-slip fault zone cross-section showing schematic variations in possible strain distribution with depth.	10
Figure 1.3 Schematic generalised fault zone model of Imber et al. (2008).	12
Figure 2.1 Fault map of western Tibet showing major structures superimposed on a Landsat 7 image montage.	19
Figure 2.2 The Karakoram fault zone, Ladakh, NW India.	21
Figure 2.3 The Nubra fault strand of the Karakoram Fault (KF).	24
Figure 2.4 The Saser Formation (SF) in Sumur gorge.	24
Figure 2.5 The Pangong Metamorphic Complex between Muglib and Pangong Tso.	25
Figure 2.6 The Pangong Transpressional Zone (PTZ).	27
Figure 2.7 Cross-polarised photomicrograph of the Arganglas Diorite.	28
Figure 2.8 Cross-polarised photomicrograph of protomylonitic Late Cretaceous diorite near Darbuk.	28
Figure 2.9 Cross-polarised photomicrograph of the 68 Ma Tirit granite.	30
Figure 2.10 Leucogranite (Lgr) pods and sheets intruding the Nubra Formation in Sumur gorge.	33
Figure 2.11 Stereographic projections of foliation (S) and lineation (L) data from the different portions of the Karakoram fault zone.	35
Figure 2.12 Stereographic projections of foliation (S) and mineral alignment and stretching lineation (L) measurements for the Nubra fault strand.	36
Figure 2.13 The Nubra strand fault core in Sumur gorge.	36
Figure 2.14 Blocky brecciation of Saser Formation marble.	37
Figure 2.15 Variation in deformation fabric intensity within the South Tangtse Granite.	39
Figure 2.16 The Taruk shear zone.	41
Figure 2.17 Cross-polarised photomicrograph of the Taruk leucogranite.	42

Figure 3.1 The KFZ with Harvard Centroid Moment Tensor (CMT) solutions, International Seismological Centre and National Earthquake Information Centre data and historic earthquakes during the period 1964-2003.....	50
Figure 3.2 Central portion of the KFZ, Ladakh, N. India (modified from Phillips, 2008; Phillips and Searle, 2007, and Phillips et al., 2004).....	53
Figure 3.3 a) Cliff cross-section through the Nubra fault strand in Yulskam gorge.	54
Figure 3.4 Deformation fabrics on the Nubra fault strand.	56
Figure 3.5 Evidence of hydrothermal activity on the Nubra fault strand. a) Active hydrothermal springs and travertine deposits on the fault trace at Panamik. b) Travertine deposits within the fault core at Sumur indicate palaeohydrothermal activity.....	60
Figure 3.6 Deformation microstructures on the Tangtse fault strand.	64
Figure 3.7 Deformation microstructures on the Arganglas fault strand.	70
Figure 3.8 Schematic diagram of the KFZ showing the depths at which fault weakening mechanisms are inferred to have operated on each fault strand.	73
Figure 4.1 Location maps.	85
Figure 4.2 Field photographs of the Eastern Karakoram Metamorphic Complex.....	88
Figure 4.3 Microstructures within the Eastern Karakoram Metamorphic Complex.....	89
Figure 4.4 Microstructures in W11/30 Nubra Formation metapelite.	92
Figure 4.5 Negative correlation between biotite Ti content and Mg/(Mg+Fe) in metapelite samples P85 and P146.	97
Figure 4.6 Ti-in-biotite thermometry results for Nubra Formation metapelite sample P85 ordered by temperature.....	100
Figure 4.7 Pressure-temperature-time paths of the Eastern Karakoram Metamorphic Complex.	102
Figure 5.1 Simplified sketch map of the geology of the Nubra Valley region of Ladakh, NW India, after Phillips (2008).....	114
Figure 5.2 Simplified geological map of the Nubra fault strand in Yulskam gorge, showing the studied band of phyllonite and sample location.	115
Figure 5.3 Cross-polarised optical photomicrographs of the Nubra Formation phyllonite.....	115
Figure 5.4 Backscattered electron atomic number contrast images of the Karakoram Fault Zone phyllonite.....	117

Figure 5.5 Electron backscattered diffraction (EBSD) and energy dispersive X-ray (EDX) analysis of domainal phyllonite microstructure.....	119
Figure 5.6 Electron backscattered diffraction (EBSD) and energy dispersive X-ray (EDX) analysis of muscovite-rich domain.	120
Figure 5.7 Microphysical model for frictional-viscous flow defined by Bos and Spiers (2002) and Niemeijer and Spiers (2005).....	129
Figure 5.8 Strength-depth plot for the Nubra Formation phyllonite (bold curves), calculated for strain rates of 10^{-10} and 10^{-12} s^{-1} according to equations 1-5, and Niemeijer and Spiers (2005).....	131
Figure 6.1 Geological map of the Karakoram Fault Zone, Ladakh, NW India, showing lithotectonic units, sample locations and transects A-A' and B-B' shown in Figures 5.10 and 5.11.	137
Figure 6.2 Quartz microstructures in the Nubra-Siachen leucogranite showing increasing intensity of deformation fabric a-d approaching the Nubra fault strand.	140
Figure 6.3 Relationships between quartz slip systems, deformation temperature and CPO.....	142
Figure 6.4 Pole figures showing the distribution of quartz crystal orientations as the (c) and <a> axes and the poles to the {m} (prism), {r} and {z} (rhomb) planes for 46 samples across the KFZ (Figure 6.1, Table 6.1).	152
Figure 6.5 a-axis and c-axis CPO for three typical samples with well developed CPO plotted in the finite strain reference frame to facilitate identification of dominant slip systems.	153
Figure 6.6 Examples of variation in quartz c-axes CPO intensity with increasing simple shear strain from viscoplastic self-consistency modelling.	156
Figure 6.7 Comparison of different measures of quartz c-axis CPO strength for profiles A-A' and B-B' in the Nubra and Tangtse areas respectively (Figure 6.1).....	163
Figure 6.8 Variation in quartz c-axes CPO intensity (I, Lisle, 1985) as a proxy for strain.....	164
Figure 6.9 Quartz c-axis (0001) pole figures from four granitoids deformed by KFZ shear zone strands plotted in the kinematic reference frame (X = lineation, Z = pole to foliation).....	166
Figure 6.10 Al-content in electron microprobe transects across 5 amphibole grains in sample P141 of the South Tangtse granite.	172
Figure 6.11 Quartz-strain-rate-metry results after Boutonnet et al., 2013, Figure 5.	176
Figure 6.12 Published strain profiles across predominantly strike-slip shear zones discussed in the text.....	181

Figure 7.1 Summary schematic cross-section of the structure of the KFZ in the Nubra area, also showing changes in deformation mechanisms, dominant fault rock and fault weakening mechanisms with depth.	195
Figure 7.2 Summary schematic cross-section of the structure of the KFZ in the Tangtse area, also showing changes in deformation mechanisms, dominant fault rock and fault weakening mechanisms with depth.	196
Figure 7.3 Sketch map of the tectonic features of the north Tibet region showing the major faults and localities discussed in the text.	201

1. Microgeodynamics of Strike-Slip Faults: Overview and Rationale

Abstract

Large-scale strike-slip faults, 100s km in length, are of importance to continental tectonics and present a significant seismic hazard. Fundamental characteristics of such faults are however often poorly constrained. These include changes in fault zone architecture, shear strength and strain distribution with depth. Progress in developing and testing integrated models of fault zone structure, strength and seismicity has been hindered by the paucity of exhumed strike-slip faults displaying complete fault rock series formed over wide depth ranges. Similarly, the role of strike-slip faults in accommodating orogenic deformation has been the subject of considerable debate and requires constraints (age, offset, slip-rate, structure) provided by geological investigations of the fault zones involved.

Detailed microgeodynamic study of one such fault, the Karakoram Fault Zone (KFZ), NW India, may provide insights into variations in fault structure, deformation processes and rheology throughout the upper- to mid-crust. Exhumed ductile to brittle fault rocks within the KFZ allow characterisation of deformation mechanisms, strain distributions and their spatio-temporal relationships to igneous intrusions and metamorphic country rocks. Such observations will allow models of the complete fault zone structure to be constructed, providing constraints for models of seismogenesis in continental strike-slip faults. Improved constraints on the relationships between KFZ deformation and regional tectono-metamorphic and magmatic events will allow the role of the fault within the India-Asia collision zone to be assessed.

1.1 Introduction

Strike-slip fault zones are common structures in zones of continental deformation where they accommodate horizontal crustal displacements. As well as being key structures in the field of continental tectonics, active strike-

slip fault zones are often highly seismogenic. It is pertinent therefore to investigate the structure and microstructure of such fault zones in order to constrain their deformation mechanisms, strain distributions and spatial-temporal evolution. The micro-geodynamic approach provides a powerful means of assessing the links between micro-scale structures/processes and their regional-scale impacts by making detailed grain-scale observations/measurements and interpreting their macroscopic significance. This approach benefits from on-going advances in quantitative microstructural characterisation (e.g. electron backscattered diffraction, Prior et al., 1999; Wilkinson and Hirsch, 1997), which are allowing new assessments of structural and mechanical characteristics of fault rocks and fault zones (e.g. strain distributions, deformation mechanisms, etc.), resulting in new geodynamic interpretations (e.g. Barth et al., 2013; Halfpenny et al., 2012; Singleton and Mosher, 2012; Brownlee et al., 2011; Dempsey et al., 2011; Lloyd et al., 2011; Pearce et al., 2011; Toy et al., 2008).

Although continental strike-slip fault zones have been subject to wide ranging methods of investigation (e.g. geological, geophysical and numerical modelling studies), fundamental characteristics such as the width of the deforming zone(s), strain gradients, deformation processes and fault rock shear strengths often lack precise constraints. Such characteristics are known to vary both along strike and with depth within fault zones and may evolve through time (e.g. Walker et al., 2012; Mizuno et al., 2008; Sibson, 1986). A highly informative approach to investigating fault zone structure and processes is to examine fault rocks exhumed from variable depths within the crust. These may record changes in mineralogy, deformation mechanisms and strain intensity across a range of pressure and temperature conditions. Whilst studies in this field are well advanced (see reviews by Bürgmann and Dresen, 2008; Imber et al., 2008; Wibberley et al., 2008), an on-going challenge is to accurately determine the physical and chemical conditions (e.g. temperature, stresses, strain rate and fluid activities) of deformation, the deformation mechanisms induced, and the strain gradients produced over the complete range of depths within fault zones.

A long-standing issue in the study of fault zones is to better understand how the shallower seismogenic faults continue down dip through the frictional-viscous transition zone and relate to underlying ductile shear zones (Handy et al., 2005). In particular, it is a challenge to quantitatively assess the strain distributions within mid- to lower-crustal shear zones and evaluate their structural and mechanical relationships to the shallower portions of fault zones (Cowie et al., 2013; Bürgmann and Dresen, 2008; Sibson, 1983).

In order to describe rock rheology and deformed rock microstructure under the wide range of geological conditions, several terms are used within the literature and within this study that require early clarification. *Frictional* and *viscous* describe deformation mechanisms for which shear strength is controlled by either the coefficient of friction or viscosity respectively. *Brittle* and *ductile* originate from experimentally observed stress-strain evolutions which respectively exhibit or lack a sudden stress drop associated with localised macroscopic failure of the material. As such deformed rock structures which exhibit a sharp strain discontinuity at the scale of observation are termed *brittle*, whereas those in which the strain distribution is continuous at the scale of observation are termed *ductile*. This usage of the terms involves the associated stress-strain responses. *Elastic* and *plastic* describe the propensity of a material to undergo recoverable strain or permanent strain respectively and also refer to characteristic portions of empirical stress-strain curves before and after yield. In geological usage, deformation that is dominantly *elastic* is typically associated with formation of *brittle* microstructures by *frictional* mechanisms. On the other hand, deformation that is dominantly *plastic* is typically associated with formation of *ductile* microstructures by *viscous* mechanisms. It should be noted however that there are geological exceptions to these simplifications (e.g. a *ductile* stress-strain response can be achieved by pervasive *frictional* microfracturing). These concepts are discussed further by Rutter (1986) and Schmid and Handy (1991).

This chapter develops the thesis rationale by providing an overview of the tectonic and seismogenic significance of continental strike-slip fault zones, and current models of their structure, deformation processes and mechanical properties. The thesis rationale is then presented as a series of

aims targeted at characterising the deformation processes, strength and strain distribution within a continental strike-slip fault zone throughout the upper- to mid-crust.

1.2 Strike-Slip Fault Zones: Tectonic and Seismogenic Significance

Strike-slip faults accommodate lateral displacements of adjacent rock masses across a wide range of scales. This thesis focuses on the macro- and micro- geodynamics of deformation within the largest scale of strike-slip fault, several hundred kilometres in length and showing 10s to 100s of kilometres offset. Such faults control the horizontal component of the regional response of continental crust to orogenic stresses. Thus, an in-depth understanding of the structural and mechanical properties of these fault zones is fundamental to the characterisation of continental deformation (Searle et al., 2011; Bürgmann and Dresen, 2008). Furthermore, continental strike-slip faults present a significant source of seismic hazard and have been demonstrated to pose a considerable risk to human populations living in zones of active continental deformation (England and Jackson, 2011; Jackson, 2001). Accurate hazard assessment and risk mitigation require thorough understanding of the operative seismogenic processes, which in turn requires knowledge of spatial and temporal variations in fault zone structure, rheology and deformation processes.

Orogenic zones of deformation within the continental crust typically show extensive and often complex systems of strike-slip faulting. This is well demonstrated by the Himalayan-Tibetan orogen where strike-slip faults are widespread in varying orientations (e.g. Figure 1 of Searle et al., 2011) allowing them to accommodate crustal deformation in response to loading by both plate motion boundary forces and internal buoyancy forces resulting from variations in gravitational potential energy (Thatcher, 2009). Other active large-scale strike-slip fault systems occur in orogenic settings worldwide, including the Anatolian fault system (Turkey), San Andreas Fault (California), Alpine Fault (New Zealand) and Liquiñe-Ofqui fault zone (Chile).

Whilst the theory of plate tectonics has had great success at predicting the motions of thin and rigid portions of oceanic lithosphere, the assumptions upon which the theory is based appear to break down within the continental lithosphere (Molnar, 1988). Oceanic lithosphere typically deforms by horizontal motions accommodated in highly localised zones that bound competent and undeforming plates. This contrasts with the continental lithosphere where deforming regions (e.g. orogens) cover broad areas (100-1000s of km across) in which more distributed deformation and vertical thickening/thinning may also play significant roles (e.g. Tibetan plateau, Andean cordillera, Basin and Range province). As such, the characterisation of continental deformation and the extent to which it differs from the plate tectonics of the oceanic lithosphere have been the subject of considerable and on-going debate (e.g. Thatcher, 2009; England and Houseman, 1988; Molnar, 1988; Tapponnier and Molnar, 1976;).

Interpretations of continental deformation range between two end-member models. The first considers deformation to be focussed onto individual faults that divide the deforming region into relatively undeformed plates or micro-plates (Thatcher, 2007; Peltzer and Saucier, 1996; Avouac and Tapponnier, 1993; Tapponnier and Molnar, 1976;). These may be laterally extruded (Peltzer and Tapponnier, 1988; Tapponnier et al., 1982) and/or rotated (England and Molnar, 1990) to accommodate continental convergence. Such a configuration would result from high strength contrasts between strong dry intact continental crustal blocks and relatively weaker intervening fault zones and underlying mantle rocks (Thatcher, 2009; Bürgmann and Dresen, 2008; Jackson et al., 2008; Jackson, 2002). This contrasts with the opposing view that continental crust deforms in a distributed and more pervasive manner as a result of weak crust being transported by a stronger and continuously deforming upper mantle (Hirth and Kohlstedt, 2003; Burov and Watts, 2006; Burov and Diament, 1995; England and Houseman, 1986; Chen and Molnar, 1983).

The role of individual strike-slip faults is an important consideration in models of continental deformation and varies between the two end-members. As such, it is essential to understand and characterise deformation in these fault zones as this may be used to discriminate

between the end-member models and intermediary possibilities (Searle *et al.*, 2011; Thatcher, 2009; Phillips *et al.*, 2004). One end-member strike-slip fault model considers continental deformation to be focused onto a relatively small number of faults which separate less deformed micro-plates and requires these fault zones to be highly localised, showing large offsets, high long term slip-rates and long lifespans within the orogenic cycle (e.g. Valli *et al.*, 2007, 2008; Lacassin *et al.*, 2004). The other end-member strike-slip fault model considers individual faults to play only a minor role and hence continental deformation is distributed and approaches that of a viscous continuum, with brittle faulting being the passive surface expression of pervasive ductile deformation at depth (Phillips *et al.*, 2004; England and Molnar, 1997; England and McKenzie, 1982, 1983). In such a context, individual faults will be more numerous, with each exhibiting small offsets, low long term slip-rates and shorter or incipient periods of activity in the history of the orogen (Searle *et al.* 2011; Searle and Phillips, 2007; Phillips *et al.*, 2004).

Given these disparate end-member models, it is crucial to assess the detailed characteristics of large-scale strike-slip fault zones which have potential to accommodate significant crustal deformation. It follows that, in order to understand the controls on how the continents deform, it is necessary to investigate in detail the structure, rheology and history of the zones wherein the deformation occurs – the fault zones.

Alongside the geodynamical significance of understanding deformation with continental strike-slip faults, an additional motive is provided by the seismogenic potential of such fault zones. This seismicity poses a significant risk to human populations living in zones of active continental deformation. Indeed, England and Jackson (2011) have emphasised recently the need for further focussed research into the seismic potential of the continental crust.

The strength of rock increases dramatically with increasing confining pressure and hence depth (Byerlee, 1978). The greatest crustal stresses therefore are typically borne at the base of the brittle upper crust, making this the region in which large earthquakes often nucleate (Sloan *et al.*, 2011; Marone and Scholz, 1988; Sibson, 1982). At greater depths a temperature-

controlled transition occurs, whereby frictional deformation gives way to viscous deformation, primarily by crystal plasticity, which operates at considerably lower differential stresses and is 'aseismogenic' (Sibson, 1982). The depth, structure and operative deformation processes in this frictional-viscous transition zone are the controlling factors on the seismogenic character of a fault zone. These factors are considered in detail in Chapter 3.

In order to interrogate the kinematics of fault zones at seismogenic depths, it is necessary to constrain the relationship between deformation in the ductile mid-lower crust and the stronger and seismogenic brittle upper crust.

Continuous ductile flow of a lower crustal shear zone beneath a locked brittle fault leads to time dependent accumulation of differential stress in the brittle upper crust and an increase in the vertical strain gradient across the brittle-plastic transition (Sanders, 1990). Continued loading of differential stress in the upper crust, until the failure strength of the rock is reached, results in sudden stress release as a seismic rupture. This process may repeat cyclically and is potentially responsible for the majority of large earthquakes on continental strike-slip faults (Sanders, 1990; Byerlee and Brace, 1968; Brace and Byerlee, 1966). Alternatively, large earthquakes in the upper crust may promote transient weakening and localised creep in the underlying ductile shear zones or rupture them during a co-seismic event (Yamasaki et al., 2014; Oskin et al., 2008; Sibson, 1980). Better understanding of the kinematics of these processes may result from quantitative assessment of the strain distribution over a range of depth intervals extending from the brittle upper-crust into ductile shear zones beneath. For example, Ellis et al. (2006) used numerical modelling with geophysical and geological constraints to investigate stress transfer between the frictional upper crust and ductile mid-crust in the Alpine Fault, New Zealand. They modelled the elastic and inelastic strain distribution beneath the fault over the course of seismic cycles to investigate where elastic strain accumulates, the controls on strain localisation and whether the frictional fault loads the mid-crust or vice versa. In particular, geologic constraints from the width of the exhumed mylonite zone were used to assess the validity of the predicted strain concentration down dip of the frictional fault tip (Ellis et al., 2006).

In summary, continental strike-slip faults are significant in characterising continental deformation in relation to, and deviation from, plate tectonic theory as applied to the oceanic lithosphere. They are common structures in zones of active continental deformation but the role of strike-slip faults and their impact on the evolution of orogenic systems is the subject of much debate. Further, deformation within such fault zones presents a seismic hazard and better understanding of strain accommodation at depth is required to assess deformation in the whole fault zone system. Each of these problems will benefit from a quantitative assessment of the structure, strain distribution and deformation processes operating across a range of depths within continental strike-slip fault zones.

1.3 Models of Fault Zone Structure and Deformation Processes

Models of continental fault zone structure, based primarily on exhumed fault rocks, seismology, materials science and rock deformation experiments, have been in place for several decades (Scholz, 1988, 1989; Sibson, 1977, 1982, 1983, 1986), the most successful of which has been termed the 'Sibson-Scholz' model (Figure 1.1, e.g. Imber et al., 2001). This model was based around a generalised fault structure reconstructed from the commonly observed distributions and inferred depths of formation of common quartzo-feldspathic fault rock types (Scholz, 1988, 1989; Sibson, 1977, 1983, 1986; Anderson, 1983). Within this model, relatively localised deformation (10^{-2} - 10^2 m across) in the upper crust, at temperatures below c. 300°C, is accommodated by abrasive wear during elasto-frictional deformation, forming gouges, breccias and cataclasites (Figure 1.1). At c. 300°C, the onset of quartz crystal plasticity (Tullis and Yund, 1977) defines the quartz brittle-plastic transition and the upper limit of semi-brittle shear zones, 10s of metres thick and dominated by mylonites and phyllonites, within quartzo-feldspathic rocks (Figure 1.1). At >450°C, the onset of feldspar crystal plasticity (Voll, 1976) leads to the formation of fully quasi-plastic shear zones, which generally broaden downwards from 10^2 - 10^4 m across (Figure 1.1).

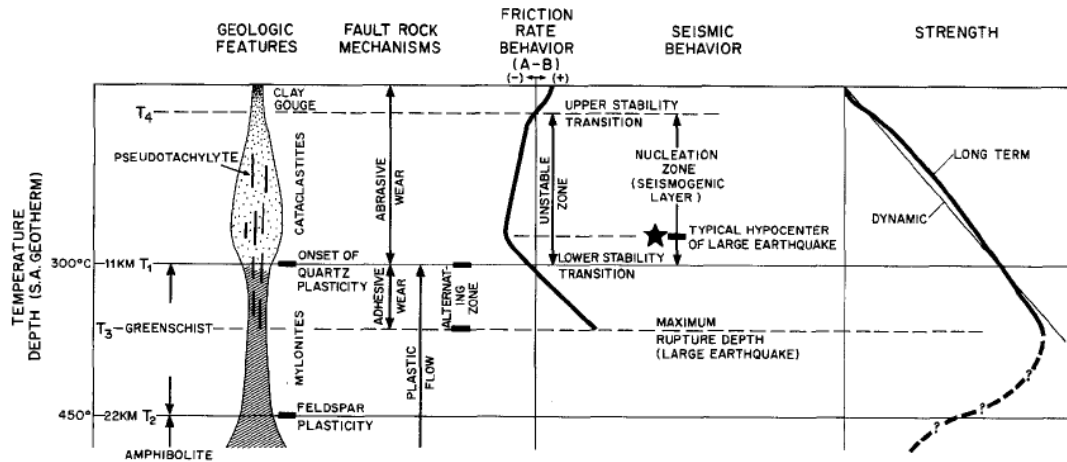


Figure 1.1 Schematic generalised strike-slip fault zone model of Scholz (1988). Major geological and seismological features are shown as a function of depth and temperature (assuming a geothermal gradient typical of the San Andreas, S.A., Fault). Friction rate behaviour is described by the A-B parameter of Ruina (1983), where positive values indicate velocity strengthening and negative values indicate velocity weakening.

These changes in fault zone structure and deformation mechanisms were broadly associated with changes in shear strength with depth. In the elasto-frictional regime, increasing lithostatic pressure, and hence normal stress on slip surfaces, results in increasing shear strength with depth, described by friction coefficients in the range 0.6-0.85 (Figure 1.1, Byerlee, 1978). Below the frictional-viscous transition however, the onset of temperature-dependent dislocation glide and creep processes results in rapidly decreasing shear strength with depth (Figure 1.1). Crustal strength in this simple two-layer model is predicted to peak therefore at c. 100-200 MPa in the bulk rock frictional-viscous transition of strike-slip faults (Scholz, 1988; Sibson, 1986). Within this model, seismogenic ruptures are predicted to nucleate within a frictionally unstable velocity weakening zone (c. 100-300°C), with the largest earthquakes forming close to the brittle-ductile transition, where crustal strength, distortional strain energy and co-seismic stress drops are typically greatest (Figure 1.1; Scholz, 1989; Sibson, 1983, 1986).

In developing the aforementioned model, Sibson (1983) raised the questions of how continental strike-slip fault/shear zones typically continue down dip within the mid- to lower-crust, and how best to characterise the structure of their ductile portions. Three possibilities were raised (Figure 1.2): (1) low grade shear zones continue down dip as similarly localised structures

throughout much of the crust/lithosphere; (2) shear zones broaden significantly downwards with boundaries diverging by up to c. 40°; and (3) steeply dipping shear zones root into shallowly dipping decollements at depths greater than c. 15 km. These questions remain pertinent and, in particular, have significant implications for models of crustal/lithospheric rheology (e.g. Cowie et al., 2013; Platt and Behr, 2011, 2012; Bürgmann and Dresen, 2008) and the nature of continental deformation (e.g. Searle et al., 2011; Vauchez and Tomassi, 2003).

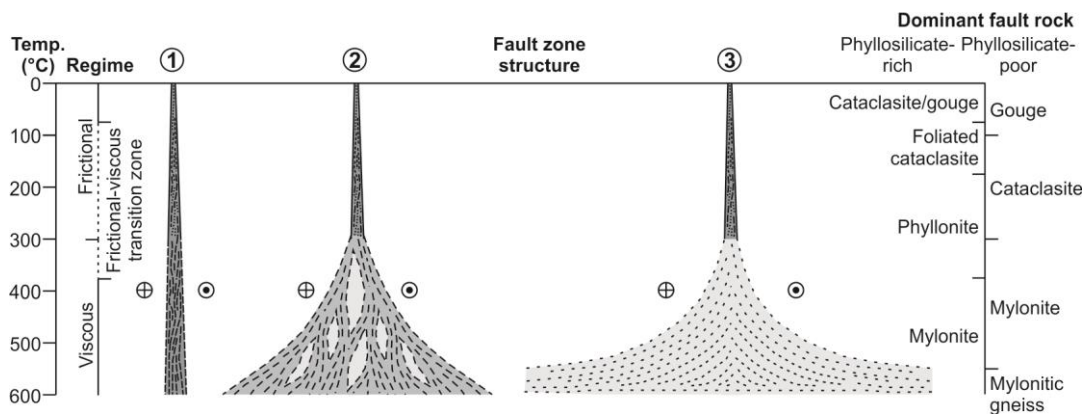


Figure 1.2 Generalised strike-slip fault zone cross-section showing schematic variations in possible strain distribution with depth. 1) Highly localised shear zone continues into mid-lower crust. 2) Broader shear zone consisting of multiple strands separating less deformed lenses and widening with depth. 3) Shear zone broadens into pervasive sub-horizontal deformation of mid-lower crust. Also shown are generalised deformation regimes and dominant fault rock types in phyllosilicate-rich and -poor lithologies. Modified from Imber et al. (2008), Holdsworth (2004) and Sibson (1983).

Many investigations have focussed on the structure, kinematics and deformation processes of exhumed strike-slip mid- to lower-crustal shear zones (e.g. Cole et al., 2007; Sartini-Rideout et al., 2006; Vauchez and Tomassi, 2003; Corsini et al., 1996; Leloup et al., 1995; Hanmer, 1988; Sørensen, 1983; Grocott and Watterson, 1980; Berthe et al., 1979). However, further studies that constrain both shear zone strain distributions and depths of formation, particularly in relation to shallower fault zone portions, are required in order to characterise complete fault zone architecture (Cowie et al., 2013; Bürgmann and Dresen, 2008).

At the time of development of the Sibson-Scholz fault zone model, field evidence for deformation mechanisms unaccounted for by the two layer rheological model was mounting (e.g. fluid-assisted diffusive mass transfer,

Mitra, 1978; Brock and Engelder, 1977; McClay, 1977), but experimental investigations (e.g. Rutter 1976, 1983) were not yet sufficiently advanced to incorporate the rheological effects of such mechanisms into fault zone models (Sibson, 1986). Subsequent studies of natural fault zones (e.g. Barth et al., 2013; Collettini et al., 2009a, 2009b; Marsh et al., 2009; Faulkner et al., 2008; Jefferies et al., 2006a, 2006b; White, 2001; Stewart et al., 2000;), along with rock/analogue deformation experiments and theoretical modelling (Niemeijer and Spiers, 2005; Bos and Spiers, 2000, 2001, 2002; Chester, 1995; Chester and Higgs, 1992), have increasingly recognised the importance of both fluids and low friction minerals in altering fault zone rheology (e.g. by promoting inter-crystalline diffusive mechanisms, fracturing, frictional sliding, hydrolytic weakening and metamorphic reactions). These effects are particularly pronounced in the frictional-viscous transition zone where deformation occurs by a complex combination of both normal stress-sensitive (i.e. frictional) and strain rate-sensitive (i.e. viscous) mechanisms (Imber et al., 2008; Bos and Spiers, 2002). Such processes are commonly associated with deformation at low shear stresses, such that the peak in the two-layer strength-depth profile is dramatically reduced, and have prompted on-going modifications to the Sibson-Scholz model (Figure 1.3; Imber et al., 2001, 2008; Holdsworth, 2004).

The recognition of such complex deformation within the upper- to mid-crust has prompted experimental and theoretical investigations into the controls on both seismic and aseismic deformation under a wide range of physical conditions and strain/slip-rates, in order to characterise the styles of deformation likely to dominate in any given setting (see reviews by Brantut et al., 2013; Gratier et al., 2013; Wibberley et al., 2008; Kanamori and Brodsky, 2004). Such studies are recognising increasingly complex processes and feedbacks that potentially operate within fault/shear zones, such as dynamic co-seismic frictional weakening (Kirkpatrick et al., 2013; Di Toro et al., 2011; Goldsby and Tullis, 2011; Han et al., 2011), the temperature and slip-rate dependence of friction coefficients (e.g. den Hartog et al., 2013; Wibberley et al., 2008; Niemeijer and Spiers, 2007) and multi-mechanism frictional-viscous creep (Bos and Spiers, 2000, 2001, 2002). Field studies that aim to constrain the complex deformation processes within natural fault zones are

relatively commonplace (see above). Very few strike-slip fault zones have been documented however that display a near continuous sequence of fault rocks from ductile shear zones to those formed at near surface depths (e.g. the Median Tectonic Line, Japan, Jefferies et al., 2006a, 2006b; the Salzachtal-Ennstal-Mariazell-Puchberg Fault, Austrian Alps, Frost et al., 2009, 2011; Cole et al., 2007). This general dearth of fully exposed fault/shear zones has hindered better appreciation of complete fault zone architecture and deformational and mechanical interactions between the different depth levels within fault zones (Cole et al., 2007).

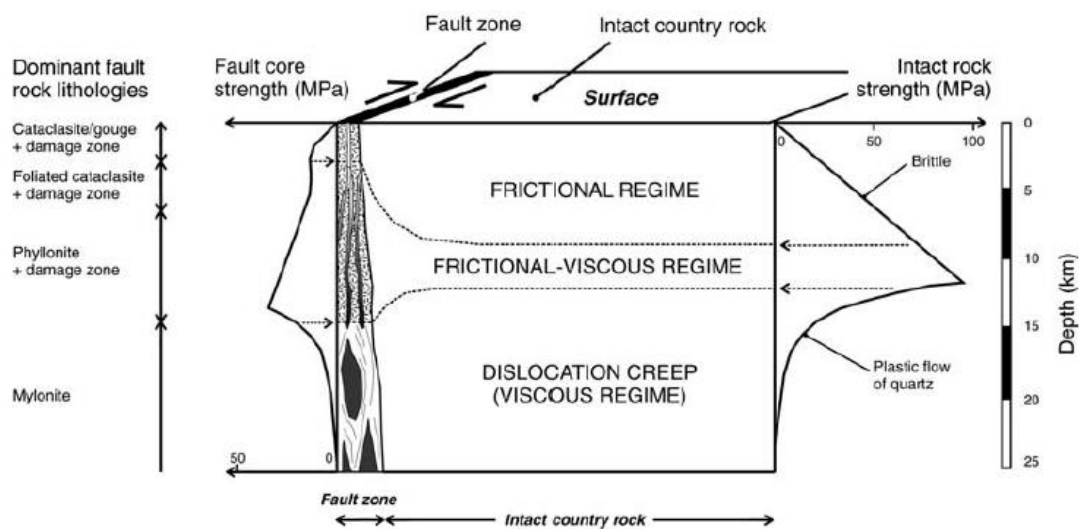


Figure 1.3 Schematic generalised fault zone model of Imber et al. (2008). Foliated fault rocks within the fault core are significantly weaker than the intact wall rock. The depth range of the frictional-viscous regime is extended within the fault core compared to the wall rock due to the contrasting rheologies of the fault and wall rock materials. Deformation within the frictional-viscous and viscous regimes is predicted to be largely aseismic.

1.4 Rationale for Investigating the Microgeodynamics of the Karakoram Fault Zone

In order to address the above questions regarding the structure, strength and deformation processes that operate within large-scale continental strike-slip faults, there is a clear need for detailed field and laboratory investigations of exhumed fault zones. In particular, examples of fault zones that contain exposed fault rocks formed across a wide range of crustal depths will provide the most information on the complete fault zone architecture and inter-relationships between deformation at different crustal

levels. The objective of this thesis is to provide such a study, using the example of the deeply exhumed Karakoram Fault Zone (KFZ), NW India, which contains a near complete fault rock sequence formed within the upper-middle continental crust.

By determining the macroscopic structure and strain distribution of the KFZ across a range of palaeo-depths, the full architecture of the fault zone can be reconstructed. Interpretation of the variations in deformation mechanisms and shear strength with depth will provide comprehensive characterisation of the processes that operated within the active fault zone. Such insights will also constrain the age, offset and thermal regime of the KFZ, allowing its role in accommodating deformation within the India-Asia collision zone to be assessed, thereby providing the tectonic context of the study. Thus, the thesis rationale is as follows.

1. To examine the geology of the central KFZ in Ladakh, NW India, including previously mapped fault rock distributions, in order to collate available data on the structure and deformation processes within the fault (Chapter 2).
2. To synthesise existing interpretations of the age, offset, slip-rate and depth extent of the KFZ, and thereby present the contrasting end-member models for the role of the fault in the evolution of the Himalayan-Tibetan orogen (Chapter 2).
3. To provide detailed descriptions of fault rock distributions and the range of fault rock microstructures present within the KFZ, in order to interpret the mechanisms and conditions of deformation and to infer approximate shear strengths during strike-slip deformation (Chapter 3).
4. To establish the relationships between the KFZ deformation reported in Chapter 3 and the pressure-temperature-time evolution of the eastern Karakoram terrane using quantitative thermobarometry and microstructural information. This will constrain the age and offset of the KFZ, conditions of deformation within it and the potential interactions between deformation, metamorphism and magmatism (Chapters 4 and 5). By demonstrating the pre-kinematic nature of leucogranite bodies which form a large proportion of the study area

(Chapter 4), strain profiles across the KFZ may then be determined (Chapter 6).

5. To provide a detailed examination of KFZ quartz crystal plastic deformation superimposed on the Eastern Karakoram Granitoids, in order to develop the use of quartz crystal preferred orientation intensity as a proxy for the strain distribution across the KFZ shear zone (Chapter 6).
6. To synthesise the geological, structural and thermobarometric data, in order to (Chapter 7): (a) evaluate the age, offset, slip-rate and thermal regime of the KFZ and its role in accommodating India-Asia convergence; (b) construct generalised cross-sections through the KFZ to elucidate its macroscopic architecture and distribution of deformation and weakening processes; and (c) examine the extent to which the structure and deformation processes of the KFZ provide analogues for those in other major active seismogenic strike-slip faults.
7. To draw conclusions on the architecture, styles of deformation and role in continental deformation of the KFZ (Chapter 8).

2. Structural and Geological Framework of the Central Karakoram Fault Zone

Abstract

The Karakoram fault zone (KFZ) is an orogen scale strike-slip fault zone delineating the western margin of the Tibetan plateau. This chapter begins with an outline of the suitability of the KFZ as an analogue for the deep portions of other active strike-slip faults. The principle lithological units in the eastern Karakoram are then introduced and the macroscopic architecture, age, offset and slip-rate of the central portion of the KFZ are discussed.

Progressive deformation within the KFZ has occurred whilst the presently exposed structural level has been exhumed since the mid-Miocene. As a result, a wide range of down-temperature overprinting fault rocks, including mylonite, phyllonite, cataclasite and gouge, crop out at the surface and are well exposed and preserved in the arid climate of the Eastern Karakoram. These fault rocks are the result of deformation of the Karakoram terrane, which consists of medium- to high-grade metamorphic country rock intruded by the Karakoram batholith. The composite Karakoram batholith is comprised of Cretaceous I-type and Miocene S-type granitoids emplaced during northward subduction and post-collisional crustal anatexis respectively.

The central portion of the KFZ consists of four geomorphologically prominent NW-SE striking fault strands linked by a transpressional restraining jog. These contain microstructural evidence for ductile deformation under upper-greenschist to lower-amphibolite grade conditions. Lower temperature fault rocks are variably distributed with phyllonite and cataclasite occurring on the Nubra strand and fault gouge occurring on the Pangong strand. Previous findings and new field work show that further deformation is distributed across several other minor faults and shear zones and that additional work is required to fully characterise the distribution and mechanisms of deformation within the KFZ. The age, offset and slip-rate of the KFZ are the subject of debate but the most reliable estimates suggest that the fault has

accommodated c. 120 km offset since 15.7-13.7 Ma at a slip-rate of c.8 mm/yr.

2.1 Suitability of the Karakoram Fault Zone for Study of Strike-slip Fault Properties, Processes and Evolution

To study the wide-ranging processes of strain accommodation within mature continental-scale strike-slip faults a suitable example to act as a natural laboratory is required. In order to be suitable such a fault should exhibit the following characteristics:

- It must be greater than several hundred kilometres in length, therefore representing the largest scale of faulting seen on the continents.
- It must have geological offsets of 10s to 100s of kilometres, therefore being a mature fault zone and typical of large continental strike-slip faults (e.g. San Andreas Fault, Alpine Fault, North Anatolian Fault, Dead Sea Fault).
- It must contain fault rocks exposed at the surface that were originally formed at depth within the crust. Ideally the fault should have been active during exhumation such that fault rocks formed at a range of depths (i.e. ranging from mylonite to gouge) are now exposed.
- It must have excellent exposure allowing regular sample collection across the fault at a range of distances from the fault trace and be situated in a suitable (e.g. arid/semi-arid) climate allowing preservation of friable fault rocks from erosion
- It should preferably be associated with an existing dataset of maps, lithological and geochronological data and be well constrained in terms of its geological history.

The Karakoram fault zone (KFZ), NW Himalaya (Figure 2.1), is a c. 800 km long strike-slip fault with dextral geological offsets of up to 120-150 km (Searle et al., 2011). It is therefore of comparable scale to the aforementioned continental scale strike-slip faults. Furthermore, the rocks at the exposed structural level of the KFZ have been deformed at a variety of depths within the mid-upper crust, resulting in a range of fault rocks, including mylonites, phyllonites, cataclasites and gouges, being currently

exposed at the surface (Phillips and Searle, 2007). The central portion of the KFZ in Ladakh, NW India, is situated in a high altitude desert environment and typically receives <100 mm rainfall per year. As a result, sparse vegetation coverage provides near 100% geological exposure across much of the region and friable fault rocks such as fault gouge are preserved from erosion. In Ladakh, the KFZ is accessible in the Nubra Valley and Tangtse regions (Figure 2.2). Access is restricted however to the Siachen region in the north and the Pangong Tso region to the south due to political tension at India's borders with Pakistan and China respectively. The central KFZ in Ladakh is therefore a suitable area to study fault zone structure and processes as an analogue for the deep portions of other active strike-slip faults.

Fieldwork was carried out along the central portion of the KFZ in Ladakh, NW India, during August 2010 and June-July 2011 (Figure 2.1). This portion of the fault has been mapped previously at both regional and outcrop scales (Phillips, 2004, 2008; Rutter *et al.*, 2007). The existing maps were used to guide fieldwork and new maps were prepared only where necessary. Fieldwork was undertaken in the two most accessible and best exposed portions of the KFZ in the Nubra valley and the region between Tangtse village and Pangong Tso (Figure 2.2), with an aim to sample transects across and approximately perpendicular to the KFZ in these two areas. In total, 153 samples were collected, along with associated structural data (e.g. foliation, lineation, fold and fault measurements) from each of the sample localities. Sample spacing was chosen based on qualitative assessment of variations in deformation fabric intensity visible in outcrop, varying between c. 500 m in areas of little variation to c. 20 m in areas of pronounced fabric intensity gradients. The geology of the central KFZ is introduced below as a synthesis of existing literature, supplemented by new photomicrographs and structural measurements along with new observations of the geology of the region SW of Tangtse village in Section 2.4.5.

2.2 Geological and Kinematic Setting of the Karakoram Fault Zone

The KFZ strikes $\sim 140^\circ$ and delineates the western margin of the Tibetan Plateau between the Mt. Kailas region of SW Tibet in the south and the Pamirs in the north (Figure 2.1). In the vicinity of the KFZ, the Himalayan-Tibetan orogen is comprised of three terranes accreted to the Asian margin (Figure 2.1; Searle and Phillips, 2007). To the west of the KFZ, the Karakoram terrane is accreted onto Asia along the Rushan-Pshart suture. These correlate across the KFZ with the Qiangtang terrane of Tibet and the Jinsha suture. Immediately south of the Karakoram terrane lies the Kohistan-Ladakh arc, a calc-alkaline island arc terrane accreted to the Karakoram terrane along the Shyok suture. These correlate with the Gandese batholith, which forms the southern margin of the Lhasa block in Tibet, and the Bangong suture where the Lhasa block meets the Qiangtang terrane. At the southern edge of this arc terrane the Indus and Yarlung-Tsangpo sutures mark the site of final collision between India and Asia and delineate the northern extent of India derived Himalayan units (terrane and suture correlations from Searle and Phillips, 2007). In the study area, the KFZ forms the contact between the Asian rocks of the Eastern Karakoram to the NE and the accreted Ladakh-Kohistan arc rocks and associated Shyok suture zone to the SW (Figure 2.2).

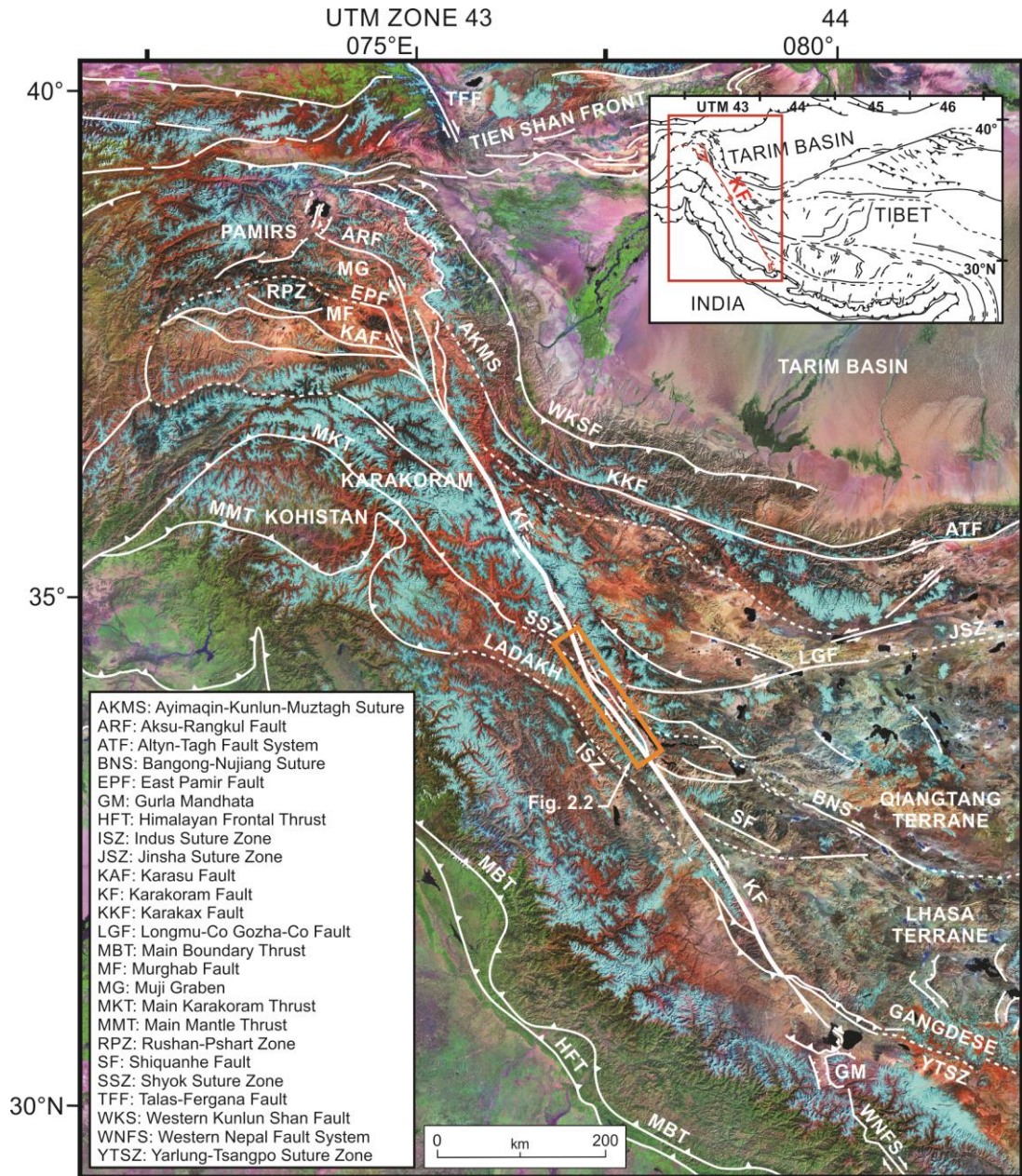
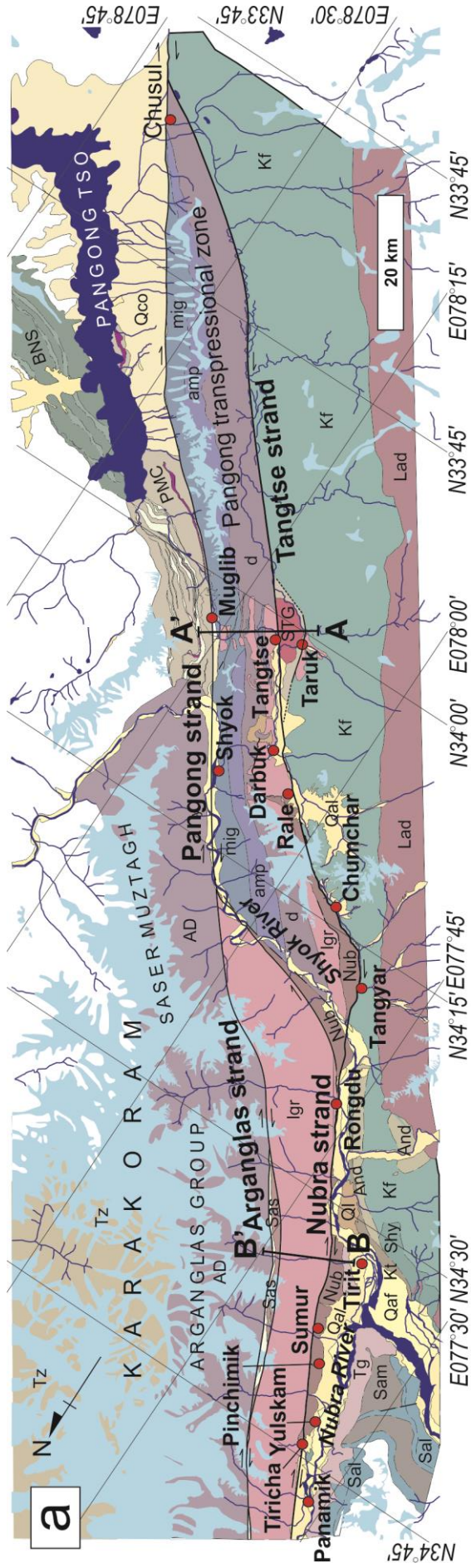


Figure 2.1 Fault map of western Tibet showing major structures superimposed on a Landsat 7 image montage. The Karakoram fault zone is highlighted (centre) and the portion enlarged in Figure 2.2 is marked by the orange rectangle. Inset shows the tectonic framework of Tibet. Modified from Phillips (2008).



KARAKORAM TERRANE		LADAKH TERRANE		QUATERNARY UNITS	
lgr	22-13 Ma Bitmstgrt monzogranites inc Nubra-Slachen and Tangtse-Darbuk lgr	Kt	Khalisar Thrust Zone: sheared greenschists	[Blue box]	Permanent snow & ice
STG	18.5 Ma South Tangtse Granite	Shy	Shyok Formation: basalts and quartzites	Qaf	Flood plain deposits: pebble gravel, sand & silt
d	Hbl+Bt monzogranite pluton	And	Khardung Andesites	Qal	Alluvial deposits: cobble-pebble gravel, sand, silt & clay
mig	82 Ma hbl+bt diorite & <15 Ma bitmstgrt monzogranite dykes	Kf	Khardung Fm: 63 Ma rhyolitic pyroclastics & volcaniclastics	Qco	Colluvial deposits: boulder-cobble-pebble, gravel & sand
AD	Migmatite: 107 Ma hbl+bt diorite melanosome & 17 Ma bt+ms monzogranite leucosome	Lad	<65 Ma Ladakh calc-alkaline granitoids	Qtr	River terrace deposits: cobble-pebble gravel, sand and silt
Tz	108 Ma Arganglas Hbl+bt diorite	Tg	68 Ma Tirit granitoids: diorites-granites	Ql	Post-glacial lacustrine deposits: gravel, sand & silt
amp	Karakoram Teihyan Zone: limestone & calcareous sandstone	Sam	Saltoro Molasse: shales, silts, sandstones & conglomerates		
PMC	EKMC: Amphibolite & <15 Ma bitmstgrt monzogranite dykes	Sal	Saltoro Fm: slates, phyllites, silts		
Sas	EKMC: Pangong Metamorphic Complex: grt-st schist, marble & amphibolite	BNS	limestones marbles and volcanics		
Nub	EKMC: Saser Fm metapelites and marble		Bangong-Nujiang suture zone		
	EKMC: Nubra Fm metapelites, metavolcanics & marble				

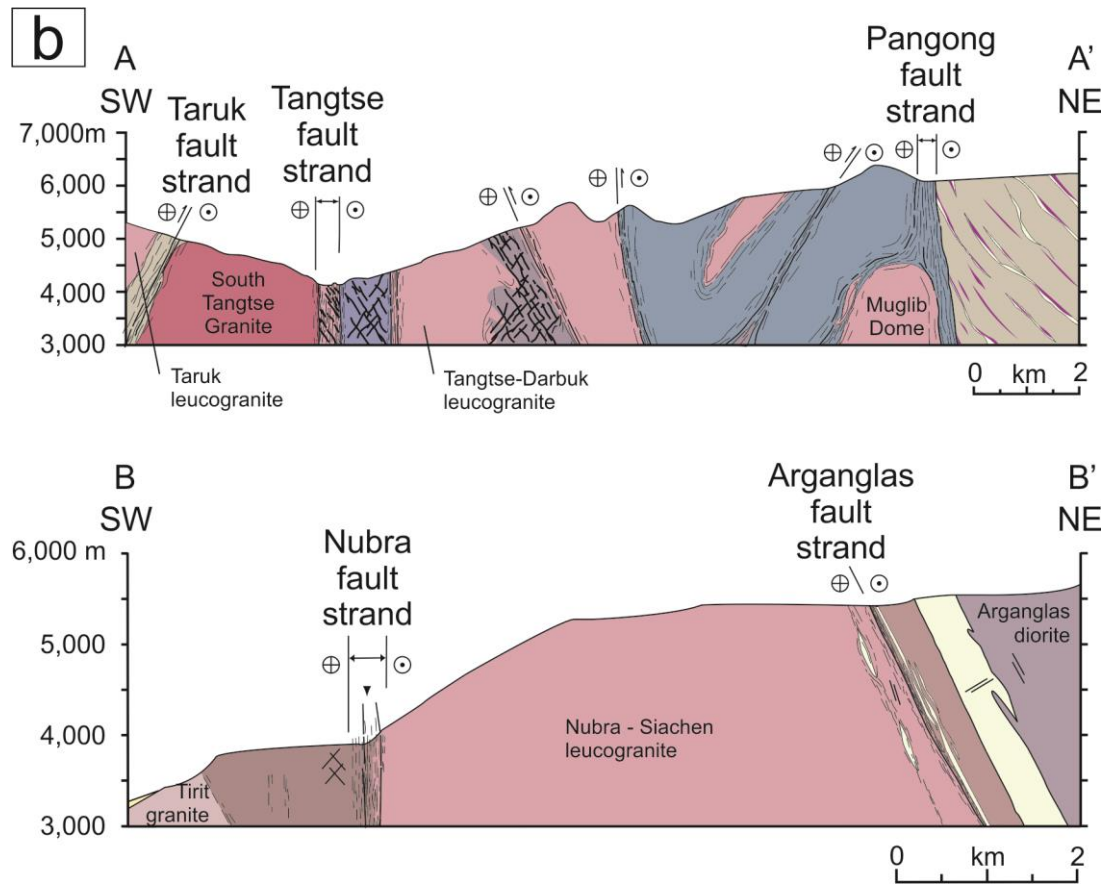


Figure 2.2 The Karakoram fault zone, Ladakh, NW India. a) Geological map of the central Karakoram fault zone showing the principle lithological units, major fault strands and geographic features mentioned in the text. Positions of cross-sections shown in Figure 2.2b are marked A-A' and B-B' b) Geological cross sections A-A' and B-B' marked on Figure 2.2a. Major fault strands and granitoid bodies mentioned in the text are labelled. Modified from Phillips (2008).

The KFZ is orogen-parallel in the NW Himalaya and partitions much of the right-lateral motion (14 mmyr^{-1} , $\text{N}145^\circ$) resulting from oblique India-Eurasia convergence (33 mmyr^{-1} , $\text{N}016^\circ$) from orogen-perpendicular shortening on the Himalayan thrusts (29 mmyr^{-1} , $\text{N}045^\circ$) (Houlié and Phillips, 2013). At its northern extremity in the Pamirs, the KFZ branches into numerous splays, including the Aksu-Rangkul, Aksu-Murghab, East Pamir and Karasu strike-slip faults, and may be kinematically linked to N-verging thrusts in the Rushan-Pshart zone (Figure 2.1) (Strecker et al., 1995). At its southern tip the KFZ has been suggested to transfer dextral slip along the Yarlung-Tsangpo suture (Lacassin et al., 2004, Peltzer and Tapponnier, 1988) or to link with the South Tibetan Detachment (Pêcher, 1991). However, structural mapping, geochronology and kinematic data suggest that the KFZ instead links with the Gurla Mandhata detachment system, which may form the

extensional terminus of the fault (Murphy et al., 2002). Recent mapping in western Nepal indicates also that some slip may be transferred through the Himalaya on the Western Nepal Fault System to the Main Himalayan Thrust, marking the SE limit of strain partitioning in the NW Himalaya (Murphy et al., 2014).

2.3 Geological Units

The central portion of the KFZ in the Eastern Karakoram cuts through granitoids and metamorphic country rocks of the Karakoram terrane and juxtaposes them with intrusive and extrusive igneous units of the Ladakh terrane (Figure 2.2). The metamorphic rocks of the Karakoram terrane are termed the Eastern Karakoram Metamorphic Complex (EKMC), which is comprised of the predominantly amphibolite grade Pangong Metamorphic Complex (PMC), Pangong Transpressional Zone (PTZ), Saser Formation and Nubra Formation (Phillips, 2008). These consist variably of amphibolites, metapelites, marbles, psammites and metavolcanics. The EKMC is intruded by three suites of granitoids of mid-Cretaceous, late-Cretaceous and Miocene age (Phillips et al., 2013). The Ladakh terrane consists of calc-alkaline granodiorites and associated volcanics of the Ladakh arc (Weinberg and Dunlap, 2000). These units are introduced in more detail below.

2.3.1 Eastern Karakoram Metamorphic Complex

The EKMC includes all of the metamorphic country rocks of the Karakoram terrane within the Eastern Karakoram. Subdivisions of the unit were formalised by Phillips (2008) as the Nubra Formation, Saser Formation, Pangong Metamorphic Complex (PMC) and Pangong Transpressional Zone (PTZ) (Figure 2.2). These subdivisions are followed throughout this thesis. Several previous authors have noted the close comparison between the EKMC and the Karakoram Metamorphic Complex of the central-western Karakoram in Pakistan, suggesting that the EKMC represents its along strike continuation offset by the KFZ (Phillips et al., 2013; Streule et al., 2009; Searle and Phillips, 2007).

The Nubra Formation crops out between Tiricha and Rale as a band of steeply bedded marble, basic-intermediate metavolcanics and metapelites up to 2.5 km thick (Figures 2.2 and 2.3). The outcrop runs parallel to the KFZ and the Nubra and Shyok rivers. Based on fossil fauna, Thakur et al. (1981) suggested that sedimentary protoliths of the Nubra Formation were deposited during the Permian. Metavolcanics within the formation are predominantly greenschist facies and metapelites range from greenschist to biotite-garnet-kyanite grade, with local andalusite growth adjacent to the Miocene leucogranite. Mylonitic and phyllonitic deformation microstructures are present within the Nubra Formation and in the Nubra area these generally increase in intensity towards the NE contact with the Nubra-Siachen leucogranite.

The Saser Formation crops out as a 35 km long band between the Nubra-Siachen leucogranite and Arganglas diorite in the Saser Muztagh range (Figure 2.2). It consists of bands of pure calcite marble and Qtz+Bt+Fsp+Ms±grt metapelite dipping c.60° NE and forming a maximum structural thickness of c. 900 m (Figure 2.4). Due to its high altitude and remote location the Saser Formation has previously been little studied (Phillips and Searle, 2007). Dark brown metapelites dominate the lower portion of the Saser Formation adjacent to the Nubra-Siachen leucogranite and display mylonitic fabrics. The upper section of the sequence is dominated by coarse grained pure marbles that are relatively less deformed.

The PMC lies to the NE of the Pangong strand of the KFZ, extending from the NW shore of Pangong Tso to the Shyok river (Figure 2.2, Phillips 2008), and consists of a sequence of interlayered amphibolites, marbles, psammites and Grt+St metapelitic schists (Figure 2.5). Grt+St metapelites were metamorphosed at peak sillimanite-grade conditions at c. 108 Ma (Streule et al., 2009) and then subsequently metamorphosed under staurolite-grade conditions of 585-605 °C, 605-725 MPa prior to initiation of the KFZ (Streule et al., 2009). Calcite grain size in PMC marbles records grain growth under temperatures of 300-480 °C, in accord with a temperature of 460±92 °C estimated from the mineralogy of an interlayered Bi+Pl schist (Rutter et al., 2007). Deformation fabric intensity in each lithology increases towards the Pangong strand of the KFZ, which forms the

SW margin of the PMC. Well developed mylonitic fabrics are present in marbles deformed within the Pangong strand (Rutter et al., 2007).

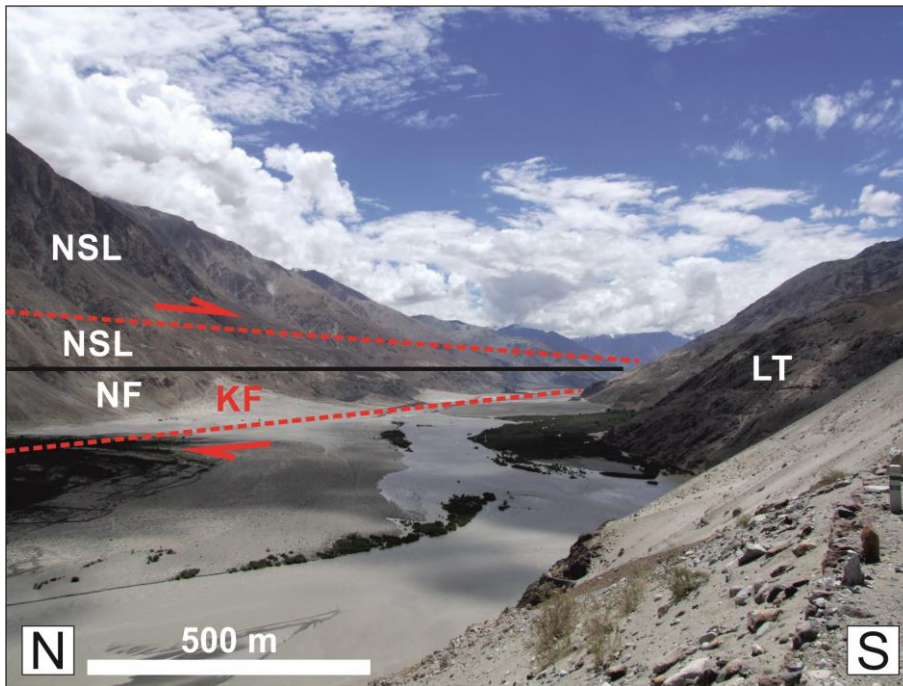


Figure 2.3 The Nubra fault strand of the Karakoram Fault (KF) in the Nubra valley follows the contact between the Nubra Formation (NF) and the Nubra-Siachen Leucogranite (NSL) and juxtaposes these units of the Karakoram Terrane with the Ladakh Terrane (LT) to the SW.

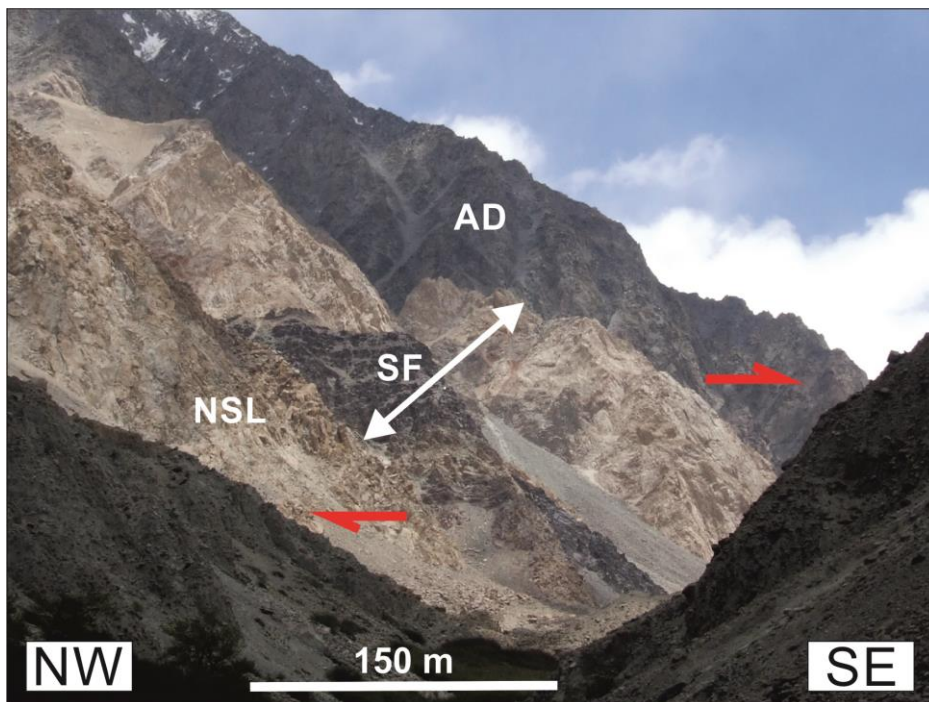


Figure 2.4 The Saser Formation (SF) in Sumur gorge is deformed by the dextral Arganglas fault strand and bounded by the Nubra-Siachen Leucogranite (NSL) and Arganglas Diorite (AD).

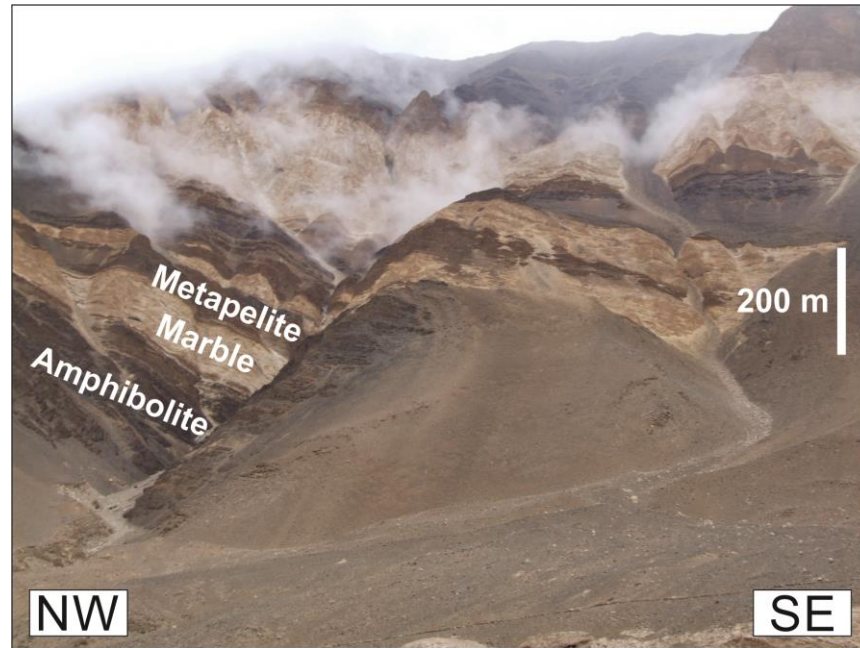


Figure 2.5 The Pangong Metamorphic Complex between Muglib and Pangong Tso consisting of thick steeply-dipping bands of dark amphibolite, brown metapelites and pale marble.

The rocks of the PTZ constitute the 6000 m high transpressionally uplifted Pangong range that is mainly bounded by the Tangtse and Pangong strands of the KFZ (Figures 2.2 and 2.6a). Prograde metamorphism of the PTZ is recorded by Grt+Ky+St metapelites in which garnets have Mn-rich, Fe-poor cores overgrown by Mn-poor, Fe-rich rims at 680 °C, 850 MPa (Thanh et al., 2011). Rolland and Pêcher (2001) proposed that peak metamorphic granulite facies conditions of >800 °C, c. 550 MPa were attained on the basis of the assemblage Cpx+Prg+Scp+Spl+Qtz+Pl. However, such high temperature scapolite-bearing assemblages have not been recognised by other workers and more widely preserved mineral assemblages span upper amphibolite (Figure 2b) to greenschist facies (Reichardt et al., 2010) and have been suggested to record conditions of 700-750 °C, 400-500 MPa and 350-400 °C, 300-400 MPa respectively (Rolland et al., 2009; Rolland and Pêcher, 2001). Extensive migmatization of metapelites, Bt-psammities and Cretaceous granodiorites is evident within the PTZ (Figure 2.6b). Reichardt et al. (2010) proposed that this anatexis occurred at 675-750 °C, 600-800 MPa by the reaction $Bt+Pl+Qtz+fluid=Hbl+melt\pm Kfs$. Migmatization of the currently exposed structural level occurred at c. 17.4 Ma, whilst leucogranitic dykes and plutons in the PTZ span 22-13 Ma (Phillips et al., 2013). The retrograde path of the PTZ is constrained by $^{40}Ar/^{39}Ar$ thermochronology of

Hbl, Kfs, Bt and Ms, which show cooling through c. 510 °C between 13-15 Ma and through 300-400 °C between 7-12 Ma (Boutonnet et al., 2012; Mukherjee et al., 2012; Dunlap et al. 1998). Zones of variably intense mylonitic deformation fabrics are distributed throughout the PTZ, typically at the contacts between different lithologies. However, the intensity of deformation fabrics increases markedly within a few hundred metres of the Tangtse and Pangong fault strands which bound the PTZ (Phillips and Searle, 2007).

2.3.2 Eastern Karakoram Granitoids

The EKMC is intruded by the Karakoram batholith, a composite batholith formed of middle and late Cretaceous subduction-related I-type diorites, monzo-diorites, granodiorites and tonalites along with post-collisional Miocene S-type monzogranites and leucogranites (Figure 2.2; Phillips et al., 2013). The middle Cretaceous suite consists of the Arganglas hbl+bt diorite pluton along with sheets of dioritic hbl+bt±cpx orthogneiss and migmatite restite within the PTZ. The late Cretaceous suite consists of bands of monzodiorites and syenogranites within the PTZ. The Miocene suite is formed of the qtz+pl+kfs+bt±ms±grt Nubra-Siachen, Tangtse-Darbuk, Muglib and Taruk leucogranite plutons along with numerous leucogranitic and pegmatitic dykes which intrude throughout the Karakoram terrane.

The middle Cretaceous suite consists of metaluminous calc-alkaline diorites intruded into the Karakoram terrane at c. 109 Ma above a north-dipping subduction zone (Phillips et al., 2013). The 108.6 Ma Arganglas diorite intrudes rocks of the Karakoram Tethyan zone in the Saser Muztagh range above the Nubra Valley (Phillips et al., 2013). It is a relatively homogenous pl+hbl+bt+kfs+qtz±cpx tonalite-diorite (Figures 2.4 and 2.7). Deformation is relatively minor and restricted to the southern margin of the Arganglas diorite where it borders the Arganglas fault strand of the KFZ. In the PTZ, diorites of similar age have gneissose texture and underwent partial migmatisation during the Miocene (Phillips et al., 2013).

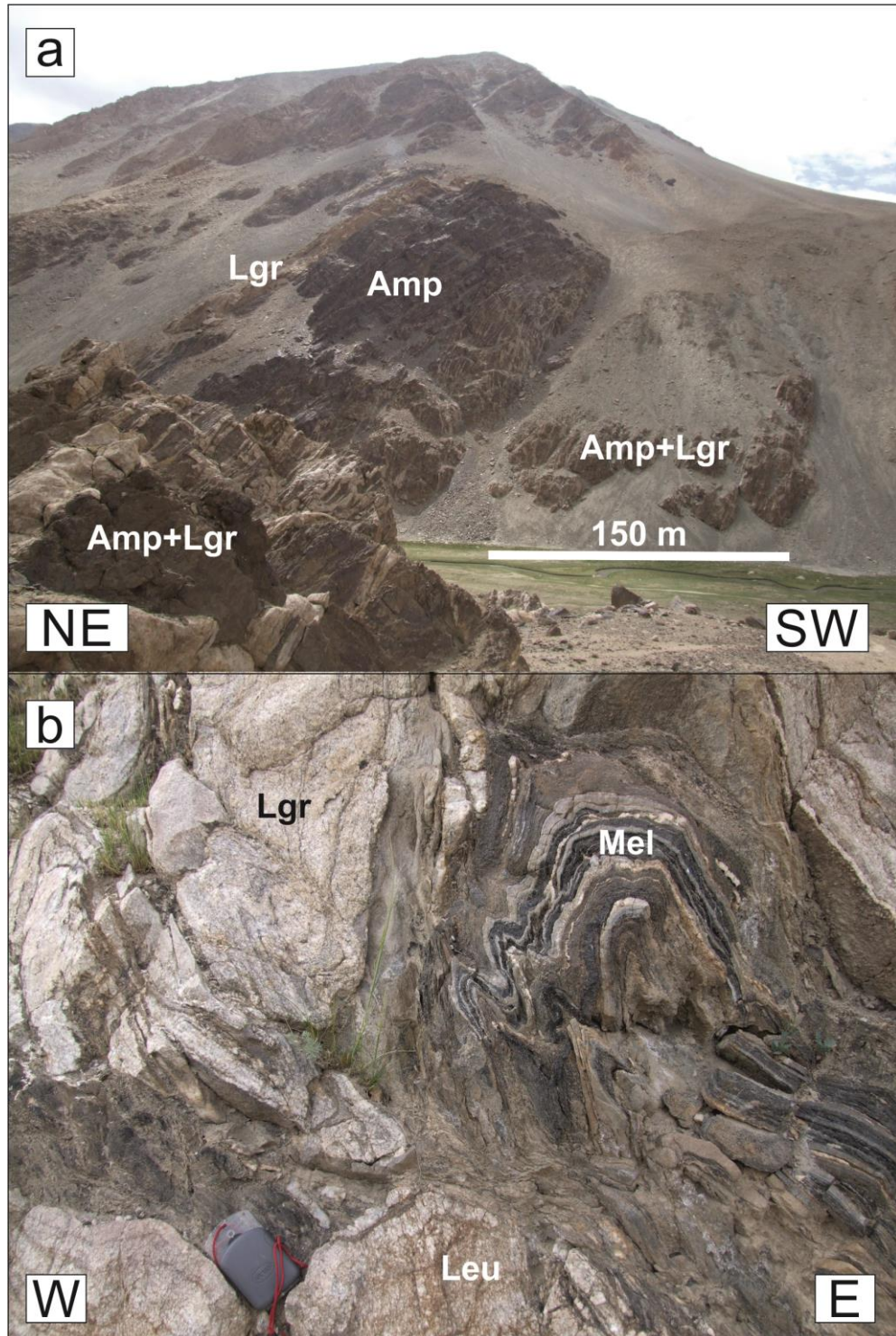


Figure 2.6 The Pangong Transpressional Zone (PTZ). a) The SW portion of the PTZ near Tangtse village, consisting of amphibolite (Amp) and diorite intruded by leucogranite (Lgr) dykes (foreground and centre right) and large sheets (top left). b) Folded diatexite migmatite in the NE PTZ in the Tangtse-Muglib gorge, consisting of amphibolitic melanosomes (Mel), leucogranitic leucosomes (Leu) and segregated leucogranite layers (Lgr). Compass clinometer 11 cm in length.

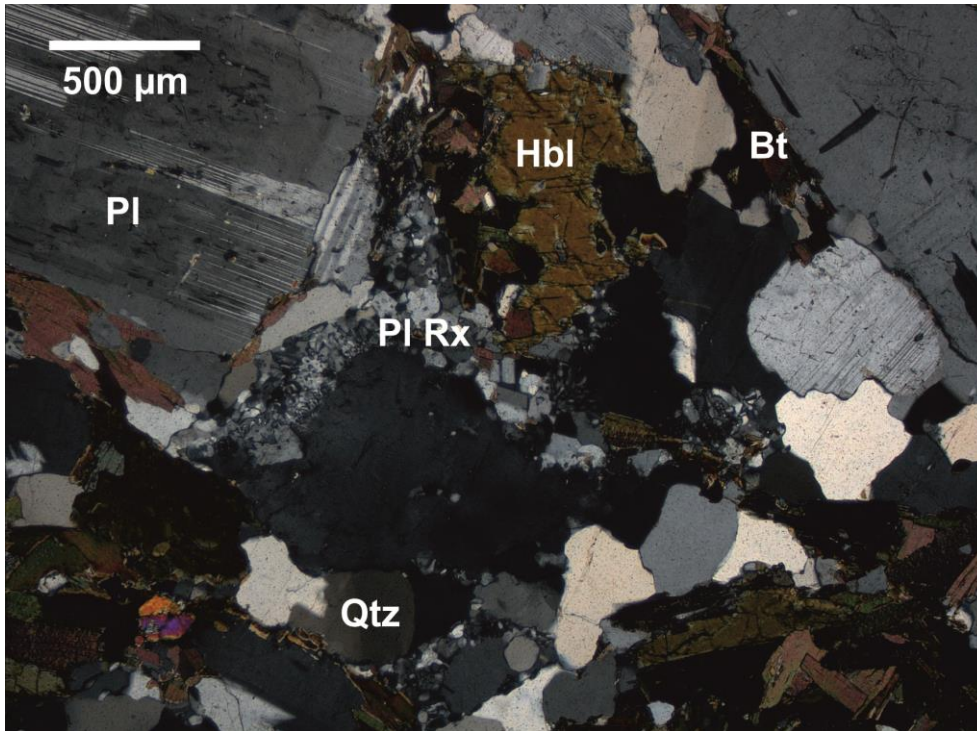


Figure 2.7 Cross-polarised photomicrograph of the Arganglas Diorite showing coarse grained weakly deformed plagioclase (PI), hornblende (Hbl), quartz (Qtz) and finer recrystallised plagioclase (PI Rx).

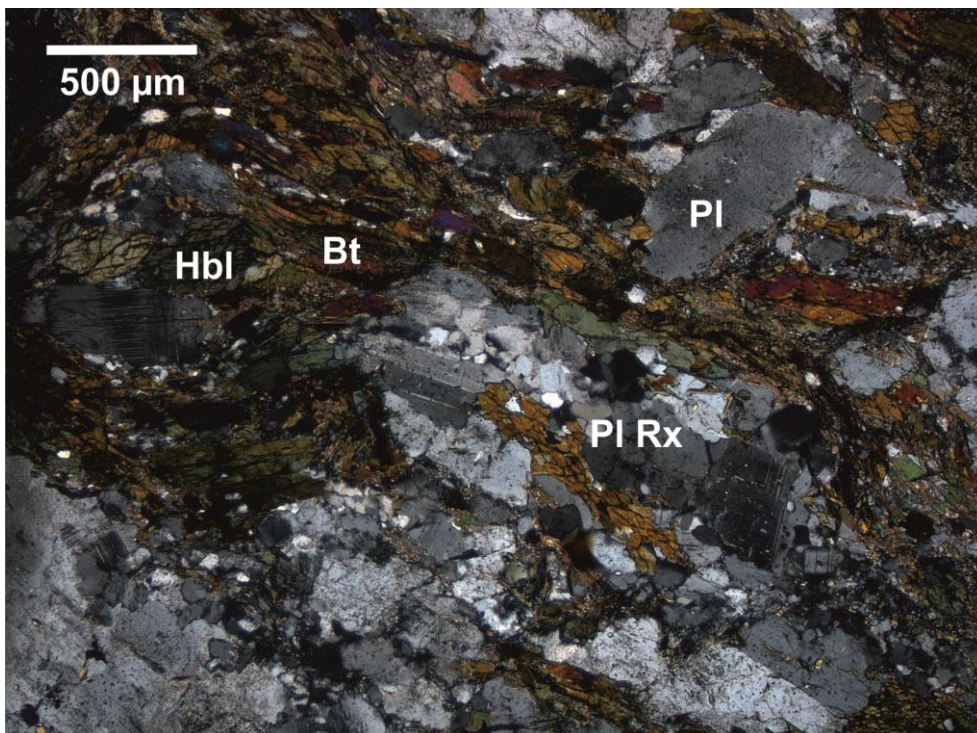


Figure 2.8 Cross-polarised photomicrograph of protomylonitic Late Cretaceous diorite near Darbuk. Plagioclase (PI) has undergone moderate dynamic recrystallisation (PI Rx) and grain size reduction. Layers of splintered hornblende (Hbl) and biotite (Bt) impart gneissosity.

Late Cretaceous granitoids occur within the PTZ and range in composition from monzodiorite to syenogranite with varying proportions of $pl+hbl+bt+kfs+qtz\pm cpx$. Ages for this suite span 82.7-69.0 Ma, with magmatism interpreted as having resulted from prolonged closure of a back arc basin between the Ladakh island arc and the Karakoram terrane (Phillips et al., 2013). Rocks of the Late Cretaceous suite are typically coarse grained with some gneissosity in dioritic lithologies. Protomylonitic textures are present adjacent to the Pangong strand of the KFZ near Darbuk (Figure 2.8).

The Miocene suite consists of a sequence of progressively more evolved intrusions emplaced between 22 and 13 Ma (Phillips et al., 2013). Bt monzogranites are generally the oldest and form the bulk of large plutons including the Nubra-Siachen and Tangtse-Darbuk leucogranites (Figure 2.3). These are associated with generally younger marginal $bt\pm ms\pm grt$ leucogranite sheets and kilometric plutons such as the Muglib leucogranite dome and the Taruk leucogranite. Deformation is typically localised at the margins of the larger leucogranite bodies, with the plutons appearing weakly deformed or undeformed in their centres. $Bt\pm ms\pm grt$ leucogranite dykes radiate from the margins of the plutons and are also emplaced more widely throughout the Karakoram terrane. These are either concordant or discordant with the country rock foliation. The latest stage of magmatism exposed in the Eastern Karakoram consists of leucocratic pegmatite dykes which typically cross-cut all ductile deformation fabrics.

2.3.3 Ladakh Terrane Granitoids

The Ladakh batholith is c. 30 km wide and situated between the Indus suture in the south, Shyok suture in the north and KFZ in the east. It consists of a calc-alkaline suite of arc-related plutonic rocks ranging from olivine-norite to granite with $pl+Kfs+qtz+hb+bt+ttn$ granodiorite being most abundant. The Ladakh batholith forms the along strike continuation of the Kohistan and Gangdese batholiths in Pakistan and Tibet respectively. In Ladakh, ages for the batholith span 70-50 Ma corresponding to the duration of subduction of Tethyan oceanic crust in this region (Weinberg and Dunlap, 2000). Much of the batholith is isotropic and undeformed. However, large ductile shear zones have been recognised near Leh and Thanglasgo and are regarded as

having been active prior to the initiation of localised shearing along the KFZ (Weinberg and Dunlap, 2000).

The Tirit granite is a distinct elongate (c. 35x6 km) body of calc-alkaline granite located at the confluence of the Nubra and Shyok rivers. It ranges from pl+hbl+bt+Kfs+qtz±cpx diorite to granite (Figure 2.9) and was emplaced within the Nubra and Saltoro formations at 68 Ma (Weinberg et al., 2000). On the basis of its age, mineralogy and geochemistry the Tirit granite is considered to have formed during the same subduction-related phase of magmatism as the Ladakh batholith (Weinberg et al., 2000). The Tirit granite is isotropic and undeformed.

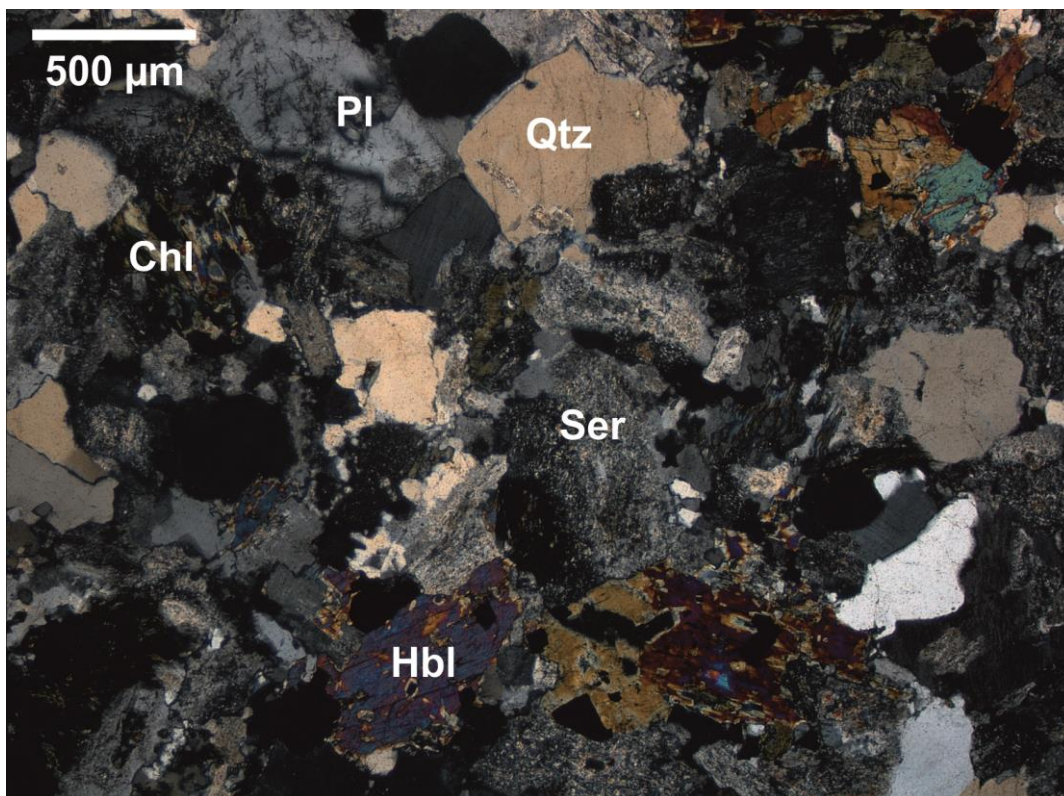


Figure 2.9 Cross-polarised photomicrograph of the 68 Ma Tirit granite, showing hornblende (Hbl), plagioclase (Pl), sericite/saussurite (Ser), chlorite (Chl) and strain free quartz (Qtz).

2.3.4 Ladakh Terrane Volcanics

The Ladakh volcanics are situated along the NE margin of the Ladakh terrane and are the extrusive products of Ladakh arc magmatism. The Ladakh volcanics include the Khardung Formation, Khardung Andesites and the Shyok Formation.

The Khardung Formation is a suite of predominantly volcanic rocks situated along the NE margin of the Ladakh terrane. They outcrop along the length of the KFZ in Ladakh from the Shyok River southwards. The volcanics are primarily intermediate to felsic in composition with pyroclastics, volcanoclastics and tuffs interbedded with chert and limestone in its upper portions (Thakur and Misra, 1984). The Khardung Formation was deposited between 68-60 Ma, coincident with the emplacement of the Ladakh batholith (Dunlap and Wysoczanski, 2002; Srimal et al., 1986b). A c. 2 km wide outcrop of andesite is exposed in the Khardung and Khalsar areas and is termed the Khardung Andesite. The Khardung Formation is tilted moderately NE but internally is little deformed. Deformation fabrics within the Khardung Formation increase in intensity towards the Khalsar thrust at their northern margin, but fabrics attributable to KFZ deformation are sparse. The Khardung Formation unconformably overlies the Shyok Formation, a series of Early Cretaceous metasediments and metavolcanics exposed near Deshkit (Dunlap and Wysoczanski, 2002).

2.3.5 Shyok Suture Zone

The Shyok suture zone separates the Ladakh terrane in the SW from the Karakoram terrane in the NE and intersects the KFZ at the confluence of the Shyok and Nubra rivers. In this region the suture zone consists of a c. 10 km wide zone of ultramafic, mafic and sedimentary rocks forming an ophiolitic sequence termed the Saltoro Formation (Phillips, 2008; Searle, 1991). The Saltoro Formation is unconformably overlain by a c. 500 m thick continental molasse unit termed the Saltoro molasse which truncates older thrusts and contains boulders derived from the Ladakh batholith (Phillips, 2008; Searle, 1991; Thakur and Misra, 1984). Srimal (1986a) has reported similarity between the rocks of the Shyok suture zone and those of the Bangong-Nujiang suture zone outcropping at the northern tip of Pangong Lake. Since both the Shyok suture zone and Bangong-Nujiang suture zone lie within areas of restricted access at India's borders with Pakistan and China respectively, these rocks are not considered further in this study.

2.4 Structural Architecture of the Central Karakoram Fault Zone

In Ladakh, the central portion of the KFZ consists of two dominant fault strands linked by a left-hand restraining bend (Figure 2.2). In the Nubra area, they are termed the Nubra and Arganglas strands. These continue into the Tangtse area as the Tangtse and Pangong strands respectively. The fault strands vary from moderately NE dipping to subvertical. Shallowly dipping lineations (mineral alignment and stretching) and shear sense indicators (e.g. S-C fabrics, asymmetric mantled porphyroclasts) show that motion on each of these fault strands is dominated by dextral strike-slip (Phillips and Searle, 2007). Compression against the restraining bend has resulted in the formation of a well developed transpressional zone termed the Pangong Transpressional Zone (PTZ) (Figure 2.2). Numerous ductile shear zones and minor brittle faults are distributed throughout the PTZ with lineations plunging *c.* 20° NW indicating an oblique component to the deformation (Searle et al., 1998). Thermochronometric data show that rocks in the vicinity of the KFZ have been continuously exhumed and cooled since at least 20 Ma (Boutonnet et al., 2012; Mukherjee et al., 2012; Bhutani et al., 2003; Dunlap et al., 1998; Searle et al., 1998). As a result, the KFZ contains a wide range of fault rock types formed at different crustal depths and temperatures (Phillips and Searle, 2007). The structure, kinematics and fault rocks of each of the main strands of the KFZ are described in more detail below.

2.4.1 Nubra strand

The Nubra fault strand runs along the Nubra valley and the SW margin of the Nubra-Siachen leucogranite at its contact with the adjacent Nubra Formation (Figures 2.2 and 2.3). In Sumur gorge, leucogranite dykes and larger sheets extend from the main body of the leucogranite into the Nubra Formation, demonstrating that the fault strand approximately follows the original intrusive contact (Figure 2.10). Both the leucogranite and the Nubra Formation metapelites display protomylonitic-mylonitic deformation fabrics visible in outcrop for several hundred metres either side of the contact with fabric intensity increasing towards the contact (Phillips and Searle, 2007).

Both the mylonitic foliation and lineation show moderate variation in orientation, but their mean orientations of 138/85NE and 19/133 (Figure 2.11) respectively indicate dominantly strike-slip motion with a minor normal component. Both NE and SW dipping foliations have both NW and SE plunging lineations, suggesting that two sets cannot be distinguished on this basis (Figure 2.12). Numerous, more localised zones of deformation overprint the mylonitic shear zone and are interpreted to have formed at lower temperatures and shallower depths during exhumation (Phillips and Searle, 2007). The mylonitic Nubra Formation metapelites are overprinted by a <10 m wide band of phyllonite with foliation and lineation oriented 140/70SW and 20/140 respectively (Figure 2.11). A <2m wide subvertical zone of cataclasite is present at the margin of the leucogranite in Sumur gorge (Figure 2.13) and more minor cataclastic faults of variable orientation are present for at least 1 km into the batholith.

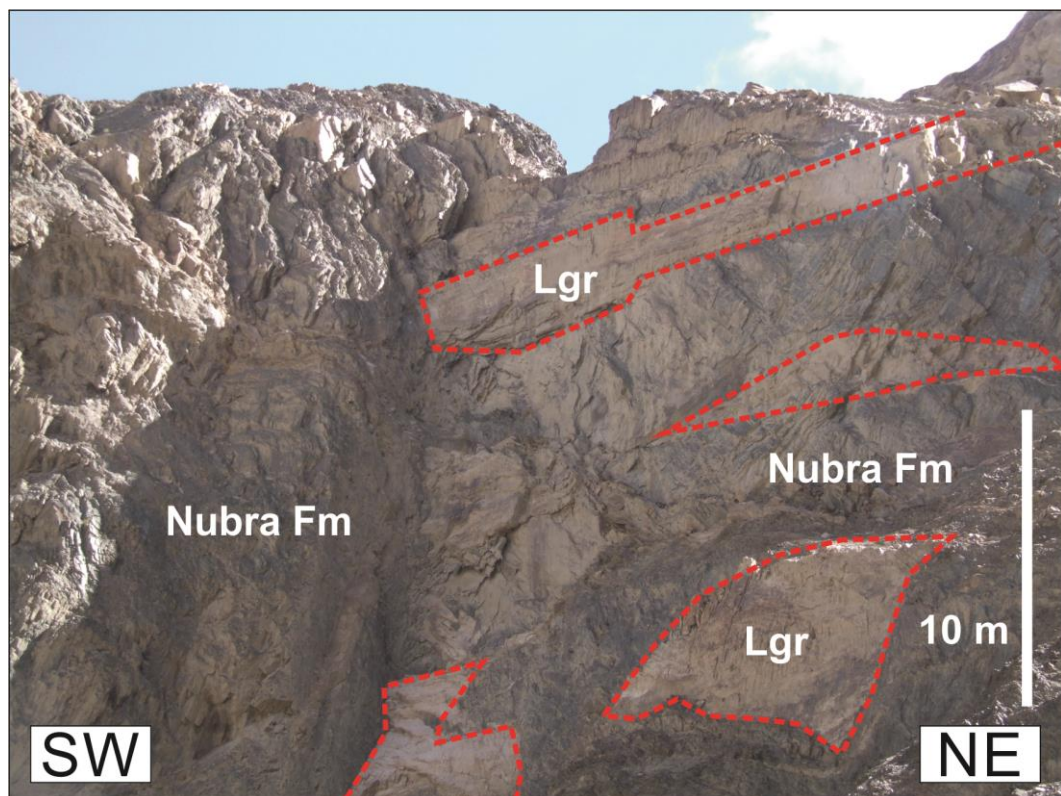


Figure 2.10 Leucogranite (Lgr) pods and sheets intruding the Nubra Formation in Sumur gorge. Leucogranite emanates from the main body of the Nubra-Siachen leucogranite slightly out of shot to the right.

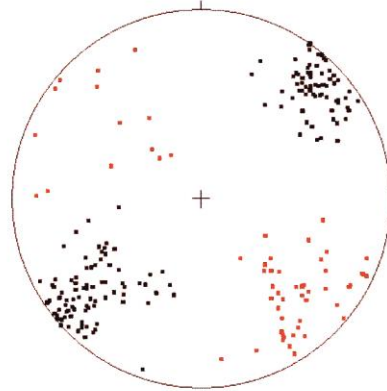
2.4.2 Arganglas strand

The Arganglas fault strand follows the Saser Formation between the Nubra-Siachen leucogranite and Arganglas diorite in the Arganglas group of the Eastern Karakoram range (Figures 2.2 and 2.4). Metapelites of the Saser Formation display mylonitic fabrics, whilst protomylonitic fabrics are also present in the adjacent Nubra-Siachen leucogranite to the SW and Saser Formation marbles to the NE. Whilst mylonitic deformation is limited within the marble, zones of blocky brecciation are present towards its NE margin (Figure 2.14) and narrow (<5 cm) cataclasite filled faults are present throughout. Deformation fabrics are very weak within the Arganglas diorite, which remains largely undeformed (Figure 2.7). The Arganglas strand is moderately NE dipping (mean foliation 141/61NE) with subhorizontal lineations (mean 07/325) (Figure 2.11).

2.4.3 Pangong strand

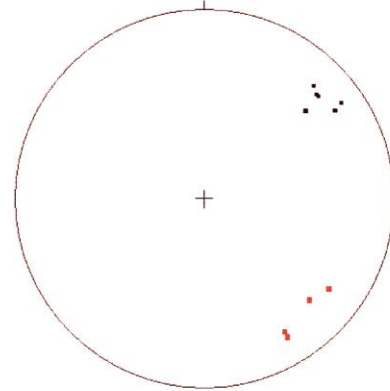
The Pangong fault strand forms the SE continuation of the Arganglas fault strand (Phillips, 2008) and is best exposed between the village of Muglib and Pangong Tso (Figure 2.2). Here it is a steeply-moderately NE-dipping structure (mean foliation 142/66NE, Figure 2.11) forming the NE margin of the PTZ and its contact with the PMC. Lineations within the Pangong strand are subhorizontal to gently NW-SE plunging (McCarthy and Weinberg, 2010). Strong mylonitic fabrics are present within both the granitoids of the PTZ and marbles and metapelites of the PMC within the Pangong strand. Mylonitic fabrics in the PMC marbles are overprinted by cataclasite and c. 10 m wide band of phyllosilicate-rich gouge, providing evidence that this strand has been active during exhumation to shallow depths of a few km (Rutter et al., 2007). Debris flows offset by >2 m across the Pangong strand show that earthquakes of $M_w > 7.0$ have occurred on this strand since 1-2 ka (Brown et al., 2002).

Nubra strand



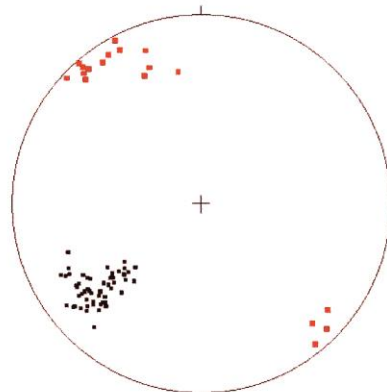
n(S)=156 n(L)=59

Nubra phyllonite



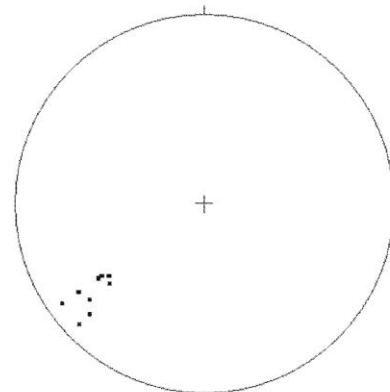
n(S)=6 n(L)=4

Arganglas strand



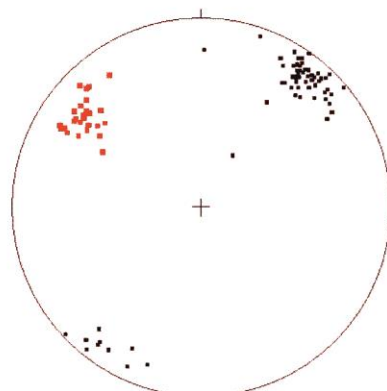
n(S)=54 n(L)=18

Pangong strand



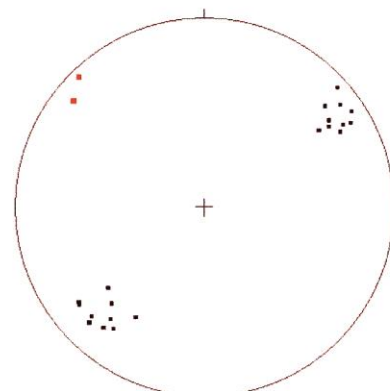
n(S)=9

Tangtse strand



n(S)=68 n(L)=35

Taruk strand



n(S)=20 n(L)=2

Figure 2.11 Stereographic projections of foliation (S) and lineation (L) data from the different portions of the Karakoram fault zone. Lineations are from mineral alignment (predominantly feldspar megacrysts or amphibole) or stretching (predominantly quartz, feldspar or calcite).

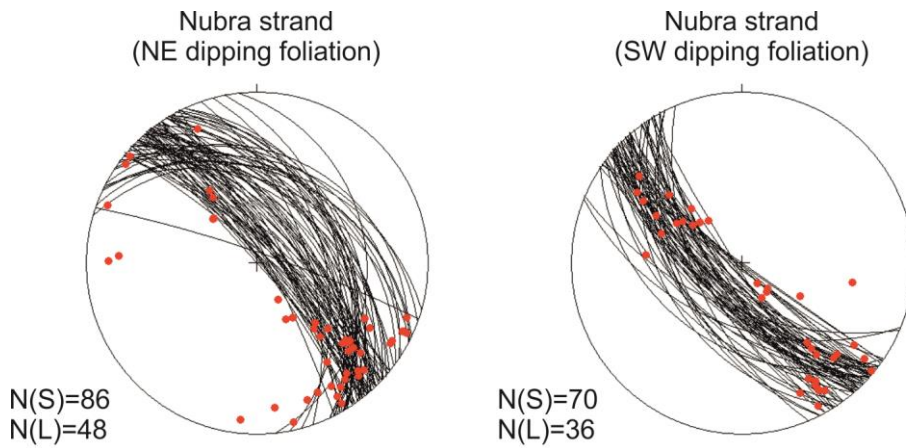


Figure 2.12 Stereographic projections of foliation (S) and mineral alignment and stretching lineation (L) measurements for the Nubra fault strand separated into NE and SW dipping foliation subgroups.

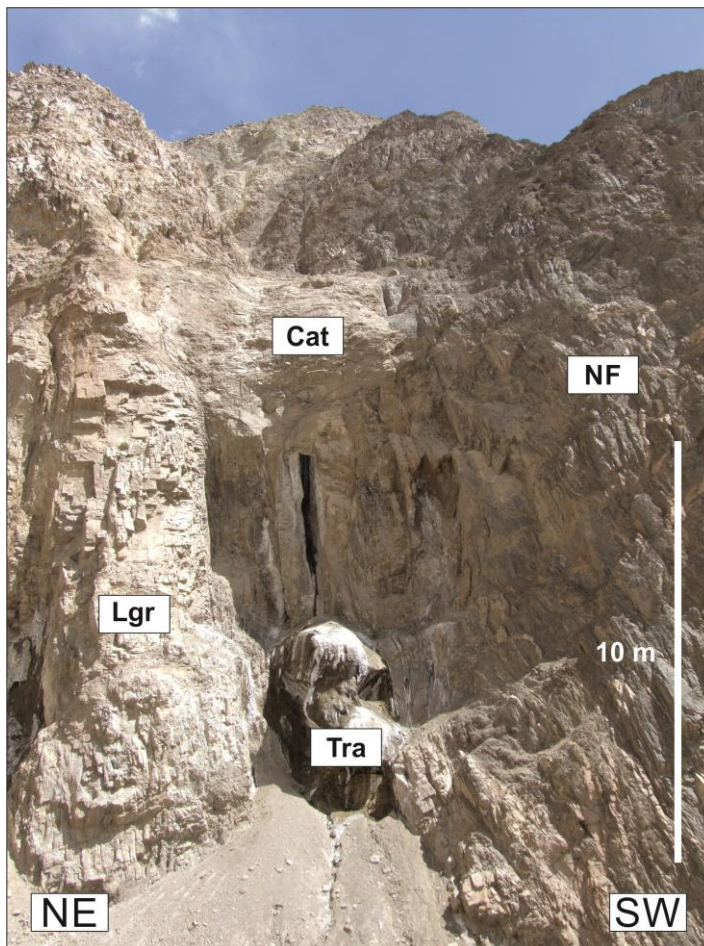


Figure 2.13 The Nubra strand fault core in Sumur gorge localised at the contact of the mylonitic Nubra Formation (NF) and Nubra-Siachen Leucogranite (Lgr). The fault core consists of a c. 2 m thick zone of cataclasite (Cat). Travertine (Tra) deposited onto the fault core provides evidence for recent fluid flow to the surface within the fault strand.



Figure 2.14 Blocky brecciation of Saser Formation marble within the Arganglas fault strand in Sumur gorge. Subangular clasts are supported in a brown cohesive matrix. Notebook 20 cm.

2.4.4 Tangtse strand

The Tangtse fault strand follows the Tangtse valley between the villages of Darbuk and Tangtse and forms the SW limit of the Pangong range (Figure 2.2). For most of its length the Tangtse strand juxtaposes amphibolite grade lithologies of the PTZ with low grade volcanics of the Ladakh terrane (Figure 2.2). The Tangtse strand follows a band of metasedimentary lithologies of the EKMC that show strong mylonitic fabrics overprinted by rare cataclastic textures. Adjacent leucogranites and diorites within the PTZ contain well developed mylonitic and protomylonitic textures and commonly show dextral S-C fabrics (Searle et al., 1998). Mylonitic foliation within the Tangtse strand has variable orientations averaging 128/80 SW, whilst lineations consistently plunge c. 20° NW (average 21/308) (Figure 2.11), indicating predominantly strike-slip with a subordinate component of normal motion. Between the villages of Darbuk and Tangtse, another shear zone branches off to the SW from the Tangtse strand. This strand has not previously been studied and is described in detail below.

2.4.5 New Observations: The Taruk Fault Strand

Previous studies in the Tangtse area have focussed on the structural, magmatic and metamorphic processes within the Tangtse and Pangong fault strands and the intervening PTZ (above). The Tangtse fault strand has been considered to form the southern margin of the PTZ and the Karakoram

terrane in this region (e.g. Leloup et al., 2011; Phillips and Searle, 2007; Phillips et al., 2004; Dunlap et al., 1998). Near Tangtse village, the SW margin of the Tangtse fault strand consists of a <3 km wide I-type qtz+Kfs+hbl+bt+pl+ttn monzogranite. Dunlap et al. (1998) provided a basic map of this granite but, in the absence of crystallisation ages, they assumed it to be part of the Ladakh batholith on the basis of its similar mineralogy. However, subsequent U-Pb zircon ages of 18.5-18.8 Ma have since distinguished this granite from the Ladakh batholith, and led to its recognition as part of the Miocene magmatic suite (Boutonnet et al., 2012; Leloup et al., 2011). As such, it is now termed the South Tangtse granite rather than Ladakh batholith (Leloup et al., 2011). Dunlap et al. (1998) recognised a fault strand forming the southern margin of the South Tangtse granite in their mapping (Figure 2 of Dunlap et al., 1998) but omitted it from their cross-section and did not discuss it further as they presumed it to be entirely within the Ladakh terrane and unrelated to the KFZ. Previous studies have examined deformation fabrics within the South Tangtse granite adjacent to the Tangtse fault strand but no studies have extended more than a few hundred metres from the Tangtse fault strand (Boutonnet et al., 2012; Leloup et al., 2011; Phillips and Searle, 2007).

During the present study, a transect extending c. 2.5 km SW from the Tangtse fault strand and across the South Tangtse granite was examined (Figure 2.2). Adjacent to the Tangtse fault strand, the South Tangtse granite preserves a strong strain gradient visible in the field over distances of a few hundred metres (Figure 2.15). It has been suggested that this deformation occurred either entirely in the solid state (Phillips and Searle, 2007) or with a prior sub-magmatic (i.e. in the presence of vestigial melt prior to full solidification) component of deformation (Boutonnet et al., 2012; Leloup et al., 2011). In its central portion, 0.5-1 km from the Tangtse fault strand, the South Tangtse granite looks relatively undeformed in the field (Figure 2.15). A weak primary igneous foliation (mean orientation 119/65 SW) is present as aligned biotite and weakly aligned K-feldspar megacrysts. Quartz occurs as isolated patches that do not appear stretched by solid state deformation. Within c. 300 m of its SW margin the primary fabric of the South Tangtse granite is overprinted by a solid state deformation fabric (mean foliation

orientation 145/89 NE) visible in the field as alignment of feldspar megacrysts and quartz ribbons, grain size reduction of megacrysts and formation of protomylonitic textures (Figure 2.15). This fabric increases in intensity towards the SW.

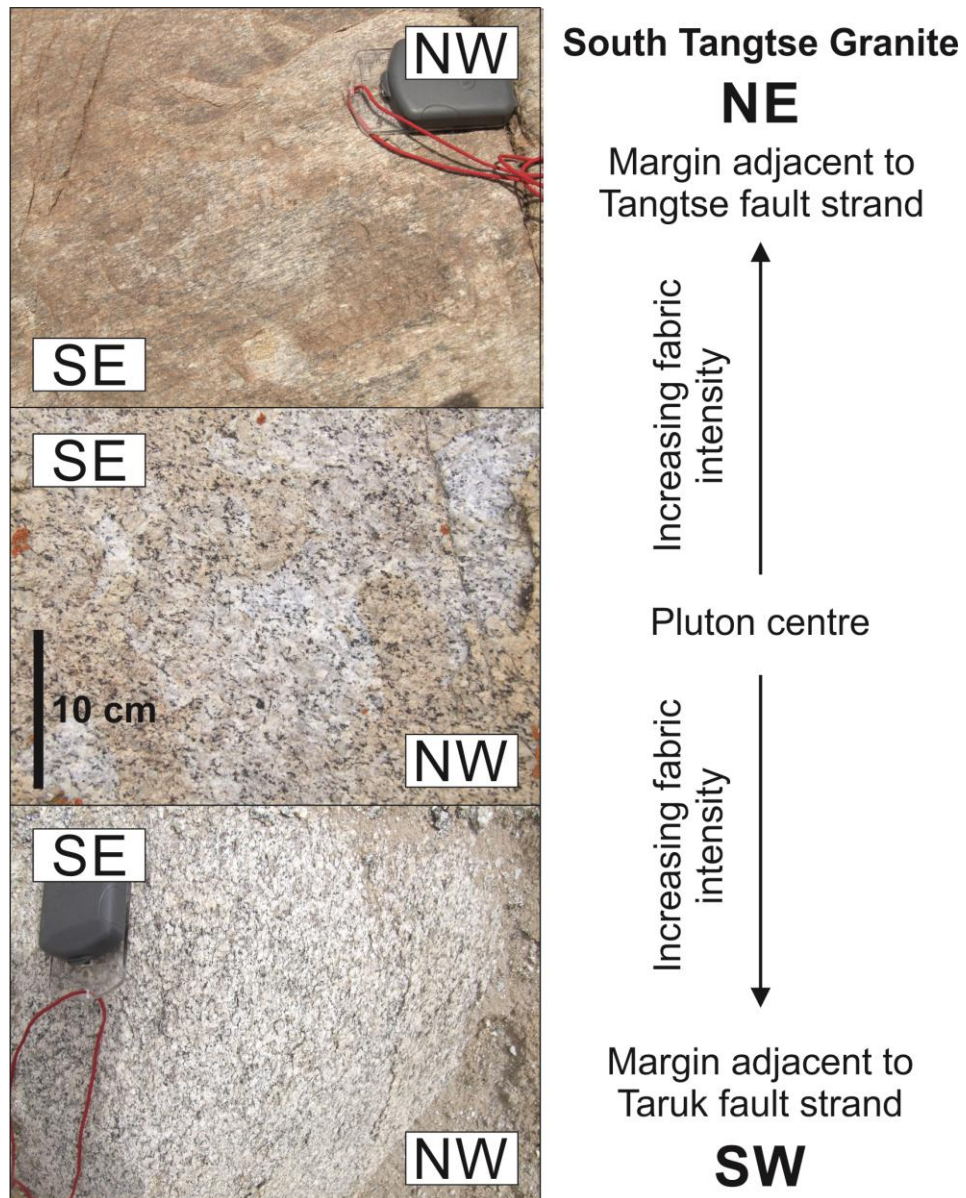


Figure 2.15 Variation in deformation fabric intensity within the South Tangtse Granite. The granite shows a mylonitic fabric within the Tangtse fault strand and protomylonitic fabric within the Taruk fault strand but is undeformed in the pluton centre. Compass clinometer 11 cm.

At the SW margin of the South Tangtse granite, near the village of Taruk, the fault strand mapped by Dunlap et al., (1998) is visible as a prominent NW-SE striking 800 m wide shear zone, consisting of dark mylonitic amphibolite hosting decametre-scale lenses of mylonitic South Tangtse granite,

leucogranite and numerous concordant and discordant leucogranite dykes (Figure 2.16a). Mean foliation within this shear zone is oriented 140/87 NE with mean lineation oriented 09/313 (Figure 2.11). Asymmetric granitic pods within the shear zone show dextral shear sense (Figure 2.16b). As this shear zone cross-cuts the South Tangtse granite it must have been active after 18.5 Ma. This shear zone is termed the Taruk fault strand. The Taruk fault strand shares a similar orientation and kinematics with the KFZ in this region (Tangtse fault strand mean foliation 128/80 SW and lineation 21/308) and was active at a similar time. It is interpreted therefore as a branch of the KFZ, possibly occupying a Riedel shear (R1) orientation.

Adjacent to the Taruk fault strand at its SW margin is an S-type $\text{qtz}+\text{pl}+\text{Kfs}+\text{bt}+\text{ms}+\text{grt}$ leucogranite (Figures 2.16a and 2.17). This leucogranite has not previously been described in the literature as it has been mapped as either the Ladakh batholith (Phillips, 2008; Dunlap et al., 1998) or South Tangtse granite (Boutonnet et al., 2012; Leloup et al., 2011), both of which are I-type hbl-bearing granitoids. Instead, this body is termed the Taruk leucogranite. The Taruk leucogranite is clearly cut by the Taruk fault strand and contains a moderately intense SL fabric (mean foliation 137/71 SW, mean lineation 37/155). Although the Taruk leucogranite has yet to be radiometrically dated, its size and mineralogy are comparable to the Miocene leucogranite plutons within the Karakoram terrane, in particular the 15.1 ± 0.6 Ma grt-2 mica leucogranite Muglib dome. For logistical reasons it was not possible to explore further SW, beyond the Taruk leucogranite, during the present study.

As no large bodies of leucogranite or amphibolite have been described within the Ladakh terrane, but are abundant within the Karakoram terrane, the findings from this transect demonstrate that the Tangtse fault strand does not form the SW margin to the Karakoram terrane in the Tangtse region. Rather the South Tangtse granite, Taruk fault strand and Taruk leucogranite sit within the Karakoram terrane. The SW margin of the Karakoram terrane must occur at another fault strand situated further SW from the Taruk leucogranite. The Taruk fault strand displays similar kinematics (SE-striking foliation, gently NW-plunging lineation) to the

Tangtse fault strand and the wider PTZ, demonstrating that transpressional tectonics occurred across this region. The mylonitic amphibolite country rock within the Taruk fault strand correlates with leucogranite-hosting amphibolite within the PTZ near Tangtse and is therefore designated to the PTZ subgroup of the EKMC.

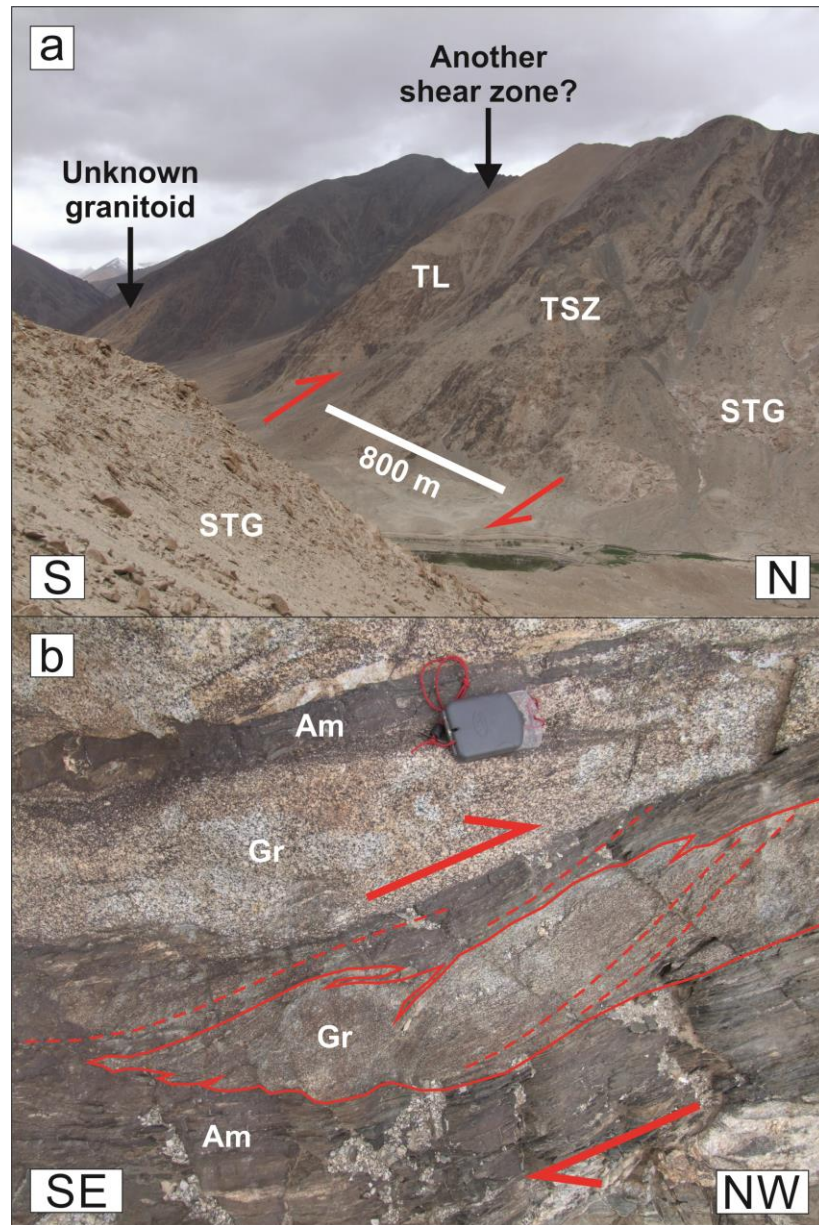


Figure 2.16 The Taruk shear zone. a) Dark amphibolite and leucocratic granitic sheets of the Taruk shear zone (TSZ) cut across the South Tangtse granite (STG) and Taruk leucogranite (TL). Also shown are the positions of another potential shear zone which may form the SW boundary of the Karakoram terrane and an unidentified granitoid body. b) Asymmetric granitic enclaves (Gr) in amphibolite (Am) and the foliation trace (dashed lines) showing dextral shear sense within the Taruk shear zone. Compass clinometer 11 cm.

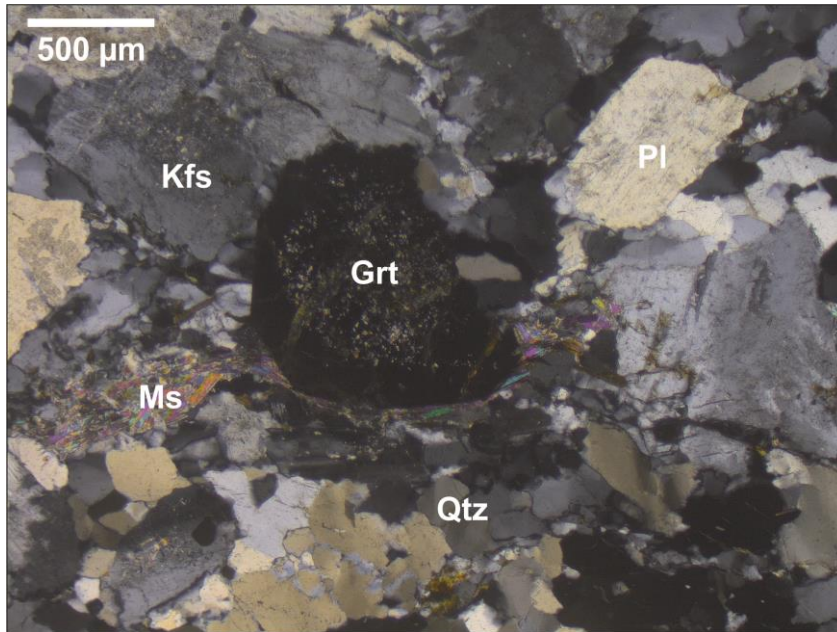


Figure 2.17 Cross-polarised photomicrograph of the Taruk leucogranite showing garnet (Grt), muscovite (Ms), plagioclase (Pl), K-feldspar (Kfs) and quartz (Qtz).

2.5 Age of the Karakoram Fault Zone

Estimates of the age of initiation of the KFZ vary widely between as early as ~32 Ma (Lacassin et al., 2004) and no earlier than ~16 Ma (Phillips et al., 2004). These age estimates are based on interpretation of the relationships between deformation fabrics and datable igneous rock units. Maximum age constraints for ductile motion on the fault are provided by datable igneous rocks displaying solid-state deformation fabrics superimposed after complete crystallisation of the igneous body. On the other hand, magmatic or sub-magmatic deformation fabrics (e.g. Paterson et al., 1989, 1998) show that radiogenic ages of crystallisation provide only a minimum age constraint on the timing of motion on the fault (Phillips and Searle, 2007). The correct interpretation of deformation fabrics and microstructures is therefore crucial to understanding the age of initiation and duration of motion on the fault. The microstructural criteria required for solid state and sub-magmatic interpretations of deformation fabrics were recently summarised by Phillips and Searle (2007).

A well constrained age bracket of 15.68 ± 0.52 to 13.73 ± 0.28 Ma for motion on the Tangtse strand of the fault zone is provided by Phillips et al. (2004) based on U-Pb isotope dilution thermo-ionisation mass spectrometry (ID-

TIMS) dating of the cross-cut Tangtse-Darbuk leucogranite and younger undeformed dykes that cross-cut the ductile foliation. At a similar time, Lacassin et al. (2004) proposed that motion on the fault must have initiated before 23 Ma and possibly as early as 32 Ma. These ages were based on U/Pb sensitive high resolution ion microprobe (SHRIMP) dating of zircons from leucocratic veins adjacent to a more southern portion of the fault, which were interpreted as synkinematic on the basis of field relationships with the mylonitic foliation. However, Searle and Phillips (2004) contest the synkinematic interpretation of the deformed leucogranites, suggesting that the lack of *in situ* pervasive migmatisation, possible rotation of prekinematic veins into parallelism with the mylonitic foliation and comparison with prekinematic intrusive bodies further north militate against synkinematic intrusion. Further, recent work by Wang et al. (2009) has found that the 47 Ma Ayilari granite along the southern portion of the KFZ, only 60-80 km East of the area studied by Lacassin et al. (2004), records a metamorphic cooling (rather than magmatic crystallisation) age of ~32 Ma and does not record a cooling event at 23 Ma. Rather, a cooling event at ~12 Ma recorded by $^{40}\text{Ar}/^{39}\text{Ar}$ ages of mica is suggested to mark the propagation of the KFZ through this southern portion. In addition, more extensive mapping of the Aji Shan region by Zhang et al. (2011) has demonstrated that the deformation fabrics reported by Lacassin et al. (2004) and Valli et al. (2007, 2008) result from motion on adjacent Oligocene detachment faults, rather than the KFZ, and that these detachments are cross-cut by the KFZ.

Some authors suggest that the Tangtse-Darbuk leucogranite (Sen et al., 2014; Rolland et al., 2009) and South Tangtse granite (Boutonnet et al., 2012, Leloup et al., 2011) show microstructures indicative of syn-kinematic emplacement, and argue that their respective ~16 Ma and ~18 Ma U-Pb zircon ages provide a minimum age for the fault. Reichardt et al. (2010) propose that S-C fabrics in the PTZ record submagmatic deformation in the least deformed leucogranite sheets but do not suggest a more precise date than the approximate duration of magmatism in the region (20-13.5 Ma). These views are opposed by others who show that the large granite bodies are cut by the fault and interpret the deformation microstructures as having formed under lower amphibolite-greenschist grade (i.e. solid state)

conditions, and that the ages of the granites therefore give a maximum age for the fault (Wallis et al., 2014b; Phillips et al., 2004, 2013; Phillips and Searle, 2007).

2.6 Geological Offsets Across the Karakoram Fault Zone

Estimates of the geological offset across the KFZ have ranged widely from as little as 66 km (Murphy et al., 2002) to as great as 1000 km (Peltzer and Tapponnier, 1988) and are the subject of much disagreement. Based on offset of the Ladakh and Gangdese granodiorites on either side of the fault, Peltzer and Tapponnier (1988) inferred a total offset of ~1000 km across the fault zone. Subsequent work by Searle (1996) has demonstrated this offset to be misjudged, and revised estimates based on offset pre-kinematic leucogranites and correlation of the Shyok-Bangong Nujiang suture range between 120-150 km (Searle et al., 1998; Searle, 1996). Lacassin et al. (2004) have proposed offset of ~280 km based on correlation of the Shyok suture with the Shiquanhe suture and >400 km on the basis of correlation of the Bangong suture with the Rushan-Pshart suture. The same correlations are made by Valli et al. (2008), who propose offsets across the KFZ of 200-480 km. However, Phillips et al. (2004) argue, by consideration of the geology and histories of these suture zones, that such correlations are incorrect and demonstrate a maximum offset of the Baltoro granite of 150 km. This argument has been vindicated by recent mapping of the exposure limits of the Late Triassic-Early Jurassic Aghil formation which shows offset of 149-167 km across the northern portion of the KFZ (Robinson, 2009a). Further, ~120 km offset of the antecedent Indus River across the KFZ is widely recognised (Searle, 1996; Lacassin et al., 2004; Phillips et al., 2004; Gaudemer et al., 1989).

2.7 Geological, Quaternary and Present-Day Slip-rate Estimates

In order to determine accurate long-term slip rates along a fault zone, precise knowledge of the duration and magnitude of slip are required. Due to the wide variation in estimates of both the timing of initiation and magnitude of geological offset for the KFZ, estimates of the long-term (>Myr timescale)

slip-rate range widely between 3 mm yr^{-1} and 32 mm yr^{-1} (Valli et al., 2008; Phillips et al., 2004).

Estimates of the long-term slip-rate, based on offset geological units (Robinson, 2009a; Phillips et al., 2004; Searle et al., 1998), the offset Kailas thrust (Murphy et al., 2002) and the offset Indus River (Valli et al., 2007) are commonly below 10 mmyr^{-1} . Long-term slip-rate estimates of $>10 \text{ mmyr}^{-1}$ (Valli et al., 2008; Lacassin et al., 2004) are based on correlation of the Shyok suture with the Shiquanhe suture and of the Bangong suture with the Rushan-Pshart suture; a correlation shown to be incorrect by Phillips et al. (2004) and Robinson (2009a) (see above).

Estimates of Quaternary-present day slip-rates on the KFZ are similarly diverse. Calculated Quaternary slip-rates based on dated and offset glacial moraines range between $4\text{-}5 \text{ mm yr}^{-1}$ (Brown et al., 2002, 2005) and 32 mm yr^{-1} (Chevalier et al., 2005; Lui, 1993). Present day slip-rates derived from geodetic measurements from Ladakh ($3\pm 5 \text{ mm yr}^{-1}$, Jade et al., 2004) and Tibet ($11\pm 4 \text{ mm yr}^{-1}$, Banerjee and Bürgmann, 2002; $1\pm 3 \text{ mm yr}^{-1}$, Wright et al., 2004; $4\text{-}10 \text{ mm yr}^{-1}$, Zhang et al., 2004) consistently indicate slip-rates little in excess of 10 mm yr^{-1} and average $\sim 5.5 \text{ mm yr}^{-1}$. These lower slip rates are supported by examples of both continuum ($3\text{-}4 \text{ mm yr}^{-1}$, England and Molnar, 2005) and microplate modelling ($0\text{-}6 \text{ mm yr}^{-1}$, Meade, 2007). However, slip-rate estimates derived from modelling of the regional strain field are somewhat higher at $\sim 10 \text{ mm yr}^{-1}$ (Holt et al., 2000; England and Molnar, 1997), whereas those derived from 3D mechanical modelling ($14\text{-}18 \text{ mm yr}^{-1}$, He and Chery, 2008) and analogue block modelling (20 mm yr^{-1} , McCaffrey and Nabelek, 1998) are greater still.

In contrast to the above, Robinson (2009b) observed that 150 Ka alluvial fans on the fault trace show no offset, suggesting that the most northerly portion of the KFZ is presently inactive. Houlié and Phillips (2013) explain the recent inactivity of the northern portion of the KFZ in terms of Coulomb stress interaction with the subducting Indian plate via the Himalayan Frontal Thrust, which promotes slip of the southern KFZ but inhibits slip in the north. While the majority of studies support lower slip-rates of $\sim 10 \text{ mm yr}^{-1}$ or less, improved constraints on the duration of motion and magnitude of offset

along the fault are required in order to understand the long- and short-term slip-rates of the KFZ.

2.8. Summary

The eastern Karakoram terrane in Ladakh, NW India, consists of varied medium- to high-grade Palaeozoic-Mesozoic metamorphic rocks. These are intruded by the composite Karakoram batholith. The batholith is comprised of Cretaceous I-type granitoids resulting from Neotethyan subduction beneath the south Asian margin and collision of the Kohistan-Ladakh arc terrane, which are in turn intruded by Miocene S-type granitoids formed during post India-Asia collision crustal thickening, heating and anatexis. The Karakoram terrane is juxtaposed with the Ladakh arc terrane to the SW by the Karakoram fault zone (KFZ). The Ladakh terrane consists of predominantly intermediate plutonic and volcanic units. The majority of KFZ deformation occurs within the Karakoram terrane, whereas portions of the Ladakh terrane deformed by the KFZ are poorly exposed or difficult to access. Four strands of the KFZ are most geologically and geomorphologically prominent; the Nubra, Tangtse, Arganglas and Pangong strands. Within these strands, intense deformation is typically focussed along lithological boundaries but strain gradients over several hundred metres can be recognised in the field. Previous studies, along with new field observations, indicate however that several other zones of deformation are present within the KFZ and further work is required to characterise the structure of the fault zone. Estimates of the age, offset and slip-rate of the KFZ vary widely, but the best estimates suggest that the fault has accommodated c. 120 km offset since 15.7-13.7 Ma at an average slip-rate of c. 8 mm/yr.

3. Fault weakening across the frictional-viscous transition zone, Karakoram Fault Zone, NW Himalaya

Abstract

Exhumed fault rocks formed in the frictional-viscous transition zone (FVTZ) provide test material that can be used to assess the strength of natural fault zones. This chapter, modified from Wallis et al. (2013), describes deformation microstructures exhumed from a wide range of depths within the Karakoram Fault Zone (KFZ). These microstructures are interpreted in terms of the deformation mechanisms and weakening mechanisms operative within the fault. The KFZ fault rocks contain evidence of several long-term weakening mechanisms associated with reduced coefficients of friction (<0.4).

The Nubra, Tangtse and Arganglas strands of the KFZ are focussed along metavolcano-sedimentary formations, indicating weakness relative to the bounding granitoids. Synkinematic retrogression suggests that reaction softening has weakened the margins of granitoids along the Nubra and Tangtse strands and the Nubra Formation within the Nubra strand. The resultant phyllosilicates have formed well developed interconnected weak layers within phyllonites and granitic mylonites. Micaceous foliae with increased proportions of opaque minerals in granitic mylonites suggest that fluid assisted diffusive mass transfer aided deformation within the Nubra and Tangtse strands. Microstructures within Nubra strand phyllonites suggest that frictional-viscous flow accommodated deformation at low shear stresses in the FVTZ. Multiple generations of veining within each strand indicate overpressured pore fluids within the fault zone across a range of depths. Active springs and travertines along the fault indicate ongoing suprahydrostatic fluid flow within the KFZ.

Despite such evidence for weakening mechanisms the KFZ is currently locked and potentially could most likely generate moment magnitude 7.5+ earthquakes. Evidence for multiple fault weakening mechanisms reduce potential for shear heating within the KFZ and suggests that the long-term

strength of the lithosphere must reside below the depth of penetration of the fault.

3.1 Introduction

Investigating the frictional strength of fault zones is critical to determining their slip stability (Ikari et al., 2011) and to characterising the micro- to macroscopic deformation of the continental lithosphere (Rutter et al., 2001). Relative weakness between fault zones and intact crust, or between lithologies of differing rheologies, can be inferred on the basis of strain localisation into the weaker material. However, it is also pertinent to determine whether faults are weak in an absolute sense, i.e. able to deform at shear stresses significantly lower than those possible for dry rock with a Byerlee coefficient of friction (μ) in the range 0.6-0.85 (Byerlee, 1978). Absolute weakness may occur when the rock deforms with lower values of μ or when elevated pore fluid pressures reduce the effective normal stress, thus enabling slip at lower shear stresses. Such absolute weakness may be inferred on the basis of relating observed deformation fabrics and microstructures to experimental or modelled results of weakening mechanisms that reduce frictional strength.

Whilst the crust outside major fault zones has been shown to be strong (Townend and Zoback, 2000; Zoback and Harjes, 1997), evidence for the absolute weakness of several major faults has been put forward. These include strike-slip faults such as the Punchbowl/North Branch San Gabriel Faults, California (Wilson et al., 2003; Chester and Chester, 1998; Chester and Logan, 1986), Carboneras Fault, Spain (Faulkner et al., 2003), Great Glen Fault Zone, Scotland (Stewart et al., 2000), Median Tectonic Line, Japan (Jeffries et al., 2006a, 2006b) and Alpine Fault Zone, New Zealand (Barth et al., 2013; White and White, 1983), as well as low-angle normal faults such as the Zuccale Fault, Elba (Collettini *et al.*, 2006).

In the India-Asia collision zone large scale fault zones are abundant (Figure 3.1 insert). However, despite their considerable seismogenic potential, their significance for understanding the evolution of the Himalayan-Tibetan orogen (Searle et al., 2011) and widespread interest in the macroscopic

strength of the lithosphere in the region (e.g. Cook and Royden, 2008; Jackson, 2002), no geological studies have yet investigated the absolute strength of fault rocks formed at depth in these structures. The strength of fault zones can also impact processes such as shear heating (Leloup et al., 1999) and metamorphism (Steffen et al., 2001) within them, which can in turn also affect the fault strength. This study investigates deformation microstructures preserved in fault rocks from one of the most prominent faults in the India-Asia collision zone, the Karakoram Fault Zone (KFZ). Evidence for the operation of various deformation mechanisms is described and interpreted in terms of the operative fault weakening processes. The implications for seismicity, shear heating and continental lithospheric strength are then explored.

Large scale fault zones can contain a wide range of fault rocks formed by a variety of deformation processes. In order to describe and distinguish between these processes and their products the following definitions are used: the terms brittle and ductile are used to describe fault rocks/fabrics that respectively display or lack significant discontinuities at the scale of observation. The terms frictional and viscous are reserved to describe the interpreted deformation mechanism.

Central to determining the frictional strength of faults is the identification of potential fault weakening mechanisms and the recognition of evidence for their presence within fault zones (Imber et al., 2008). A broad range of potential weakening processes have been recognised that may variably impact fault strength over a range of depths and timescales. Key weakening mechanisms proposed to operate in the upper crust within large displacement faults include the presence of low-friction phyllosilicate rich fault gouges (Boulton et al., 2012; Saffer et al., 2001; Morrow et al., 2000; Scholz, 1998), elevated pore fluid pressures (Smith et al., 2008) and frictional-viscous flow within phyllosilicate-rich fault rocks (Niemeijer and Spiers, 2005; Holdsworth, 2004; Bos and Spiers 2001, 2002; Chester, 1995; Chester and Higgs, 1992). Additionally, processes such as grain size reduction (De Bresser et al., 2001), reaction weakening (Wintsch et al., 1995), thermal perturbations and the addition of melt (Leloup et al., 1999)

may weaken fault rocks, particularly in the deeper portions of fault zones. A separate category of dynamic weakening processes has been suggested to occur during the coseismic interval and include fault lubrication (Di Toro et al. 2011) and thermal pressurisation (Wibberley and Shimamoto, 2005).

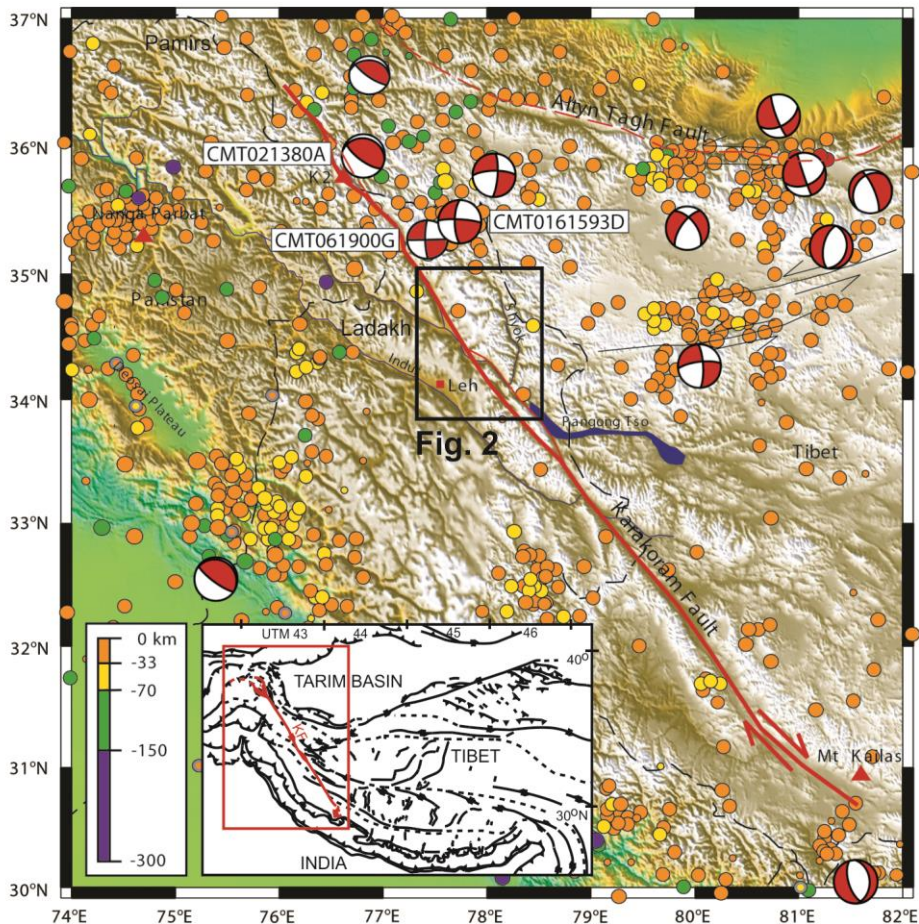


Figure 3.1 The KFZ with Harvard Centroid Moment Tensor (CMT) solutions, International Seismological Centre and National Earthquake Information Centre data and historic earthquakes during the period 1964-2003. Body-wave magnitudes ranged from 3.0-5.3 for the ISC/NEIC data and 4.5-6.5 for the Harvard CMT data. Insert shows location of main figure. The KFZ has been largely seismically inactive during the 40 year recording period. Earthquake CMT021380A has a depth of 80 km and may be associated with transpression in the vicinity of K2. CMT061900G and CMT0161593D may result from dextral slip on a slightly contorted Karakoram fault-plane striking 179°-188°, but equally could be associated with widespread sinistral strike-slip faulting in the northern Tibetan plateau. The black box marks the study area shown in Figure 3.2. From Phillips (2004).

In order to investigate fault strength and deformation processes over a broad range of upper-mid crustal depths, together with their evolution over

geological time, it is necessary to investigate exhumed fault zones that exhibit fault rocks formed at depth within the crust. If a fault continued to be active during exhumation, a sequence of progressively lower temperature overprinting fault rocks may form, providing information on deformation over a wide range of depths.

Of particular interest are deformation processes and weakening mechanisms that operate in the transitional zone between the brittle upper crust and ductile mid-lower crust. This is typically the strongest portion of the upper crust and hence the region where the effects of weakening processes can be most pronounced (e.g. Holdsworth, 2004). In the shallower brittle regime, deformation occurs predominantly by fracturing, dilatancy and frictional sliding/flow (Scholz, 1998). At greater depths, increased temperature results in viscous flow dominated by intra-crystalline plasticity and diffusional deformation processes (Bürgmann and Dresen, 2008). The intervening zone is considered to be a complex region where lithological and structural factors (Stewart et al., 2000), syn-kinematic metamorphism (Brodie and Rutter, 1985), changes in grain-size (White et al., 1980), the mechanical and chemical effects of pore fluids (Tullis and Yund, 1980), along with strain-rate, pressure and temperature (Hirth and Tullis, 1994) may all control deformation. This frictional-viscous transition zone (FVTZ) generally occurs at depths of c. 10-15 km (Stewart et al., 2000). However, processes such as fluid influx, grain size refinement, metamorphic reactions and changes in geothermal gradient may contribute also to its spatial evolution over time (e.g. shallowing, sometimes to as little as 5 km depth, Imber et al., 2001).

This chapter presents field and microstructural evidence for a range of fundamental fault weakening processes including the effects of pore fluids, reaction softening and interconnected weak layer development in fault rocks exhumed from the frictional-viscous transition zone within the KFZ, NW Himalaya (Figure 3.2). The impact of these fault weakening mechanisms is considered in terms of seismicity on the fault and the character of continental lithospheric deformation.

3.2 Deformation Mechanisms Within the Karakoram Fault Zone

3.2.1 Deformation on the Nubra Fault Strand

3.2.1.1 Deformation Microstructures within the Nubra Formation

On the Nubra fault strand, metapelites of the Nubra Fm. (Figure 3.3) show mylonitic-ultramylonitic tectonic fabrics (Figure 3.4a, samples P85, P86, P156 and W11/7). These contain varying proportions of Qtz+Fsp+Ms+Bt±Grt±Ky±Chl±Cal. Quartz invariably shows almost complete grain size reduction to <50 µm. Within monomineralic polycrystalline quartz aggregates, grain boundaries are rounded-interlobate whereas the boundaries of isolated grains (typically bounded by micas) are rounded-straight. 20-30 µm quartz subgrains are extensively developed. Feldspar porphyroclasts in W11/7 are fractured, elongate and ~50% altered to sericite. Foliation within the metapelites is defined by alignment of muscovite, biotite and kyanite. The micas form either through-going subparallel bands (W11/7) or dextral S-C' fabrics (P85). These constitute up to 35% of the minerals visible in the plane of section (i.e. parallel to lineation and perpendicular to foliation; the XZ plane of finite strain). Micas show undulose extinction with split and stacked cleavage planes and bent grains. Muscovite is typically coarser than biotite and forms dextral fish structures.

Metavolcanics of the Nubra Fm. show protomylonitic-mylonitic tectonic fabrics. The metavolcanic mineralogies indicate andesitic (varying proportions of Pl+Kfs+Ep+Qtz+Ms+Chl+Hbl+Cal, samples P77, P78 and P89/2) or basaltic (Pl+Cpx+Opx+glass, sample P80) protoliths. In the andesitic samples quartz has undergone extensive grain size reduction. The few remaining porphyroclasts (~300 µm) are generally rounded with undulose extinction, whereas ~35 µm matrix grains typically have lobate grain boundaries and contain numerous subgrains. Both the metavolcanics (P89/2) and metapelites (P86) of the Nubra Formation contain monomineralic layers of either calcite (P89/2) or quartz (P86). In P89/2, <650 µm thick folded calcite layers are parallel to the folded cleavage of the andesitic metavolcanic (Figure 3.4b). The layers have sharp contacts with the metavolcanic host material. Individual ~50 µm grains have highly

irregular bulging boundaries and contain numerous 20-30 μm subgrains. In P86, 200-300 μm quartz layers are parallel to the straight cleavage of the metapelite and again have sharp contacts.

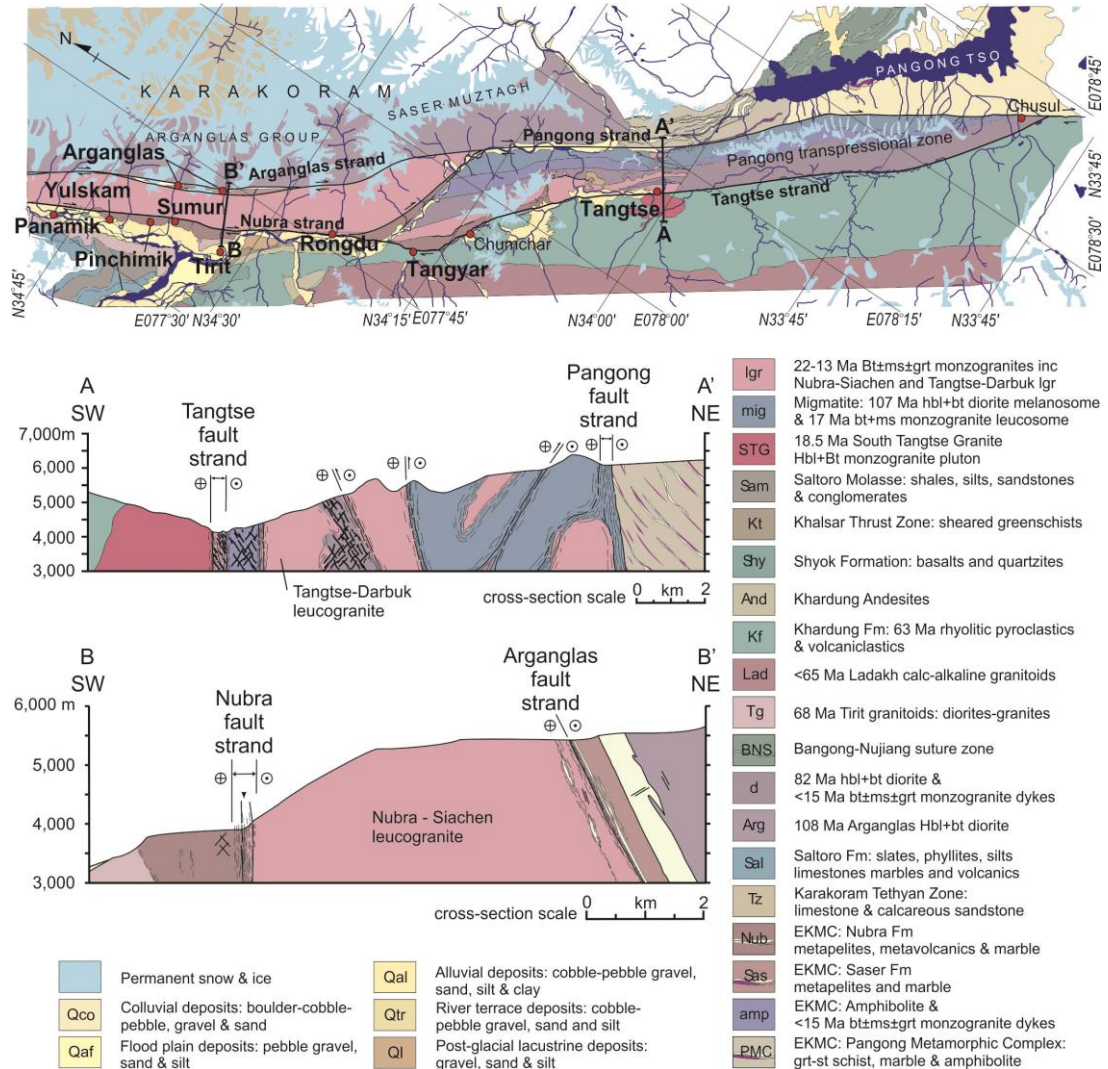


Figure 3.2 Central portion of the KFZ, Ladakh, N. India (modified from Phillips, 2008; Phillips and Searle, 2007, and Phillips et al., 2004). Cross section A-A' shows the Tangtse and Pangong fault strands near Tangtse. Cross section B-B' shows the Nubra and Arganglas fault strands in Tirit gorge. Sample localities are marked: Pinchmik – MLA1B, W11/1; Panamik - P72a, P72b-3; Yulskam - P77, P78, P80, P82, P83, P85, P86, P87/1-2, P88, P89/1, P89/2, W11/7; Sumur - W11/20, W11/29 and W11/41; Arganglas - P144, P145, P146, P149, P150, W11/49, W11/52, W11/56; Rongdu - P152, P155, P156; Tangyar - P185, P187, P189; Tangtse - P1, P4, P10, W11/66, W11/102, W11/109.

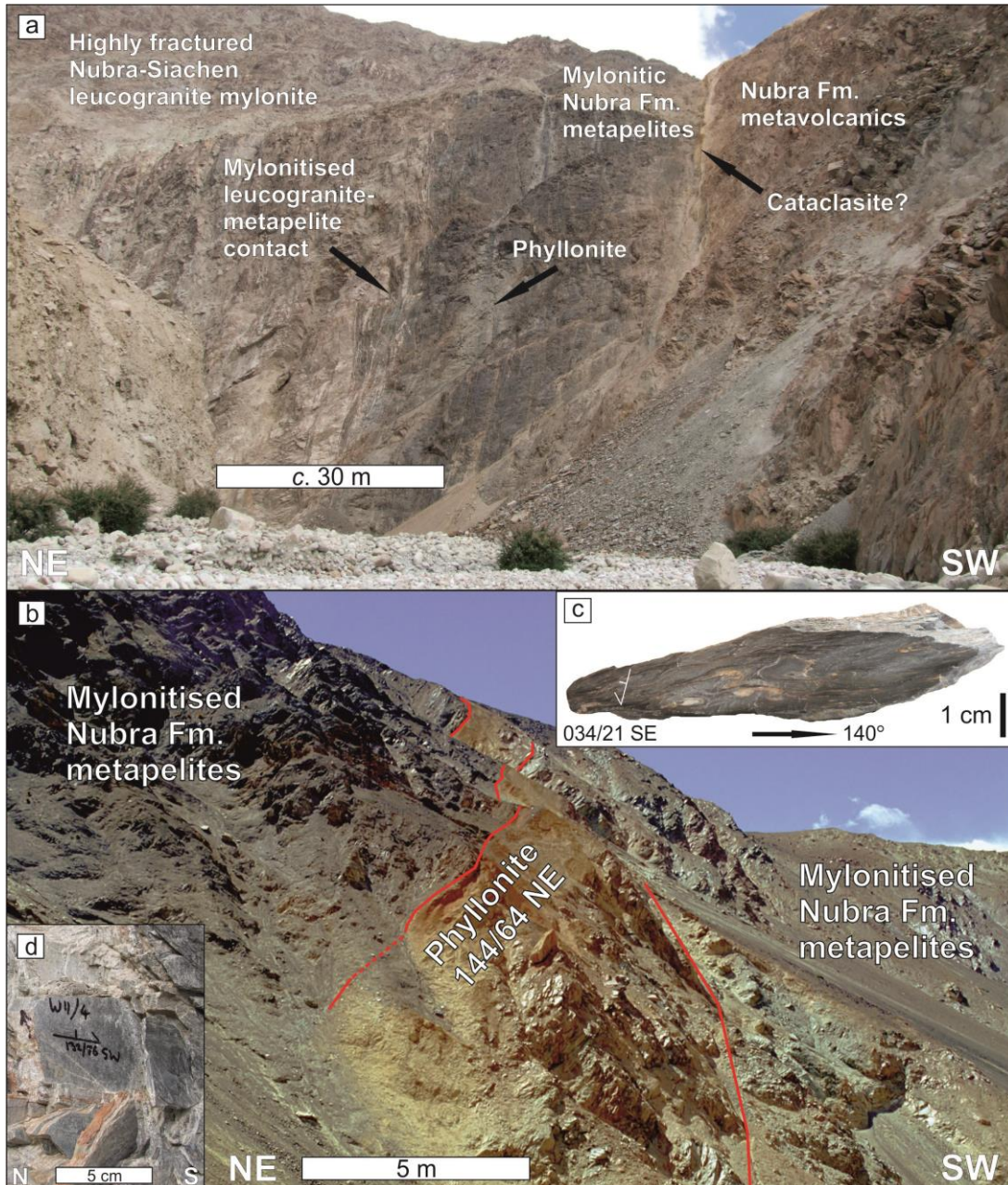


Figure 3.3 a) Cliff cross-section through the Nubra fault strand in Yulskam gorge. Mylonitised leucogranite and metapelites are overprinted by phyllonite, cataclasite and distributed fracturing. b) ~10 m thick phyllonite band within mylonitised metapelites of the Nubra Formation near Yulskam (from Phillips, 2004). Strike of phyllonite foliation (144/64NE) is subparallel to the regional-scale orientation of the Nubra fault strand (138/85NE). c) Polished XZ surface of phyllonite from Yulskam. Coarser grained phyllosilicate bands (black) form interconnected layers through fine grained matrix of phyllosilicates and framework silicates (dark grey) and deformed quartz veins (light grey) (Sample W11/2). d) Mylonitised metapelites of the Nubra Formation near Yulskam. Foliation (marked) is oriented subparallel to the regional-scale orientation of the Nubra fault strand (Sample W11/4).

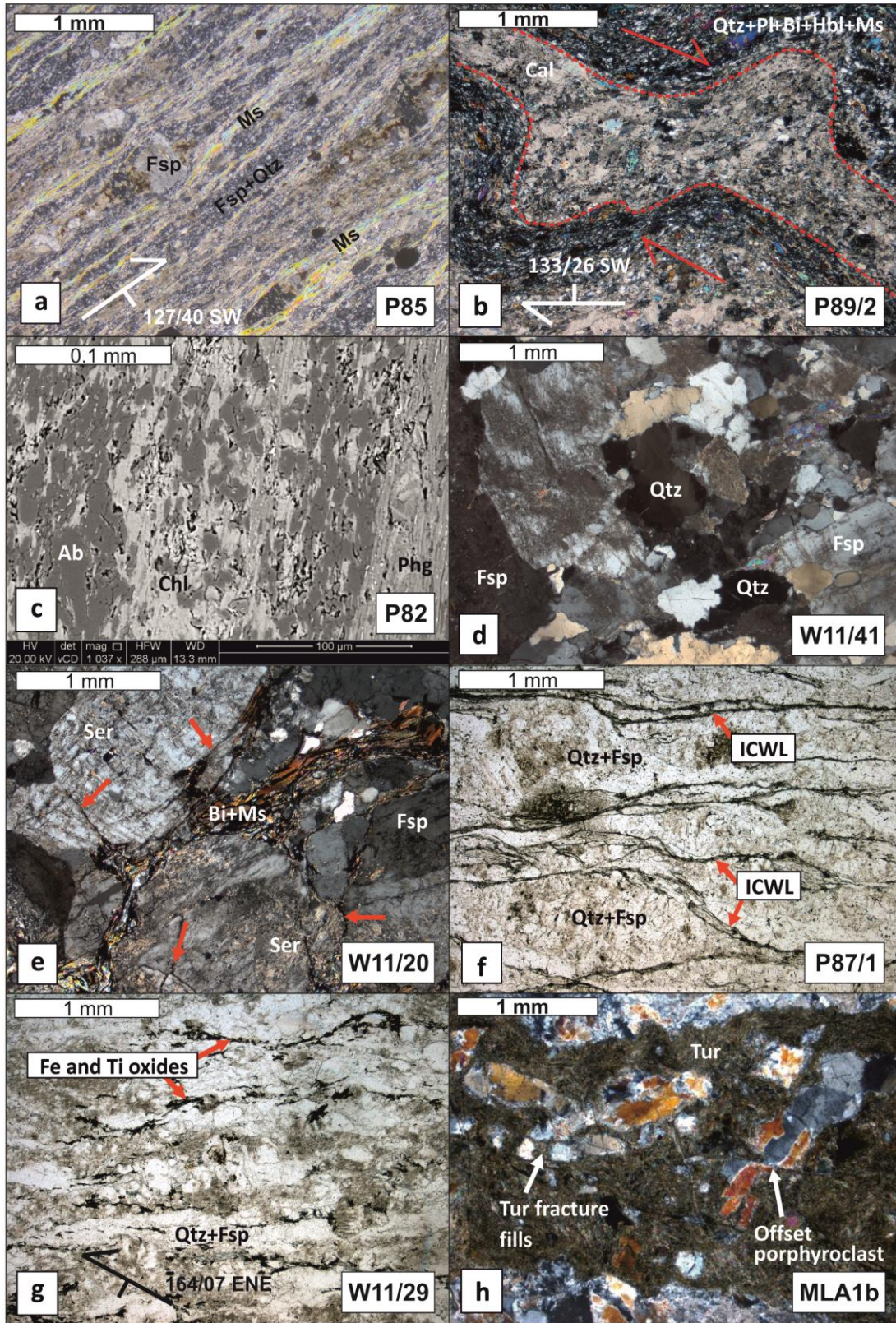


Figure 3.4 Deformation fabrics on the Nubra fault strand. a-c: Nubra Formation, d-h: Nubra-Siachen leucogranite. a, b, d, e and h are crossed-polar optical images, c is SEM backscattered electron atomic number contrast and f and g are plane polarised optical images. a) Mylonitic metapelite with through going bands of muscovite (Ms) separating layers of fine grained quartz (Qtz) and feldspar (Fsp). Sample P85. b) Dextrally sheared calcite vein in mylonitic andesitic metavolcanics. Sample P89/2. c) Phyllonite with layers of phengite (Phg) and chlorite (Chl) wrapped around albite (Ab) grains. Albite grains indent one another at contacts. Sample P82. d) Coarse grained leucogranite from centre of Nubra-Siachen batholith. Sample W11/41. e) Leucogranite 70 m from SW margin of batholith. Microfractures (red arrows) are associated with sericite (Ser). Biotite (Bi) and Muscovite (Ms) form layers. Sample W11/20. f) Leucogranite from margin of batholith with interconnected weak layers (ICWL) of fine grained biotite and muscovite porphyroblasts. Sample P87/1. g) Leucogranite from margin of batholith with abundant Fe and Ti oxides along sericitic layers (brown). Sample W11/29. h) Breccia and cataclasite generated from leucogranite protolith and entrained within infiltrating green-brown ultrafine-grained tourmaline (Tur) veins. Fractures are mostly extensional (left) but some show dextral offset (right). Sample MLA1B.

Unlike the folded calcite veins, quartz veins show occasional boudinage. The <70 µm quartz within these layers has aspect ratios of ~2:1 with a shape preferred orientation aligned 25° to the foliation and layer margins. ~30 µm rounded quartz subgrains are ubiquitous within these layers.

Marbles are found locally within the Nubra Fm. at Rongdu (samples P152 and P155, Figure 3.2). These are composed of calcite with minor isolated grains of quartz and muscovite. Calcite consists of 250-300 µm porphyroclasts with bulging grain boundaries and mantles of 30-40 µm irregular shaped grains. Porphyroclasts contain <30 µm wide curved and wavy twins (i.e. type III of Burkhard,1993).

3.2.1.2 Deformation Microstructures within Nubra Formation

Phyllonites

The metavolcanics and metapelites are cut by a <10 m wide phyllonite band (Figure 3.3) showing a (Pl+Qtz+Chl+Phg) greenschist facies assemblage (samples P82, P83 and W11/1), with abundant sericitic layers and foliation parallel layers of pure calcite visible in outcrop. In coarser grained phyllonite at Yulskam (sample W11/1, Figure 3.2), 250-400 µm thick porphyroclastic quartzo-feldspathic domains are separated by much finer grained 150-200 µm thick bands rich in sericite (50-100%). These bands define a well-

developed S-C' fabric. ~250 µm quartz porphyroclasts show strong undulose extinction, occasional 40 µm marginal subgrains and bulging grain boundaries. Matrix quartz (<20 µm) has irregular shaped boundaries and aspect ratios of <3:1. ~300 µm feldspar porphyroclasts are rounded and highly sericitised. In finer grained phyllonites at Rongdu (Samples P82 and P83, Figure 3.2) S-C' fabrics are locally preserved in thin section but the microstructure is dominated by subparallel and anastomosing 100-300 µm thick layers of chlorite and phengitic white mica, which are interlayered with 40-200 µm thick quartzo-feldspathic domains and define the foliation. Layer composition varies between pure phyllosilicates, pure framework silicates and mixtures of the two. In backscattered electron images (Figure 3.4c), chlorite and phengite are present as interconnected layers that wrap around aligned ~10x20 µm grains of albite. Albite generally exhibits straight grain boundaries forming the sides running parallel to foliation, but sutured and indented boundaries where the ends of albite grains come in contact along sides running normal to foliation. The phyllonites at both localities generally lack microscopic evidence of brittle deformation (e.g. fractures or relict fragments of cataclasis).

3.2.1.3 Deformation Microstructures within the Nubra-Siachen Leucogranite

The NE margin of the Nubra fault strand consists of garnet 2-mica leucogranite (Qtz+Ksf+Pl+Bt+Ms+Grt) and K-feldspar megacrystic monzogranite (Qtz+Ksp+Pl+Bt±Ms) of the Nubra-Siachen leucogranite batholith. Furthest from the Nubra and Arganglas fault strands (i.e. near the centre of the batholith, Figure 3.4d, sample W11/41, 1890 m NE of the Nubra strand) these granites contain c. 1 mm grained feldspars with numerous feldspar-feldspar contacts, euhedral-subhedral morphologies and well preserved igneous zoning. Feldspars have been altered by 0-50% to patchy sericite. Rare transgranular fractures cross-cut each mineral and show no particular spatial relationship to sericite. Quartz is typically coarse grained (250-500 µm) with lobate grain boundaries and patchy undulose extinction. Primary micas (<5%) are coarse grained (<0.5 mm), have weak undulose extinction, show a weak grain shape preferred orientation and are isolated amongst quartz and feldspar.

In samples closer to the margin of the batholith and within the Nubra fault strand (W11/20, 70 m NE of the batholith margin and samples P72a, P87/1, P87/2, P88 and P89/1) feldspars are still coarse grained (<10 mm) but intercrystalline microfractures are abundant within them. These microfractures are spatially associated with an increased proportion of sericite, which has replaced 50-100% of the area of the feldspar grains (Figure 3.4e). Mixtures of aligned biotite (<300 µm) and sericite are found as through-going bands c. 100-300 µm thick that anastomose and wrap around feldspar grains, closely following feldspar grain boundaries. These bands form an irregular but semi-continuous network throughout the rock mass. Feldspars show intragranular crystal plastic deformation microstructures such as bent and tapered deformation twinning and patchy undulose extinction, along with bulging grain boundaries and thin (c. 100 µm) mantles of fine grained neoblasts. Quartz is considerably finer grained (50-500 µm) than in the centre of the batholith. Its grains have highly irregular interlobate boundaries, ubiquitous 50 µm rounded subgrains and neoblasts and are locally highly flattened (axial ratios >5:1) where they appear 'squeezed' between feldspar grains. Individual c. 300 µm grains of calcite are occasionally present.

In leucogranite from the very SW margin of the batholith and within the centre of the Nubra fault strand (sample W11/29), feldspar grain size is considerably reduced (<500 µm) and fine grained matrix neoblasts of feldspar are abundant and intermixed with quartz. However, sericite has almost completely replaced (>80%) original feldspar such that sericite constitutes <40% of the rock. Sericite patches and bands are therefore highly interconnected forming a foliation parallel network (Figure 3.4f). Where preserved, crystal plastic deformation microstructures in feldspar are similar to those in sample W11/20, as are those in quartz. Sample W11/29 shows abundant strings of opaque Fe- and Ti-oxide grains along the fine grained micaceous foliae (Figure 3.4g). Here the opaques are considerably more abundant than in samples with less intense tectonic fabrics or in portions of the sample lacking in mica foliae. This sample also contains 1-2 mm thick foliation parallel quartz veins. Quartz within the veins shows

lobate/cusped grain boundaries and abundant subgrains, identical to quartz microstructures in the host leucogranite.

3.2.1.4 Tourmaline±quartz Veins on the Nubra Fault Strand

Ultrafine-grained tourmaline±quartz veins <1 mm up to a few cm thick are emplaced within the Nubra-Siachen leucogranite along the Nubra fault strand (Figure 3.4h). These were originally identified as pseudotachylytes based on field observations (Phillips and Searle, 2007). However, scanning electron microscope and electron microprobe analyses have subsequently been used to determine their tourmaline-rich mineralogy (Watkins, 2011; Phillips, 2008). The veins infill brittle fractures that cross-cut ductile deformation fabrics in the leucogranites and monzogranites. The veins strike 050-070° approximately perpendicular to the strike of the KFZ (Watkins, 2011). The tourmaline veins commonly include numerous fragments of fractured host mylonitic leucogranite. Occasionally, shear offsets of host rock grains across the veins are visible in thin section. More commonly, host rock fragment geometries suggest vein normal extensional opening.

3.2.1.5 Hydrothermal Springs along the Nubra Fault Strand

Hydrothermal springs emerge along the fault trace around Panamik village (Figure 3.5a). The hydrothermal fluids emerge at 28-76°C and contain 2-8 mg/kg of boron (Absar et al., 1991). The active springs at Panamik are immediately adjacent to travertine deposits. Similar travertines are found precipitated onto the exhumed core of the Nubra fault strand in Sumur gorge within a c. 2 m wide zone of cataclasite along the margin of the Nubra-Siachen leucogranite (Figure 3.5b). It is clear from field relations that the travertine in Sumur gorge post-dates the foliated mylonites and cataclasites onto which it is deposited but also that hydrothermal fluids must recently have flowed through the fault to the surface at this locality. Other active hydrothermal springs also occur on the trace of the KFZ in the Nubra valley at Changlung and Pulithang, 15 km NW and 5 km SE from Panamik respectively (Absar et al., 1991).

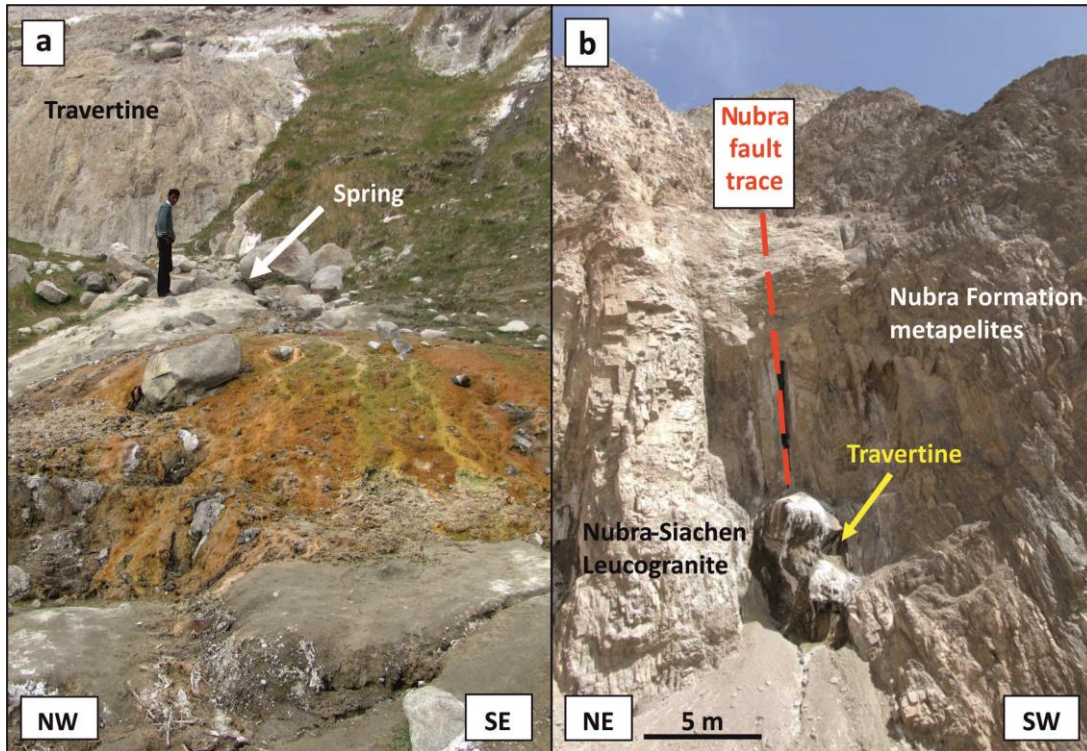


Figure 3.5 Evidence of hydrothermal activity on the Nubra fault strand. a) Active hydrothermal springs and travertine deposits on the fault trace at Panamik. b) Travertine deposits within the fault core at Sumur indicate palaeohydrothermal activity.

3.2.2 Interpretation of Deformation Mechanisms within the Nubra Fault Strand

In order to estimate the depth of operation of particular deformation processes, the temperature at which they operated is estimated and typical geological shear zone strain rates of 10^{-12} - 10^{-14} s⁻¹ (a reasonable assumption in the KFZ, see above) and an average geothermal gradient of 35°Ckm⁻¹ (as indicated by thermobarometry of Miocene migmatite in the PTZ, Chapter 4) are assumed. This thermal state prevailed across much of the wider Baltoro Karakoram region as a result of crustal thickening (e.g. Palin et al., 2012) and therefore does not suggest significant localised shear heating within the fault zone as proposed by Rolland et al. (2009) (*cf.* section 4.7). In order to estimate the time at which particular deformation processes operated, the estimated deformation temperatures are compared to published thermochronometric data.

Quartz microstructures within both the metavolcanics and metapelites of the Nubra Formation are characteristic of deformation by grain boundary migration (GBM) and subgrain rotation (SGR) dynamic recrystallisation

(Stipp et al., 2002). These combined deformation mechanisms suggest that deformation occurred at temperatures of 450-550°C (13-16 km depth) (Stipp et al., 2002). Feldspar microstructures are characteristic of deformation by bulging (BGL) dynamic recrystallisation and are broadly consistent with the quartz-based temperature estimate (Passchier and Trouw, 2005). Split and stacked cleavage in micas indicate that they deformed by frictional slip on these planes. The presence of strong undulose extinction suggests that dislocation climb was limited and therefore that recovery dominated dynamic recrystallisation was not a significant deformation mechanism for micas.

Quartz and calcite veins within the Nubra Formation are recrystallised. Quartz subgrain microstructures in the veins indicate SGR deformation at 400-500°C. Larger quartz grains with lobate/cusped boundaries indicative of GBM are absent from the veins. This suggests either that significant deformation at >500°C did not affect the veins (i.e. they were emplaced during deformation and exhumation) or that GBM microstructures have been overprinted at lower temperatures by extensive SGR. As much of the host rock preserves GBM quartz microstructures, it is tentatively suggested that the veins were emplaced during deformation at 400-500°C (11-14 km depth). If this is correct then the veins provide evidence for boron-rich pore fluids at pressures great enough to promote fracturing during vein formation at depths where deformation was otherwise dominantly ductile. Calcite microstructures in marble pods and lenses at Rongdu (Figure 3.2) are characteristic of BGL dynamic recrystallisation at >250°C whilst type III twinning is evidence for ongoing deformation at 200-250°C (>7 km and 6-8 km respectively) (Burkhard, 1993).

Phyllonites within the Nubra strand consist of fine grained intermixed and layered phyllosilicates and framework silicates. The abundant chlorite, phengite and finer grained sericite are well aligned in interconnected layers and would have deformed easily by slip on basal (001) planes oriented (sub-)parallel to the macroscopic fault shear plane. Rare dynamic recrystallisation microstructures and undulose extinction in quartz and feldspar suggest that dislocation climb was limited and therefore indicates that deformation in the phyllonites occurred at <400°C (<11 km depth). At these lower temperatures feldspar grains would have behaved as rigid bodies. In samples P82 and

P83 elongate feldspar grains can be seen to indent one another where their ends come into contact, showing the effects of removal of material by dissolution. The combination of frictional slip on phyllosilicate foliae and dissolution of rigid clasts at high stress sites suggests that the phyllonite deformed by frictional-viscous flow (Bos and Spiers, 2002). The microstructure of the phyllonite bears remarkable resemblance to the microphysical model microstructure of frictional-viscous flow of Bos and Spiers (2002). Bhutani et al. (2003) obtained an Ar-Ar age of 13.9 ± 0.1 Ma for biotite from sheared granite near Panamik. This age provides an indication of the approximate time at which the rocks of the exposed structural level on the Nubra strand cooled through the greenschist facies conditions under which phyllonitisation occurred.

In the centre of the Nubra-Siachen leucogranite batholith, the leucogranite is essentially undeformed. Quartz shows some evidence of grain boundary migration but feldspars are undeformed and sericitisation is patchy and limited to <50%. The numerous feldspar-feldspar contacts and only isolated grains of biotite and muscovite indicate that the rheology of the rock is that of a relatively rigid load bearing framework (Handy, 1990). The leucogranite has a weak primary fabric defined by poorly aligned biotite and feldspar megacrysts but lacks evidence of any significant sub-magmatic deformation (e.g. imbricated feldspars or late magmatic mineral growth in pressure shadows).

In samples approaching the margin of the batholith and the Nubra fault strand, quartz grain shapes still indicate GBM dynamic recrystallisation but increasingly reduced grain size and subgrain development indicate a significant contribution of SGR. Microstructures in unaltered feldspar indicate deformation by BGL dynamic recrystallisation. As in the Nubra Formation, these quartz and feldspar deformation mechanisms indicate deformation temperatures of c. 500°C (c. 14 km depth). Interconnected bands of sericite and coarser grained micas in samples within the fault strand are inferred to have deformed by frictional slip on their aligned basal (001) planes. The increased abundance of opaque phases adjacent to the phyllosilicate foliae indicates that they are residual from dissolution of quartz or feldspar. Grain boundary contact with mica or clay minerals is known to enhance rates of

pressure solution in quartz (Hickman and Evans, 1995; Hippertt, 1994; Dewers and Ortoleva, 1991; Houseknecht, 1988). The increased abundance of opaques at quartz/feldspar boundaries in contact with mica suggests that micas acted to enhance the rate of dissolution of the adjacent minerals. Quartz veins present in one such sample (W11/29) contain quartz microstructures indicative of combined GBM+SGR dynamic recrystallisation. These veins are therefore inferred to have formed at a similar depth (i.e. similar time) to the deformation microstructures in the leucogranite. These veins provide evidence for silica saturated fluids within the rock. This suggests that veining provided a sink for material dissolved at mica grain boundaries. These observations indicate that fluid assisted diffusive mass transfer contributed to strain accommodation in the high strain zone.

Tourmaline±quartz veins emplaced within the Nubra-Siachen leucogranite cross-cut ductile deformation fabrics and are associated with pervasive fractures and host rock cataclasite. They formed therefore under temperatures of <300°C, at shallow depths of <9 km.

3.2.3 Deformation on the Tangtse Fault Strand

3.2.3.1 Deformation Microstructures within the Tangtse Strand EKMC

On the Tangtse fault strand mylonitic fabrics are preserved within metapelites, metavolcanics and marbles that form the EKMC country rocks to the Cretaceous and Miocene intrusions within the PTZ. Metapelites (Ms+Qtz+Cal+Fsp, sample P185) contain well aligned 100 µm flakes of muscovite (50-70%) in highly interconnected layers that are folded into 300 µm crenulation cleavage domains and cm-scale microfolds (Figure 3.6a). Quartz and calcite veins are present in the hinge regions of these folds, which are up to a few mm thick at fold hinges but taper out on the fold limbs. Calcite (300-450 µm) in the veins is flattened with irregular shaped boundaries and curved and tapered type III twinning (Burkhard, 1993). Quartz (c. 400 µm) in the veins has lobate grain boundaries, deformation lamellae and undulose extinction. Quartz in the muscovite rich matrix on the other hand is finer grained (50x100 µm) with straight grain boundaries in contact with muscovite and 30 µm subgrains. Feldspar occurs in the matrix as c. 50 µm rounded grains.

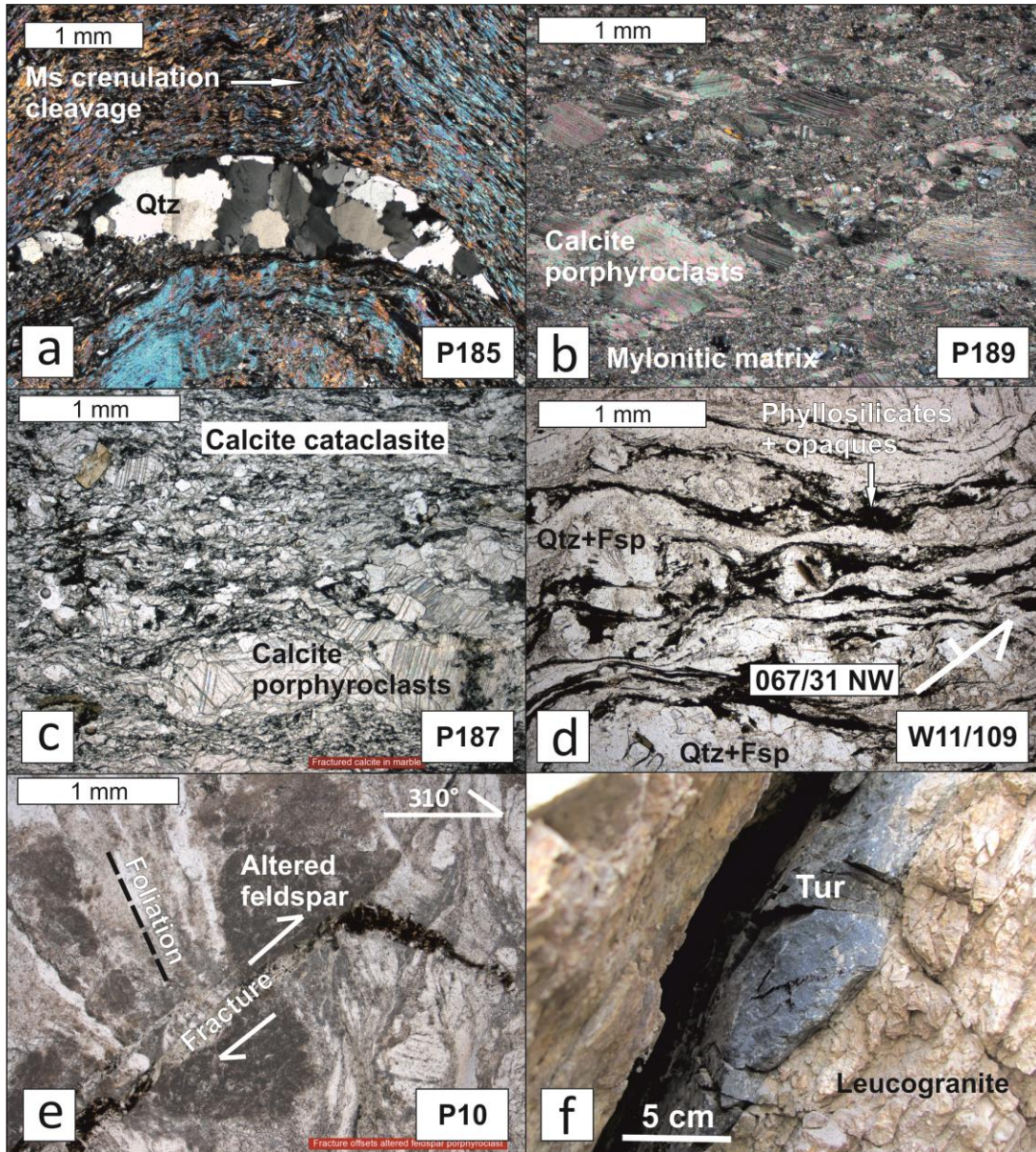


Figure 3.6 Deformation microstructures on the Tangtse fault strand. a-c) EKMC, d-f) Tangtse-Darbuk leucogranite. a and b are cross-polarised optical images and c-e are plane polarised. a) Folded metapelite with tapered quartz (Qtz) vein across fold hinge and M-fold muscovite crenulation cleavage. Sample P185. b) Calc-mylonite with elongate twinned porphyroclasts in fine mylonitic matrix. Sample P189. c) Marble cataclasite with angular fractured porphyroclasts and cataclastic matrix. Sample P187. d) Leucogranite from SW margin of Tangtse-Darbuk leucogranite pluton. Through going fine grained black bands are composed of phyllosilicate and opaque minerals. These separate domains of highly deformed quartz and feldspar (Fsp). Sample W11/109. e) Leucogranite from SW margin of Tangtse-Darbuk leucogranite pluton. Ductile foliation is cross-cut by dextral shear fracture with millimetric offset. Sample P10. f) Black foliation parallel tourmaline (Tur) vein emplaced within leucogranite.

Calc-mylonites (Cal+Act+Czo, sample P189) contain flattened calcite porphyroclasts up to 100x300 μm with abundant curved and tapered type III twins (Burkhard, 1993) and bulging grain boundaries (Figure 3.6b). These are supported within and between 0.5-1 mm thick bands of <30 μm rounded calcite grains. Foliation in the calcite is defined by alignment of elongate porphyroclasts and grain size banding. 2-20 mm thick foliation parallel bands of actinolite+clinozoisite consist of straight and bent <100 μm grains aligned with the calcite foliation. Quartz occurs amongst the calcite as isolated rounded 50-100 μm grains with diffuse subgrain boundaries and undulose extinction.

Brittle deformation has not previously been reported on the Tangtse fault strand but marble cataclasites crop out near Tangyar (Figure 3.6c, sample P187). These are nearly pure calcite marbles with minor quartz. Coarse (<250 μm) grained domains up to 1 mm thick show granoblastic textures with thick type II twins (Burkhard, 1993). These are separated by <800 μm thick zones of pervasive anastomosing fractures aligned subparallel to fracture zone margins. Calcite within the fractured zones occurs as elongate angular 30-50 μm fragments.

3.2.3.2 Deformation Microstructures within the Tangtse-Darbuk Leucogranite

The Tangtse-Darbuk leucogranite adjacent to the Tangtse fault strand shows similar microstructures to those in the Nubra-Siachen Leucogranite. At the NE margin of the Tangtse-Darbuk leucogranite (1420 m from the SW margin of the leucogranite, Sample W11/66), feldspar within the leucogranite is coarse grained (1-2 mm) with occasional myrmekite, poorly developed mantles of fine grained feldspar, minor-moderate intra- and intergranular fractures and c. 40% sericite. Feldspars are frequently in grain boundary contact. Quartz aggregates are present as elongate foliation parallel ribbons, within which grains are relatively coarse (200-600 μm) with lobate grain boundaries, weak undulose extinction and few subgrains. Primary igneous micas are present as isolated grains and the microstructures lacks interconnected layers of phyllosilicates. Opaque minerals are rare.

In the margins of the Tangtse fault strand (sample W11/102, 690 m from the SW margin of the leucogranite), feldspar porphyroclasts are coarse (0.8-2 mm) but have bulging grain boundaries and well developed mantles of fine grained feldspar. Fracturing and sericitisation (20-40%) of porphyroclasts are limited. However sericite is abundant in the matrix in association with fine grained matrix feldspar and forms narrow (20-100 μm thick) elongate layers with primary biotite. Whilst extensive, these layers are only partially interconnected and most do not cross an entire thin section. Phyllosilicate layers are decorated with fine grained opaques. Quartz is flattened with highly irregular grain boundaries, numerous 40-50 μm subgrains and strong sweeping undulose extinction.

Within the Tangtse fault strand (sample W11/109, 390 m from the SW margin of the leucogranite) feldspar porphyroclasts are smaller (300-1500 μm) and the proportion of fine grained matrix is increased. Few intra- or inter-granular fractures are present within porphyroclasts. Phyllosilicate rich layers are extensive, well interconnected and can be traced across the length of thin sections (Figure 3.6d). These layers are again associated with fine grained opaque Fe- and Ti-oxides. At the SW margin of the leucogranite (Sample P10) transgranular fractures crosscut the mylonitic foliation at angles of c. 45° and show millimetric dextral offsets of altered feldspar porphyroclasts (Figure 3.6e).

Further brittle deformation on the Tangtse fault strand is evident as ultrafine grained black tourmaline veins emplaced within the Tangtse-Darbuk leucogranite, similar to those on the Nubra fault strand (Figure 3.6f). These range from stockworks of sub-mm veins that pervade disaggregated leucogranitic host rock to massive veins up to a few cm thick. Unlike on the Nubra strand, the tourmaline veins on the Tangtse strand strike subparallel to the ductile foliation.

3.2.4 Interpretation of Deformation Mechanisms within the Tangtse Fault Strand

Metapelites within the Tangtse fault strand contain abundant muscovite that deformed by folding in the hinge regions of crenulations and cm-scale folds. As muscovite makes up the majority of the rock volume and is highly

interconnected it is also likely to have deformed by frictional slip on its basal (001) planes. Subgrains within matrix quartz grains indicate SGR dynamic recrystallisation but migration of grain boundaries appears to have been hindered by pinning against the abundant muscovite. This suggests 400-500°C as a minimum deformation temperature estimate (Stipp et al., 2002). Quartz and calcite veins, present only in fold hinge regions, indicate that vein formation was synkinematic and that fluid pressures were high enough to induce extensional failure parallel to the minimum principle stress direction. Quartz microstructures in the veins indicate GBM dynamic recrystallisation with a weak low temperature (<300°C) overprint. Consideration of matrix and vein quartz deformation microstructures suggests therefore that deformation occurred at up to c. 550°C (<16 km depth). Type III twins (Burkhard, 1993) in calcite veins suggest further deformation at 200-250°C (6-7 km depth).

Calc-mylonites contain calcite deformation microstructures indicative of extensive mylonitisation by BGL dynamic recrystallisation, suggesting deformation temperatures of >250-300°C (7-9 km depth). Type III twinning (Burkhard, 1993) in calcite porphyroclasts is inferred to have formed at lower temperatures of 200-250°C (6-7 km depth). In the marble cataclasites, pervasive fracturing affected previously relatively undeformed marble at low temperatures (<200-250°C, <7 km depth).

The Tangtse-Darbuk leucogranite is relatively undeformed at its NE margin, distal to the Tangtse fault strand, with its primary igneous microstructure largely preserved. Evidence of sub-magmatic deformation, such as imbricated grains or magmatic mineral growth in pressure shadows or fractures, is absent. Due to limited sericitisation, low primary mica content, frequent feldspar-feldspar contacts and coarse grained quartz, this weakly deformed leucogranite is inferred to possess a load bearing framework rheology (Handy, 1990).

Towards the SW margin of the leucogranite and the Tangtse fault strand, both quartz and feldspar show increasing dynamic recrystallisation. Deformation microstructures indicate that recrystallisation was dominated by SGR+GBM mechanisms in quartz and BGL in feldspar, suggesting deformation temperatures of 450-550°C (13-16 km depth). As the volume of

recrystallised feldspar increases so does the proportion of sericite within it, such that it appears that grain size reduction promoted retrogressive sericitisation. This may have been facilitated by increased intergranular fluid pathways and increased surface area available for reaction. The sericite, particularly in the through going interconnected layers, is inferred to have deformed by frictional sliding. As in the Nubra-Siachen leucogranite, the increased abundance of opaque minerals associated with the phyllosilicate layers are interpreted as the result of removal of material by dissolution during diffusive mass transfer. The extent and high interconnectivity of the phyllosilicate layers suggests that they allowed the rock to deform with an interconnected weak layer rheology (Handy, 1990). The fact that water-rich fluids were present at midcrustal depths at least as early as ~20 Ma is indicated by water-fluxed anatexis in the PTZ at this time (Reichardt and Weinberg, 2012; Reichardt et al., 2010; Weinberg and Mark, 2008) and primary CO₂- and NaCl- rich fluid inclusions in zoned plagioclase in the Tangtse-Darbuk leucogranite (Mukherjee et al., 2012).

The ages at which sericitisation occurred within both the Tangtse-Darbuk leucogranite and Nubra-Siachen leucogranite are poorly constrained. Que and Allen (1996) investigated sericitisation of the Rosses Granite Complex, Ireland, and found that it occurred in association with fluid induced microfracturing relatively soon after crystallisation, at temperatures of 600-400°C. This may also be the case in the leucogranites of the KFZ as sericitisation was coeval with development of microstructures indicating operation of grain boundary migration (>500°C) and subgrain rotation (400-500°C) of quartz and bulging dynamic recrystallisation (450-600°C) of feldspar as the dominant crystal plastic deformation mechanisms. Boutonnet et al. (2012) modelled the thermal history of the Tangtse strand using U-Pb zircon and Ar-Ar amphibole, white mica and biotite dating, building on an earlier study by Dunlap et al. (1998). Their model predicts cooling to 400°C by 12-13 Ma. Mukherjee et al. (2012) also obtained Ar-Ar biotite ages for the Tangtse strand from which they interpret cooling through a suggested closure temperature of 400-350°C at 10.34-9.84 Ma, ~2 Ma more recent than the model of Boutonnet et al. (2012). However, if the 10.34-9.84 Ma age is instead taken to reflect cooling through a closure temperature of

320±40°C (Harrison et al., 1985) as used by Boutonnet et al. (2012), then the results of both studies are in close agreement. 12-13 Ma is taken therefore as the time by which sericitisation of the leucogranites at the exposed structural level had occurred. Sericitisation has also been found to occur at lower temperatures (e.g. 180-320°C, Eberl et al., 1987) through the action of heated meteoric waters. Similar retrogression may have affected the Tangtse-Darbuk leucogranite and Nubra-Siachen leucogranite as they were exhumed to shallower structural levels.

Formation of the foliation parallel tourmaline veins on the Tangtse fault strand would have required extensional opening (i.e. the minimum principle stress direction) normal to the foliation. This suggests that they formed after the main phase of ductile deformation on the Tangtse strand. However they do provide evidence for high pressure fluid flow at shallower levels (<13 km depth) within this strand of the fault zone. Evidence for brittle deformation during dextral simple shear is provided by closed brittle fractures that offset porphyroclasts in the leucogranite.

As on the Nubra fault strand, active hot hydrothermal springs emerge along the Tangtse strand at Chumchar and Chushul (Figure 3.2), although no data on the temperature or chemistry of these springs are as yet available.

3.2.5 Deformation on the Arganglas Fault Strand

Within the Arganglas fault strand, Qtz+Bt+Fsp+Ms metapelites of the Saser formation show mylonitic fabrics (samples P146 and W11/52). Their fine grained matrix consists of rounded feldspar and slightly elongate 40-70 µm quartz with aligned 100-300 µm biotite (30-50%). Quartz commonly contains subgrains. Biotite is distributed throughout the matrix but also concentrated in c. 400 µm thick subparallel layers that anastomose in dextral S-C-C' fabrics and can be traced across entire thin sections (Figure 3.7a). Sample P146 contains <1.5 mm feldspar porphyroclasts with bulging grain boundaries and mantles of fine grained rounded feldspar. These mantled porphyroclasts have strongly asymmetric dextral sigmoidal forms (Figure 3.7b). The same sample also contains dextral sigmoidal and rhomboidal muscovite mica fish. Sample W11/52 contains monomineralic layers of coarse grained quartz (Figure 3.7c). These layers are folded with dextral

vergence. Quartz in fold limbs is coarse (<700 μm) with strongly interlobate grain boundaries, sweeping undulose extinction and deformation lamellae. Within fold hinge regions quartz is finer grained (70-100 μm) and contains numerous subgrains. An isolated metapelitic pod within marble (sample P145) consists of a coarse grained Bt+Fsp+Tr+Cal mineral assemblage with an isotropic granoblastic texture. Constituent minerals show undulose extinction but lack other deformation microstructures. Fracturing is absent from all metapelitic samples.

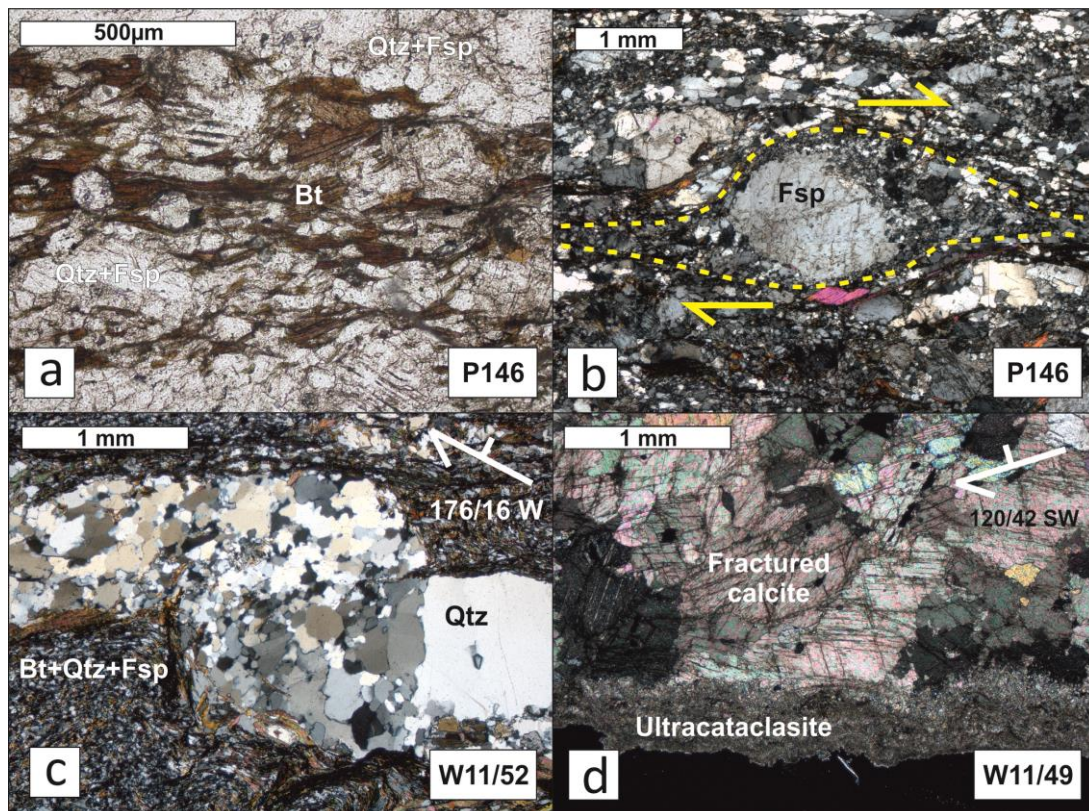


Figure 3.7 Deformation microstructures on the Arganglas fault strand. a-c) Saser Formation metapelites, d) Saser Formation marble. a is optical plane polarised and b-d are cross-polarised optical images. a) Interconnected layers of biotite (Bt) wrap around rounded porphyroclasts of quartz (Qtz) and feldspar (Fsp). Sample P146. b) Dextral sigmoidal mantled porphyroclast of feldspar. Sample P146. c) Dextrally folded quartz vein with coarser grained quartz in fold limb and fine grained quartz around fold hinges. Sample W11/52. d) Highly fractured calcite marble with ultracataclasite band. Sample W11/49.

Marbles of the Saser formation typically consist of c. 90% calcite, 10% dolomite. Calcite is coarse (c. 800 μm) with somewhat lobate grain boundaries and abundant type II (Burkhard, 1993) twinning (samples P144, P149 and W11/56). Sample W11/56 is cut by bands where calcite

porphyroclasts have occasional finer (100-150 μm) rounded grains at grain boundaries. Sample P150 has 150-200 μm elongate grains (axial ratio c. 3:1) with straight or gently curved grain boundaries, weak undulose extinction and type II twinning. Sample W11/49 is mostly coarse grained (c. 700 μm) but grains are highly dissected by numerous intergranular fractures (Figure 3.7d). This sample contains an ultrafine grained zone of calcite cataclasite. In the field, broad zones of blocky breccia occur at the margins of the marble bands and more intense deformation is evident in cm-scale cataclasite filled faults that cut the marble mylonites at high angles.

3.2.6 Interpretation of Deformation Mechanisms within the Arganglas Fault Strand

Metapelites within the Arganglas fault strand contain quartz and feldspar deformation microstructures indicating that these minerals deformed by dynamic recrystallisation dominated by SGR+GBM and BGL mechanisms respectively. These mechanisms suggest that deformation occurred at 450-550°C (13-16 km depth). Layers of biotite within these rocks are inferred to have deformed by frictional slip on their aligned (001) planes. Dextral S-C-C' fabrics, sigmoidal mantled porphyroclasts and mica fish are consistent with previous reports of dextral strike-slip motion on this fault strand (Phillips and Searle, 2007).

The monomineralic quartz layers in sample W11/52 are interpreted as quartz veins on the basis of their coarse grain size and absence of other minerals. Interlobate grain boundaries and subgrains within the veins indicate deformation by GBM and SGR respectively at c. 500°C, consistent with deformation in the host metapelite. These veins formed therefore either before or during deformation. Comparison with similar veins within the Nubra fault strand suggests that these veins may be the result of elevated pore fluid pressures and fluid assisted diffusive mass transfer during motion of the Arganglas fault strand.

The majority of marbles from the Saser formation (samples P144, P149 and W11/56) show coarse, somewhat lobate grains that indicate limited deformation by GBM dynamic recrystallisation. Finer grains along grain boundaries in sample W11/56 may be the result of limited SGR or BGL

dynamic recrystallisation affecting narrow bands of the unit. The microstructure of one sample (P150) suggests the operation of grain boundary area reduction effects during static recrystallisation. The variety of microstructures preserved in the marbles suggests that ductile deformation was heterogeneously distributed within them, in contrast to the ubiquitous mylonitisation of the metapelites. Marble cataclasites observed in outcrop and thin section (sample W11/49), along with brecciation at the margins of marble bands, show that brittle deformation was widespread within the marbles. Fractures overprint crystal plastic deformation microstructures in the marbles and are inferred therefore to have formed subsequently at lower temperatures (<250°C) and shallower depths (<7 km).

3.3 Discussion: Fault Weakening Mechanisms and Their Tectonic Significance

Along each fault strand of the KFZ deformation is localised on bands of metavolcano-sedimentary lithologies and their contacts with adjacent granitoids. This indicates the relative weakness of the metavolcano-sedimentary units. In addition, several deformation mechanisms inferred to have operated within the FVTZ on each fault strand have the potential to have been weak in an absolute sense, as detailed below (Figure 3.8). As the pre-requisites of these weakening mechanisms are still present at depth within the fault zone (i.e. the fault is likely to be deforming similar protoliths at depth to those exposed at the surface and fluid flux is ongoing), the weakening mechanisms inferred from surface exposures may be analogous to processes currently operating at depth.

3.3.1 Weakening Mechanisms on the Nubra Fault Strand

The bulk of the Nubra Formation records ductile deformation at upper greenschist-lower amphibolite grade (450-550°C, 13-16 km depth). At these conditions quartz and feldspar deformed by dynamic recrystallisation whereas micas deformed by frictional slip on their cleavage planes. Both muscovite and biotite have been experimentally demonstrated to be frictionally weak with $\mu=0.35-0.43$ for muscovite and $\mu=0.25-0.40$ for biotite (Ikari et al., 2011; Scruggs and Tullis, 1998). Their low frictional strength and abundance in the metapelites (<35%) likely resulted in a low long term shear

strength of the bulk rock (Figure 3.8). These pre-existing weak lithologies within the Nubra (and also Tangtse and Arganglas strands) strand were present at the time at which the KFZ initiated.

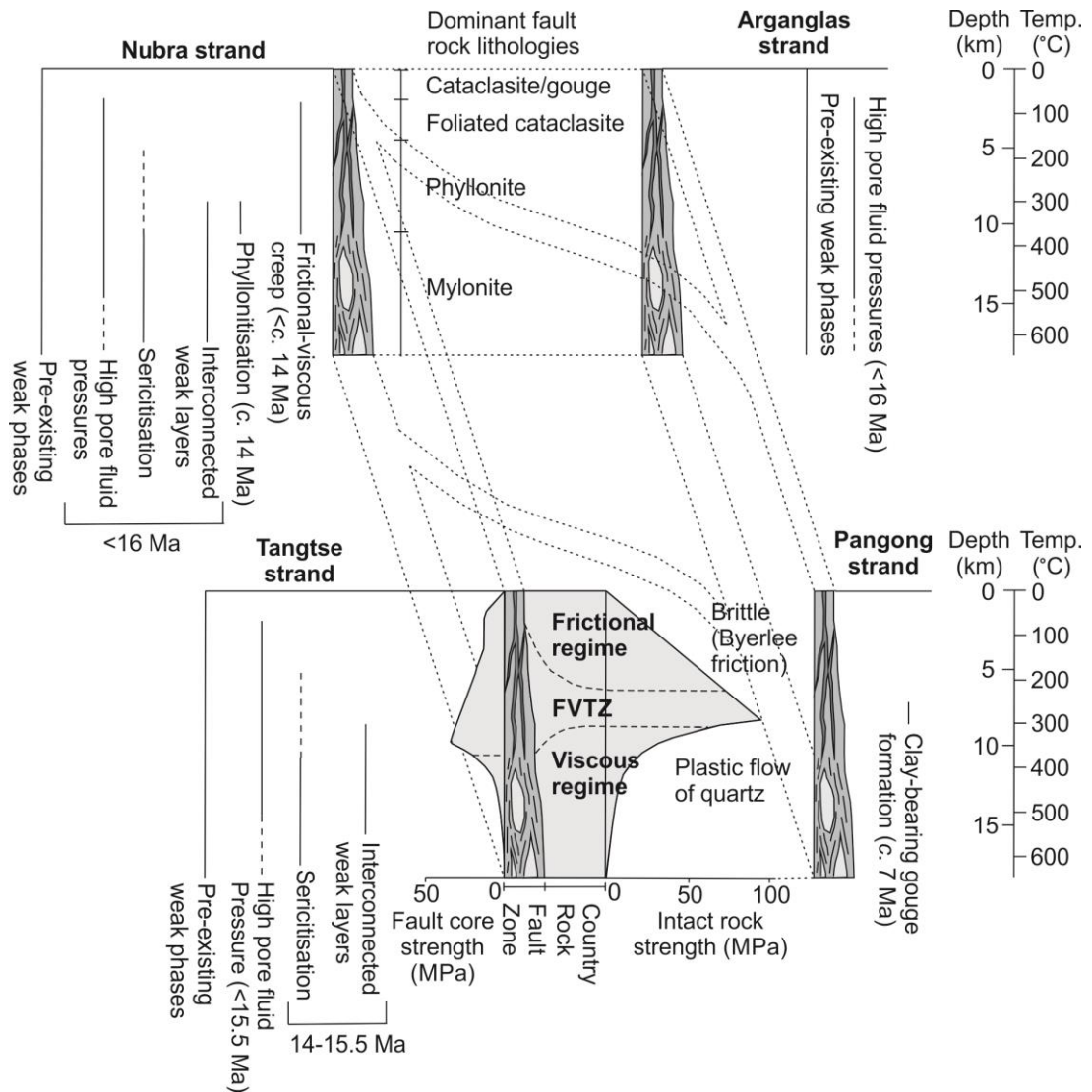


Figure 3.8 Schematic diagram of the KFZ showing the depths at which fault weakening mechanisms are inferred to have operated on each fault strand. Also shown are the ages at which these mechanisms began to operate, the depths typically dominated by particular fault rocks and generalised strength-depth profiles for a weakened strike-slip fault zone and intact wall (modified from Imber et al., 2008; Jefferies et al., 2006a; Holdsworth, 2004). Temperature-depth scale assumes a geothermal gradient of 35°C/km (see main text). Inferred depth extents of fault weakening mechanisms in the KFZ inferred from metamorphic and deformation temperatures (see main text). Pre-existing weak phases include biotite, muscovite, chlorite and calcite.

The main phase of ductile deformation in the Nubra-Siachen leucogranite also occurred at depths of 13-16 km. The association between microfractures and sericitisation of feldspars in the deformed leucogranite

suggests that fracturing facilitated fluid flow and thus promoted retrogression. Sericitisation of load bearing feldspars resulted in reaction softening and development of interconnected weak layers of phyllosilicates that deformed by frictional slip ($\mu \approx 0.4$) on cleavage planes (Figure 3.8). Once these weak layers formed a through-going network they dramatically reduced the strength of the bulk rock (Handy et al., 1999; Tullis et al., 1991; Handy, 1990). In addition, the formation of these phyllosilicate foliae increased the area of phyllosilicate-framework silicate grain boundary contact. This appears to have promoted dissolution of material at the contacts, allowing fluid assisted diffusive mass transfer. Material removed in solution was redeposited as quartz veins. The veins provide evidence for pore fluids at these depths that, at least intermittently, were at pressures sufficient to promote hydrofracturing of the rock. The pore fluid pressure would have reduced the effective normal stress allowing failure at lower shear stresses than in dry rock (Figure 3.8). The presence of these fluids would also likely have reduced the strength of quartz during dynamic recrystallisation through hydrolytic weakening (Blacic and Christie, 1984). This phase of deformation is constrained by pre- and post-kinematic leucogranites to between 15.9-13.7 Ma (Phillips et al., 2004). Weakening processes in the leucogranites therefore began to operate in the Nubra strand <2 Ma after the initiation of faulting.

Quartz veins within the Nubra Formation formed under upper greenschist conditions (400-500°C, 11-14 km depth). Their presence shows that elevated pore fluid pressures acted to weaken the rock at these slightly shallower depths (Figure 3.8).

Phyllonitisation affected the metapelites of the Nubra Formation under lower greenschist conditions (<400°C, <11 km depth) at c. 14 Ma. The resulting phyllonite shows microstructures suggestive of frictional-viscous flow (Figure 3.4c). This has been modelled to proceed with an apparent friction coefficient of 0.25-0.35 (Bos and Spiers, 2002). The localised retrograde formation of phyllonites, within a c. 10 m wide zone, suggests that the fault zone allowed fluid influx into crust that was otherwise fluid under-saturated at this depth and time. Once formed, this mineral assemblage would have

had potential to deform with less than Byerlee friction whilst being exhumed to depths of only a few km (Bos and Spiers, 2002) (Figure 3.8).

Tourmaline±quartz veins formed within the leucogranite at depths of <9 km and provide evidence for low shear stress hydrofracturing at these shallow depths. This suggests that contrasting weakening mechanisms operated at similar depths in the phyllonites (frictional-viscous flow) and the leucogranite (hydrofracturing) within the shallow crust.

3.3.2 Weakening Mechanisms on the Tangtse Fault Strand

Metapelites of the EKMC within the Tangtse fault strand contain a high proportion of muscovite (<70%). Low friction slip on muscovite foliation planes ($\mu \approx 0.4$) would therefore have dominated deformation of the rock. Further, quartz and calcite veins in fold hinge regions show that pore fluid pressures were sufficiently high during deformation to produce an extensional minimum principle stress. Shear stresses during deformation must therefore have been low. Quartz deformation microstructures suggest that this deformation occurred at 400-550°C (11-16 km depth) (Figure 3.8).

Operative weakening mechanisms within the Tangtse-Darbuk leucogranite at 11-16 km depth were similar to those in the Nubra-Siachen leucogranite. However, in the Tangtse-Darbuk leucogranite, sericitisation appears to scale more closely with increasing recrystallisation of feldspar, rather than microfracturing. It appears therefore that grain size reduction during recrystallisation increased both intergranular pathways for fluids and surface area available for reaction. The ensuing sericitisation resulted in significant reaction softening of the rock and the development of through-going weak phyllosilicate layers (Figure 3.8). Increased opaque minerals along these layers again suggest that the phyllosilicates promoted fluid assisted diffusive mass transfer during deformation at 15.6-13.7 Ma for the exposed structural level (Phillips et al., 2004), consistent with the thermochronological models that predict cooling through 400°C at c. 12-13 Ma (Boutonnet et al., 2012). Thus, weakening processes in the leucogranites began to operate <2 Ma after the initiation of faulting on the Tangtse strand.

Tourmaline veins on the Tangtse strand cross-cut the ductile deformation fabrics are inferred therefore to post-date the main phase of ductile

deformation. As on the Nubra strand, they provide evidence for fluid overpressure and hydrofracturing once the rocks had been exhumed to shallower crustal levels. Other brittle structures within the Tangtse strand, such as shear fractures in leucogranite and marble cataclasites, show that the fault strand continued to be a zone of relative weakness following exhumation and cooling to <250-300°C (<7-9 km depth).

3.3.3 Weakening Mechanisms on the Arganglas Fault Strand

Metapelites of the Saser Formation within the Arganglas fault strand contain a high proportion of aligned biotite (<50%). The abundance and low frictional strength ($\mu=0.25-0.40$) of biotite would have resulted in low shear strength of the bulk rock. Deformed quartz veins within the metapelites again suggest elevated pore fluid pressures during deformation; although on the Arganglas strand they cannot be conclusively demonstrated to be synkinematic with respect to the KFZ. This deformation occurred at depths of 13-16 km (Figure 3.8) and post-dates emplacement of the c. 16 Ma Nubra-Siachen leucogranite (Phillips and Searle, 2007; Phillips et al., 2004). Undeformed pods of metapelite within marble provide evidence for the weakness of the metapelite relative to the marble. Marble breccias and cataclasites indicate that the Arganglas strand continued to represent a zone of relative weakness following exhumation and cooling to <250-300°C (<7-9 km depth).

3.3.4 The Pangong Fault Strand

The Pangong fault strand is the fourth major strand of the KFZ in the study area, and runs parallel to the Tangtse strand (Figure 3.2). Between Muglib and Pangong Lake, the Pangong strand cuts primarily through marbles of the Pangong Metamorphic Complex. The comparative lack of phyllosilicate rich lithologies in this portion of the fault indicates that it would likely be relatively strong. Calcite twinning incidence and calcite recrystallised grain size palaeopiezometry indicate stresses of <250 MPa and 40-110 MPa respectively (Rutter et al., 2007). The twinning incidence result of <250 MPa shows that for at least part of its lifespan the Pangong strand sustained high differential stresses in the region of the FVTZ. However, the deformed marbles are cross-cut by a later <10 m wide gouge zone bearing chlorite, muscovite and illite (along with quartz, calcite and minor dolomite,

microcline, saponite and gypsum) that, based on the illite Kübler index, formed at c. 300°C (Rutter et al., 2007). This estimate overlaps with the likely temperatures at which calcite develops twins and so may reflect an evolution from a strong fault to a potentially weaker phyllosilicate-rich zone of deformation (Figure 3.8). Such an interpretation is supported by recent experimental results from chlorite, muscovite/illite and saponite bearing gouges from the Alpine Fault, New Zealand, which found that the gouges deformed with low coefficients of sliding friction in the range 0.28-0.37 and exhibited velocity strengthening behaviour (Barth et al., 2013; Boulton et al., 2012). According to the cooling model of Boutonnet et al. (2012) for the Pangong strand (their 'Muglib strand'), cooling through 300°C occurred at c. 7 Ma. This date is proposed therefore for the time at which the Pangong strand may have begun to behave with a reduced coefficient of friction.

3.3.5 Hydraulic Characteristics of the Nubra Fault Strand

The impact of pore fluids on frictional rock shear strength depends on whether pore fluid pressures can be sustained at elevated levels. Sustained high fluid pressures reduce the effective normal stress on fractures and promote slip at reduced values of shear stress. However, open fractures potentially create sufficient permeability for fluids to remain at relatively low hydrostatic pressures (Townend and Zoback, 2000). These opposing effects are controlled in part by the bulk behaviour of the fault zone, either as a conduit or a barrier to fluid flow (Caine et al., 1996), and in part by the effect of those fluids in causing fracture induced permeability or permeability reduction by cement precipitation (e.g. Collettini and Holdsworth, 2004).

The exposed lithologies on the Nubra fault strand provide an opportunity to examine the hydraulic characteristics of the fault. In the fault core, foliated cataclasites would likely act as a barrier to fluid flow at the depths of the FVTZ. The observed tourmaline±quartz veins and travertine deposits, inferred to have formed at shallower depths, together with present day hydrothermal springs on the fault trace, show that abundant fluid flow occurs in the brittle regime. In the less intensely deformed leucogranites, microfracturing associated with sericitisation of feldspars, along with multiple generations of tourmaline±quartz veins (Figure 3.6f; Watkins, 2011), indicate that the fault damage zone largely acted as a conduit for fluid flow. Repeated

fracturing and sealing during formation of the tourmaline±quartz veins indicates cyclicity in pore fluid pressure build-up, leading to microfracturing (Watkins, 2011). These observations suggest that the Nubra fault strand may be classified (in the sense of Caine et al., 1996) as a distributed conduit at shallow levels, transitioning to a combined conduit-barrier to hydrous and boron-rich fluids at depths approaching the FVTZ. Boron within the tourmaline was likely sourced from the metasedimentary lithologies, as recognised in other metasomatic intrusive settings (e.g. Corteel and De Paepe, 2003). Precipitation of tourmaline±quartz veins and travertine within this system acted to occlude permeability, leading to elevated pore fluid pressures, and resulting in hydrofracture. Thus, it is possible that effective fracture sealing, particularly in the fault core, could have led to deformation at low values of shear stress.

At depths of 9-11 km phyllonitisation resulting from hydrous retrograde mineral reactions affected a c. 10 m wide band of the Nubra Formation. This suggests therefore that the fault acted as a distributed conduit within this zone at these depths. At the somewhat greater depths of 11-16 km, sericitisation affected the leucogranites across a zone several hundred metres in width. The fault acted therefore as a widely distributed conduit at these depths.

3.3.6 Seismogenic potential of the KFZ

The operation of fault weakening mechanisms on some faults has been suggested to promote aseismic creep at the expense of generating large earthquakes. These mechanisms include the presence of weak mineral phases (San Andreas fault, Carpenter et al., 2011), interconnected weak layers of phyllosilicates (Zuccale fault, Collettini et al., 2009) and fluid overpressure (Byerlee, 1990), all of which are evident in the KFZ. Faults that are creeping at shallow crustal levels show a distinctive displacement discontinuity in InSAR data (e.g. Lyons and Sandwell, 2003; Bürgmann et al., 2000). The KFZ however lacks this distinctive signature (Wang and Wright, 2012; Wright et al., 2004) showing that it is not creeping at shallow depths. Rather the InSAR data show that the fault is currently accumulating displacement at c. 5 mm/yr in its central portion but that this is distributed

over a broad region, consistent with the seismogenic layer being fully locked (Wang and Wright, 2012).

Fault scaling relationships show that moment magnitude (M) 7 and 8 earthquakes on strike-slip faults typically produce displacements of c. 1 m and 10 m respectively (Wells and Coppersmith, 1994). Thus the 120 km offset accumulated on the KFZ over 15 Ma (Phillips et al., 2013; Searle et al., 2011; Phillips et al., 2004) could be produced by M7 earthquakes with 125 year average recurrence intervals or M8 earthquakes with 1250 year average recurrence intervals. Brown et al. (2002) utilised ^{10}Be dating of an offset debris flow on the Pangong strand to determine that 2-2.5 m offset had occurred in the last 1-2 kyr and suggested that it resulted from a single earthquake. This offset would typically require a c. M7.5 earthquake on a strike-slip fault (Wells and Coppersmith, 1994). Brown et al. (2002) also report an 11-14 ka debris flow offset by 40 ± 5 m, which would require such M7.5 events to occur with a recurrence interval in the range 488-1000 years. These recent and long term considerations suggest that the seismicity on the KFZ may be characterised by c. M7.5+ events with recurrence intervals of the order of 1000 years. This is the same as the seismogenic potential calculated from the regional stress and strain field (Houlié and Phillips, 2013). Coulomb stress modelling suggests that the rupture history of the KFZ may be modulated by seismic activity along the subduction plane of the Indian Plate to the SW (Houlié and Phillips, 2013).

The characteristics of a fault showing potential for frictional weakness but also seeming to deform by large magnitude earthquakes, are remarkably similar to observations on the southern onshore portion of the Alpine Fault, New Zealand. There, frictionally weak (steady state friction coefficients 0.12-0.37), velocity strengthening fault core gouges (expected to deform by slow aseismic slip) are associated with a palaeoseismic record of large magnitude earthquakes over the last 8000 years (Barth et al., 2013 and references therein). This was attributed in large part to switches between velocity strengthening/weakening behaviour with increasing temperature in a variety of materials, along with variable rheological behaviour resulting from varied mineral proportions, fault roughness, pore fluid pressure fluctuations and competing deformation mechanisms (Barth et al., 2013). The results of this

study suggest that all of these may be important factors also impacting seismicity on the KFZ, making it difficult to infer the seismic nature of the fault from study of the exposed fault rocks alone.

3.3.7 Frictional heating on the KFZ

It has been suggested that frictional heating on the KFZ may have led to synkinematic metamorphism and anatexis (Rolland et al., 2009; Valli et al., 2007, 2008; Lacassin et al., 2004a,b). This suggestion was considered as evidence that the KFZ has a high slip-rate over geological time-scales and is lithospheric in scale, allowing it to accommodate eastward extrusion of Tibet in a plate-like manner (Lacassin et al., 2004a,b; Rolland and Pêcher, 2001). However, this interpretation has been contested on the grounds that not only do peak metamorphism (Streule et al., 2009) and anatexis (Phillips et al., 2013) pre-date the fault zone, but also are widespread in occurrence away from the KFZ and hence were not produced by the KFZ (Phillips and Searle, 2007; Phillips et al., 2004; Searle and Phillips, 2004; Searle et al., 1990, 1998). The potential for the KFZ to have deformed with a reduced coefficient of friction documented in this study makes it unlikely that the fault could have generated significant shear heating, particularly given its low slip rate (LeLoup et al., 1999). Further, the evidence for fluid flow at variable crustal depths indicates that any frictional heat generated would be advected towards the surface, as is happening today by hydrothermal systems, making it unlikely that the temperatures could be significantly raised due to faulting. This is supported by the observations of retrograde greenschist facies assemblages in the phyllonites and sericitisation in the granites, which show that the deformation was associated with retrograde rather than prograde metamorphism. Concomitantly, crustal thickening is likely responsible for the prograde metamorphism and anatexis of the extensive Karakoram Metamorphic Complex of the Asian margin (Leloup et al., 2011; Searle et al., 2010). The findings of this study support the conclusion that the KFZ has not generated significant shear heating.

3.3.8 Fault Weakening and Implications for Continental Lithospheric Strength

Studies into the characteristics of continental deformation have tried to determine the main load bearing depth range within the continental lithosphere (Chen et al., 2012; Hirth and Kohlstedt, 2003; Jackson, 2002). Various models have been put forward in which the maximum lithospheric strength resides in the upper crust, lower crust or upper lithospheric mantle (Bürgmann and Dresen, 2008; Burov, 2011). A prediction of models for which the crust is the strongest portion of the lithosphere is that deformation will be accommodated on a small number of laterally extensive and narrow faults that penetrate the entire crust with high slip rates and shear heating (e.g. Avouac and Tapponnier, 1993). Such faults would be capable of accommodating plate-like motion of fault-bounded rigid crustal blocks and in the Himalayan-Tibetan orogen are used to support plate-like motion of Tibet (Peltzer and Tapponnier, 1988). If such a fault zone slipped with a much reduced coefficient of friction ($\mu < 0.4$), it would exhibit large offsets and high slip-rates due to the reduced resistance (He and Chéry, 2008) but would not cause significant shear heating. The KFZ has previously been demonstrated to have a fairly low offset (40-150 km) (Wang et al., 2012; Searle, 1996; Gaudemer et al., 1989) and low slip rate ($\leq 10 \text{ mmyr}^{-1}$) (Chevalier et al., 2012; Wang and Wright, 2012; Meade, 2007; Brown et al., 2005; England and Molnar, 2005; Phillips et al., 2004; Molnar and Lyon-Caen, 1989), making it unlikely to have played a major role in accommodating plate-like motion of Tibet (Searle et al., 2011). Evidence for the potential weakness of the KFZ strengthens this argument as, even with a potentially low coefficient of friction, it has only a limited offset and low slip rate, making only a limited contribution to plate-like deformation of the Asian crust. The low offset and slip rate, even on a potentially weak fault, argues that the main load bearing region of the lithosphere must be beneath the depth of penetration of the fault, and lie within the lower crust or upper mantle. Such a situation would occur in the presence of dry rocks dominated by either feldspar in the lower crust or olivine in the lithospheric mantle (Bürgmann and Dresen, 2008; Jackson, 2002) and is inconsistent with models where continental lithospheric strength is concentrated in the upper crust (Jackson, 2002).

3.4. Conclusions

Fault rocks presently exposed along the KFZ in Ladakh, NW Himalaya, record deformation at depths spanning the FVTZ and reveal evidence for the operation of several fault weakening mechanisms, including exploitation of pre-existing weak mineral phases, reaction softening, interconnected weak layer development and high pore fluid pressures. These suggest that the KFZ has had potential to act as a weak fault, deforming with significantly less than Byerlee friction. These weakening mechanisms are likely to have operated in the exposed structural level since at least 14-15 Ma and may continue to do so at depth.

The fault rocks exposed along the KFZ provide field examples of fault rocks in which experimentally predicted fault weakening mechanisms such as frictional-viscous deformation may have operated. Additionally the KFZ can be regarded as an analogue for other potentially weak active strike-slip fault zones where such weakening mechanisms may be active at depth. Unlike some faults where weakening has been associated with aseismic creep or small earthquakes, the KFZ is currently fully locked and likely generates M7-8 earthquakes with c. 1000 year recurrence intervals.

The operation of low friction deformation mechanisms within the KFZ, coupled with thermal advection by fluids, make it unlikely that shear heating could have significantly raised mid-crustal temperatures to result in peak metamorphism and anatexis in the fault zone. Instead, high grade metamorphic rocks and migmatites are likely the result of orogenic crustal thickening, in accord with their widespread occurrence across the Karakoram. Fault related metamorphism on the other hand is retrogressive sericitisation and phyllonitisation.

If the KFZ does indeed act as a weak fault, then its low slip-rate and limited offset suggest that the long-term strength of the lithosphere in this region occurs beneath the depths where weakening processes operate, in the lower crust or lithospheric mantle. These observations demonstrate the need to consider fault zone strength when assessing the role of faults in accommodating orogenic deformation.

4. Evolution of the Eastern Karakoram Metamorphic Complex, Ladakh, NW India, and its relationship to magmatism and regional tectonics

Abstract

The eastern Karakoram terrane, N.W. India, records crustal evolution in the core of the Himalayan-Tibetan orogen. Recent debate has centred on whether prograde metamorphism, anatexis and leucogranite emplacement were the result of localised shear heating and magma advection within the Karakoram Fault Zone (KFZ) or instead predate the KFZ and were the result of regional tectonometamorphic events. This chapter, based on Wallis et al. (2014a), presents microstructural observations and geothermobarometric determinations to constrain the relationships between metamorphism, magmatism and deformation. The results place constraints on the conditions and timing of deformation within the KFZ and provide further tectonic context for the evolution of the KFZ.

Andalusite porphyroblasts that grew in metapelites during 15.7 Ma leucogranite emplacement show pre-kinematic microstructures, demonstrating that the KFZ initiated after this time. Therefore, earlier anatexis and metamorphism are the result of regional metamorphic events. Amphibole-plagioclase thermobarometry on a c. 17 Ma migmatite melanosome, later exhumed within a transpressional zone of the KFZ, shows that melting occurred at 688 °C and 522 MPa. Amphibolites record an older kyanite-grade metamorphic event that occurred at 677-736 °C and 875-1059 MPa. Metapelites also record a kyanite-grade event which is constrained by Ti-in-biotite thermometry to have occurred at 622 °C and >650 MPa. The tectonometamorphic history of the eastern Karakoram correlates closely with that of the central Karakoram away from the KFZ. This correlation supports the interpretation that metamorphism and anatexis were regional in extent and also indicates a limited offset of <150 km on the KFZ.

4.1 Introduction

Understanding the evolution of the continental crust during the orogenic cycle, the pressure-temperature paths experienced by metamorphic rocks and their relationship to magmatic and deformation processes are fundamental but challenging issues. The complex histories of rocks in continental collision zones must be deciphered to place constraints on the evolution of an orogen. The Karakoram-Qiangtang terrane in the Himalayan-Tibetan orogen (Figure 4.1a) provides an opportunity to investigate the former south Asian active margin, which later became the core of the orogen, and hence holds key information on crustal evolution in these tectonic settings. The Karakoram terrane in Pakistan is relatively well studied and has yielded much information on its complex history (e.g. Palin et al., 2012; Foster et al., 2004; Fraser et al., 2001; Villa et al., 1996). However, surface exposures of its correlative, the Qiangtang terrane in Tibet, consist predominantly of supracrustal and early Mesozoic metamorphic lithologies, which record little information on crustal processes around the time of India-Asia collision (Pullen et al., 2011). The Eastern Karakoram in Ladakh, NW India, geographically links the central Karakoram with the Qiangtang terrane and contains exposures of basement lithologies exhumed from a range of depths. However, metamorphism in this region remains relatively less studied and has therefore potential to further our understanding of these key terranes.

The Karakoram terrane in the Hunza and Baltoro regions of Pakistan has experienced five metamorphic events (M_0 - M_4). M_0 is represented in Hunza by Early Cretaceous andalusite-grade contact metamorphism during subduction prior to closure of the Shyok suture (Palin et al., 2012). Late Cretaceous closure of the Shyok suture resulted in regional sillimanite-grade M_1 metamorphism in Hunza, culminating in Eocene migmatization following closure of the Indus suture during India-Asia collision (Foster et al., 2004; Fraser et al., 2001). Oligo-Miocene kyanite-grade M_2 metamorphism in Hunza and Baltoro was closely followed by an M_3 staurolite-grade event during the mid-Miocene in Hunza (Palin et al., 2012; Fraser et al., 2001; Villa et al., 1996). M_4 Mio-Pliocene sillimanite-grade metamorphism is

represented by migmatisation in the Bullah and Dassu domes in the Baltoro (Fraser et al., 2001).

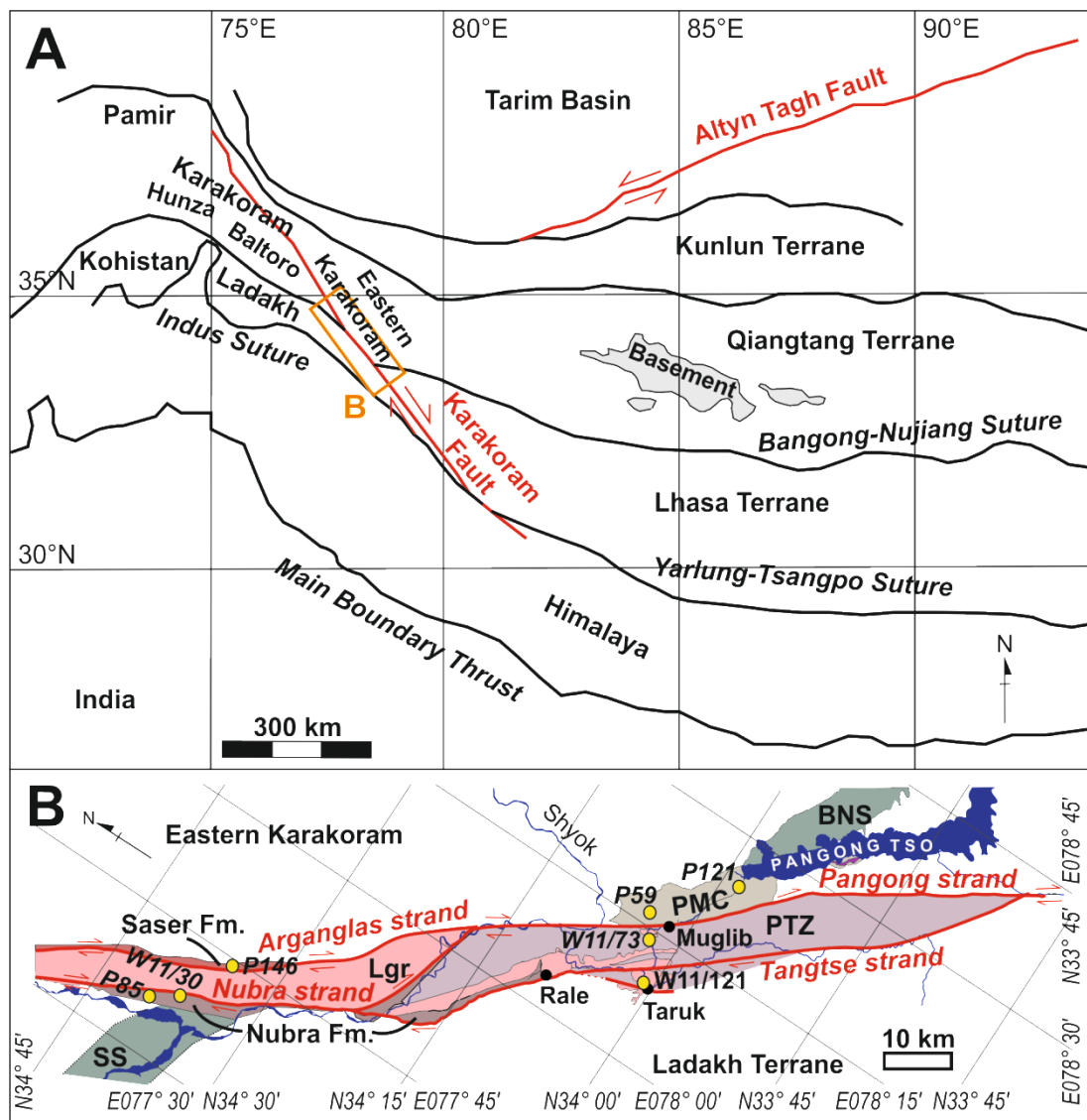


Figure 4.1 Location maps. (a) Simplified terrane map of the Himalaya and Tibet showing the location of the Hunza, Baltoro and Eastern Karakoram (modified from Searle et al., 2011). Also shown is the extent of basement exposure within the Qiangtang terrane in Tibet (from Pullen et al., 2011). The study area is marked by the orange box and expanded in part (b). (b) The central portion of the Karakoram fault zone in Ladakh, NW India showing the four subunits of the Eastern Karakoram Metamorphic Complex; the Pangong Transpressional Zone (PTZ), Pangong Metamorphic Complex (PMC), Nubra Formation and Saser Formation. Also shown are the major bodies of Miocene leucogranites (Lgr), Bangong-Nujiang suture (BNS) and Shyok suture (SS). Sample localities are marked in yellow. Modified from Phillips (2008).

The Qiangtang terrane contains a 600x150 km Palaeozoic tectonic mélangé equilibrated at 425-660 °C, >1 GPa during low-angle subduction (Pullen et

al., 2011; Kapp et al., 2003). Eclogites within this belt record conditions of 2.0-2.5 GPa, 482-625 °C (Zhang et al., 2006). The melange is structurally overlain by Upper Palaeozoic-Mesozoic strata and is adjacent to the Gondwanan basement of the Qiangtang terrane but none of these units provide significant information on the late Mesozoic-Cenozoic tectonics associated with the India-Asia collision (Pullen et al., 2012).

In the Eastern Karakoram, the Karakoram Fault Zone (KFZ) cuts through medium-high grade metamorphic rocks of the Karakoram terrane and is spatially associated with exposed migmatite and large volumes of leucogranite (Phillips, 2008). Recent debate has centred on whether prograde metamorphism resulted from shear heating and/or fault-guided magmatic advection within the KFZ (Rolland et al., 2009; Valli et al., 2008; Rolland and Pêcher, 2001), or alternatively was the result of widespread crustal thickening (Searle et al., 1998, 2011; Streule et al., 2009). Rolland and Pêcher (2001) and Rolland et al. (2009) propose that high geothermal gradients within the KFZ demonstrate that it is a lithospheric-scale fault that has generated shear heating and channelled magmas during plate-like extrusion of the Tibetan Plateau. Elevated $^3\text{He}/^4\text{He}$ ratios from geothermal springs on the fault have also been put forward as evidence that the KFZ accesses the mantle (Klemperer et al., 2013). However, cross-sections based on shortening estimates across the Himalaya require that the KFZ is confined within the Tibetan crust as it must be underlain by subducted Indian lithosphere for much of its length (Searle et al., 2010). Also, peak metamorphism adjacent to the KFZ predates strike-slip deformation on the fault (Streule et al., 2009) and can be correlated with metamorphic events away from the KFZ in the Hunza region of the Karakoram (Palin et al., 2012; Fraser et al., 2001). Thus, prograde metamorphism throughout the Karakoram may be the result of regionally extensive crustal thickening and magmatism, rather than localised deformation. Wallis et al. (2013) reported that deformation within the KFZ is associated with retrograde metamorphism during exhumation and fluid flux, rather than prograde metamorphism.

The age of the KFZ has also been contested and depends primarily upon the relative ages of the fault and Miocene granitoid intrusions along its length. Interpretations that the intrusions are synkinematic with respect to

the KFZ have led some authors to suggest that the KFZ initiated as early as 22-34 Ma (Boutonnet et al., 2012; Leloup et al., 2011, 2013; Weinberg et al., 2009; Valli et al., 2008; Lacassin et al., 2004). These suggestions are based on synkinematic interpretations of outcrop-scale structures or microstructures. However, such interpretations are made more difficult and potentially less reliable by overprinting of high temperature microstructures by later lower temperatures deformation fabrics and by the potential for older pre-KFZ outcrop- to micro-scale structures to rotate into alignment with the fault during later deformation. Alternative prekinematic interpretations of the intrusions, based on regional mapping, thermochronology and field and microstructural criteria, have also been put forward as evidence that the KFZ initiated after c. 15.7 Ma and is therefore a significantly more recent structure (Wang et al., 2011, 2014; Phillips and Searle, 2007; Phillips et al., 2004; Searle, 1996). If this is the case then the KFZ cannot have been the cause of anatexis and leucogranite generation between c. 22-16 Ma (Phillips et al., 2013). In this chapter I investigate metamorphism throughout the Eastern Karakoram Metamorphic Complex (EKMC, Figure 4.2) and its relationship to regional and local (i.e. KFZ) tectonic events.

4.2 Mineralogy and microstructure

The mineralogy and microstructures of seven samples, covering the four subunits of the EKMC (locations in Table 4.1), were analysed using standard optical microscopy and the FEI Quanta 650 FEG-ESEM at the University of Leeds.

W11/73 (Figure 4.2a) is a melanocratic migmatite restite from the NE PTZ close to Muglib (Figure 4.1b), with the assemblage Am+Pl+Bt+Qtz+Kfs (Figure 4.3a). It has a fresh coarse grained c. 0.5 mm nematoblastic texture. Amphiboles show green-light brown pleochroism and lack intragranular deformation. Plagioclase shows occasional subgrains. Foliation is defined by aligned amphibole, biotite and elongate plagioclase.

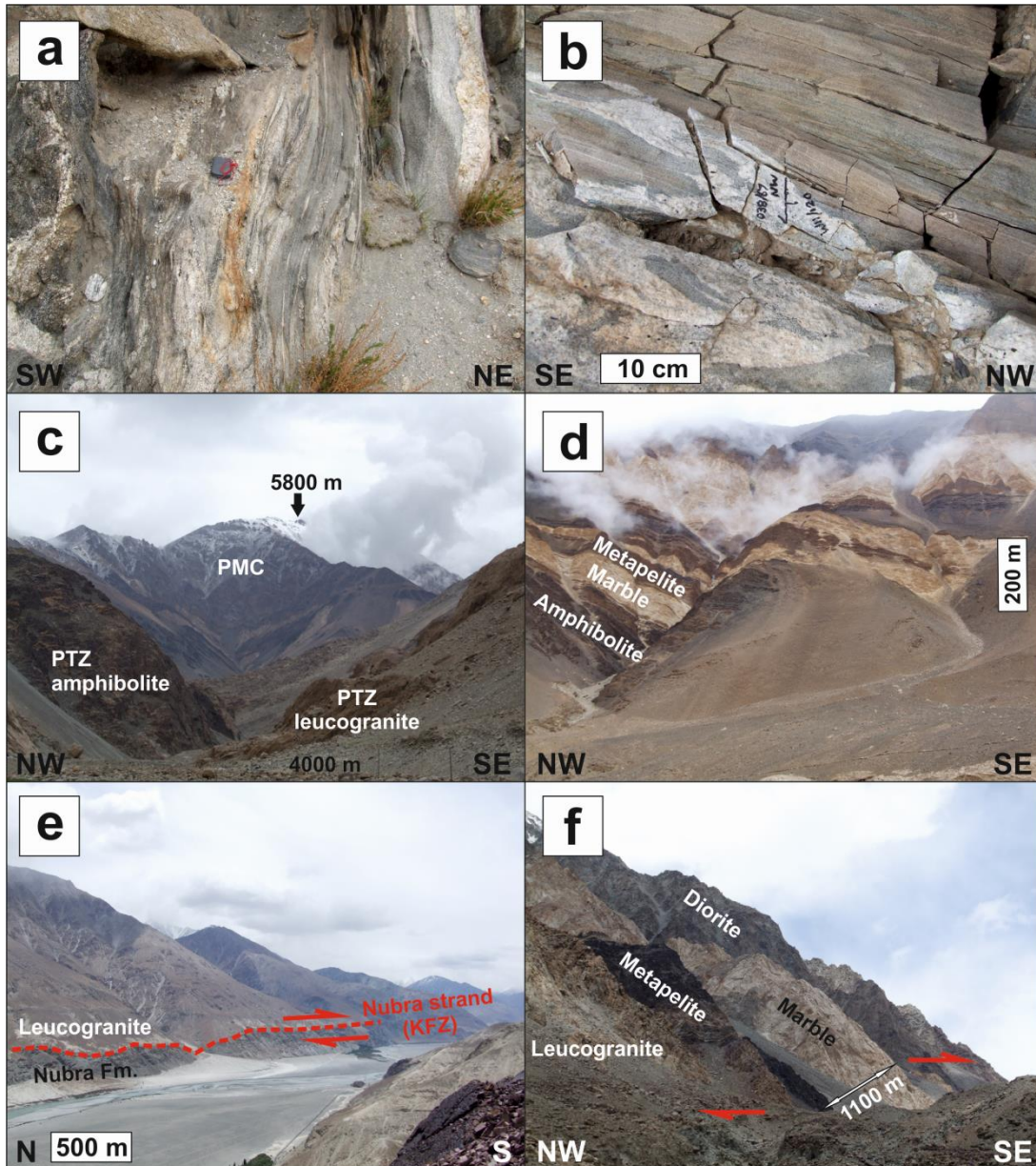


Figure 4.2 Field photographs of the Eastern Karakoram Metamorphic Complex. (a) Diatexite migmatite in the PTZ near Muglib. Migmatite is partitioned into leucosome and melanosome (centre) and leucogranitic melt segregations (far right). Compass-clinometer (centre) is 8 cm. (b) Amphibolite (grey) intruded by irregular leucogranite dykes (white) in the PTZ near Taruk. (c) Gorge between Tangtse and Muglib. PTZ lithologies are juxtaposed with the PMC by the Pangong fault strand (out of shot at base of mountain). Foreground field of view is 450 m. (d) Layered sequence of PMC marble, amphibolite and metapelite near Pangong Tso. Field of view is 2.3 km. (e) The Nubra Formation juxtaposed with the Nubra-Siachen leucogranite by the Nubra fault strand of the KFZ in the Nubra Valley. (f) The Saser Formation in Sumur gorge. Metapelites and marbles within the Arganglas fault strand have accommodated dextral offset of the Nubra-Siachen leucogranite and Arganglas diorite.

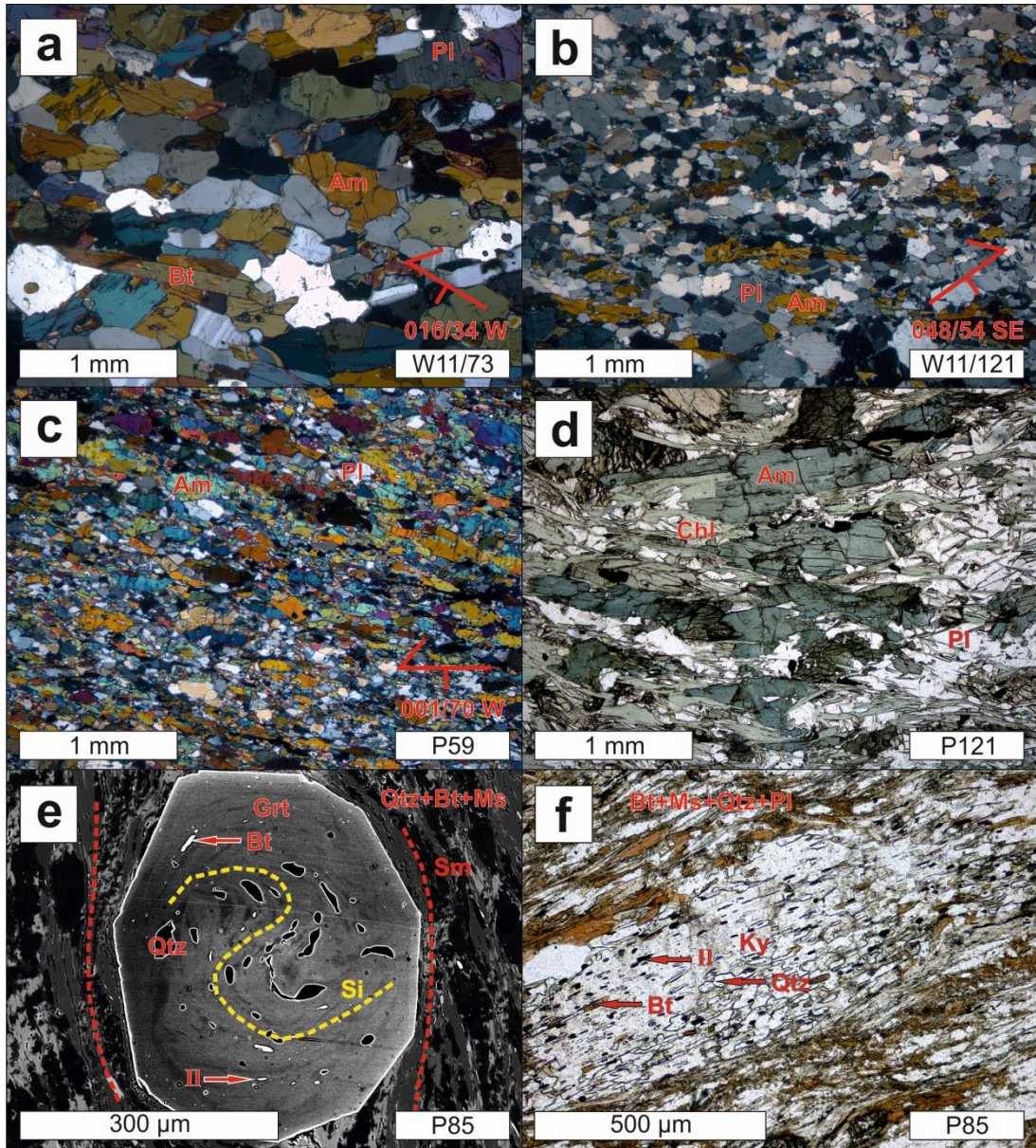


Figure 4.3 Microstructures within the Eastern Karakoram Metamorphic Complex. (a)-(c) are cross-polarised optical photomicrographs. (d) and (f) are plane-polarised optical photomicrographs. (e) is a composite backscattered electron atomic number contrast image with brightness/contrast adjusted separately for garnet and matrix. (a) W11/73, PTZ, coarse grained migmatite restite with weak grain alignment fabric. (b) W11/121, PTZ, plagioclase-rich amphibolite with elongate amphiboles. (c) P59, PMC, amphibolite with strong amphibole grain alignment fabric. (d) P121, PMC, amphibolite with blue-green amphiboles in chloritic matrix. (e) P85, Nubra Formation metapelite. Sigmoidal zoning and Qtz+Bi+Il inclusion fabric (Si) is discordant with matrix foliation (Sm). (f) P85, Nubra Formation metapelite. Kyanite porphyroblast with Qtz+Bi+Il inclusions. Am=amphibole, Bt=biotite, Chl=chlorite, Grt=garnet, Il=ilmenite, Ky=kyanite, Ms=muscovite, Pl=plagioclase, Qtz=quartz.

W11/121 (Figure 4.2b) is a fine grained nematoblastic amphibolite from the SW PTZ near Taruk (Figure 4.1b) and consists of Pl+Qtz+Am+Ep+Ttn (Figure 4.3b). Amphiboles are fragmented and anhedral with green-brown pleochroism. Plagioclase contains subgrains and quartz has irregular lobate grain boundaries.

P59 (Figure 4.2c) is a fine grained nematoblastic amphibolite from the PMC near Muglib (Figure 4.1b), consisting of Am+Pl+Qtz+Il (Figure 4.3c). Amphiboles are brown in plane polarised light with subgrains visible in cross-polarised light. Plagioclase also contains subgrains and quartz has irregular lobate grain boundaries.

P121 (Figure 4.2d) is a coarse grained amphibolite from the PMC near Pangong Tso (Figure 4.1b), with the assemblage Am+Pl+Chl+Qtz+Cal+Rt (Figure 4.3d). Alignment of c. 1 mm amphibole and c. 0.5 mm chlorite grains imparts a nematoblastic-lepidoblastic texture. Amphiboles show green-blue pleochroism, undulose extinction and are fractured. Plagioclase contains subgrains and has bulging grain boundaries.

P85 (Figure 4.2e) is fine grained metapelite from the Nubra Formation (Figure 4.1b), consisting of Bt+Ms+Qtz+Pl+Grt+Ky+Il (Figures 4.3e and 4.3f). It comprises a matrix of strongly lepidoblastic Bt+Ms+Qtz+Pl, which asymmetrically wraps around idioblastic garnet and nematoblastic kyanite porphyroblasts to define a dextral S-C fabric striking c. 140° parallel to the macroscopic trend of the KFZ. Garnet and kyanite porphyroblasts contain quartz, biotite and ilmenite inclusions. In kyanite these inclusions are aligned parallel to the long axis of kyanite blades (Figure 4.3f). In garnet the inclusions define straight or sigmoidal fabrics, both of which are discordant to the matrix foliation (Figure 4.3e). Quartz ribbons within the matrix contain abundant subgrains.

W11/30 (Figure 4.2e) is a porphyroblastic metapelite from the Nubra Formation adjacent to the Nubra-Siachen leucogranite batholith (Figure 4.1b), with the assemblage Bt+Qtz+And+Grt+Ms. Andalusite porphyroblasts up to 5 mm in length are aligned within a fine grained, well foliated Qtz+Bt+Ms matrix and contain quartz and biotite inclusions. The latter are of similar size to matrix biotite but show little or no preferred alignment (Figure

4.4a-c). The quartz inclusions are very fine grained rods aligned sub-perpendicular to the long axis of andalusite blades. Andalusite grain boundaries are irregular and overgrown by a thin layer of muscovite that coarsens into pressure shadows (Figure 4.4b). Coarse grained quartz also occurs in these pressure shadows (Figure 4.4b), as well as in monomineralic layers. In these microstructures, quartz has irregular lobate grain boundaries, weak subgrain development but strong undulose extinction. Finer grained matrix quartz shows abundant subgrains. Small garnets occur within andalusite-free layers. A few contain fine graphite inclusions but most are optically inclusion free. The Bt+Ms foliation is oriented 138/80 NE, parallel to the macroscopic orientation of the KFZ and wraps around both andalusite (Figure 4.4c) and garnet (Figure 4.4d) porphyroblasts with dextral asymmetry. Andalusite growth only occurs within a few metres of the Nubra-Siachen leucogranite batholith. At greater distances, kyanite bearing assemblages (P85) are preserved.

P146 (Figure 4.2f) is a K-feldspar megacrystic lepidoblastic metapelite from the Saser Formation (Figure 4.1b), with the assemblage $Pl+Kfs+Qtz+Bt+Ms+Il$ (Wallis et al., 2013). Alignment of micas and quartz ribbons form a strong dextral S-C fabric showing subhorizontal simple shear, consistent with the KFZ deformation in the Arganglas strand of the fault (Phillips and Searle, 2007). The same dextral shear sense is also shown by σ -type mantled feldspar porphyroclasts and sigmoidal and rhomboidal muscovite fish. Ribbon quartz shows interlocking lobate grain boundaries, whereas feldspars show bulging grain boundaries and fine grained recrystallised mantles (Wallis et al., 2013).

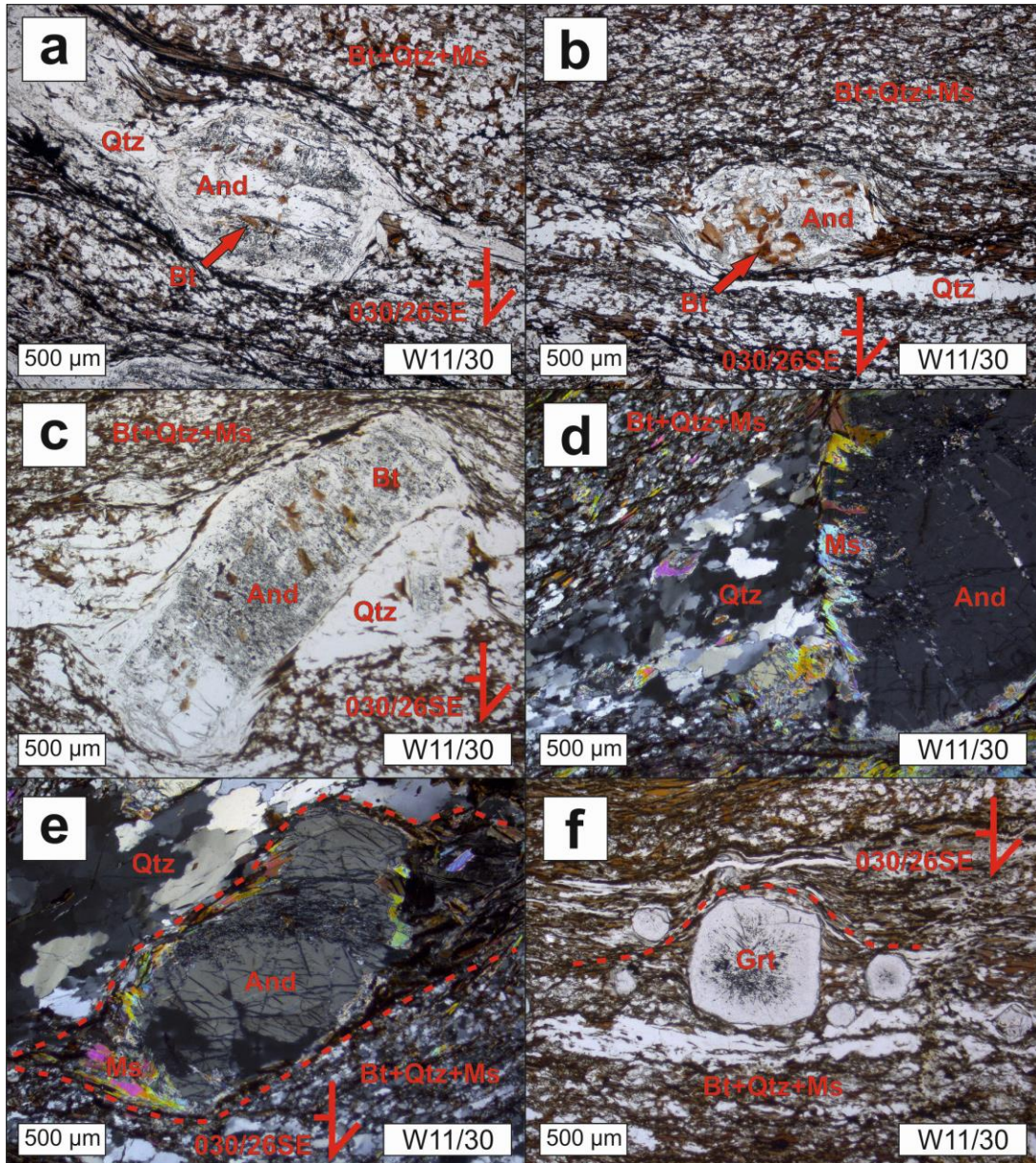


Figure 4.4 Microstructures in W11/30 Nubra Formation metapelite. (a-c and f) are plane-polarised optical photomicrographs. (d) and (e) are cross-polarised optical photomicrographs. (a-c) Andalusite porphyroblasts with randomly oriented biotite inclusions and quartz pressure shadows (a and c), wrapped by Bt+Qtz+Ms matrix with dextral shear sense (c). (d) Andalusite porphyroblast with muscovite overgrowth and coarse quartz pressure shadow. (e) Andalusite porphyroblast with muscovite overgrowth and biotite pressure shadow showing dextral shear sense. (f) Foliation wrapping around garnet porphyroblast. Bt=biotite, Qtz=quartz, Ms=muscovite, And=andalusite and grt=garnet.

4.3 Data collection and geothermobarometers

4.3.1 Amphibole-plagioclase thermobarometry

Amphibole and plagioclase major element data were collected using wavelength-dispersive X-ray spectroscopy on the Jeol 8230 electron microprobe at the University of Leeds. Amphibole analyses were collected using 15 kV accelerating voltage, 15 nA beam current and a $<1 \mu$ focussed beam. Peak and background count times were respectively 30 s and 15 s for Fe, 20 s and 10 s for Si and Al and 10 s and 5 s for remaining elements (see Tables 4.1, A.1 and A.3). Plagioclase analyses were collected using 15 kV accelerating voltage, 10 nA beam current and a $2 \mu\text{m}$ beam. Peak and background count times were respectively 30 s and 15 s for Fe and 10 s and 5 s for remaining elements (see Tables 4.1, A.1 and A.3). Measurements were made in pairs from the margins of adjacent amphibole and plagioclase grains. 35 amphibole-plagioclase pairs were analysed for W11/73, 32 for W11/121 and 15 pairs each for P59 and P121 (Tables A.1 and A.3).

Pressure estimates were derived using the geobarometric calibrations of Anderson and Smith (1995) and Bhadra and Bhattacharya (2007). The geobarometer of Anderson and Smith (1995) is based on increasing Al-content of amphibole with pressure. It accounts for the effects of temperature and $f\text{O}_2$ and is valid in the range 100-1000 MPa and 675-760 °C. This barometer was experimentally calibrated using igneous melt-bearing assemblages and therefore is most appropriate to these rock types. The barometer of Bhadra and Bhattacharya (2007) is based on elemental distributions between equilibrated amphibole-plagioclase pairs and was calibrated against experimental quartz-bearing assemblages for the range 1-15 MPa and 650-950°C, with the aim of developing a barometer applicable to garnet-free metamorphic rocks. Two calibrations of the Bhadra and Bhattacharya (2007) barometer were developed using different input parameters for regression. These two expressions yield similar results for the samples in question, differing by only 20 MPa on average, so the average of the two results is reported. Due to the different calibration assemblages of the two barometers the Anderson and Smith (1995) barometer is most appropriate for rocks that equilibrated in the presence of

melt (i.e. migmatite W11/73), whereas the Bhadra and Bhattacharya (2007) barometer is most appropriate for amphibolites (i.e. W11/121, P59 and P121). The results of both calibrations for all four of these samples are included for comparison.

Sample	W11/73		W11/121		P59		P121	
Rock type	Migmatite melanosome		Amphibolite		Amphibolite		Amphibolite	
Lat.	34°02.738'		34°00.838'		34°04.512'		33°57.889'	
Long.	078°13.452'		078°08.925'		077°35.274'		078°24.613'	
Mineral	Am	PI	Am	PI	Am	PI	Am	PI
SiO ₂	44.02	61.26	42.44	59.60	44.75	56.77	42.37	62.09
TiO ₂	0.99	0.03	0.57	0.02	0.63	0.01	0.50	0.03
Al ₂ O ₃	10.73	24.58	11.06	26.09	13.58	27.92	15.23	24.45
Cr ₂ O ₃	0.08	na	0.04	na	0.12	na	0.10	na
Fe ₂ O ₃	2.88	0.19	4.05	0.13	2.47	0.18	3.24	0.14
FeO	12.24	na	15.78	na	11.58	na	12.79	na
MnO	0.41	0.01	0.78	0.06	0.38	0.00	0.30	0.01
MgO	11.98	0.00	8.74	0.03	11.68	0.00	9.97	0.01
CaO	11.89	6.19	11.89	7.50	11.41	9.58	11.35	5.54
Na ₂ O	1.42	8.23	1.21	7.36	1.49	6.45	1.87	8.94
K ₂ O	1.29	0.29	1.33	0.12	0.27	0.05	0.28	0.07
H ₂ O	2.00	na	1.90	na	2.07	na	2.03	na
F	0.04	na	0.11	na	0.00	na	0.00	na
Cl	0.03	na	0.08	na	0.00	na	0.02	na
Ba	na	0.14	na	0.00	na	0.00	na	0.00
Sum	100.00	100.92	99.98	100.91	100.43	100.96	100.05	101.28
Oxygens	23	8	23	8	23	8	23	8
Si	6.522	2.706	6.442	2.637	6.488	2.528	6.241	2.725
Ti	0.110	0.001	0.065	0.000	0.069	0.000	0.055	0.001
Al	1.874	1.280	1.978	1.360	2.320	1.465	2.644	1.265
Cr	0.009	na	0.004	na	0.014	na	0.012	na
Fe ₃	0.321	0.006	0.462	0.004	0.269	0.006	0.359	0.005
Fe ₂	1.517	na	2.003	na	1.404	na	1.575	na
Mn	0.052	0.000	0.100	0.002	0.046	0.000	0.037	0.000
Mg	2.646	0.000	1.977	0.002	2.524	0.000	2.189	0.001
Ca	1.888	0.293	1.934	0.355	1.773	0.457	1.792	0.260
Na	0.408	0.705	0.356	0.631	0.419	0.557	0.534	0.760
K	0.244	0.016	0.257	0.007	0.049	0.003	0.052	0.004
Ba	na	0.002	na	0	na	0.000	na	0.00
Sum	15.591	5.009	15.578	4.998	15.375	5.016	15.490	5.021
XAn	-	28.79	-	36.23	-	46.03	-	27.07

Table 4.1 Sample locations and representative chemical compositions of minerals used for amphibole-plagioclase geothermobarometry.

Temperature estimates were made using the geothermometer calibrations of Holland and Blundy (1994) and Otten (1984). The Holland and Blundy (1994) calibration is based on the reaction edenite+albite=richterite+anorthite (Anderson 1996) and was calibrated

using both experimental data and natural igneous and metamorphic assemblages. The Otten (1984) thermometer uses an empirical calibration of the Ti-content of natural igneous amphiboles, but lacks the thermodynamic rigour of the Holland and Blundy (1994) geothermometer. As the Holland and Blundy (1994) thermometer was calibrated for both igneous and metamorphic assemblages and has a strong thermodynamic basis, it is favoured over the Otten (1984) geothermometer. Nevertheless, the Otten (1984) temperature estimates are included for comparison with the Holland and Blundy (1994) amphibole-plagioclase estimates and the Henry et al. (2005) Ti-in-biotite geothermometer (Section 4.2). Pressures using the Anderson and Smith (1995) calibration and temperatures using the Holland and Blundy (1994) and Otten (1984) calibrations were determined using the “Plagioclase-Hornblende Thermobarometry” spreadsheet available from the Mineralogical Society of America at www.minsocam.org/MSA/RIM/RiM69_Ch04_hbld_plag_thermo-jla.xls. Pressures from the Bhadra and Bhattacharya (2007) geobarometer were also used as input to this spreadsheet to determine the corresponding Holland and Blundy (1994) temperatures.

4.3.2 Ti-in-biotite geothermometry

Major element data were collected on biotites using the Jeol 8230 electron microprobe at the University of Leeds. Analysis conditions were 15 kV accelerating voltage and 15 nA beam current. Count times for peaks and backgrounds were respectively 60 s and 30 s for Ti and 15 s and 7 s for remaining elements (Tables 4.2 and A.4). Measurements were collected from biotite margins adjacent to ilmenite grains to ensure that the biotite is Ti-saturated. In total, 79 analyses were made on sample P85 and 41 on P146 (Table A.4).

Temperature estimates were derived using the Ti-in-biotite geothermometer of Henry et al. (2005), which is based on the increase in Ti content of biotite with increasing temperature for given Mg/(Mg+Fe). This geothermometer is best applied to graphitic metapelites containing ilmenite/rutile, quartz and an aluminous phase (e.g. staurolite, cordierite or Al_2SiO_5), which respectively set Ti, Si and Al to maximum levels in the biotite. The calibration range of the

geothermometer is 400-600 MPa pressure, $Mg/(Mg+Fe)=0.275-1.0$ and $Ti=0.04-0.6$ atoms per formula unit.

Sample	P85	P146
Rock type	Meta-pelite	Meta-pelite
Lat.	34°42.644'	34°35.425'
Long.	077°35.274'	077°44.262'
Mineral	Bt	Bt
SiO ₂	35.60	35.11
TiO ₂	2.12	2.76
Al ₂ O ₃	19.59	17.96
Cr ₂ O ₃	0.12	0.01
Fe ₂ O ₃	0.00	0.00
FeO	20.72	22.38
MnO	0.20	0.38
MgO	8.34	7.53
CaO	0.03	0.01
Na ₂ O	0.24	0.13
K ₂ O	8.63	9.43
H ₂ O	3.95	3.89
F	na	na
Cl	na	na
Ba	na	na
Sum	99.54	99.59
Oxygens	22	22
Si	5.406	5.418
Ti	0.242	0.320
Al	0.912	0.685
Cr	0.014	0.001
Fe ₃	0.000	0.000
Fe ₂	2.631	2.888
Mn	0.026	0.049
Mg	1.888	1.733
Ca	0.006	0.002
Na	0.070	0.040
K	1.672	1.858
Ba	na	na
Sum	12.867	12.994
XMg	0.42	0.38

Table 4.2 Sample locations and representative chemical compositions of minerals used for Ti-in-biotite geothermometry.

Both P85 and P146 contain ilmenite and quartz and have Ti and $Mg/(Mg+Fe)$ within the calibration range. Graphite is absent from the metapelites but the effect of this is currently poorly constrained. Éric et al. (2009) compared Ti-in-biotite temperature estimates for non-graphitic metapelitic assemblages against garnet-biotite, garnet-muscovite and THERMOCALC 3.21 temperature estimates. They found that the

temperature estimates compared favourably in samples where Ti-content showed a negative correlation with Mg/(Mg+Fe) (a principle of the Ti-in-biotite method), but found discrepancies of up to 110 °C for samples where biotites showed a positive correlation. As biotites in both P85 and P146 show negative correlation between Ti-content and Mg/(Mg+Fe) (Figure 4.5) the Ti-in-biotite temperatures may not be greatly affected by the absence of graphite. Nevertheless at present the pressure of metamorphism remains unconstrained.

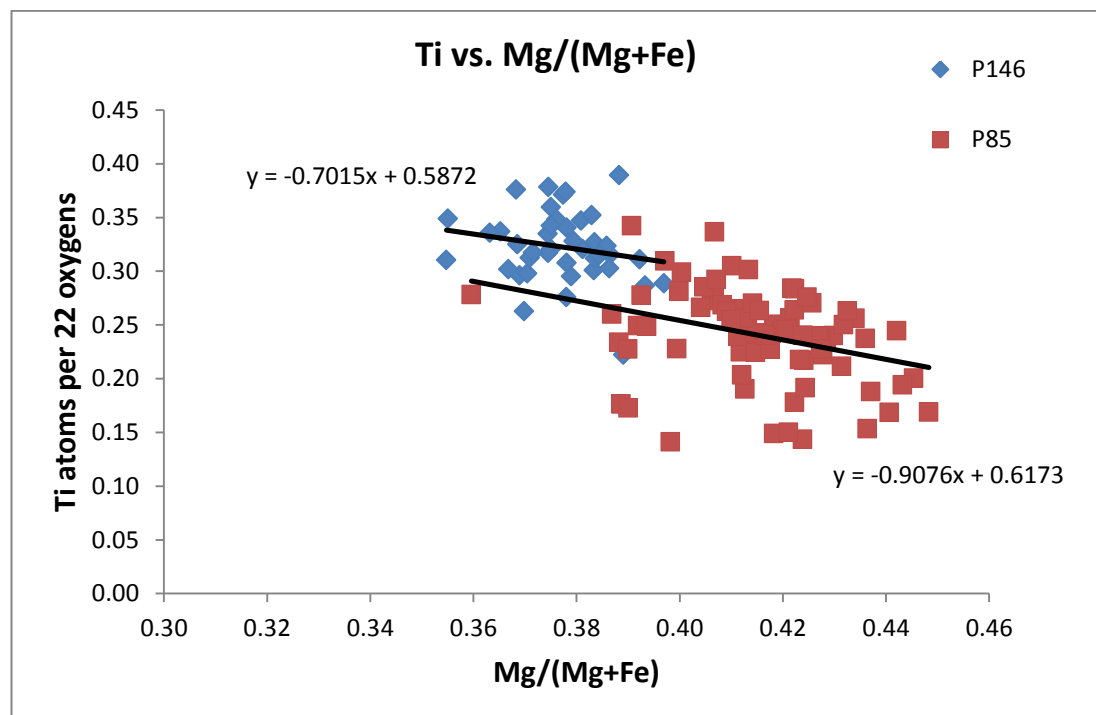


Figure 4.5 Negative correlation between biotite Ti content and Mg/(Mg+Fe) in metapelite samples P85 and P146.

Pressures <400 MPa would result in an overestimation of temperature, whereas pressures over 600 MPa would result in underestimation of temperature. The P146 paragenesis lacks an Al-saturating phase so its Ti-in-biotite temperature may be an overestimate (Henry et al. 2005). As P85 only contains ilmenite as inclusions within garnet and kyanite, but not in its matrix, biotite in the matrix is likely to be Ti-undersaturated. Measurements were only taken therefore from biotite grains included within garnet and kyanite porphyroblasts. As a result, the Ti-in-biotite temperature for P85 records the temperature at the time of, or prior to, garnet and kyanite growth. The precision of the thermometer is estimated to be ± 24 °C at <600 °C, improving to ± 12 °C at >700 °C (Henry et al. 2005). Temperatures were

determined using the “TilnBiotiteThermometer” spreadsheet available at <http://www.geol.lsu.edu/henry/Research/biotite/TilnBiotiteGeothermometer.htm> (Henry et al., 2005). Garnet-biotite geothermometry was not used as it is unclear in our garnet-bearing samples (P85, W11/30) whether the preserved garnet and biotite grew in equilibrium with one another.

4.4 Geothermobarometry Results

4.4.1 Amphibole-plagioclase chemistry and P-T estimates

Representative amphibole and plagioclase compositional data are summarised in Tables 4.1, A.1 and A.3, whilst thermobarometry results are summarised in Table 4.3. The quadratic errors of the calibration error and two standard deviations of the measured results are reported in the text.

Amphiboles in W11/73 are dominantly edenite. They have low Al-contents of 1.51-1.96 atoms per 23 oxygens and mean Ca and Na of 1.89 and 0.39 respectively. Plagioclases are dominantly oligoclase with An in the range 27.3-31.6 with a mean value of 28.8. These compositions give a relatively small spread of amphibole-plagioclase temperature and pressure estimates with mean values of 688 ± 44 °C and 522 ± 91 MPa respectively. Ti-contents of amphibole (mean 0.10 atoms per 23 O) give a temperature of 667 ± 35 °C, just within error of the amphibole-plagioclase temperature.

Amphiboles in W11/121 are dominantly potassic-hastingsite or magnesiohornblende. They have high Ca-content of 1.90-1.95 atoms per 23 oxygens. Mean Al-content is 1.91 atoms per 23 O. Plagioclases are dominantly andesine with An in the range 28.1-41.6 and a mean value of 36.2. These compositions give amphibole-plagioclase temperature and pressure estimates of 728 ± 56 °C and 875 ± 227 MPa. Mean amphibole Ti-contents of 0.06 atoms per 23 O give a temperature of 620 ± 39 °C, significantly lower than the amphibole-plagioclase temperature.

Amphiboles in P59 are magnesiohornblende and tschermakite. They have high Al-content of 2.06-2.39 atoms per 23 oxygens and mean Ca and Na of 1.78 and 0.41 respectively. Plagioclases are andesine with An in the range 37.3-50.3 and a mean value of 44.3. These compositions give amphibole-plagioclase temperature and pressure estimates of 736 ± 47 °C and

1059±219 MPa. Mean amphibole Ti-contents of 0.08 atoms per 23 O give a temperature of 634±27°C, c. 100°C lower than the amphibole-plagioclase temperature.

<i>Amphibole-plagioclase thermobarometry</i>						
Sample	Barometer and calibration error	Pressure (MPa) ($\pm 2 \sigma$)	Temperature (°C)		Geothermal Gradient (°C/km)	
			HB94 ($\pm 40^\circ\text{C}$) ($\pm 2 \sigma$)	O84 ($\pm 25^\circ\text{C}$) ($\pm 2 \sigma$)	T from HB94	T from O84
W11/73	AS95 (± 60 MPa)	522±68	688±18	667±24	36±7	35±6
	BB07 (± 200 MPa)	439±67	684±18		43±21	42±20
W11/121	AS95 (± 60 MPa)	550±100	711±40	620±30	36±8	31±7
	BB07 (± 200 MPa)	875±108	728±39		23±6	19±5
P59	AS95 (± 60 MPa)	720±64	699±24	634±11	28±4	24±3
	BB07 (± 200 MPa)	1059±90	736±24		19±4	16±3
P121	AS95 (± 60 MPa)	898±254	679±44	597±25	21±6	18±5
	BB07 (± 200 MPa)	893±80	677±32		21±5	18±5
<i>Ti-in-biotite thermometry</i>						
Sample	Geothermometer and calibration error				T (°C) ($\pm 2 \sigma$)	
P85	H05 ($\pm 20^\circ\text{C}$)				622±36	
P146	H05 ($\pm 20^\circ\text{C}$)				656±36	

Table 4.3 Amphibole-plagioclase thermobarometry and Ti-in-biotite thermometry results and estimated geothermal gradients. Most appropriate geothermometer-barometer combinations for each sample are highlighted in bold (see main text). Calibration errors are given with the calibrations. P-T results are given with two standard deviations of the spread of results within each sample. Errors on the geothermal gradient estimates were propagated from quadratic errors of the temperature and pressure estimates. AS95 and BB07 are the barometer calibrations of Anderson and Smith (1995) and Bhadra and Bhattacharya (2007) respectively. HB94, O84 and H05 are the thermometer calibrations of Holland and Blundy (1994), Otten (1984) and Henry et al. (2005) respectively.

Amphiboles in P121 are predominantly tschermakite with some magnesiohornblende, pargasite and alumino pargasite. They have the highest Al-contents of 1.92-2.95 atoms per 23 O. They also have the lowest Ca and highest Na with mean values of 1.77 and 0.53 atoms per 23 oxygens respectively. Plagioclases are dominantly oligoclase with An in the range 22.9-36.0 and a mean value of 26.3. These compositions give temperature and pressure estimates of 677±51 °C and 893±215 MPa. Mean amphibole

Ti-contents of 0.04 atoms per 23 O give a temperature of $597\pm 35^\circ\text{C}$, again significantly lower than the amphibole-plagioclase temperature.

4.4.2 Biotite chemistry and temperature estimates

Representative biotite compositional data are given in Table 4.2, whilst Ti-in-biotite thermometry results are summarised in Tables 4.3 and A.4. The quadratic errors of the calibration error and two standard deviations of the measured results are reported in the text.

Biotites in P85 range in composition, with Mg/Mg+Fe of 0.36-0.45 (mean 0.42) and Ti-contents ranging between 1.24-2.89 weight percent or 0.14-0.34 atoms per 22 oxygens (mean 0.24). These compositions give a temperature estimate of $605\pm 45^\circ\text{C}$. Of the 79 temperature estimates, 78.5% are closely grouped within the top portion of the range ($592\text{-}669^\circ\text{C}$) (Figure 4.6). The remaining 21.5% of the estimates drop off rapidly to temperatures as low as 479°C (Figure 4.6), suggesting that these measurements were made on biotites equilibrated with the Ti-undersaturated matrix. This may result from the grains not being fully encased by host garnet or kyanite in directions out of section. If these anomalously low temperatures ($<592^\circ\text{C}$) are excluded, a more refined estimate of $622\pm 41^\circ\text{C}$ is obtained.

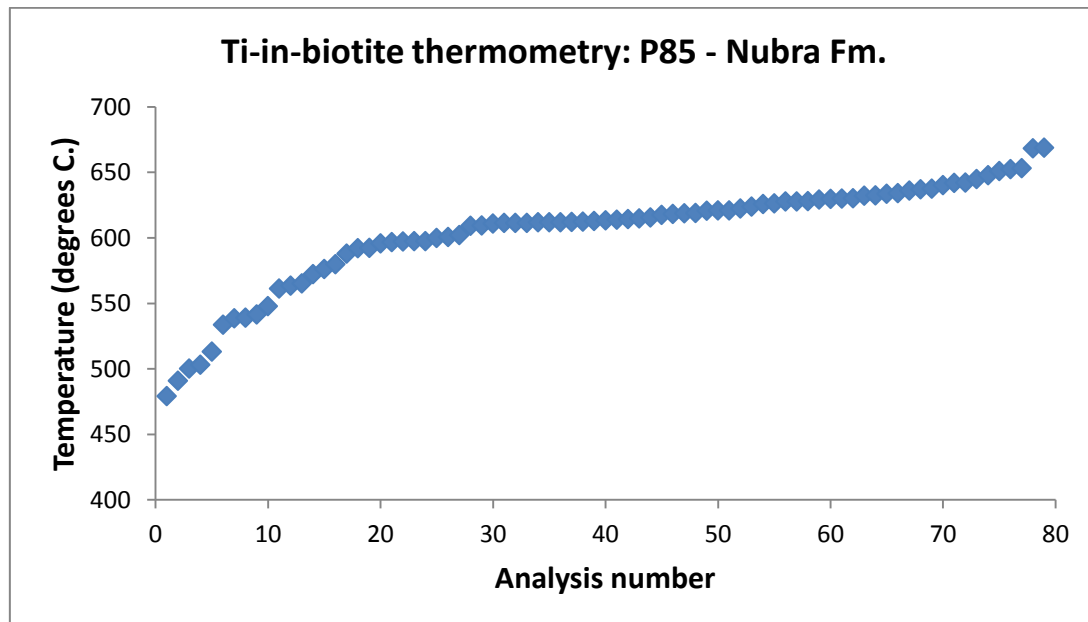


Figure 4.6 Ti-in-biotite thermometry results for Nubra Formation metapelite sample P85 ordered by temperature. Results show an inflection at 592°C

Biotites in P146 have a more limited range of compositions, with Mg/(Mg+Fe) of 0.35-0.40 (mean 0.38) and Ti-contents ranging between 1.91-3.40 weight percent or 0.22-0.39 atoms per 22 oxygens (mean 0.32). These compositions give a temperature estimate of 656 ± 41 °C.

4.5 Metamorphism and deformation of the Eastern Karakoram Metamorphic Complex

4.5.1 The Pangong Transpressional Zone

Phillips et al. (2013) determined a U-Pb age of 17.4 ± 0.4 Ma for a migmatite leucosome from the PTZ near Muglib. Amphibole-plagioclase thermobarometry of sample W11/73 provides the conditions of equilibration for a migmatite melanosome from the same unit. The results of 688 ± 44 °C, 522 ± 91 MPa (sillimanite stability field) are considered therefore to be the conditions under which anatexis occurred at c. 17-18 Ma (Figure 4.7). The temperature estimate is similar to the 675-750 °C melting temperature suggested by Reichardt et al. (2010) and the pressure estimate is within error of 570 ± 20 MPa determined for the migmatite unit by Reichardt and Weinberg (2012). These results also fall slightly above the “wet” granite solidus (Wyllie, 1977). Alignment of amphibole, biotite and elongate plagioclase indicate that migmatization occurred under deviatoric stress (Figure 4.3a). Rare plagioclase subgrains suggest limited deformation at near solidus conditions (>600 °C, Figure 4.3a; Tullis and Yund, 1985). This sample lacks evidence of lower temperature deformation (e.g. bulging grain boundaries in feldspar, Figure 4.3a).

Sample W11/121 from the opposite side of the PTZ near Taruk (Figure 4.7) yields significantly higher estimates (728 ± 56 °C, 875 ± 227 MPa, kyanite-sillimanite boundary) than W11/73, indicating that these samples record distinct portions of the pressure-temperature evolution of the evolution of the EKMC. The pressure estimate for W11/121 is within error of those for samples P59 and P121 in the PMC (see below). Subgrains in plagioclase and lobate grain boundaries in quartz indicate deformation by subgrain rotation and grain boundary migration dynamic recrystallization respectively, suggesting deformation temperatures of >600 °C (Figure 4.3b; Stipp et al., 2002; Tullis and Yund, 1985). The finer grain size and disaggregated

amphibole suggest that W11/121 experienced higher stress and higher strain than W11/73 (Figure 4.3b).

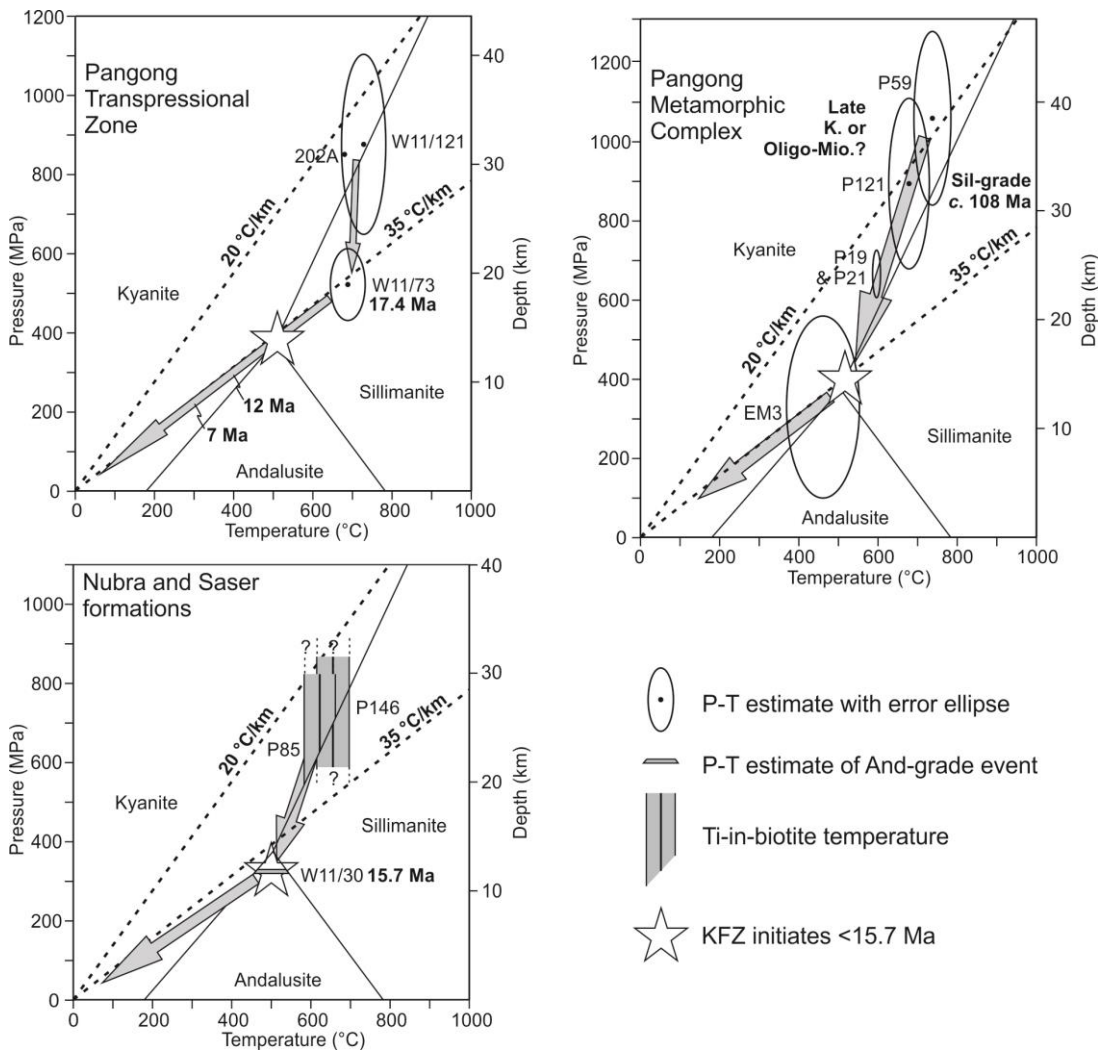


Figure 4.7 Pressure-temperature-time paths of the Eastern Karakoram Metamorphic Complex. Data compiled from this study, Phillips et al. (2004, 2013), Boutonnet et al. (2012), Reichardt and Weinberg (2012), Thanh et al. (2011), Streule et al. (2009) and Rutter et al. (2007). Also shown are geothermal gradients (dashed black lines) and Al_2O_5 polymorph stability fields after Holdaway and Mukhopadhyay (1993) and Holdaway (1971).

The amphibole-plagioclase thermobarometry results can be used to estimate an apparent geothermal gradient at the time of metamorphic equilibration (e.g. Weller et al., 2013; Palin et al., 2012) by assuming a crustal density of 2.8 g/cm^3 and converting the pressure estimate to a depth estimate. As the true geothermal gradient was unlikely to be linear, such estimates provide only an approximate depth-averaged value. Nonetheless, this approach provides a relative means to compare thermal regimes. The

thermobarometry results of W11/73 and W11/121 give geothermal gradients of $36\pm 7^\circ\text{C}/\text{km}$ and $23\pm 6^\circ\text{C}/\text{km}$ respectively (Figure 4.7). The difference between these values suggests that the two samples equilibrated under different thermal regimes, consistent with the interpretation that they record different metamorphic events. By the same assumptions, the results of Rolland and Pêcher (2001) and Rolland et al. (2009) give geotherms of $>40^\circ\text{C}/\text{km}$, $38\text{--}52^\circ\text{C}/\text{km}$ and $24\text{--}37^\circ\text{C}/\text{km}$ respectively for granulite, amphibolite and greenschist facies metamorphism within the PTZ. The result of $36\pm 7^\circ\text{C}/\text{km}$ for W11/73 suggests that the high geotherms predicted by Rolland and Pêcher (2001) and Rolland et al. (2009) may be somewhat overestimated.

Thanh et al. (2011) report conditions of 680°C , 850 MPa for a Grt+Ky+St gneiss (sample 202A) within the PTZ, defining an apparent geothermal gradient of $22^\circ\text{C}/\text{km}$. Although the age of this metamorphism is unconstrained, Thanh et al. (2011) attribute it to crustal thickening following the India-Asia collision. The pressure recorded by this sample is significantly greater than that of migmatite W11/73 but remarkably similar to that of W11/121 and also P121 from the PMC. Thus, the pressure and temperature of the Grt+Ky+St gneiss may record the same metamorphic event as the W11/121 and the PMC samples.

4.5.2 The Pangong Metamorphic Complex

Sample P59 ($736\pm 47^\circ\text{C}$, $1059\pm 219\text{ MPa}$) from the PMC records high pressure (c. 38 km burial) within the kyanite stability field. These results define a low apparent geothermal gradient of $19\pm 4^\circ\text{C}/\text{km}$, within error of those for the three other PMC and PTZ kyanite-grade samples (P121, W11/121 and 202A), but significantly lower than W11/73 in the PTZ.

Amphibole and plagioclase subgrains suggest deformation at $>650^\circ\text{C}$ (Figure 4.3c; Kruse and Stünitz, 1999; Tullis and Yund, 1985), resulting in a similar microstructure to W11/121.

Sample P121 ($677\pm 51^\circ\text{C}$, $893\pm 215\text{ MPa}$, kyanite stability field close to the sillimanite boundary) defines a low apparent geothermal gradient of $21\pm 5^\circ\text{C}/\text{km}$ (Figure 4.7). Its proximity to the Bangong-Nujiang suture, the low apparent geothermal gradient and the presence of Na-rich blue-green

amphibole (e.g. Fryer et al., 1999) provide evidence to suggest that metamorphism of P121 may have occurred within a forearc setting prior to, or around the time of, collision of the Ladakh island arc terrane with the Karakoram continental arc. This collision event and associated metamorphism of the Karakoram terrane occurred during the Late Cretaceous (Palin et al., 2012) and therefore would define the minimum age at which metamorphism of P121 occurred. Late Cretaceous sillimanite-grade metamorphism at 108 ± 0.6 Ma is recorded by sillimanite inclusions in garnet within the PMC metapelites and has been interpreted to result from Andean-type tectonism along the south Asian margin (Streule et al., 2009). Metamorphism of P121 therefore could have occurred at a similar time, corresponding to the M0 event in the Hunza and Baltoro regions.

An alternative hypothesis is that kyanite-grade metamorphism in the PMC and PTZ correlates with the M2 kyanite-grade metamorphism in the Baltoro and Hunza regions, which occurred during the Oligo-Miocene (Palin et al., 2012; Searle et al., 2010; Fraser et al., 2001). Retrograde staurolite-grade metamorphism of the PMC (585-605°C 605-725 MPa, Figure 4.7) is constrained to have occurred after Late Cretaceous sillimanite-grade metamorphism but before the initiation of the KFZ (Streule et al., 2009). If the widespread kyanite-grade metamorphism of the EKMC correlates with Oligo-Miocene kyanite-grade M2 in the central Karakoram then the two regions could have shared the same metamorphic history of Cretaceous sillimanite-grade M1, Oligo-Miocene kyanite-grade M2 and Miocene staurolite-grade M3 events (Palin et al., 2012). A comprehensive geochronological dataset aimed at constraining the timing of peak metamorphism across the EKMC is clearly required to distinguish between these correlations but is beyond the scope of the present study.

Plagioclase in P121 contains subgrains, indicating deformation at >600 °C, whilst bulging grain boundaries demonstrate that lower temperature deformation also occurred at 450-600 °C (Figure 4.3d; Tullis and Yund, 1985). Further greenschist retrograde metamorphism is evidenced by chlorite overgrowths on amphibole in P121. Greenschist facies metamorphism of a Bt+Pl schist in the PMC occurred at 460 ± 92 °C and

330±230 MPa (Figure 4.7) and was synkinematic with respect to the KFZ (Rutter et al., 2007).

4.5.3 The Nubra Formation

Metapelite P85 records a Ti-in-biotite temperature of 622±41 °C for biotite inclusions in garnet and kyanite. The stability of kyanite at 622 °C implies pressures greater than c. 650 MPa (Figure 4.7). Sigmoidal zoning and aligned inclusions in garnet are discordant with the matrix foliation resulting from KFZ deformation. Thus, garnet growth and mid-amphibolite facies metamorphism of the Nubra Formation predate initiation of the KFZ. Kyanite-grade metamorphism of the Nubra Formation, as with the PMC and PTZ, potentially correlates with the Oligocene-Miocene M2 event in the central Karakoram, which is characterised by kyanite growth in both the Hunza and Baltoro regions (Palin et al., 2012; Searle et al., 2010; Fraser et al., 2001). Thus, the KFZ cut through the region following the end of the M2 event at <21.8 Ma (Palin et al., 2012).

As andalusite growth (W11/30) occurs only within a few metres of the Nubra-Siachen leucogranite batholith, it most likely results from contact metamorphism during leucogranite emplacement at c. 15.87±0.08 Ma (Phillips et al., 2004). Al-in-hornblende geobarometry indicates that the Nubra-Siachen leucogranite was emplaced at 320-330 MPa (Reichardt and Weinberg, 2012). Similar pressures are likely to have been experienced by the adjacent Nubra Formation during contact metamorphism (Figure 4.7). Such pressures are close to the andalusite-sillimanite-kyanite triple point and therefore suggest temperatures of c. 500 °C in the wall rock metapelites. This temperature is consistent with estimates from deformation microstructures, such as quartz subgrains and lobate grain boundaries and bulging feldspar grain boundaries, formed within the KFZ shortly after leucogranite emplacement (Figure 4.4b-c, samples P85, W11/30, P146; Wallis et al., 2013; Phillips and Searle, 2007). Randomly oriented biotite inclusions within andalusite grains wrapped by foliation formed during dextral simple shear (Figure 4.4a-c) demonstrate that the KFZ initiated after leucogranite emplacement (Phillips and Searle, 2007; Phillips et al., 2004). Andalusite is found also in the Baltoro batholith aureole in Pakistan (Searle et al., 2010), which constitutes the north-western continuation of the Nubra-

Siachen leucogranite batholith (Phillips et al., 2004, 2013). This demonstrates the similar emplacement conditions of the two portions of the batholith. Subgrains and lobate grain boundaries in matrix and pressure shadow quartz (Figures 4.4b and 4.4c) indicate that KFZ deformation occurred at 400-550 °C assuming strain rates of c. 10^{-12} s^{-1} (Stipp et al., 2002).

4.5.4 The Saser Formation

Metapelite sample P146 from the Saser Formation records a Ti-in-biotite temperature of 656 ± 41 °C (Figure 4.7). P146 lacks an aluminous phase so this temperature is likely to be an overestimate as Al-undersaturation may cause changes in Ti substitution mechanism, resulting in elevated Ti levels in biotite (Henry et al., 2005; Henry and Guidotti, 2002). The true temperature of metamorphism may correlate therefore with either the slightly lower temperatures of 622 °C in the Nubra Formation or 585-605 °C for staurolite-grade metamorphism of the PMC (Streule et al., 2009). This result is the first estimate of metamorphic temperature for the Saser Formation and demonstrates that amphibolite grade metamorphism occurred across the EKMC.

4.6 Crustal evolution of the eastern Karakoram: relationship between metamorphism and strike-slip faulting

Mid-high temperature metamorphism of the EKMC in Ladakh resulted from a range of tectonic processes spanning the Early Cretaceous to Miocene. At c. 108 Ma, the eastern Karakoram formed an Andean-type margin (Phillips et al., 2013; Streule et al., 2009), resulting in sillimanite-grade metamorphism. Kyanite grade metamorphism on low geothermal gradients (c. 19-23 °C/km) occurred either in a similar setting, before or after closure of the Shyok-Bangong-Nujiang suture (M0 or M1 respectively, Palin et al., 2012), or during post-India-Asia collision crustal thickening (M2). In either case, metamorphism at 677-736 °C was pre- or syn-kinematic to similarly high temperature (>600 °C) regional deformation across the EKMC, corresponding to D0-D2 in the central Karakoram which occurred during regional crustal thickening (Phillips et al., 2013). In the PMC, this was followed by retrograde staurolite-grade metamorphism (Streule et al., 2009)

and greenschist facies metamorphism, grain growth and deformation in marbles (Rutter et al., 2007). In the PTZ, additional tectonic uplift within the KFZ has exhumed a slice of Miocene migmatites from 19-20 km depth, which record an elevated geotherm (35 °C/km), and juxtaposed them against older, more slowly exhumed, amphibolites. Pre-kinematic garnet and andalusite porphyroblasts in the Nubra Formation demonstrate that the KFZ post-dates emplacement of the Nubra-Siachen leucogranite and therefore contradicts a syn-kinematic interpretation of magmatic structures near Tangtse (Boutonnet et al., 2012; Leloup et al., 2011). As these microstructures, along with those in the leucogranites (Wallis et al., 2014b; Phillips and Searle, 2007; Phillips et al., 2004), demonstrate that the KFZ was not active in this region before c. 15.7 Ma, the 17.4 Ma migmatization in the PTZ cannot be the result of shear heating (Figure 4.7) and the KFZ cannot have acted to channel leucogranite magmas in the mid-crust (Leech, 2008, 2009; Rolland et al., 2009; Rolland and Pêcher, 2001; Lacassin et al., 2004b). These interpretations are consistent with the most recent findings along the southern portion of the KFZ, where it has been demonstrated to have initiated at c. 12 Ma (Wang et al., 2012, 2013, 2014), rather than as early as 34 Ma (Leloup et al., 2013; Valli et al., 2008; Lacassin et al., 2004). The findings of this study therefore support the interpretation that the KFZ propagated outwards from its north-central portion (Wang et al., 2011, 2013; Robinson, 2009). High geothermal gradients during the Miocene, which resulted in upper amphibolite grade anatexis, were the result of crustal thickening and radiogenic heating, possibly exacerbated by mantle-derived magma heat input, in the broadly deforming crust across the Karakoram terrane (Searle et al., 2010, 2011). Kyanite-grade metamorphism of the Nubra Formation was overprinted by an andalusite-grade event during leucogranite emplacement. Later retrograde metamorphism and metasomatism of the EKMC occurred during exhumation and deformation within the KFZ (Wallis et al., 2013).

The highest pressure rocks of the EKMC record metamorphism at depths of c.38 km (P59) and therefore do not place direct additional constraints on whether or not the fault continues down to the mantle (Klempner et al., 2013; Searle et al., 2010, 2011). However, the thermobarometric results for

migmatite sample W11/73 demonstrate that the crust was partially molten at 19-20 km depth during the mid-Miocene. Widespread mid-crustal anatexis was also occurring across the central Karakoram at this time (Searle et al., 2010). This raises the question of whether the KFZ could penetrate *c.* 70 km thick crust as a relatively localised structure whilst the crust was partially molten at *c.* 20 km depth.

The record of Cretaceous subduction and Cenozoic crustal thickening, heating and anatexis preserved in the EKMC is equivalent to events recorded in the Baltoro and Hunza Karakoram to the north west (Searle, 2013; Palin et al., 2012) and demonstrates the along-strike continuity of these processes. Pullen et al. (2011) discuss the similarities between the Qiantang mélange in Tibet and the geology of the Pamir in the northern Karakoram terrane. Whilst the eastern Karakoram has undergone a similar evolution to the southern Karakoram terrane in the Baltoro and Hunza regions, it does not reflect the antiformal structure of the Pamir and Qiangtang mélange. Nor does it contain evidence of blueschist and eclogite facies metamorphism present within the Qiangtang mélange (Pullen et al., 2011; Zhang et al., 2006; Kapp et al., 2003). Correlation of the eastern Karakoram with the southern Karakoram, and the Qiangtang mélange with the northern Karakoram/Pamir supports low offsets of <150 km across the KFZ, as previously proposed due to the offset of several other geological markers (e.g. Wang et al., 2012; Robinson, 2009; Phillips et al., 2004; Murphy et al., 2000; Searle et al., 1998). Such correlation does not support the proposed larger offsets of several hundred kilometres (Valli et al., 2008; Lacassin et al., 2004a; Peltzer and Tapponnier, 1988).

4.7 Conclusions

Each sub-unit of the Eastern Karakoram Metamorphic Complex in Ladakh has undergone mid-upper amphibolite grade peak metamorphism with varying degrees of retrogression. Early Cretaceous subduction and crustal thickening along the southern Karakoram terrane resulted in sillimanite-grade metamorphism of the Pangong Metamorphic Complex. Kyanite-grade metamorphism under low geothermal gradients of 19-23 °C/km may have occurred at a similar time or possibly later during the Oligo-Miocene.

Additional geochronological studies are required to constrain the timing of this event. Subsequent upper amphibolite grade migmatisation in the Pangong Transpressional Zone occurred at c. 17.4 Ma under a higher geothermal gradient of 35 °C/km. Microstructures in the Nubra Formation demonstrate that the Karakoram Fault Zone initiated after leucogranite emplacement at c. 15.7 Ma and after peak metamorphism. Thus the high geothermal gradients and anatexis recorded in the PTZ are not the result of shear heating but of regional crustal thickening and heating processes. The close similarity between metamorphism of the EKMC and that of the Karakoram metamorphic complex in Baltoro-Hunza supports limited offset on the KFZ of <150 km.

5. Low Effective Fault Strength due to Frictional-Viscous Flow in Phyllonites, Karakoram Fault Zone, NW India

Abstract

Phyllosilicate-rich lithologies are common in the cores of large-scale fault zones and dramatically impact fault rheology. Multi-mechanism frictional-viscous flow (FVF) has been inferred to operate in phyllosilicate-rich fault rocks based on experimental evidence and microphysical modelling. A growing body of evidence suggests that FVF may be an important mechanism for weakening the cores of large-scale faults. This chapter provides detailed descriptions of microstructures indicative of FVF in exhumed phyllonites of the central Karakoram Fault Zone (KFZ), NW India. These include highly interconnected muscovite foliae, lack of quartz/feldspar crystal preferred orientations and sutured grains and overgrowths indicative of fluid-assisted diffusive mass transfer. FVF microphysical modelling, using microstructural parameters from the natural fault rock and experimentally-derived friction and diffusion coefficients, predicts a low peak shear strength of c. 28 MPa within the frictional-viscous transition zone. Chlorite geothermometry indicates that synkinematic chlorites grew at $351 \pm 34^\circ\text{C}$ (c. 10 km depth) during FVF, immediately above the transition to quartz crystal plasticity. The velocity strengthening nature of FVF promotes stable creep in these lithologies at low strain rates. However, velocity weakening behavior and dynamic weakening induced by high slip-rates imposed by earthquake rupture propagation suggests that phyllosilicate-rich fault rocks do not act as a barrier to seismic slip. The deformation processes and low frictional strength of the exhumed KFZ fault rocks provide analogues for processes operating at depth in other faults of similar scale.

5.1 Introduction

Characterising fault rock strength and rheology is fundamental to constraining deformation processes across a range of scales, including micro-scale deformation mechanisms, earthquake nucleation/propagation

and the macroscopic rheology of the continental crust/lithosphere (Holdsworth et al., 2011; Imber et al., 2008; Holdsworth, 2004; Rutter et al., 2001). The presence of phyllosilicate-rich lithologies, including phyllonites and certain gouges and foliated cataclasites, in fault zones is thought to dramatically impact fault zone rheology (Rutter et al., 2013; Holdsworth et al., 2011; Jeffries et al., 2006a, 2006b). Phyllosilicates (e.g. micas and clays) and phyllosilicate-rich fault rocks are typically frictionally weak (coefficient of friction, μ , typically <0.4), and are associated with velocity strengthening behavior, particularly at low sliding velocities ($<1 \mu\text{s}^{-1}$), and velocity weakening at higher sliding velocities ($>1 \mu\text{s}^{-1}$) (Behnsen and Faulkner, 2012; Ikari et al., 2011; Niemeijer and Spiers, 2005, 2006, 2007). Conversely, most other mineral groups, including quartz and feldspar framework silicates, and their associated fault rocks are frictionally strong ($\mu=0.6-0.85$) and associated with velocity weakening behaviour (Ikari et al., 2011; Blanpied et al., 1995; Byerlee, 1978).

In lithologies containing both phyllosilicates and stronger minerals, normal stress and strain-rate sensitive multi-mechanism frictional-viscous flow (FVF) has been proposed on the basis of experimental observations (Bos et al., 2000; Bos and Spiers, 2001; Chester and Higgs, 1992) and theoretical modelling (Bos and Spiers, 2002; Chester, 1995). FVF occurs by frictional sliding on interconnected phyllosilicate foliae which wrap around clasts of more rigid and frictionally stronger minerals, whilst volume incompatibilities and dilation are accommodated by fluid-assisted diffusional mass transfer from high to low stress sites on the rigid clasts (Bos and Spiers, 2002). The effective strength of assemblages deforming by these combined mechanisms is subject therefore to complex control by phyllosilicate frictional strength, normal stress, pore fluid pressure, temperature, strain rate, composition, grain size and angles between sliding surfaces (Niemeijer and Spiers, 2005; Bos and Spiers, 2002).

FVF has potential to result in dramatic weakening relative to Byerlee friction or plastic flow laws, particularly at the base of the upper crust in the frictional-viscous transition zone (FVTZ) where high temperatures enhance diffusional mass transfer (Niemeijer and Spiers, 2005; Bos and Spiers, 2002; Chester, 1995). Whilst FVF has a strong experimental and theoretical basis,

an ongoing challenge is to determine the extent to which it operates within natural fault zones. In order to assess the extent to which FVF weakens faults and the conditions under which this occurs in nature, detailed descriptions of such fault rocks possibly deformed by FVF are required, in addition to constraints on the deformation conditions.

Microstructures potentially consistent with the operation of FVF have been described from faults in a range of tectonic settings, a summary of which is provided in Table 5.1. Such microstructures include interconnected and aligned phyllosilicate foliae which wrap around elongate clasts of other phases, along with evidence of fluid-assisted diffusive mass transfer (e.g. overgrowths, dissolved grain boundaries), which can potentially be related to FVF deformation mechanisms. The studies in Table 5.1 show that FVF can potentially operate in a range of fault rocks, most commonly phyllonites and foliated cataclasites, but also schists, gouges and micaceous mylonitic lithologies. The conditions under which these fault rocks form and FVF may occur span a commensurately large range, typically 200-500°C and 5-15 km depth, in broad agreement with the predications of microphysical modelling (Niemeijer and Spiers, 2005; Bos and Spiers, 2002). Many of the studies in Table 5.1 describe similar sequential fault rock evolution whereby fracturing results in grain size reduction and localized fluid influx. The ingressing fluids promote retrograde hydration alteration of frictionally strong minerals (e.g. feldspars, pyroxenes) to weaker phyllosilicates (e.g. muscovite, chlorite, talc). The resultant phyllosilicates form interconnected weak layers that wrap around more rigid relict clasts, commonly showing pressure solution seams and overgrowths indicative of fluid assisted diffusive mass transfer.

In Chapter 3, greenschist facies phyllonites within the Karakoram Fault Zone (KFZ), NW India, were described and interpreted to play a significant role in weakening this major strike-slip fault of the India-Asia collision zone. In this chapter the microstructure of these phyllonites is described in detail, the temperature of their formation is determined using geothermometry of synkinematic chlorites and their effective shear strength during FVF is modelled using microstructural and environmental parameters from the natural fault zone.

Fault	Fault Rock	Deformation Conditions	Reference(s)
Strike-slip Faults			
Median Tectonic Line, Japan	Phyllonite Foliated cataclasite	c. 10 km depth c. 5 km depth 200-300°C	Jefferies (2006b) Jefferies (2006a) Shigematsu et al. (2012)
Great Glen Fault, Scotland	Foliated cataclasite Phyllonite	8-15 km depth 250-450°C	Stewart et al. (1999) Stewart et al. (2000) Holdsworth et al. (2001)
Norumbega fault system, Maine	Act+Bt schist	400-500°C	Marsh et al. (2009)
Siberia Fault Zone, New Zealand	Foliated cataclasite	8-10 km depth 200-250°C	White (2001)
Karakoram Fault Zone, India	Phyllonite	<14 km depth <400°C	Wallis et al. (2013)
Thrust Faults			
Outer Hebrides Fault Zone, Scotland	Phyllonite	250-500°C	Butler et al. (1995) Imber et al. (1997) Imber et al. (2001)
Ser Barbier Thrust, W.Alps	Phyllonite	Greenschist	Wibberley (2005)
Moine Thrust Belt, Scotland	Foliated cataclasite & micaceous ultramylonite	5-9 km depth 250-350°C	Wibberley (2005)
Extensional Faults			
Err Detachment, Switzerland	Gouge	<300°C	Manatschal (1999)
Zuccale Fault, Elba	Foliated cataclasite	<8 km depth <400°C	Collettini and Holdsworth (2004) Collettini et al. (2009) Collettini et al. (2011)
Nordfjord-Sogn Detachment, Norway	Phyllonite	Greenschist	Braathen and Osmundsen (2004)
Wasatch Fault, Utah	Phyllonite Foliated cataclasite	<350°C <290 MPa	Parry et al. (1988)

Table 5.1 Summary of fault zones where frictional-viscous flow has been inferred or where reported microstructures are highly suggestive of such deformation. Also given are the fault rock type in which the observations were made and the inferred conditions of frictional-viscous deformation.

5.2. Structural Setting of the Karakoram Fault Zone Phyllonites

In Yulskam gorge (Figures 5.1 and 5.2), the kinematics of deformation in the Nubra Formation metavolcanics and metapelites are characterized by mean foliation oriented 142/76 NE and mean lineation oriented 17/137 (Figure 5.2). Dextral shear sense is indicated by S-C-C' fabrics, asymmetric mantled porphyroclasts and mica fish and is consistent with the macroscopic dextral

offset across the KFZ (Chapter 3). Shearing of the metapelites was therefore dominantly strike-slip with a minor extensional component. The kinematics of deformation in the phyllonite band are characterized by mean foliation oriented 140/70 SW and mean lineation oriented 20/140 (Figure 5.2). The shear sense of the phyllonite is indicated by dextral S-C' fabrics (Chapter 3). The phase of deformation that affected the phyllonite was therefore dextral strike-slip with a subordinate thrust component.

Recrystallised quartz and calcite veins within the Nubra Formation, including the phyllonite (Figure 5.3b), indicate episodic embrittlement events at depths where deformation was otherwise predominantly ductile (Chapter 3). Minor brittle faults cross-cut the Nubra Formation at variable angles and record deformation at shallower depths after phyllonitisation (Chapter 3).

Palaeoseismic evidence for large ($M_w > 6$) earthquakes in the vicinity of the Nubra strand of the KFZ includes syn-sedimentary lacustrine seismites and offset fluvio-lacustrine strata (Phartiyal and Sharma, 2009; Phartiyal et al., 2005; Upadhyay, 2001, 2003).

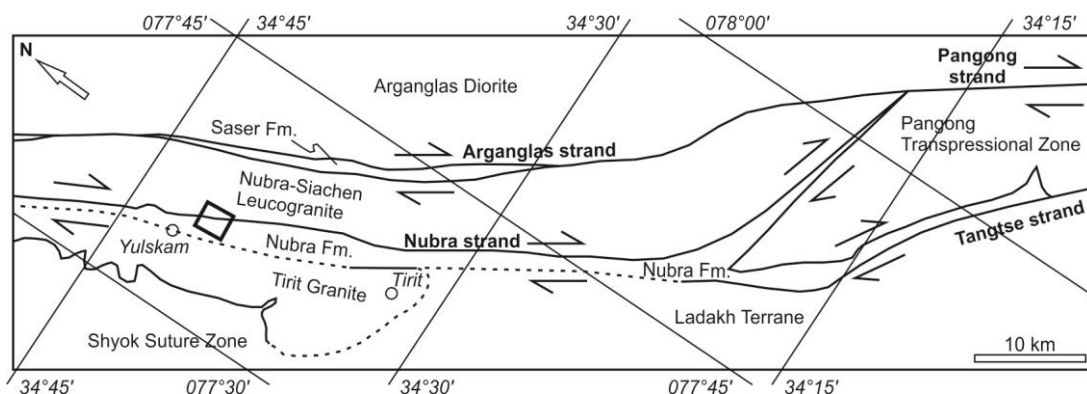


Figure 5.1 Simplified sketch map of the geology of the Nubra Valley region of Ladakh, NW India, after Phillips (2008). The bold box near Yulskam marks the location of Figure 5.2.

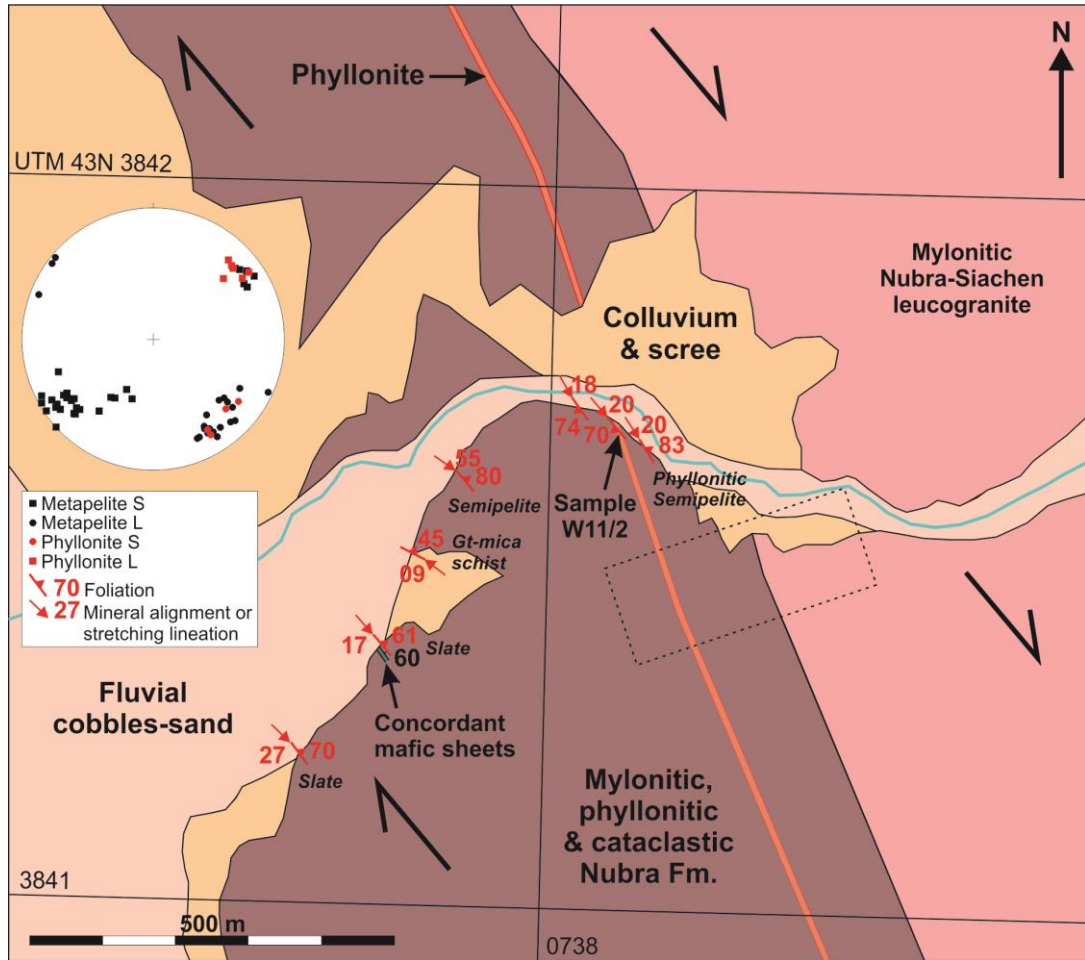


Figure 5.2 Simplified geological map of the Nubra fault strand in Yulskam gorge, showing the studied band of phyllonite and sample location. Also shown are foliation (S) and lineation (L) measurements from the phyllonite and surrounding metapelites of the Nubra Formation. Figure 3.3a and Figure 3a of Wallis et al. (2013) are marked by the dashed box.

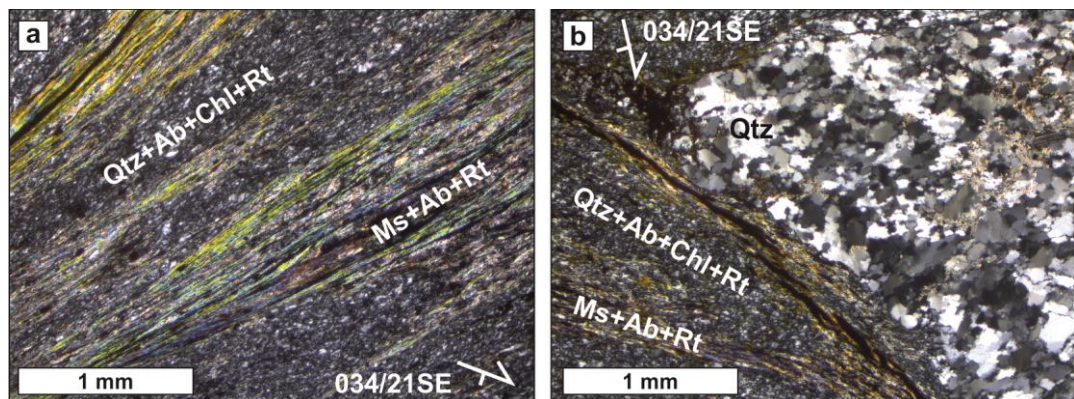


Figure 5.3 Cross-polarised optical photomicrographs of the Nubra Formation phyllonite. a) Typical domainal structure consisting of quartz+albite+chlorite+rutile (Qtz+Ab+Chl+Rt) and muscovite+albite+rutile (Ms+Ab+Rt) bands. b) Quartz clast showing ubiquitous subgrains and neoblasts typical of subgrain rotation dynamic recrystallisation, within phyllonitic matrix.

5.3. Phyllonite Deformation Microstructures and Crystal Fabrics

The KFZ phyllonite (sample W11/2, Figure 5.2, Chapter 3) consists of a domainal microstructure (Figures 5.4a and 5.5) of interlayered bands of quartz+albite+chlorite+rutile (Qtz+Ab+Chl+Rt, 60-70%) and muscovite+albite+chlorite+rutile (Ms+Ab+Chl+Rt, 30-40%). Muscovite-rich bands are interconnected and laterally continuous at thin section-hand specimen scales. Centimetre-scale folding of the layered microstructure (Figure 3.3c) indicates that deformation was ductile at the hand specimen scale. In some instances individual bands consist of >95% aligned muscovite with asymmetric aligned rutile needles demonstrating dextral shear sense (Figure 5.4b). More typically, the muscovite-rich bands consist of c. 70% aligned muscovite, which wraps around elongate clasts of albite (c. 20%) with interlayered rutile needles and chlorite sheets (Figure 5.4c-d). Chlorite is present as sheets interlayered with muscovite (Figure 5.4c-d), but is best developed in the pressure shadows of albite clasts (Figure 5.4e) and quartz rich domains (Figure 5.4f). These structures demonstrate that chlorite growth was syn-kinematic with respect to deformation of the phyllonite. The phyllonite also contains mm-scale clasts of recrystallised polycrystalline quartz (Figure 5.3b). Ubiquitous subgrains and neoblasts of equal size within the quartz clasts indicate subgrain rotation dynamic recrystallisation.

The results of two electron backscattered diffraction (EBSD) runs on the phyllonite sample are described in order to further characterise the phase distribution and to define the crystal fabrics within the specimen. EBSD data were collected using the FEI Quanta 650 FEG ESEM, equipped with an Oxford Instruments Nordlys S EBSD camera, Oxford Instruments Aztec 2.1 acquisition software and Channel 5 data processing software, at the University of Leeds. Pole figures were plotted using the program *PFch5* (Mainprice, 1990). Data were collected using 20 kV accelerating voltage, 5-15 nA specimen current and 70° tilt angle.

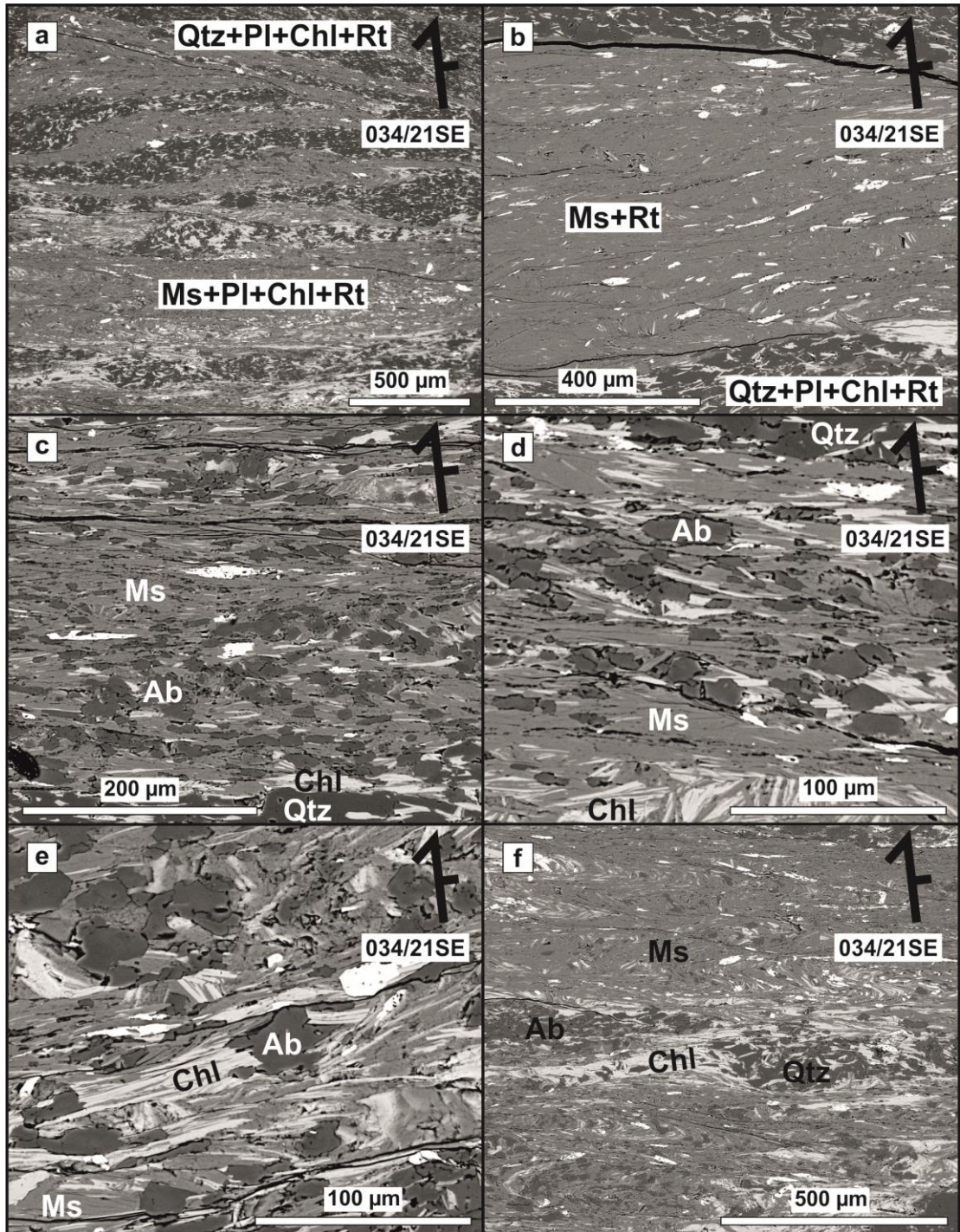


Figure 5.4 Backscattered electron atomic number contrast images of the Karakoram Fault Zone phyllonite. a) Domainal microstructure of the phyllonite consisting of Ms+Ab+Chl+Rt and Qtz+Ab+Chl+Rt domains a few hundred microns thickness. b) Ms+Rt domain consisting of >95% Ms with aligned Rt needles (white) showing dextral asymmetry. c) Ms+Ab domains, showing slightly elongate albite clasts wrapped by aligned muscovite. Subordinate chlorite intergrowths are present in d. e) Chlorite fringes on albite clasts (centre) and sutured and indented albite grains (top left). f) Chlorite fringe on quartz-rich domain with Ms+Ab domain.

Two areas were analysed using automated beam scans. The first covers a region of both Qtz+Ab+Chl+Rt and Ms+Ab+Rt domains and was acquired with a 1075x940 grid of 0.7633 μm steps (Figure 5.5). The second provides a detailed analysis of a Ms+Ab+Rt domain and was acquired with a 468x409 grid of 0.8955 μm steps (Figure 5.6). Muscovite indexing rates were low compared to other phases due to the difficulty of preparing such muscovite-rich domains. Energy dispersive X-ray (EDX) maps, acquired during EBSD analysis provide improved imaging of the elemental and hence phase distributions. Data were acquired on specimen surfaces cut parallel to the lineation and perpendicular to the foliation (i.e. the XZ plane of finite strain, with X horizontal in the images and pole figures).

EBSD and EDX map analysis of the multi-domainal region shows interleaved Qtz+Ab+Chl+Rt and Ms+Ab+Rt domains a few hundred microns in thickness (Figure 5.5a-f). The muscovite distribution is highlighted by the Al and K maps (Figure 5.5c-d), whereas the albite distribution is highlighted by the Na map (Figure 5.5e) and chlorite is highlighted in the Mg map (Figure 5.5f). Pole figures of crystal orientations within a subset consisting of a Qtz+Ab+Chl+Rt domain, show that quartz and albite have very weak, close to random crystal orientation. Chlorite has a strong crystal preferred orientation (CPO) defined by $\langle 010 \rangle$ directions strongly aligned with X, $\{001\}$ poles forming a YZ girdle with superposed maxima about Y and Z, and $\langle 100 \rangle$ directions forming maxima inclined *c.* 30° clockwise to X (Figure 5.5g).

Similar analysis of the Ms+Ab+Rt domain shows scattered albite clasts distributed throughout a matrix of aligned muscovite (Figure 5.6a-f). Again, the muscovite distribution is highlighted by the Al and K maps (Figure 5.6c-d), whereas the albite distribution is highlighted by the Na map (Figure 5.6e) and chlorite is highlighted in the Mg map (Figure 5.6f). Pole figure analysis (Figure 5.6g) shows that muscovite has a strong CPO defined by $\{001\}$ maxima parallel to Z, and $\langle 100 \rangle$ and $\langle 010 \rangle$ directions forming approximately XY girdles with superposed maxima parallel to X and Y. Albite has a weak and disordered CPO consisting of multiple scattered sub-maxima in each pole figure. Each sub-maximum likely corresponds to one, or a few, large clasts measured several times.

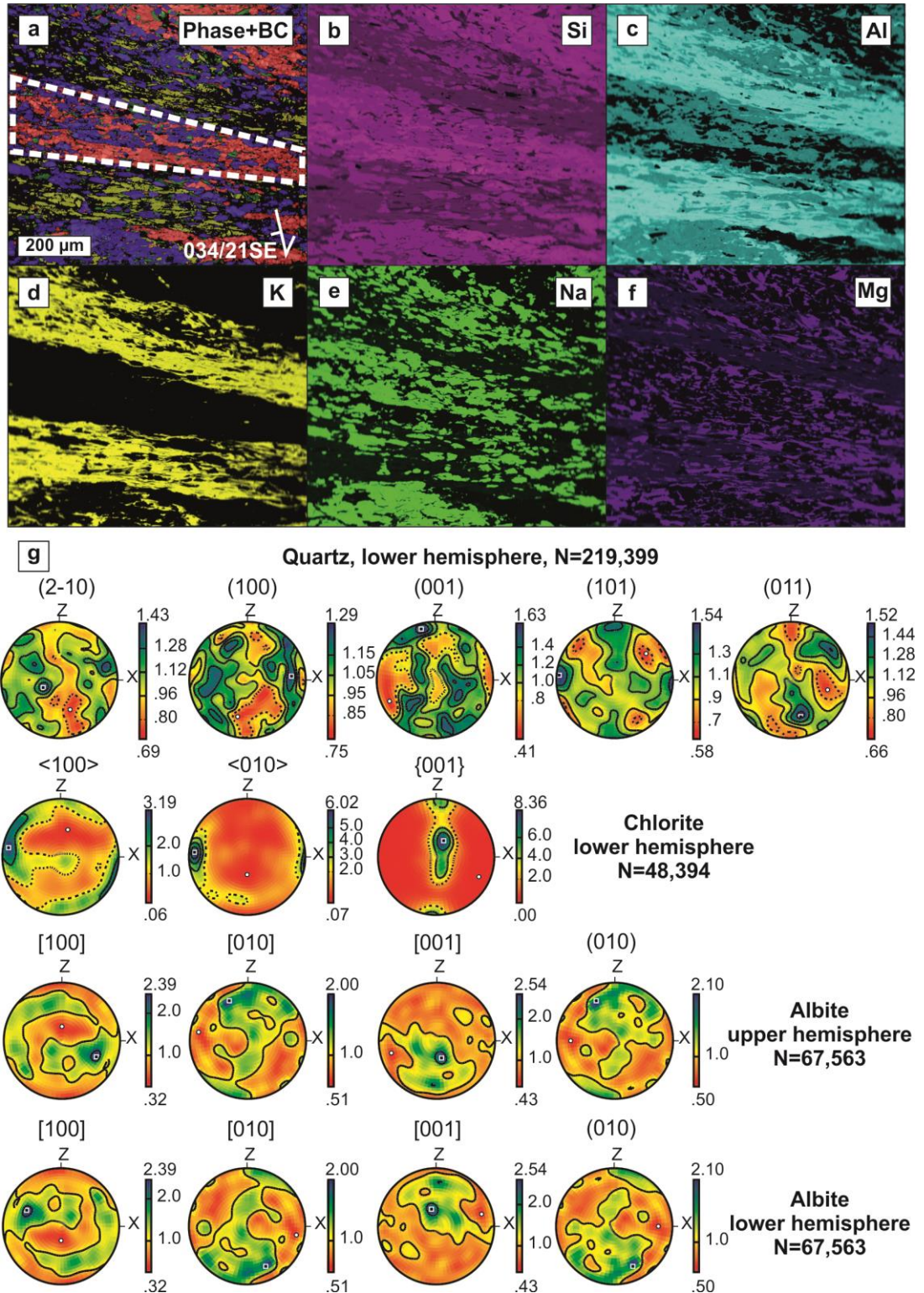


Figure 5.5 Electron backscattered diffraction (EBSD) and energy dispersive X-ray (EDX) analysis of domainal phyllonite microstructure. a) EBSD diffraction pattern band contrast map overlain with phase map. Red-quartz, blue-albite, yellow-muscovite, green-chlorite. b-f) EDX element distribution maps of the same area as (a). d) K distribution highlights muscovite. e) Na distribution highlights albite. f) Mg distribution highlights chlorite. g) Pole figures of crystal orientations in map area in (a). Contours are in multiples of uniform distribution.

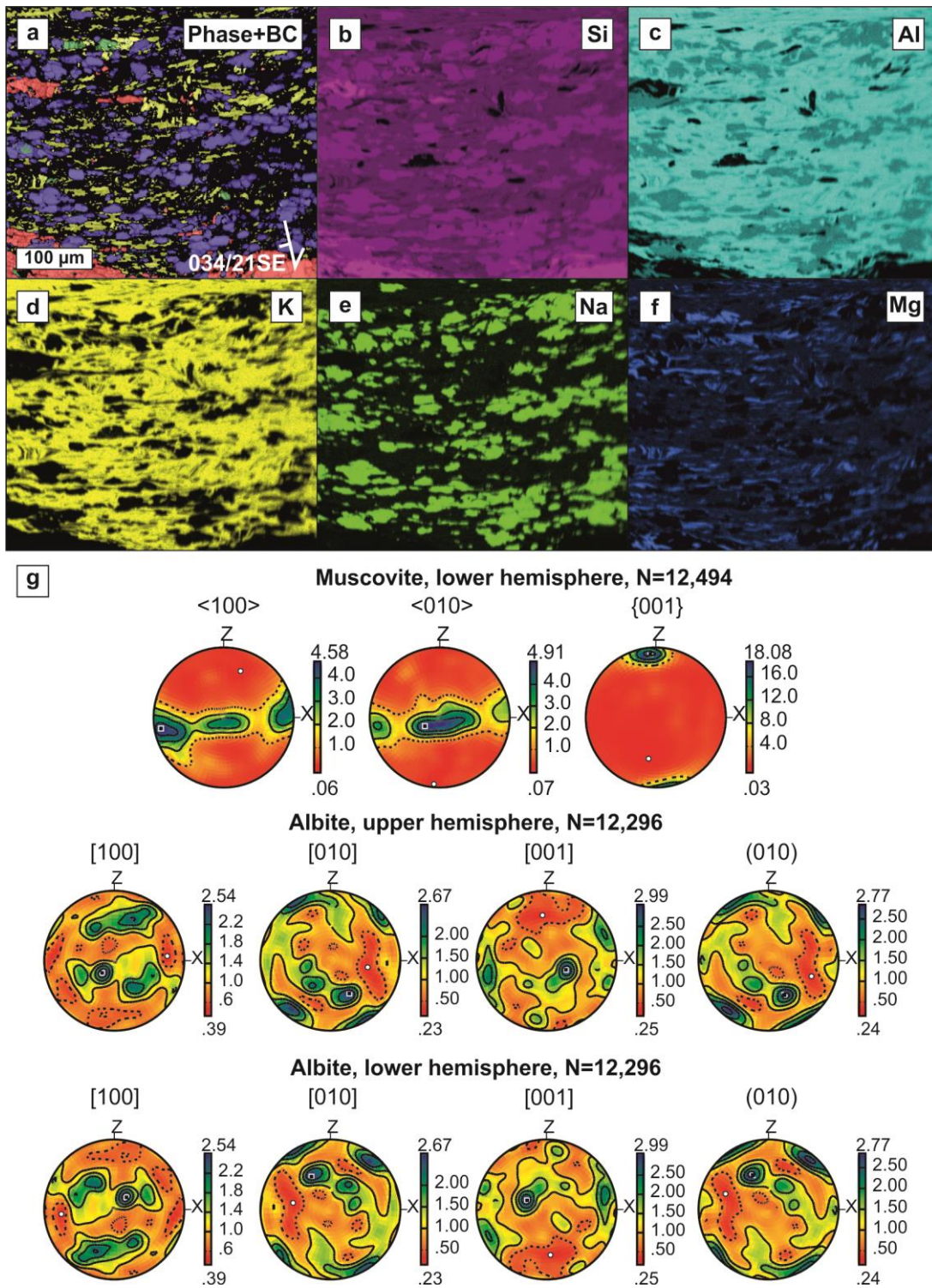


Figure 5.6 Electron backscattered diffraction (EBSD) and energy dispersive X-ray (EDX) analysis of muscovite-rich domain. a) EBSD diffraction pattern band contrast map overlaid with phase map. Red-quartz, blue-albite, yellow-muscovite, green-chlorite. b-f) EDX element distribution maps of the same area as (a). d) K distribution highlights muscovite. e) Na distribution highlights albite. f) Mg distribution highlights chlorite. g) Pole figures of crystal orientations in map area in (a). Contours are in multiples of uniform distribution.

5.4 Interpretation of Phyllonite Deformation Mechanisms

The low frictional strength of muscovite (Behnsen and Faulkner, 2012; Niemeijer and Spiers, 2012) suggests that deformation is likely to have been preferentially accommodated in the through-going muscovite-rich bands over the quartz-rich domains within the KFZ phyllonite. Within the most muscovite-rich (c. 95%) bands (Figure 5.4b), deformation is interpreted to have been partially accommodated by frictional sliding on aligned muscovite cleavage planes, accompanied by dislocation glide on the $\langle 110 \rangle (001)$ slip system resulting in the muscovite CPO. Within the muscovite+albite-rich bands (Figure 5.4c-d), muscovite grain alignment and CPO suggests that sliding in the muscovite foliae was an important deformation mechanism (Figure 5.6). Sutured/indented albite clasts (Figure 5.4c-d, Figure 5.6a) and chlorite fringes/overgrowths in pressure shadows (Figure 5.4e-f) indicate that fluid-assisted diffusive mass transfer was also significant in accommodating deformation. Poorly defined albite CPO (Figure 5.6g) suggest that albite clasts deformed as relatively rigid bodies carried within the muscovite matrix. In combination, the sliding on muscovite foliae and diffusive processes indicated by sutured albite and chlorite overgrowths, along with the macroscopically ductile nature of deformation evidenced by folding, are strongly suggestive of frictional-viscous flow (Niemeijer and Spiers, 2005; Bos and Spiers, 2001, 2002; Bos et al. 2000; Chester, 1995; Chester and Higgs, 1992). During frictional-viscous flow, sliding on aligned muscovite foliae accommodated the majority of strain. Albite clasts acted as passive rigid bodies, with volume incompatibilities removed by pressure solution when clasts become locked. Material was re-precipitated in low stress sites (including chlorite pressure shadows) at the dilational trailing edges of rigid albite clasts and quartz-rich domains.

The chlorite CPO is consistent with a linear-decussate shape preferred orientation with (001) planes parallel to the X direction as recognised in phyllonite from Merens Fault in the Axial Zone of the Pyrenees by McCaig (1987). The weak approximately XZ $\langle 100 \rangle$ and $\langle 010 \rangle$ girdles are consistent with this interpretation, whilst the superposed maxima parallel to X may suggest a component dislocation glide. It should be noted however that the data represent too few chlorite grains to draw any firm conclusions. The KFZ

phyllosilicate bears remarkable resemblance in general to that of McCaig (1987), who inferred that deformation facilitated fluid flow, promoting metamorphic reactions which in turn altered shear zone rheology.

5.5 Chlorite Geothermometry

5.5.1 Chlorite Compositions

Major element data were collected on chlorite using wavelength-dispersive X-ray spectroscopy on the Jeol 8230 electron microprobe at the University of Leeds. Chlorite analyses were collected using 15 kV accelerating voltage, 15 nA beam current and a 1 μ spot size. Peak and background count times were respectively 10 s and 5 s for Na and K, and 15 s and 7 s for remaining elements. Two to three analyses were made on each of 52 chlorite grains giving 148 analyses in total (Table A.5).

Representative chlorite analyses are shown in Table 5.2 and a summary is given in Table A.5. The chlorites are classified as ripidolite and pycnochlorite according to Hey (1954). Variation between analyses is small and suggests that the chlorites were well equilibrated (Klein and Koppe, 2000; Neall and Phillips, 1987). They have Fe/(Fe+Mg) in the range 0.56-0.61 and Si/Al in the range 0.90-1.05 (Tables 5.2 and A.5). Tetrahedral site occupation ranges between 5.08-5.93 Si and 2.07-2.92 Al^{IV} per formula unit. The presence of abundant muscovite and albite suggests that the chlorites are saturated with respect to Al, whilst the presence of Fe-oxides suggests they are saturated also with respect to Fe.

5.5.2 Chlorite Geothermometry

Chlorite geothermometry offers a means to estimate the temperature of chlorite growth within the phyllosilicate. As chlorite growth is demonstrably synkinematic (Figure 5.4e-f), chlorite geothermometry provides an estimate of the deformation temperature. Chlorite geothermometers are based on an empirical increase in Al^{IV} content with increasing temperature (Cathelineau, 1988; Cathelineau and Nieva, 1985), which occurs through the Tschermak exchange $(\text{Si}^{4+})^{\text{IV}}(\text{Mg,Fe}^{2+})^{\text{VI}} \leftrightarrow (\text{Al}^{3+})^{\text{IV}}(\text{Al}^{3+})^{\text{VI}}$ (de Caritat et al. 1993). Recently, chlorite geothermometers involving more rigorous thermodynamic models have been developed and are based on equilibrium constants for

reactions between various combinations of endmember chlorite compositions (amesite, clinocllore, daphnite and sudoite), quartz and water (e.g. Lanari et al., 2014; Bourdelle et al., 2013). However, either these require prior knowledge of pressure or Fe^{3+} content (Lanari et al., 2014), or are not calibrated for chlorites of similar composition to those of the KFZ phyllonite (Bourdelle et al. 2013).

Although there is a positive correlation between temperature and octahedral Fe, Fe and Mg contents are also strongly dependent on geological setting and solution composition (Klein and Koppe, 2000; Cathelineau, 1988; Cathelineau and Nieva, 1985). Kranidiotis and MacLean (1987) and Zang and Fyfe (1995) proposed modifications to the geothermometer of Cathelineau (1988) by adding corrections to the Al^{IV} value as a function of the $\text{Fe}/(\text{Fe}+\text{Mg})$ ratio, for low (0.18-0.64) and high (0.78-0.81) values of the ratio respectively. This ratio would in turn be affected by the fluid to rock ratio, $f\text{O}_2$, $f\text{S}_2$, pH and hydrothermal fluid composition (Klein and Koppe, 2000).

Klein and Koppe (2000) summarised several criticisms of simple Al^{IV} -based chlorite geothermometers. These are that 1) mixed layers and fine intergrowths can result in contamination of microprobe analyses by other minerals (Jiang et al., 1994), 2) chlorites from different geological settings can show different temperature-composition relationships (De Caritat et al., 1993) and 3) chlorite and smectite represent a continuum between pure smectite (<180°C) and chlorite (>270°C) (Schiffman and Fridleifsson, 1991). The chlorites in the KFZ phyllonite contain however very low levels of Ca, Na and K (means <0.2 atoms per formula unit) and cation totals on the octahedral site are very close to the ideal figure of 12 (11.87 ± 0.16 , 1σ), suggesting that “contamination” by mixed layers or intergrowths is minimal in these analyses (Klein and Koppe, 2000; Jiang et al., 1994). Furthermore, the geological context of the phyllonites suggests that they formed at >270°C (Chapter 3) and should therefore be close to pure chlorite (Schiffman and Fridleifsson, 1991).

Analysis	C1	C2	C3	C4	C5	C6	C7	C8
Oxide weight %								
SiO₂	23.80	23.64	23.36	23.02	23.98	23.80	23.50	21.81
TiO₂	0.08	0.04	0.05	0.05	0.08	0.07	0.03	0.08
Al₂O₃	21.35	22.05	21.65	21.42	21.21	22.01	21.40	20.38
FeO*	28.21	28.26	28.48	28.43	28.72	28.56	28.10	28.00
MnO	0.39	0.44	0.41	0.42	0.41	0.38	0.34	0.00
MgO	11.16	10.96	11.46	11.31	11.36	11.28	11.02	11.54
CaO	0.01	0.07	0.03	0.03	0.08	0.01	0.02	0.01
Na₂O	0.01	0.05	0.02	0.03	0.04	0.00	0.00	0.00
K₂O	0.05	0.04	0.02	0.04	0.04	0.07	0.05	0.04
Total	85.06	85.55	85.48	84.75	85.92	86.18	84.46	81.86
Cations per 28 oxygens								
Si	5.29	5.22	5.17	5.15	5.29	5.22	5.26	5.08
Al^{IV}	2.71	2.78	2.83	2.85	2.71	2.78	2.74	2.92
Al^{VI}	2.87	2.96	2.82	2.81	2.80	2.91	2.90	2.67
Fe	5.24	5.22	5.28	5.32	5.30	5.24	5.26	5.45
Mn	0.07	0.08	0.08	0.08	0.08	0.07	0.07	0.00
Mg	3.69	3.61	3.79	3.78	3.73	3.69	3.68	4.00
Ca	0.00	0.02	0.01	0.01	0.02	0.00	0.00	0.00
Na	0.01	0.02	0.01	0.01	0.02	0.00	0.00	0.00
K	0.02	0.01	0.01	0.01	0.01	0.02	0.01	0.01
Ti	0.01	0.01	0.01	0.01	0.01	0.01	0.01	0.01
Total	19.91	19.93	20.01	20.03	19.97	19.94	19.93	20.14
Oct. total	11.87	11.87	11.97	11.99	11.91	11.91	11.91	12.12
Fe/(Fe+Mg)	0.59	0.59	0.58	0.59	0.59	0.59	0.59	0.58
Si/Al	0.95	0.91	0.92	0.91	0.96	0.92	0.93	0.91

Table 5.2 Representative chlorite compositional analyses as oxide wt.% and cations per 28 oxygen formula unit.

In order to address the variability of chlorite compositions between different geological settings the procedure of Klein and Koppe (2000) is followed, by choosing the geothermometer for which the chlorite compositions of the calibration dataset most closely match those of the KFZ phyllonites (Table 5.3). The calibration of Cathelineau (1988) does not show a satisfactory match for the KFZ phyllonite chlorites as all of the key parameters are out of the calibration range (Table 5.3). Similarly, the geothermometer of Zang and Fyfe (1995) was calibrated using chlorites with higher Fe/(Fe+Mg) and Si/Al than those from the KFZ phyllonite (Table 5.3). Bourdelle et al., 2013 produced a geothermometric calibration incorporating the results of several recent studies and spanning a range of 1.70-2.42 Al^{IV} per formula unit. The KFZ phyllonite chlorites however have considerably higher Al^{IV} contents up to 2.92 per formula unit (Table 5.3). The chlorites used to calibrate the

geothermometer of Kranidiotis and MacLean (1987) are most similar to those of the KFZ phyllonite as they include compositions up to 2.83 Al^{IV} per formula unit and the other parameters are highly comparable between the two datasets (Table 5.3). The Kranidiotis and MacLean (1987) geothermometer is therefore most appropriate for estimating the temperature of chlorite growth in the KFZ phyllonite. The error associated with this calibration, arising from the spread of measurements in the original Cathelineau and Nieva (1985) dataset, is estimated at $\pm 25^{\circ}\text{C}$. The temperature estimate for chlorite growth in the KFZ phyllonite given by the Kranidiotis and MacLean (1987) calibration is $351 \pm 34^{\circ}\text{C}$, with the reported error being the square root of the sum of the squares of the calibration error and two standard deviations of the individual temperature estimates ($\pm 23^{\circ}\text{C}$). Two important caveats to this temperature estimate are that the calculated temperature is slightly outside the calibration range, which extends up to c. 300°C , and that the effect of pressure on chlorite Al^{IV} is in general poorly constrained. The true uncertainty of the temperature estimate is likely therefore to be greater than that reported.

	KFZ phyllonite	Cathelineau (1988)	Kranidiotis and MacLean (1987)	Zang and Fyfe (1995)	Bourdelle et al. (2013)
Fe/(Fe +Mg)	0.56-0.61	0.24-0.37	0.18-0.64	0.78-0.81	0.08-0.88
Al ^{IV}	2.07-2.92	0.59-1.93	1.89-2.83	2.49-2.64	1.70-2.42
Si	5.08-5.93	2.80-3.41	5.17-5.80	5.36-5.51	
Si/Al	0.90-1.05	1.29-1.89	0.92-1.56	1.08-1.16	
T ($^{\circ}\text{C}$)		308 ± 34	351 ± 34	284 ± 34	853 ± 2231

Table 5.3 Comparison between the compositions of chlorites (28 oxygen basis) from the Karakoram Fault Zone phyllonite and those in the calibration datasets of various chlorite geothermometers. Compositions for Bourdelle et al. (2013) are those that the thermometer was tested against, as the compositions of the calibration dataset are not given. The temperatures estimated for the KFZ phyllonite chlorites are given with the quadratic error of the calibration error and two standard deviation of the results.

5.6 Frictional-Viscous Flow Modelling

5.6.1 Microphysical Modelling of Frictional-Viscous Flow in the KFZ Phyllonites

Bos and Spiers (2002) developed a microphysical model for FVF based on the results of muscovite-halite analogue experiments (Figure 5.7, Bos and Spiers, 2000, 2001). Halite was used in the experiments due to its well constrained diffusion kinetics and the model was then applied to quartz-muscovite assemblages. The model geometry and theoretical basis are described in detail by Bos and Spiers (2002), Niemeijer and Spiers (2005) and Jefferies et al. (2006a). Niemeijer and Spiers (2005) updated the original model to incorporate the effects of a component of crystal plastic deformation within the phyllosilicate foliae. This revision is significant for the present study as the muscovite CPO (Figure 5.6) suggests that at least a component of the deformation within the muscovite occurred by $\langle 110 \rangle (001)$ dislocation glide. Whilst these models are commonly invoked to describe deformation in mid-crustal phyllosilicate-rich lithologies (e.g. Marsh et al., 2009; Imber et al., 2008; Collettini and Holdsworth, 2004), their application to specific natural fault rocks has been limited to date (Jefferies et al., 2006a, 2006b). The Niemeijer and Spiers (2005) model does however offer a means to estimate the approximate effective shear strength (τ) of the KFZ phyllonite undergoing FVF in the upper- to mid-crust.

The model describes the effective shear strength (τ) of an assemblage undergoing FVF by the equation

$$\tau = \{(\tau_{gb})^{-20} + (\tau_{pl})^{-20}\}^{-0.05} + \{(\tau_{ps})^{-20} + (\tau_{dil})^{-20}\}^{-0.05} \quad (\text{Equation 1})$$

where τ_{gb} is the shear resistance due to frictional slip along phyllosilicate grain boundaries, τ_{pl} is the shear resistance due to crystal plasticity in the phyllosilicate foliae, τ_{ps} is the shear resistance resulting from pressure solution of the rigid clasts and τ_{dil} is the shear resistance resulting from dilation of the model microstructure. Each of these components are defined respectively as:

$$\tau_{gb} = P\mu_{gb}\sigma_n \quad (\text{Equation 2})$$

$$\tau_{pl} = \frac{1}{\alpha} \log \left\{ \frac{3^{0.5} \dot{\gamma}_{pl}}{C \exp(-Q/RT)} \right\} \quad (\text{Equation 3})$$

$$\tau_{ps} = \frac{RTd}{B^2 k_{s,p} \Omega_s} \dot{\gamma} \quad (\text{Equation 4})$$

$$\tau_{dil} = 0.5(\sigma_1 - \sigma_3) \sin[\tan^{-1}(1/\mu_{gb})] \quad (\text{Equation 5})$$

where: P - proportion of clast grain boundary area undergoing sliding, μ_{gb} - phyllosilicate grain boundary friction coefficient, σ_n (Pa) - effective normal stress, C (s^{-1}) and α (Pa^{-1}) are empirical constants taken from Kronenberg *et al.* (1990), $\dot{\gamma}_{pl}$ (s^{-1}) - strain rate in phyllosilicate foliae, $\dot{\gamma}$ (s^{-1}) - bulk assemblage strain rate, Q ($Jmol^{-1}$) - apparent activation energy, R ($Pam^{-3}K^{-1}mol^{-1}$) - molar constant, T (K) - absolute temperature, d (m) - average diffusion distance (grain size), B - aspect ratio of clasts, $k_{s,p}$ ($molm^{-3}s^{-1}$) - rate coefficient for dissolution (s) or precipitation (p), Ω_s (m^3mol^{-1}) - molar volume of solid and $(\sigma_1 - \sigma_3)$ is the differential stress (Figure 5.7). Equation 1 describes the shear strength as the combination of resistance from grain boundary friction, phyllosilicate dislocation glide, clast pressure-solution and microstructural dilation. Values for the parameters in equations 2-5 are taken as defined by Niemeijer and Spiers (2005) for strike-slip faults, except where they can be modified for the composition and environmental conditions of the KFZ phyllonite, as defined in Table 5.4. Where possible, and within reasonable limits of uncertainty, values are chosen that will produce a maximum effective shear strength such that the modelled strength profile approximates an upper strength limit. For instance, for μ_{gb} the chosen value is 0.38 (see below), determined by Behnsen and Faulkner (2012) for muscovite gouge in the presence of pore fluids and confining pressure, although the coefficient of friction for individual muscovite (001) surfaces is likely considerably lower (Bos and Spiers, 2002). $K_{s,p}$ for quartz were used in the absence of such data for albite. Effective shear strengths (Figure 5.8) were calculated for Byerlee type friction ($\mu=0.75$), and FVF of the albite-muscovite assemblage between 0-20 km depth following Niemeijer and Spiers (2005). Hydrostatic pore fluid pressures are assumed throughout. However, evidence for supra-hydrostatic fluid pressures within the Nubra strand of the KFZ suggests that the modelled effective normal stress distribution is an upper limit and again that the results provide a maximum

effective shear strength. The strength of quartz undergoing dislocation creep was also calculated using the wet quartzite flow law of Luan and Paterson (1992) rewritten for simple shear by Bos and Spiers (2002).

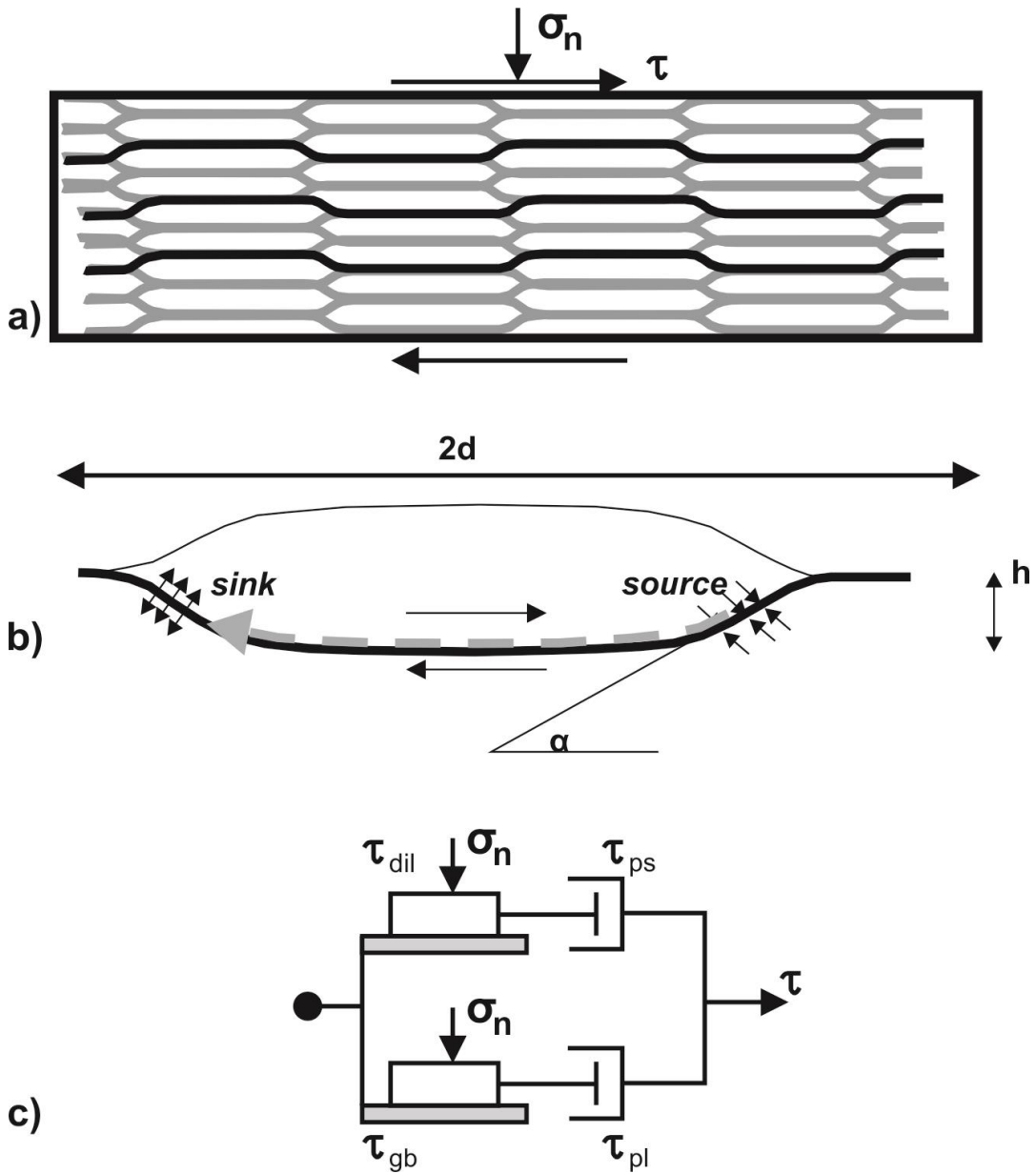


Figure 5.7 Microphysical model for frictional-viscous flow defined by Bos and Spiers (2002) and Niemeijer and Spiers (2005). a) Generalised model geometry consisting of interconnected phyllosilicate foliae (black and grey lines) which transect the microstructure and wrap around elongate clasts (white). Active slip occurs on through-going foliae (examples in black) which are, on average, parallel to the shear plane/direction. b) A single model element consisting of an elongate clast wrapped by an actively sliding (dextral) phyllosilicate layer. Clast material is dissolved in high stress source regions, and diffuses in a grain boundary fluid layer (dashed grey arrow) to be precipitated in dilational low stress sink regions. Foliation waves have amplitude h , and correspondingly the leading/trailing clast edges make an angle α to the shear plane. c) Mechanical analogue diagram showing the shear strength τ as a function of τ_{dil} (shear resistance due to dilation), τ_{ps} (shear resistance due to pressure-solution), τ_{gb} (shear resistance due to grain boundary friction) and τ_{pl} (shear resistance during phyllosilicate dislocation creep). σ_n -normal stress, τ -shear stress.

Variable	Value	Source
P	0.6	EBSD maps and backscattered electron images
μ_{gb}	0.38	Behnsen and Faulkner (2012)
T	35°C/km	Thermobarometry, Chapter 4
d	4.3 μm	EBSD maps
B	1.6	EBSD maps
Ω_s	$1.0006 \times 10^{-4} \text{ m}^3 \text{ mol}^{-1}$	Molar volume of albite from Holland and Powell (1998)

Table 5.4 Values used for frictional-viscous flow modelling of the Karakoram Fault Zone phyllonite, where derived independently from the original model of Niemeijer and Spiers (2005).

5.6.2 Effective Shear Strength of the KFZ Phyllonites

The modelling of the KFZ phyllonite predicts its effective shear strength during strike-slip deformation between 0-20 km depth (Figure 5.8), assuming that the mineral assemblage and strain rate were to remain constant across all depths. Mineral transformations and changes in strain rate that are expected to occur at depths other than those at which the phyllonite formed mean however that the model results are most appropriate for the $351 \pm 34^\circ\text{C}$ temperature range and should be treated with caution outside this range. For instance, although FVF is always weaker than quartz dislocation creep at equivalent strain rate, the phyllonite protoliths at greater depth may lack the necessary phyllosilicate content for FVF, such that quartz dislocation creep is an important deformation mechanism at >11 km depth. Uncertainty in the model results is difficult to quantify due to the large number of variables,

some of which have poorly constrained values/uncertainties themselves. The least well constrained parameters are the diffusion- and plasticity-related variables, as discussed by Bos and Spiers (2002) and Niemeijer and Spiers (2005). Changes in the strain rate estimate affect the FVF effective shear strength most at <3 and >11 km depth, where shear strength is dominantly controlled by pressure-solution and dislocation glide respectively, with greater shear resistance at higher strain rates. Within the $351 \pm 34^\circ\text{C}$ range of chlorite temperatures, shear strength is controlled primarily by the frictional strength of muscovite, reduced slightly by crystal plasticity. In this temperature range shear strength is not greatly affected by changes in strain rate due to the frictional control.

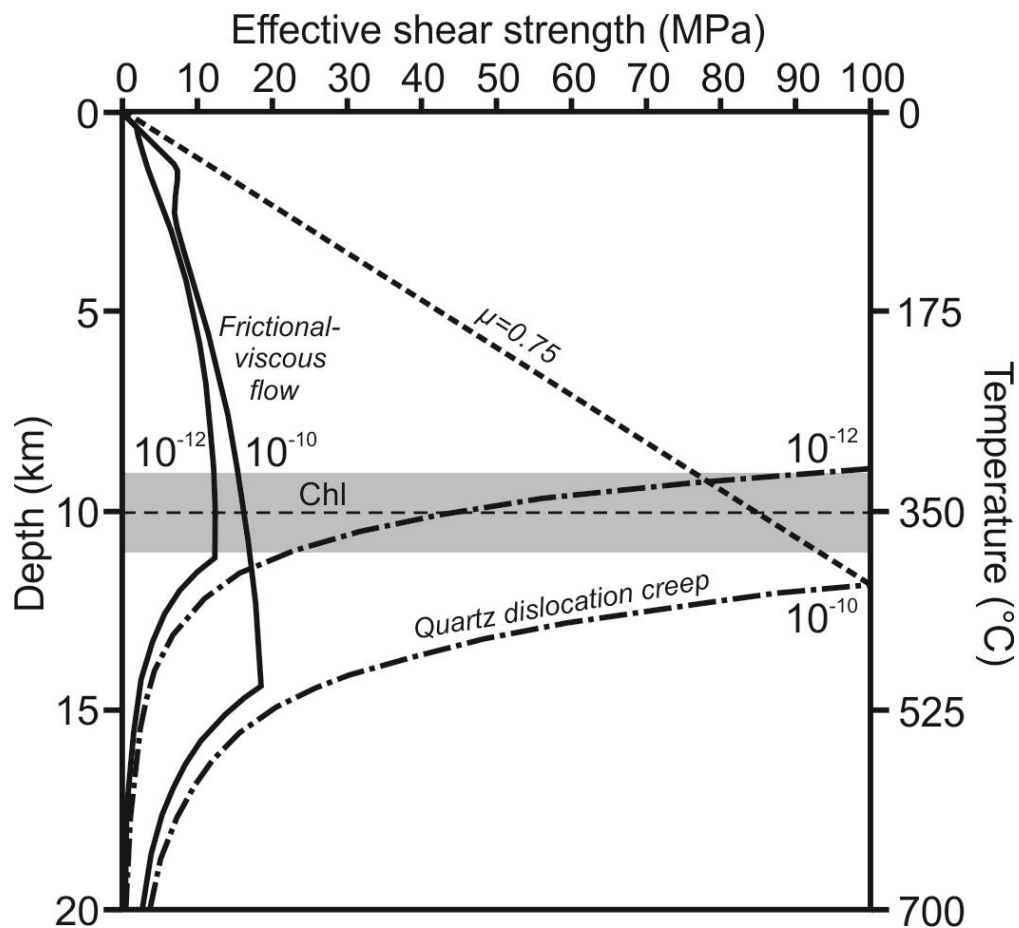


Figure 5.8 Strength-depth plot for the Nubra Formation phyllonite (bold curves), calculated for strain rates of 10^{-10} and 10^{-12} s^{-1} according to equations 1-5, and Niemeijer and Spiers (2005). Also shown are the shear strengths of frictionally strong mineral assemblages with a coefficient of friction (μ) of 0.75 (bold-dashed), and quartz undergoing dislocation creep at strain rates of 10^{-10} and 10^{-12} s^{-1} (dot-dashed). Hydrostatic pore fluid pressures are assumed throughout. Temperature scale and modelling assumes a Miocene geothermal gradient of $35^\circ\text{C}/\text{km}$ (Chapter 4). Horizontal dashed line and shaded region show the $351 \pm 34^\circ\text{C}$ temperature range determined by chlorite geothermometry.

The elevated Miocene geothermal gradient within the Karakoram terrane (*c.* $35^\circ\text{C}/\text{km}$, Chapter 4) facilitates fluid-assisted diffusive mass transfer and dislocation glide such that the KFZ phyllonite FVF strength is lower than in the generalised case ($25^\circ\text{C}/\text{km}$) calculated by Bos and Spiers (2002). Whilst pressure-solution of the albite clasts was an important microstructural process, it added little additional shear resistance, such that the FVF strength of the albite-muscovite assemblage is not significantly different to that of pure muscovite. This emphasises the need for further experimental constraints on rheology of muscovite over the wide range of crustal conditions. The chlorite geothermometry results constrain the active FVF in the KFZ phyllonite to $351 \pm 34^\circ\text{C}$ (i.e. *c.* 9-11 km depth, Figure 5.8). The primary control on the FVF strength of the assemblage, and its uncertainty, under these conditions is the muscovite friction coefficient. Behnsen and Faulkner (2012) summarized experimentally determined friction coefficients for muscovite gouge, which range between 0.35-0.47 in the presence of pore fluids. This range results in shear strengths of 15.5-18.6 MPa at 10^{-10} s^{-1} and 12.0-13.8 MPa at 10^{-12} s^{-1} at 10 km depth. A friction coefficient of 0.38 (Table 5.4) is taken as being typical (Behnsen and Faulkner, 2012) and gives maximum shear strengths of 16.3 and 12.5 MPa at the same depth and strain rates respectively (Figure 5.8).

5.7 Discussion: Deformation-Metamorphism-Fluid Interactions and Impacts on Fault Zone Rheology

Retrograde phyllonitisation of the Nubra Formation within the KFZ provides an example of interactions and feedbacks between deformation, metamorphism and fluid processes within a large-scale strike-slip fault zone.

Mylonitic deformation within the Nubra strand of the KFZ had largely ceased to affect the Nubra-Siachen leucogranite by 13.73 ± 0.34 Ma (Phillips et al., 2004). Deformation of the adjacent Nubra Formation continued however after this time, as it records mylonitic deformation to lower temperatures (c. 400°C) than those affecting the leucogranite (c. 500°C , Chapter 3, Phillips and Searle, 2007). Continued syn-kinematic exhumation and cooling of the Nubra Formation resulted in greenschist facies phyllonitisation at $351 \pm 34^\circ\text{C}$, characterised by the breakdown of biotite and synkinematic growth of muscovite and chlorite. The localised (7-10 m wide) nature of the phyllonite band suggests that this was a zone of locally elevated fluid flux, presumably resulting from a band of increased permeability induced by preceding deformation. The abundant muscovite within the phyllonite, along with the action of grain boundary fluids, allowed FVF to occur with lower shear resistance than quartz crystal plasticity at the same temperature (Figure 5.8), causing quartz and albite to behave as relatively rigid clasts. The low effective shear strength (<20 MPa) of the phyllonite undergoing FVF, further enhanced strain localisation to within the phyllonite band.

Dynamic recrystallisation microstructures preserved in relict quartz clasts (Figure 5.3b) demonstrate that the phyllonite was derived from an originally mylonitic protolith. Several previous studies of phyllonite examples (e.g. Great Glen Fault, Scotland, Stewart et al., 2000; Median Tectonic Line, Japan, Jefferies et al., 2006b; Zuccale Fault, Elba, Collettini and Holdsworth, 2004) have documented evidence for cataclasis that triggered fluid influx, resulting in the growth of low friction phyllosilicates and the onset of fluid-assisted diffusive mass transfer processes. Brittle deformation did affect the Nubra Formation mylonites prior to phyllonitisation, as recrystallised quartz and calcite veins provide evidence for episodic embrittlement events, likely driven by elevated pore fluid pressures. This is supported by the recrystallised quartz vein clast within the phyllonite. The lack of CPOs in quartz and albite, even within the more competent quartz-rich domains (Figure 5.5g), also suggest that the rock may have undergone cataclasis following mylonitisation but prior to phyllonitisation. The lack of CPOs in the quartz-rich domains may also result however from a range of other deformation processes (e.g. grain boundary sliding) during pre-

phyllonitisation deformation. From these (micro)structures, the following generalised sequence of events during exhumation and cooling can be inferred:

Mylonitic deformation of the Nubra Formation metapelites (c. 400-550°C),

Localised transient fracturing events due to elevated pore fluid pressures,

Vein precipitation resulting from fluid-assisted diffusive mass transfer and pore fluid pressure drops during fracturing,

Continued mylonitic deformation and recrystallisation of vein material (c. 400-500°C),

Phyllonitisation, potentially along a pre-existing fracture network (351±34°C),

Frictional-viscous flow within the phyllonite (351±34°C).

Experimental observations of FVF show that it is associated with strain weakening, velocity strengthening behavior (Bos and Spiers, 2000, 2001, 2002) characteristic of aseismic creep. This is consistent with cm-scale folds in the KFZ phyllonite that demonstrate that its deformation was dominantly ductile at the hand-specimen scale. Imber et al. (2008) argue however that localized, potentially seismic, frictional slip may be commonplace within phyllonitic fault cores, due to factors such as elevated pore fluid pressures, stress/strain rate fluctuations around geometric irregularities and/or reorganization of the phyllosilicate network during changes in boundary conditions and slip vector. Analogue experiments have demonstrated that assemblages undergoing FVF can display marked velocity weakening and develop cataclastic microstructures when subjected to high sliding velocities ($>1 \mu\text{m s}^{-1}$, Niemeijer and Spiers, 2006, 2007). This suggests that creeping phyllonite fault cores may be able to propagate seismic ruptures that nucleate within internal domains of velocity weakening material (such as the quartz-rich domains of the KFZ phyllonite) or in adjacent lithologies (such as the Nubra-Siachen leucogranite within the Nubra strand). Evidence for localised and potentially seismogenic frictional slip (e.g. through-going principle slip surfaces) is lacking within the KFZ phyllonites. Brittle structures are however inferred to have formed at both greater and shallower depths

than the phyllonite within the Nubra Formation and are abundant also within the adjacent leucogranite (Chapter 3; Phillips and Searle, 2007). It is likely therefore that localized brittle slip did affect the phyllonites intermittently, but that evidence for it has been obscured by subsequent FVF. It seems likely therefore that whilst the principle deformation mechanism of the phyllonite was FVF, the phyllonite band did not act as a barrier to seismic rupture propagation.

5.8 Conclusions

Phyllonites in the Nubra strand of the Karakoram Fault Zone record evidence for deformation-fluid-metamorphism interactions that resulted in low effective shear strength within the frictional-viscous transition zone. Transient fluid-related fracture events in exhuming mylonitic metapelites promoted greenschist facies phyllonitisation and development of through-going muscovite-rich domains. Frictional-viscous flow within these domains occurred at $351 \pm 34^\circ\text{C}$ with effective shear strengths of <28 MPa. The phyllonites are inferred to have deformed predominantly by aseismic creep. Potential for velocity weakening behavior at high sliding velocities however suggests that the phyllonite may have been able to propagate earthquake ruptures. The phyllonite band does not therefore preclude large magnitude earthquakes within the fault zone.

6. Quantifying strain distribution in crustal shear zones

Abstract

Strain distributions in ductile shear zones underlying active faults are often poorly constrained due to difficulties either in observing strain in situ at depth and/or in quantifying strain in exhumed fault rocks. In this chapter, a strain proxy based on quartz crystal preferred orientation (CPO) intensity is developed and applied to mylonitic granitoids of the Karakoram fault zone (KFZ). Quartz microstructures and CPOs indicate that deformation occurred by dislocation creep on the prism $\langle a \rangle$ and to a lesser extent rhomb $\langle a \rangle$ slip systems at c. 500-550°C. An eigenvector-based approach is used to quantify variations in quartz CPO “intensity” across the KFZ. The results show that strain within the KFZ shear zone was heterogeneously accommodated in multiple strands across a 7-11 km wide zone. 17.1-15.1 Ma granitoids show strong strain gradients adjacent to KFZ shear zones, but are undeformed outside of these zones and also lack near-solidus (i.e. prism $\langle c \rangle$ slip) CPO. Thus, the KFZ cross-cuts the granitoids and must have initiated after 15.7 Ma, contradicting previous suggestions of initiation as early as 32 Ma. An Al-in-hornblende geobarometric estimate (448 ± 72 MPa) for the pre-kinematic 17.12 ± 0.06 Ma South Tangtse granite shows that it was emplaced at 16.6 ± 3.7 km depth. This result defines an average post-emplacement exhumation rate of 1.0 ± 0.2 km/Myr and constrains the depth of formation of the 15.7-13.7 Ma strain profiles to c. 15 km. The KFZ strain distribution formed at c. 15 km depth represents a transition in fault zone structure between more localised deformation in the frictional-viscous transition zone (Chapter 3) and broadly distributed deformation in the partially molten mid-crust at c. 20 km depth (Chapter 4). These results provide an analogue for the deep portions of active strike-slip faults and constrain models of fault behaviour by showing that ductile shear zones can be wider and considerably more complex than are commonly modelled.

6.1 Introduction

The distribution of strain within ductile shear zones has been debated for over 30 years, and is fundamental to answering questions on fault structure (Sibson, 1983), crustal strength (Platt and Behr, 2012) and seismogenic fault mechanisms (Cowie et al., 2013). Whilst it is clear that faults and underlying shear zones generally broaden with depth (Bürgmann and Dresen, 2008) it remains unclear whether upper-crustal brittle faulting typically continues down dip into a localised shear zone, complex multi-stranded structures, or widespread sub-horizontal deformation of weak mid/lower crust (Section 1.3). Better understanding of such strain distributions will provide important constraints for models of seismogenic faults (e.g. Ellis et al., 2006; Malservisi et al., 2003). In particular, quantitative assessments of strain based on field and microstructural observations of large-scale exhumed shear zones have been lacking (Bürgmann and Dresen, 2008). This is in part because strain markers of known initial geometry (e.g. fossils, reduction spots etc.) required to determine absolute finite strain are not generally present in sufficient distribution to determine adequately strain gradients within km-scale crustal shear zones and are absent typically from mid-lower crustal igneous and metamorphic rocks. Thus, a more widely applicable strain proxy suitable for such regions and lithologies is required. This chapter develops the use of the CPO intensity of quartz, a common and relatively well-understood mineral, as a proxy for the strain distribution across ductile shear zones and presents its application to the exhumed shear zone of the KFZ, NW Himalaya (Figure 6.1).

Better constraints on the KFZ ductile strain distribution and the conditions under which it formed also have implications for interpretations of other particular characteristics of the KFZ, including the age of the fault, the strain-rate within it and the thermal regime during ductile deformation. As discussed previously (Chapters 1-4) considerable debate has occurred over the time of initiation of the KFZ. This age depends largely on the cross-cutting relationships between the fault and the Miocene granitoids along its length (e.g. Boutonnet et al., 2012; Leloup et al., 2011; Phillips and Searle, 2007; Phillips et al., 2004; Searle et al., 1998). These cross-cutting

relationships may be better elucidated by quantifying the strain distribution across the granitoids to clarify conflicting interpretations of the more subjective qualitative field and microstructural criteria (e.g. Boutonnet et al., 2012; Phillips and Searle, 2007).

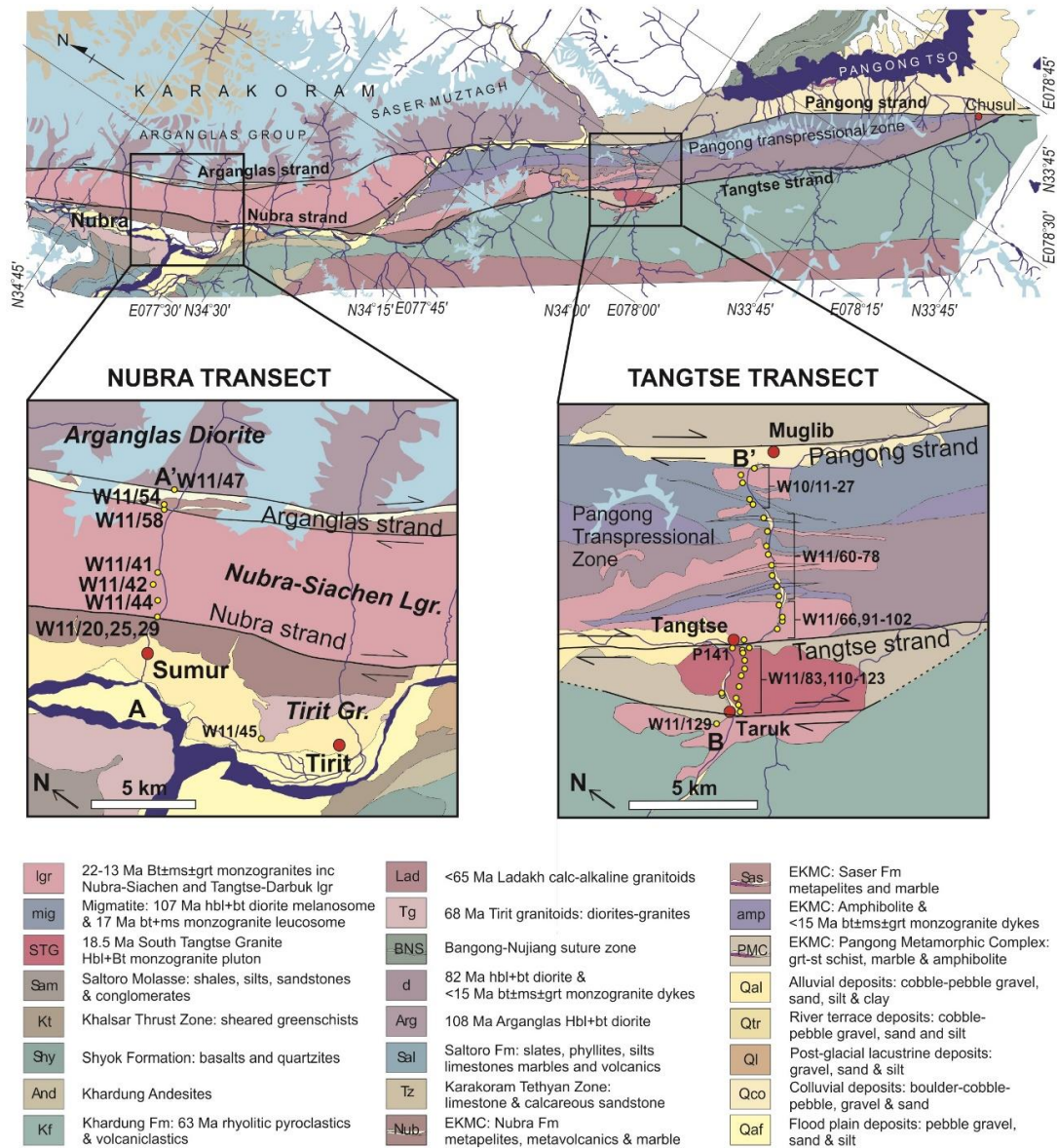


Figure 6.1 Geological map of the Karakoram Fault Zone, Ladakh, NW India, showing lithotectonic units, sample locations and transects A-A' and B-B' shown in Figures 5.10 and 5.11. Modified from Phillips (2008).

The widths of the deforming zones across the KFZ are also an important consideration in the recently proposed “quartz-strain-rate-metry” approach used by Boutonnet et al. (2013) to estimate a slip-rate of c. 11 mm/yr across the KFZ. This approach and the implications of the results presented in this chapter are discussed in detail in Section 6.6.1.2. Quantification of strain

gradients across the KFZ provides therefore important constraints on both the specific characteristics of the KFZ and on fault zone structure and deformation processes more generally.

6.2 Characterising Quartz Deformation Within The Karakoram Fault Zone

6.2.1 The Role of Quartz in the Deformed Eastern Karakoram Granitoids

In order to develop a CPO based strain proxy it is necessary to thoroughly characterise the deformation mechanisms that have operated in the rocks of interest, to determine the relative strengths of each mineral under the conditions of deformation and to infer which mineral was most significant in accommodating strain. A detailed description of deformation microstructures and inferred deformation mechanisms for each of the common minerals within the KFZ fault rocks was provided in Chapter 3. From these microstructures it is evident that, (at least) prior to the development of interconnected layers of frictionally weak phyllosilicates, the principle deformation mechanisms within the deformed granitoids of the Karakoram batholith were dynamic recrystallisation of quartz and feldspar (Section 3.2). Quartz deformed primarily by grain boundary migration (GBM) and subgrain rotation (SGR) dynamic recrystallization, whereas feldspar deformed by bulging dynamic recrystallization (BGL). Relative to quartz, feldspar typically shows less extensive recrystallisation and preserves coarser porphyroclasts exhibiting core and mantle structures. Feldspar dynamic recrystallisation and myrmekite growth are most intense at feldspar-feldspar porphyroclast contacts, indicating that these were high stress sites and that feldspar acted as the load-bearing phase. From these microstructures it is clear that feldspar was stronger than quartz under the inferred conditions of deformation (c. 500°C, fluid present) and that quartz preferentially accommodated strain. This is typical for deformation of quartz-feldspar aggregates under greenschist to lower-amphibolite grade conditions (Passchier and Trouw, 2005). The rest of this section provides a more

detailed examination of quartz deformation within the KFZ using optical microscopy and electron backscattered diffraction (EBSD).

6.2.2 Optical Microstructure of Deformed Quartz

Across the study area, quartz within granitoids deformed within the KFZ shows relatively consistent intragranular and grain boundary microstructures dominated by subgrains and lobate/irregular grain boundaries, indicative of SGR and GBM dynamic recrystallisation respectively (Figure 6.2, Chapter 3). These ubiquitous combined quartz deformation mechanisms, along with BGL dynamic recrystallization of feldspar, suggest that deformation temperature, strain rate and/or fluid activity did not vary sufficiently within/across the KFZ to cause major changes in recrystallisation regime. However, slight increases in the relative importance of SGR towards the centres of shear zones (Figure 6.2) may be due to modest decreases in temperature (i.e. more localised overprinting during exhumation) or increases in strain rate (Stipp et al., 2002). These potential changes are estimated to be no more than c. 50°C or a factor of 10 strain rate as the quartz has remained close to the transition between GBM and SGR regimes (Stipp et al., 2002). Relatively modest changes in the conditions of deformation are supported by the short duration of the main phase of ductile deformation, which is constrained to between c. 15.7-13.7 Ma (Section 6.6.1.1; Chapter 4; Phillips et al., 2004). During this time, the rocks would have only been exhumed by c. 1.6-2.4 km, given an average exhumation rate of 1.0 ± 0.2 km/Myr (Section 6.5).

Towards the centres of the main shear zones there is also a decrease in recrystallised quartz grain size (Figure 6.2, Chapter 3). This decrease is indicative of an increase in flow stress within the centres of the shear zones (Stipp and Tullis, 2003; Twiss, 1977). It is not appropriate however to use recrystallised grain size palaeopiezometric relationships to estimate the stress variation across the shear zones because a) existing palaeopiezometers are calibrated for monomineralic lithologies only and their application to polymineralic lithologies may be subject therefore to large uncertainties, and b) recrystallised quartz grain size varies considerably

within individual samples, reflecting grain-scale stress heterogeneities (e.g. where quartz appears “squeezed” between feldspar porphyroclasts).

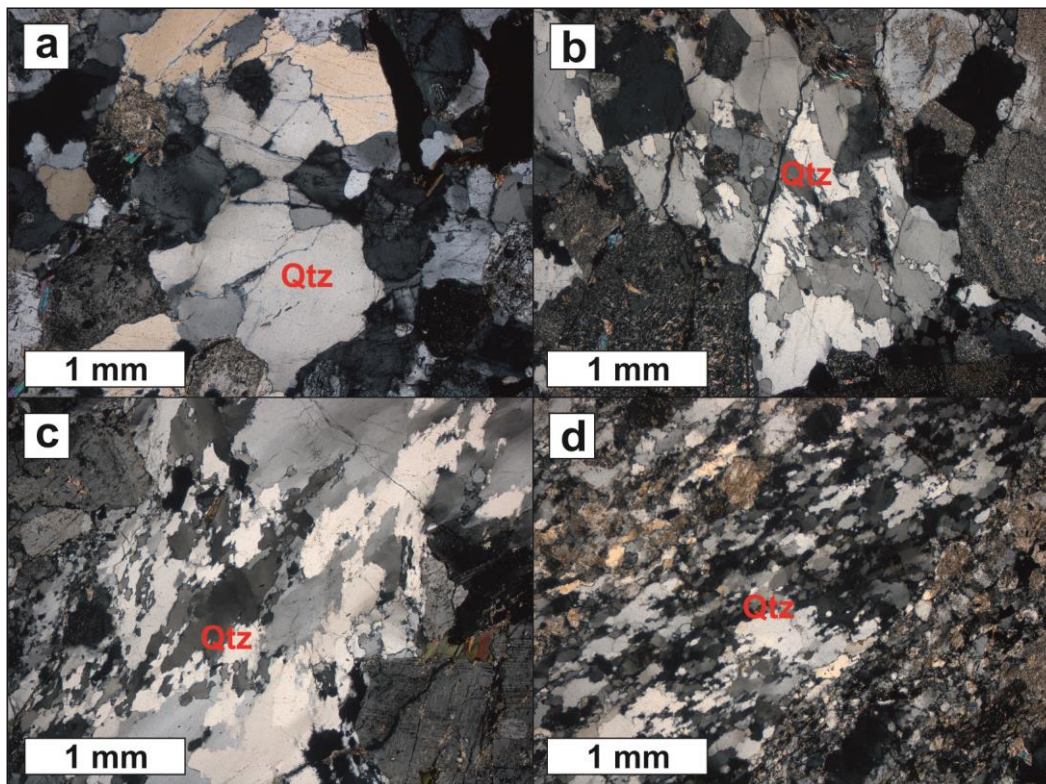


Figure 6.2 Quartz microstructures in the Nubra-Siachen leucogranite showing increasing intensity of deformation fabric a-d approaching the Nubra fault strand. All are cross-polarised optical photomicrographs. a) Weakly-undeformed quartz in the centre of the batholith (sample W11/41). b) Weak quartz deformation fabric in the margin of the Nubra strand defined by lobate grain boundaries and minor subgrain development (sample W11/42). c) Moderately deformed quartz within the Nubra strand showing highly irregular grain boundaries and numerous subgrains (sample W11/44). d) Highly deformed quartz at the margin of the leucogranite showing lobate grain boundaries and widespread subgrains (sample W11/29). These deformation microstructures indicate temperatures of 500-550°C at typical geological shear zone strain rates of $c. 10^{-12} \text{ s}^{-1}$.

6.2.3 Electron Backscattered Diffraction Characterisation of Deformed Quartz

6.2.3.1 Quartz Slip System Activity and CPO

Four dominant slip systems are known to operate in quartz: basal $\langle a \rangle$, rhomb $\langle a \rangle$, prism $\langle a \rangle$ and prism $\langle c \rangle$ (Figure 6.3; Passchier and Trouw, 2005). The relative activities of each depend on the relative magnitudes of the critical resolved shear stresses (CRSS) required to initiate dislocation glide on each system (e.g. de Bresser and Spiers, 1997). The CRSS vary

with temperature such that, broadly speaking, basal $\langle a \rangle$, rhomb $\langle a \rangle$, prism $\langle a \rangle$ and prism $\langle c \rangle$ tend to dominate respectively under greenschist, greenschist-amphibolite, amphibolite and amphibolite-granulite conditions (Barth et al., 2010; Toy et al., 2008; Mainprice et al., 1986; Blacic and Christie, 1984), although the compilation of studies by Toy et al. (2008) shows that there is variation/overlap in this trend.

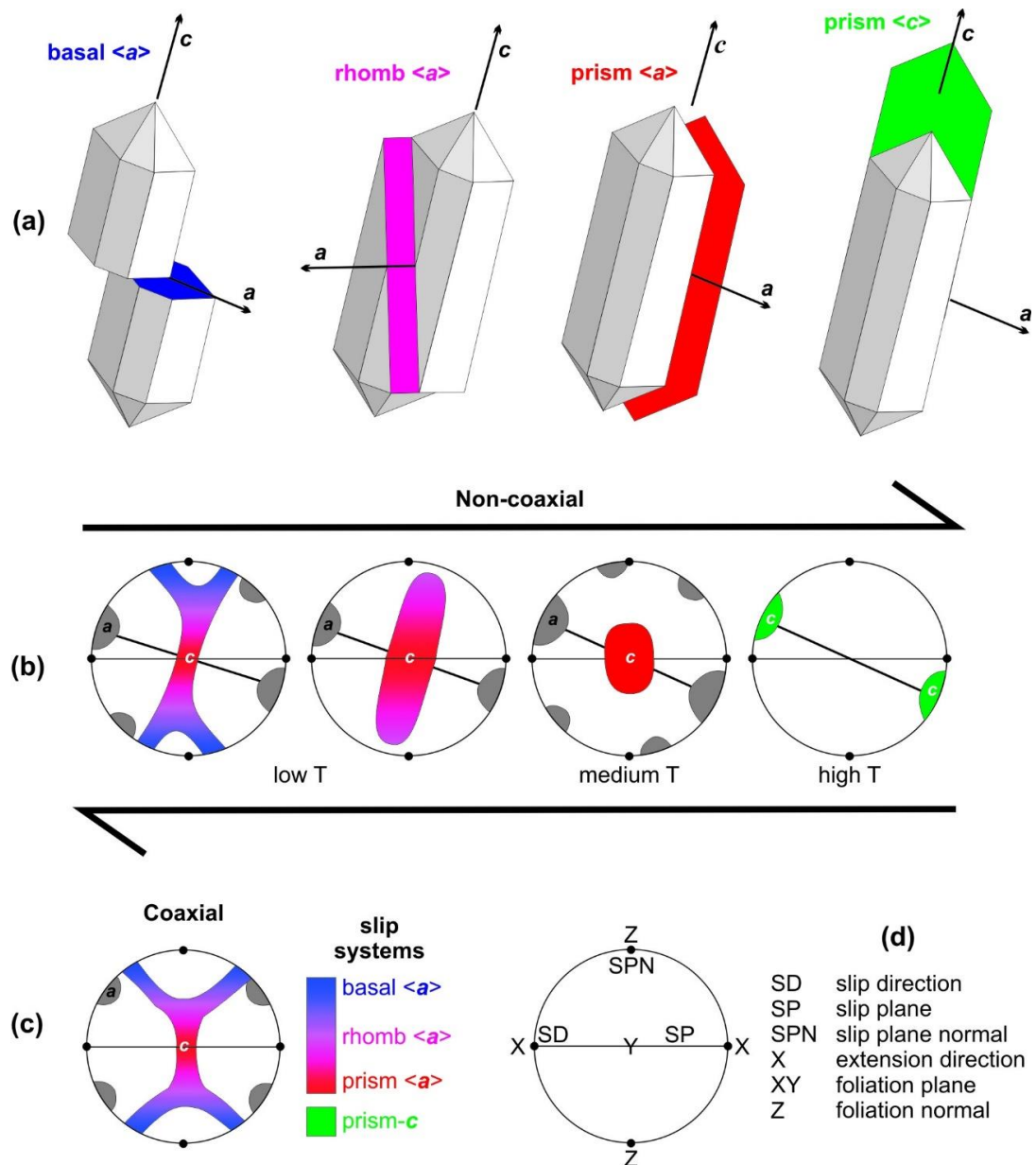


Figure 6.3 Relationships between quartz slip systems, deformation temperature and CPO. a) Simplified representation of the four main quartz slip systems showing an individual slip plane and slip direction for each case. b) (c)- and $\langle a \rangle$ - axes CPO resulting from the operation of various slip systems across a range of temperatures approximating the transition from greenschist-amphibolite-granulite grade conditions (left to right) during dextral non-coaxial (simple shear) deformation, colour-coded according to the slip-systems in (a). c) Typical (c)- and $\langle a \rangle$ -axes CPO formed during coaxial deformation. d) The geometrical relationship between slip system and kinematic reference frame that crystal orientations rotate towards during dislocation creep. Figure produced by G.E. Lloyd, modified from Passchier and Trouw (2005), after Nicholas and Poirier (1976), Lister and Hobbs (1980) and Schmid and Casey (1986).

6.2.3.2 EBSD Data Acquisition

EBSD provides a method of acquiring microstructural images and crystallographic orientation data with known relationships to the rock microstructure (Prior et al., 1999). The technique allows therefore both detailed investigations of specific microstructures and bulk characterisation of crystallographic fabrics. A total of 46 samples from the Nubra and Tangtse area, Ladakh, NW India (Figure 6.1, Table 6.1) were cut perpendicular to the foliation and parallel to the lineation, (i.e. the XZ plane of finite strain), and prepared into polished thin sections and ~15x15 mm 'syton' polished resin mounted blocks (e.g. Lloyd, 1987). Samples lacking XYZ strain indicators were cut parallel to geographic horizontal. Thin sections were analysed for mineralogy and deformation mechanisms via optical and scanning electron microscopy, the latter using a FEI Quanta 650 FEG ESEM at the University of Leeds. EBSD data were collected from the polished blocks using an Oxford Instruments Nordlys S EBSD camera and Oxford Instruments Channel 5 acquisition software. Crystal files (.cry) for major minerals were sourced from the HKL phase database and the 'Plagioclases' database produced previously at the University of Leeds. Data were collected using 20 kV accelerating voltage, 5-15 nA specimen current and 70° specimen tilt angle. Whole block areas were analysed using combined stage scan-beam scan montage with step sizes of 25-40 μm .

The EBSD data were rotated into the geographic reference frame using the program *ROTctf* (Mainprice, 1990) in order to illustrate variations in CPO orientations across the KFZ and because undeformed samples lack a

kinematic reference frame. Pole figures were plotted using the program *PFch5* (Mainprice, 1990). Both *ROTctf* and *PFch5* are available at:

<http://www.gm.univ->

[montp2.fr/PERSO/mainprice/UNICEF_Careware_Details.html](http://www.gm.univ-montp2.fr/PERSO/mainprice/UNICEF_Careware_Details.html).

Normalised eigenvalues for quartz *c*-axes were calculated using *PFch5*. Since these data were processed it has become possible to conduct the same analysis using the MTEX open source MATLAB toolbox (Hielscher and Schaeben, 2008) which provides an alternative means to analyse such data.

Sample	Northing	Easting	Lithology	Mineralogy
NUBRA TRANSECT (SW to NE)				
Tirit Granite (T.G.) 68±1 Ma (Weinberg et al., 2000)				
W11/45	34°33.904'	077°36.895'	Diorite	Pl+Qtz+Kfs+Hbl+Chl+Cpx
Nubra-Siachen Leucogranite 15.9±0.1 Ma (Phillips et al., 2013)				
W11/29	34°37.893'	077°38.393'	Bt±Ms±Grt lgr	Qtz+Pl+Kfs+Bt+Ms
W11/25	34°37.922'	077°38.419'	Bt±Ms±Grt lgr	Qtz+Pl+Kfs+Bt+Ms
W11/20	34°37.900'	077°38.397'	Bt±Ms±Grt lgr	Qtz+Pl+Kfs+Bt+Ms
W11/44	34°38.107'	077°38.864'	Bt±Ms±Grt lgr	Qtz+Pl+Kfs+Bt+Ms
W11/42	34°38.278'	077°39.115'	Bt±Ms±Grt lgr	Qtz+Pl+Kfs+Bt+Ms
W11/41	34°38.482'	077°39.453'	Bt±Ms±Grt lgr	Qtz+Pl+Kfs+Bt+Ms
W11/58	34°39.249'	077°41.323'	Bt±Ms±Grt lgr	Qtz+Pl+Kfs+Bt+Ms
W11/54	34°39.295'	077°41.353'	Bt±Ms±Grt lgr	Qtz+Pl+Kfs+Bt+Ms
Arganglas Diorite (A.D.) 108.6±1.7 Ma (Phillips et al., 2013)				
W11/47	34°39.340'	077°42.108'	Diorite	Pl+Qtz+Kfs+Hbl+Bt+Cpx
TANGTSE TRANSECT (SW to NE)				
Taruk Leucogranite (T.Lgr.)				
W11/129	34°01.290'	078°08.071'	Bt±Ms±Grt lgr	Qtz+Pl+Kfs+Bt+Ms+Grt
W11/123	34°00.838'	078°08.925'	Bt±Ms±Grt lgr	Qtz+Pl+Kfs+Bt+Ms+Grt
Taruk Amphibolite				
W11/121	34°00.838'	078°08.925'	Amphibolite	Qtz+Pl+Hbl+Kfs
South Tangtse Granite 17.12±0.06 Ma (Phillips, 2004)				
W11/120	34°00.838'	078°08.925'	Hbl+Bt mzg	Pl+Qtz+Kfs+Bt+Hbl
W11/122	34°00.838'	078°08.925'	Hbl+Bt mzg	Pl+Qtz+Kfs+Bt+Hbl
W11/124	34°00.838'	078°08.925'	Hbl+Bt mzg	Pl+Qtz+Kfs+Bt+Hbl
W11/119	34°00.866'	078°08.987'	Hbl+Bt mzg	Pl+Qtz+Kfs+Bt+Hbl
W11/116	34°00.969'	078°09.138'	Hbl+Bt mzg	Pl+Qtz+Kfs+Bt+Hbl
W11/127	34°01.391'	078°08.744'	Hbl+Bt mzg	Pl+Qtz+Kfs+Bt+Hbl
W11/126	34°01.405'	078°08.754'	Hbl+Bt mzg	Pl+Qtz+Kfs+Bt+Hbl
W11/115	34°00.949'	078°09.574'	Hbl+Bt mzg	Pl+Qtz+Kfs+Bt+Hbl
W11/114	34°01.135'	078°09.871'	Hbl+Bt mzg	Pl+Qtz+Kfs+Bt+Hbl
W11/113	34°01.165'	078°09.985'	Hbl+Bt mzg	Pl+Qtz+Kfs+Bt+Hbl
W11/112	34°01.365'	078°10.121'	Hbl+Bt mzg	Pl+Qtz+Kfs+Bt+Hbl
W11/125	34°01.417'	078°10.210'	Hbl+Bt mzg	Pl+Qtz+Kfs+Bt+Hbl
W11/83	34°01.475'	078°10.239'	Hbl+Bt mzg	Pl+Qtz+Kfs+Bt+Hbl
W11/110	34°01.347'	078°10.569'	Hbl+Bt mzg	Pl+Qtz+Kfs+Bt+Hbl
P141	34°01.506'	078°10.283'	Hbl+Bt mzg	Pl+Qtz+Kfs+Bt+Hbl
Tangtse-Darbuk Leucogranite (T.D.L.) 15.6±0.7 (Phillips et al., 2013)				

Sample	Northing	Easting	Lithology	Mineralogy
W11/91	34°01.554'	078°10.443'	Bt±Ms±Grt lgr	Qtz+Pl+Kfs+Bt+Ms
W11/101	34°01.589'	078°10.520'	Bt±Ms±Grt lgr	Qtz+Pl+Kfs+Bt+Ms
W11/109	34°01.081'	078°11.294'	Bt±Ms±Grt lgr	Qtz+Pl+Kfs+Bt+Ms
W11/102	34°01.066'	078°11.577'	Bt±Ms±Grt lgr	Qtz+Pl+Kfs+Bt+Ms
W11/66	34°01.427'	078°11.825'	Bt±Ms±Grt lgr	Qtz+Pl+Kfs+Bt+Ms
Pangong Transpressional Zone (P.T.Z.)				
W11/67	34°01.597'	078°11.943'	Diorite	Pl+Qtz+Hbl+Di+Bt
W11/69	34°01.770'	078°12.149'	Diorite	Qtz+Pl+Bt+Kfs+Di+Hbl
W11/71	34°01.886'	078°12.262'	Diorite	Qtz+Pl+Hbl+Kfs+Bt
W11/63	34°02.173'	078°12.646'	Bt lgr	Qtz+Pl+Kfs+Bt
W11/61	34°02.287'	078°12.781'	Ms quartzite	Qtz+Ms
W11/60	34°02.327'	078°12.955'	Diorite	Qtz+Pl+Kfs+Hbl+Bt
W11/78	34°02.555'	078°13.288'	Diorite	Pl+Qtz+Kfs+Hbl+Bi+Di
W11/73	34°02.738'	078°13.452'	Melanosome	Hbl+Pl+Qtz+Bt
W11/74	34°02.738'	078°13.452'	Leucosome	Pl+Kfs+Qtz+Bt+Hbl
W10/27	34°03.150'	078°13.489'	Diorite	Pl+Qtz+Kfs+Bt+Hbl
W10/26	34°03.232'	078°13.546'	Diorite	Qtz+Pl+Kfs+Aug+Chl
Muglib Dome (M.D.) 15.1±0.6 (Phillips et al., 2013)				
W10/24	34°03.549'	078°13.708'	Bt±Ms±Grt lgr	Qtz+Pl+Kfs+Bt
W10/21	34°03.781'	078°13.843'	Bt±Ms±Grt lgr	Pl+Qtz+Kfs+Bt
W10/11	34°03.502'	078°14.476'	Bt±Ms±Grt lgr	Pl+Qtz+Kfs+Bt

Table 6.1 Sample details for EBSD study. Including unit ages and abbreviations used in Figure 6.8. Sample localities marked on Figure 6.1. Mineralogies determined by optical microscopy and energy-dispersive X-ray spectroscopy. British Geological Survey mineral abbreviations. WGS 1984 reference coordinate system. lgr-leucogranite, mzg-monzogranite.

6.2.3.3 POLE FIGURE ANALYSIS

Quartz pole figures for 48 samples from two transects across the KFZ (Figure 6.1, Table 6.1) are shown in Figure 6.4. Pole figures for the <a> and (c) directions and poles to the {m} (prism), {r} and {z} (rhomb) planes are plotted in the geographic reference frame (i.e. north at top of pole figure, east on right etc.) to allow direct comparison of fabric orientations and because strain indicators (i.e. foliation, XY, and lineation, X) were not always present/recognisable in outcrop/hand specimen (e.g. in undeformed granitoids). XYZ directions are plotted on the pole figures where possible.

The principle features of samples which show distinct CPO are as follows (examples of each are marked in Table 6.2 and shown in Figure 6.4).

- 1) (c) directions typically form maxima close to the Y kinematic direction. These are often associated with short girdles or scattered sub-maxima extending towards, but generally not reaching, the Z direction.

2) $\langle a \rangle$ directions typically form XZ girdles or girdles that pass through X and bisect Y and Z. Several of the girdles have 3 superimposed sub-maxima (per hemisphere) forming 'single crystal' type CPO. Others show single maxima (sub-)parallel to X or displaced 20-30° from X.

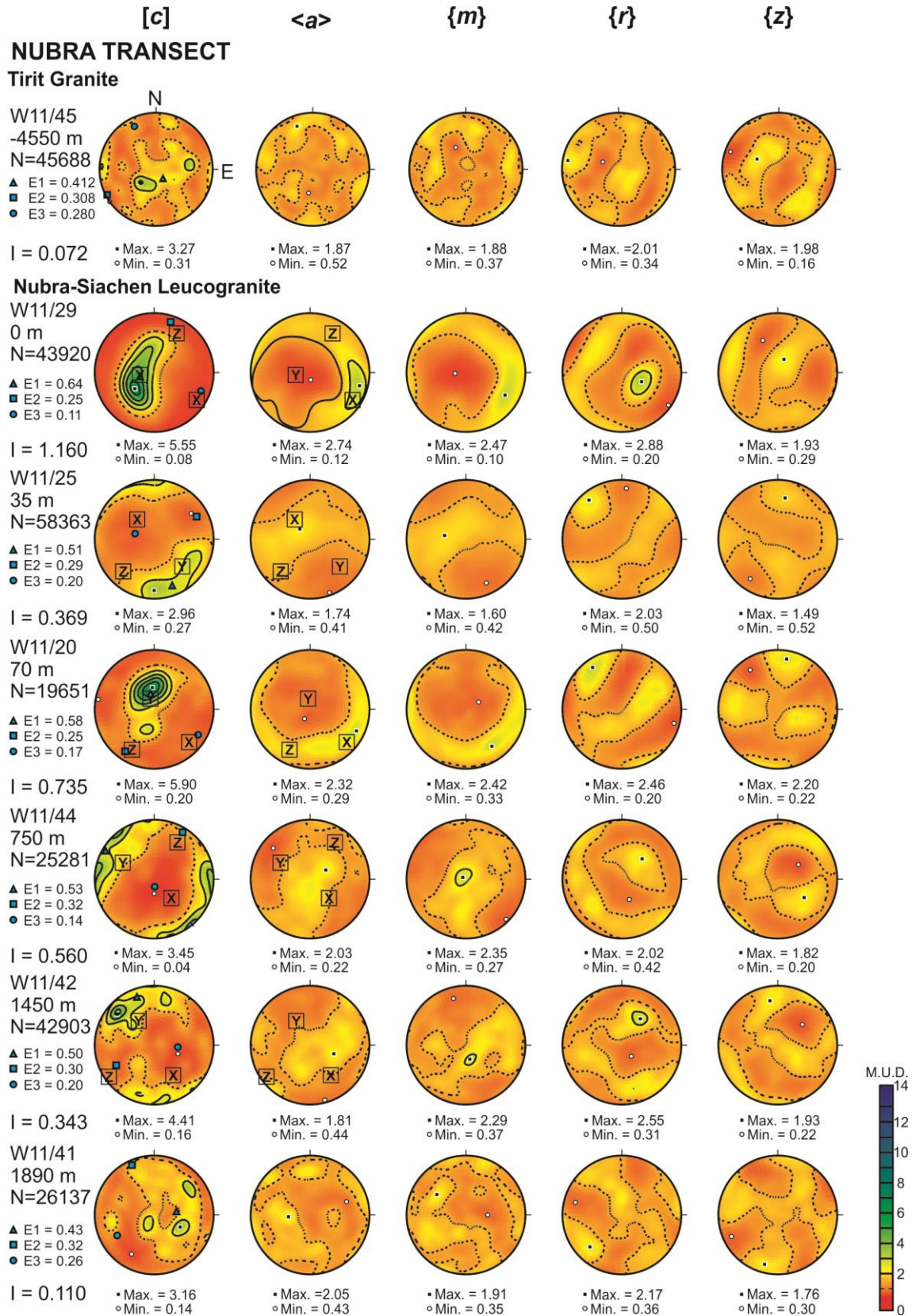
3) $\{m\}$ pole CPO closely mimic those of the $\langle a \rangle$ directions with approximately XZ girdles or 'single crystal' distributions, but with $\{m\}$ pole maxima typically (sub)parallel to X.

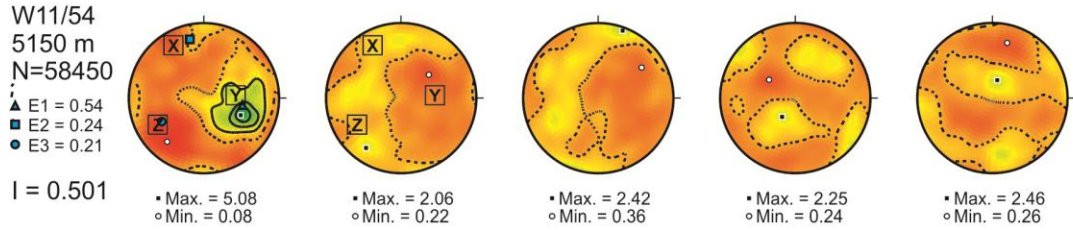
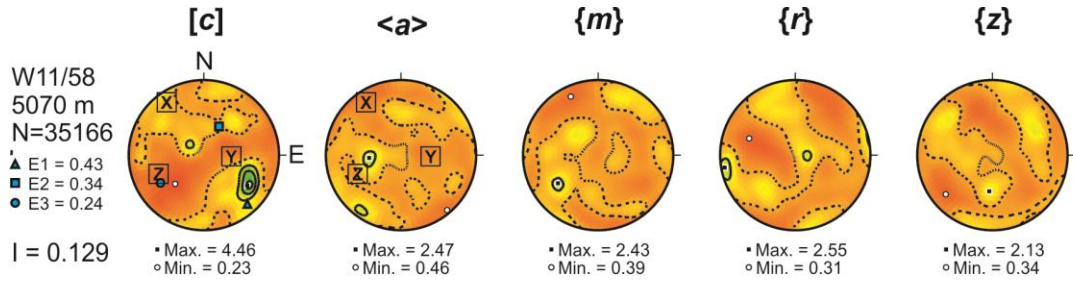
4) Poles to $\{r\}$ rhomb planes define more complex CPO. However, in samples with the best defined CPO, a recurrence of $\{r\}$ pole maxima subparallel to X accompanied by an approximately YZ girdle can be discerned.

5) Poles to $\{z\}$ rhomb planes define also complex CPO. However, in samples with the best defined CPO, $\{z\}$ poles typically form small circles, or multiple maxima with approximately trigonal symmetry, about Y.

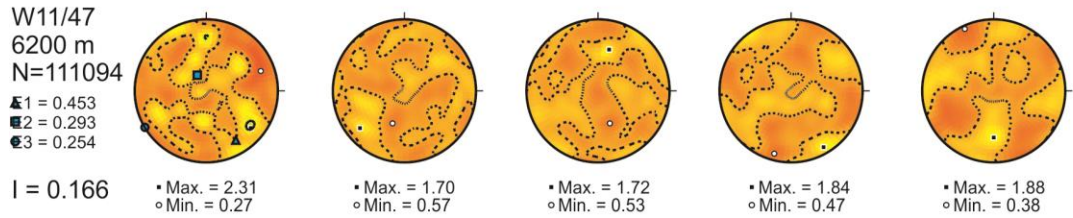
These CPO components are consistent with KFZ quartz deformation occurring primarily by prism $\langle a \rangle$ slip (i.e. $\langle c \rangle$ directions parallel to Y, $\{m\}$ poles subparallel to X and $\langle a \rangle$ directions 20-30° to X, Figure 6.5), with evidence of subordinate rhomb $\langle a \rangle$ slip (i.e. $\langle c \rangle$ directions between Y and Z and $\langle a \rangle$ directions subparallel to X) in a few samples (Toy et al., 2008; Passchier and Trouw, 2005; Mancktelow, 1987; Schmid and Casey, 1986). Rhomb $\langle a \rangle$ slip is most evident in samples at the NE margins of the Nubra-Siachen leucogranite (samples W11/29, W11/25 and W11/20, Figures 6.4 and 6.5) and Tangtse-Darbuk leucogranite (samples W11/91, W11/101 and W11/109, Figures 6.4 and 6.5) where they border the Nubra and Tangtse strand respectively (Figure 6.1) and where the microstructure indicates an increased component of SGR dynamic recrystallisation (Section 6.2.2) relative to GBM. Concentrations of $\langle c \rangle$ -axes close to Z are largely absent from the dataset, suggesting that basal $\langle a \rangle$ slip played a limited role in accommodating quartz crystal plastic deformation within the KFZ. Only one sample (W11/126) shows $\langle c \rangle$ -axes parallel to X, indicating prism $\langle c \rangle$ slip (i.e. deformation at submagmatic temperatures). This sample is an Hbl-Bt granite sheet marginal to the South Tangtse granite and appears to have been emplaced separately within the Taruk shear zone. It is inferred therefore that

this sheet was emplaced synkinematically after emplacement of the main body of the South Tangtse granite, which predates the deformation (Section 6.6.1.1).



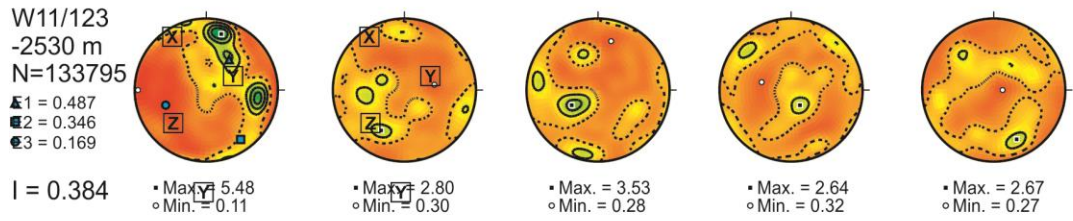
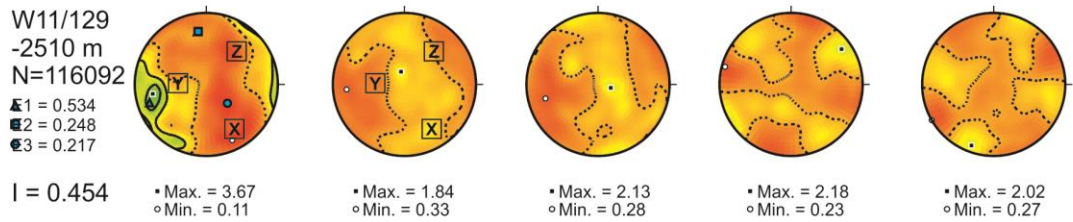


Arganglas Diorite

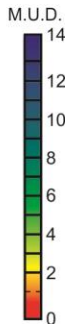
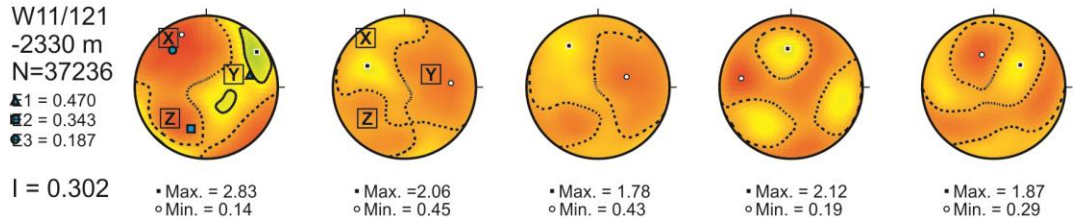


TANGTSE TRANSECT

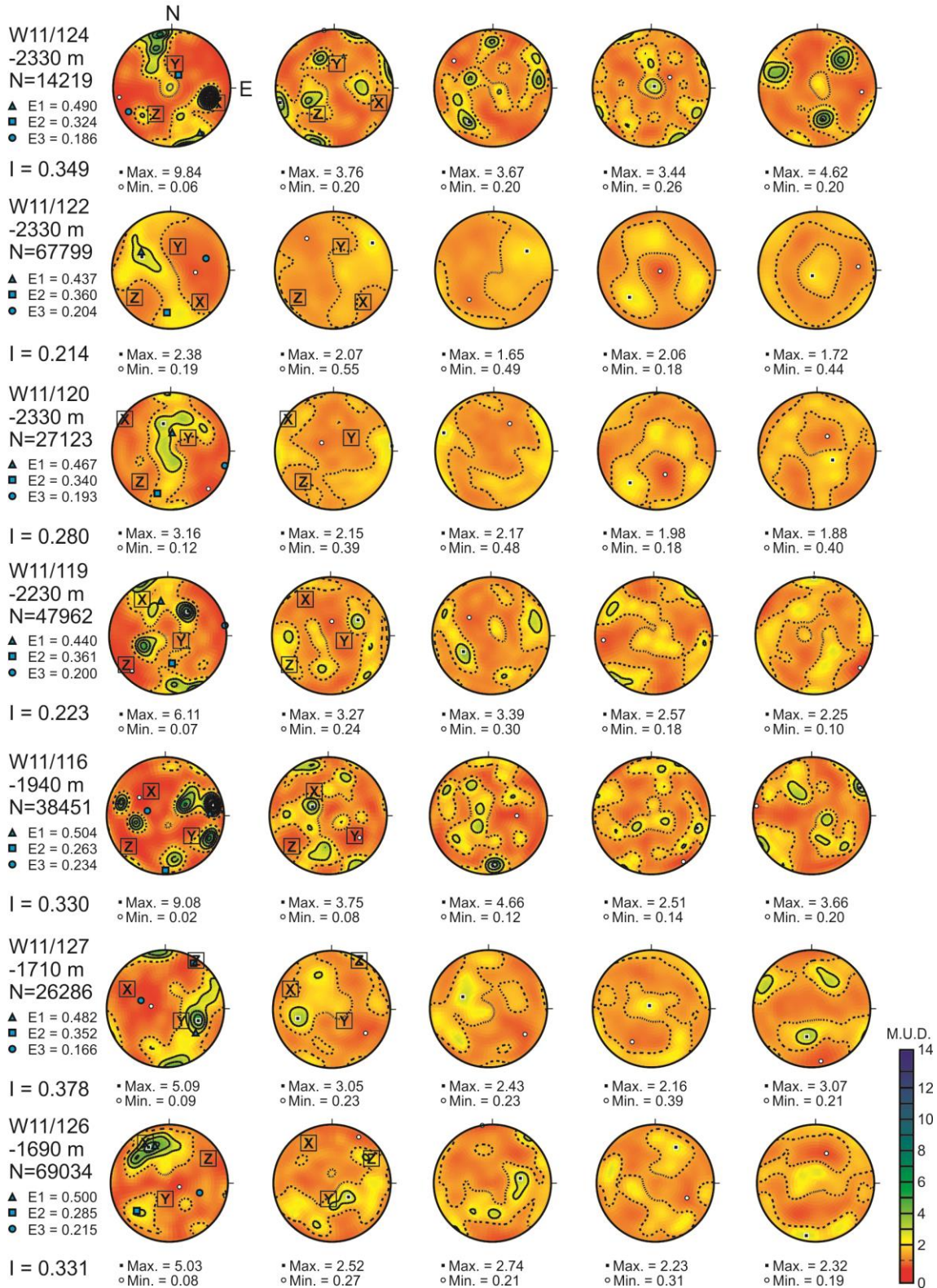
Taruk Leucogranite

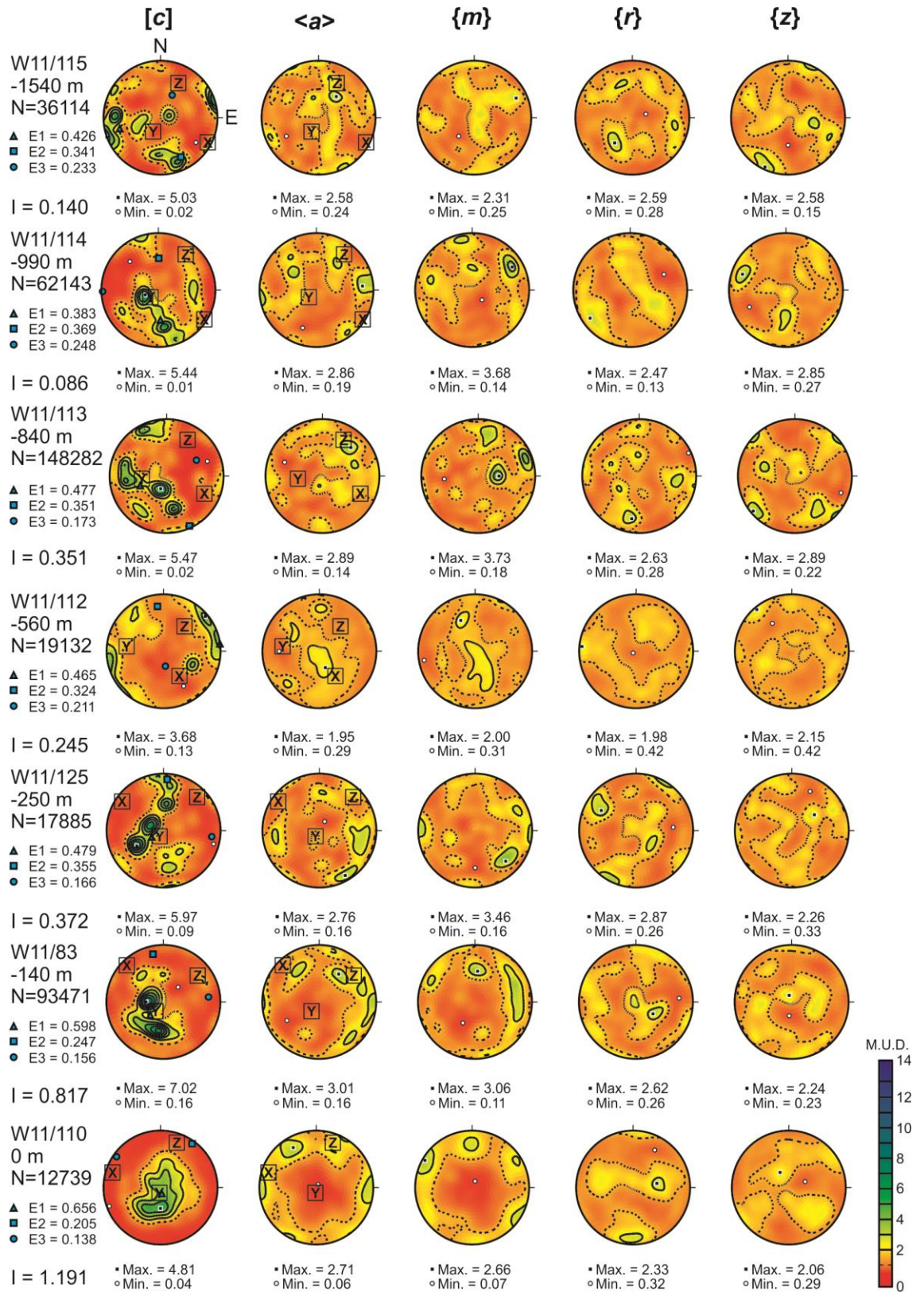


Taruk Amphibolite

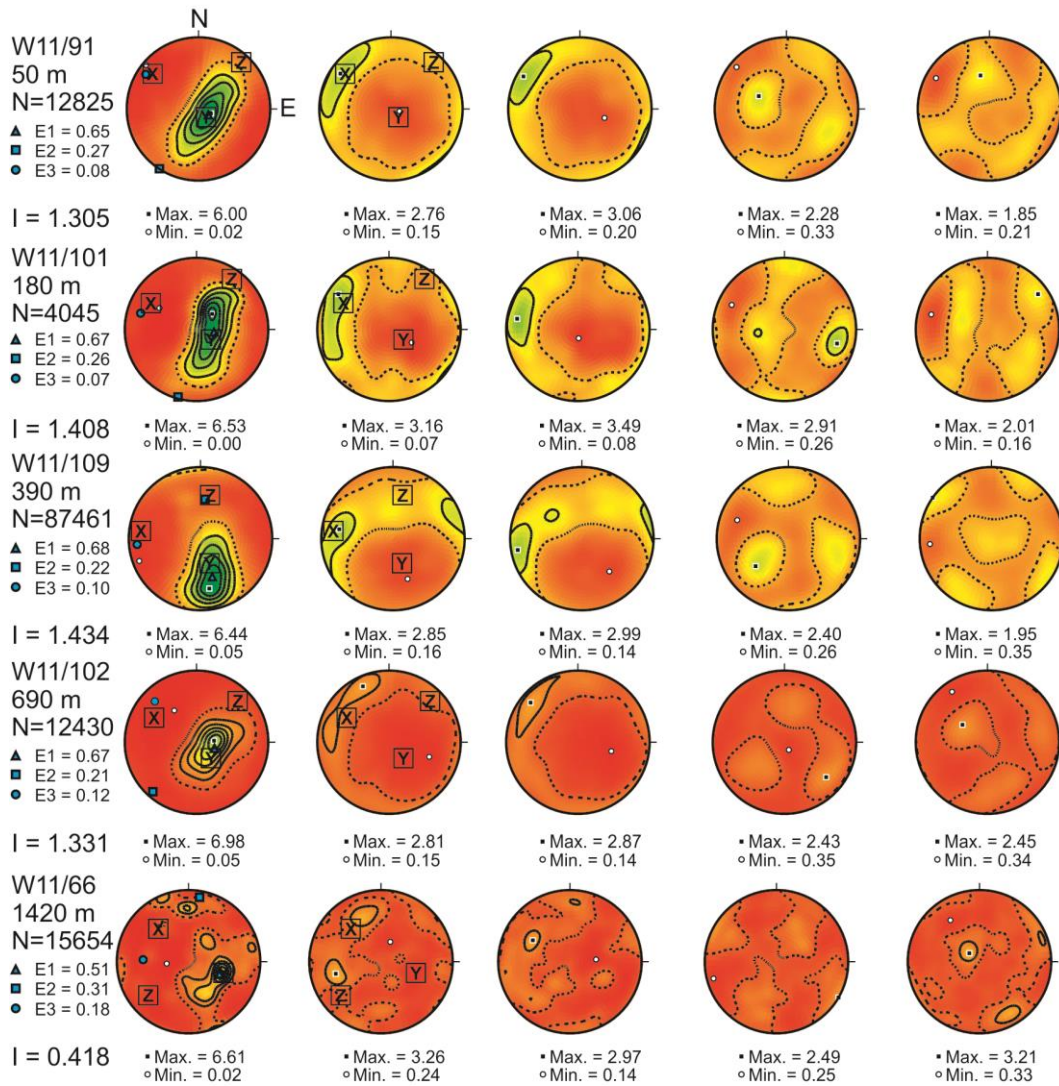


[c] <a> {m} {r} {z}
South Tangtse Granite

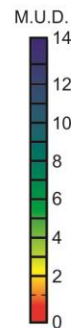
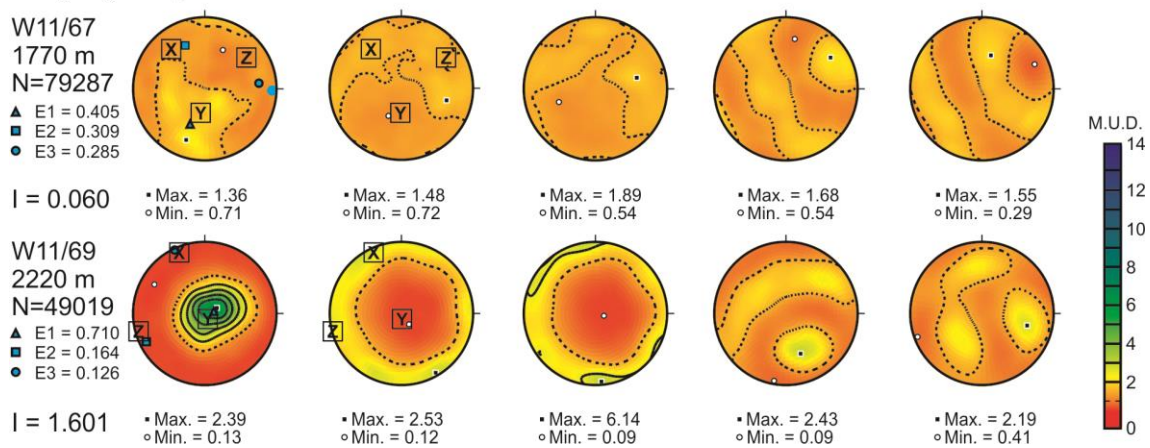


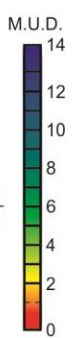
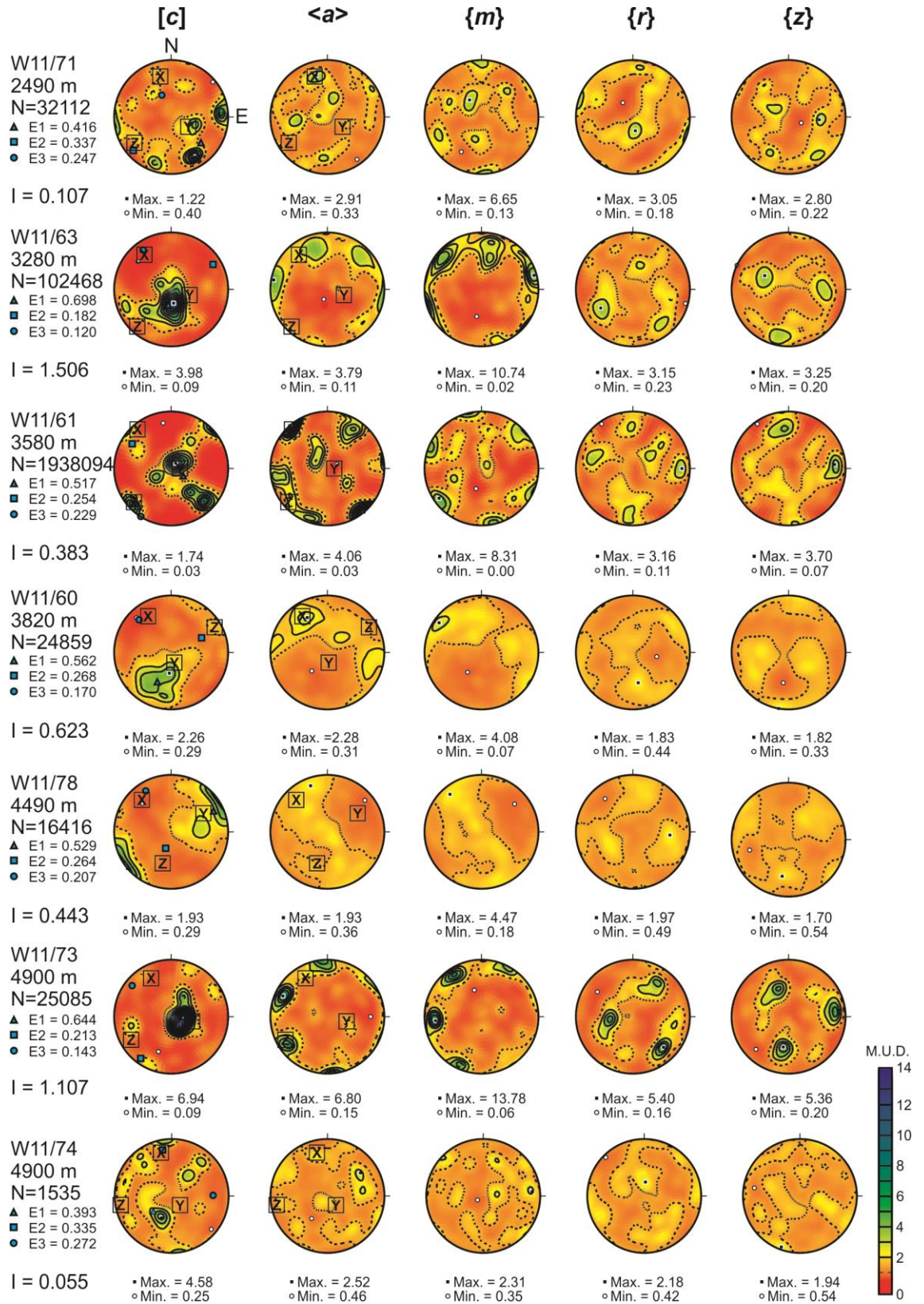


Tangtse-Darbuk Leucogranite



Pangong Trapsressional Zone





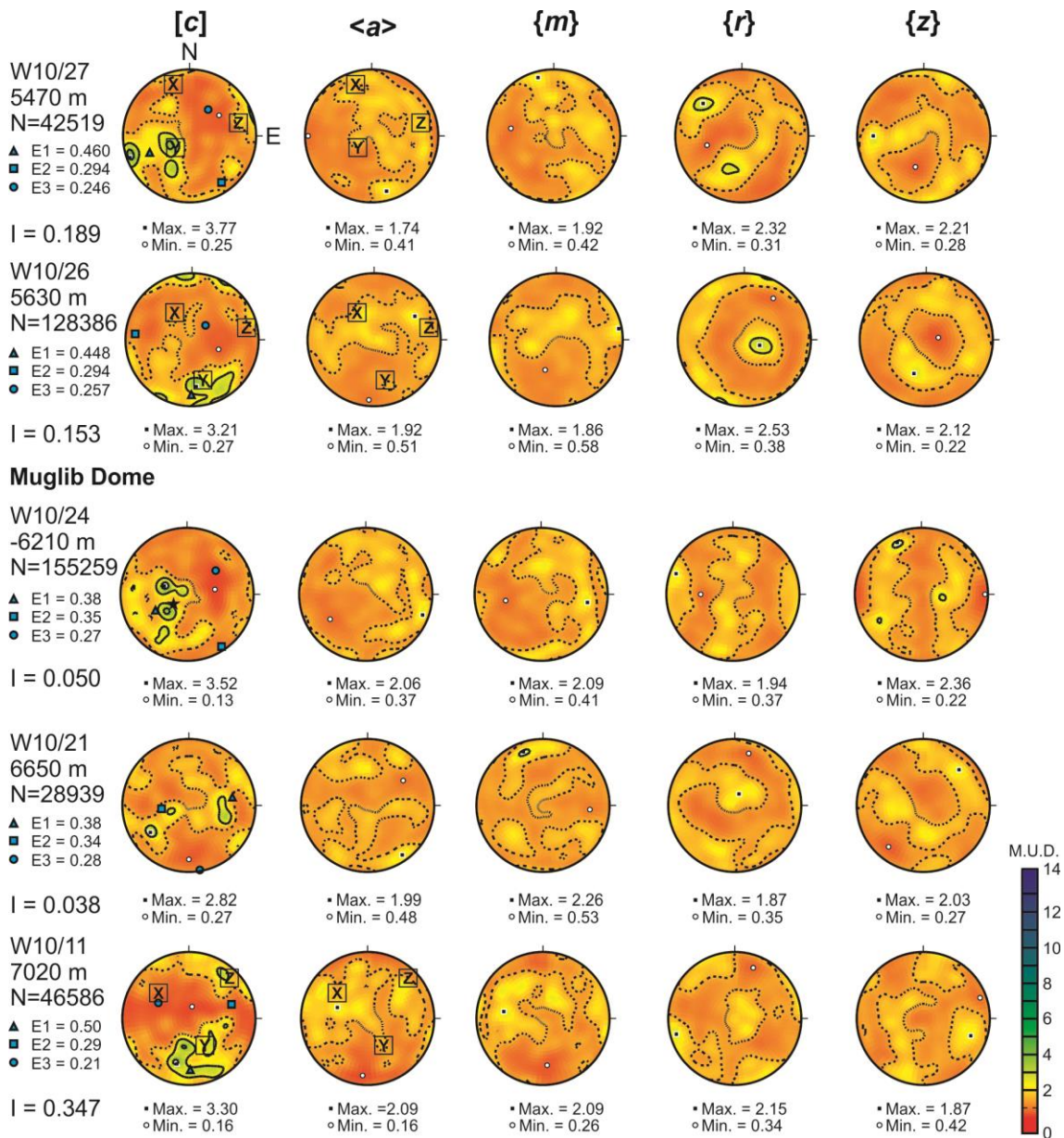


Figure 6.4 Pole figures showing the distribution of quartz crystal orientations as the (c) and <a> axes and the poles to the {m} (prism), {r} and {z} (rhomb) planes for 46 samples across the KFZ (Figure 6.1, Table 6.1). Samples are listed SW to NE in each transect. Pole figures are plotted in the geographic reference frame and contoured as multiples of uniform distribution (M.U.D.) with a contour interval of 1.0. All pole figures are plotted on the same logarithmic colour scale to facilitate comparisons and emphasise shapes within weak distributions. X, Y and Z and the directions of the maximum, intermediate and minimum principle finite strains respectively. Also given are the distance from the Nubra/Tangtse fault strand (NE positive), normalised principle eigenvalues (E1-3) and c-axes CPO intensity (I) calculated according to Equation 7.

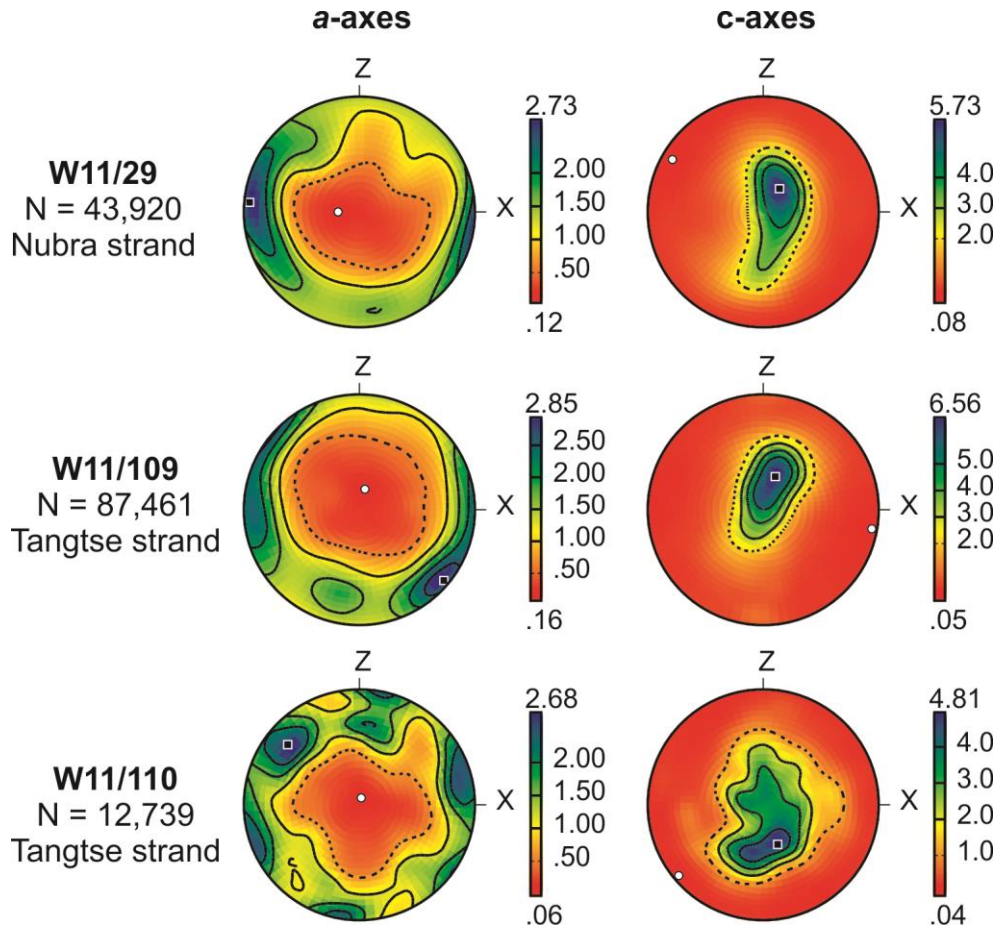


Figure 6.5 *a*-axis and *c*-axis CPO for three typical samples with well developed CPO plotted in the finite strain reference frame to facilitate identification of dominant slip systems.

Sample	(<i>c</i>) maxima subparallel to Y or short girdles from Y towards Z	< <i>a</i> > and { <i>m</i> } maxima subparallel to X or ~XZ girdles	{ <i>r</i> } poles subparallel to X with ~YZ girdle	{ <i>z</i> } small circles or maxima about Y
NUBRA TRANSECT				
Tirit Granite (T.G.) 68±1 Ma (Weinberg et al., 2000)				
W11/45				
Nubra-Siachen Leucogranite 15.9±0.1 Ma (Phillips et al., 2013)				
W11/29	✓	✓	✓	✓
W11/25	✓	✓	✓	
W11/20	✓	✓	✓	✓
W11/44	✓	✓		
W11/42	✓	✓		
W11/41				
W11/58				
W11/54	✓	✓		
Arganglas Diorite (A.D.) 108.6±1.7 Ma (Phillips et al., 2013)				
W11/47				
TANGTSE TRANSECT				
Taruk Leucogranite (T.Lgr.)				
W11/129		✓		
W11/123				✓

Sample	(c) maxima subparallel to Y or short girdles from Y towards Z	<a> and {m} maxima subparallel to X or ~XZ girdles	{r} poles subparallel to X with ~YZ girdle	{z} small circles or maxima about Y
Taruk Amphibolite				
W11/121	✓	✓	✓	
South Tangtse Granite 17.12±0.06 Ma (Phillips, 2004)				
W11/120	✓	✓		✓
W11/122			✓	✓
W11/124				
W11/119				
W11/116				
W11/127	✓		✓	
W11/126	✓	✓		✓
W11/115				
W11/114				
W11/113				
W11/112				
W11/125	✓			
W11/83	✓	✓		
W11/110	✓	✓	✓	✓
Tangtse-Darbuk Leucogranite (T.D.L.) 15.6±0.7 (Phillips et al., 2013)				
W11/91	✓	✓	✓	✓
W11/101	✓	✓	✓	✓
W11/109	✓	✓	✓	
W11/102	✓	✓		✓
W11/66	✓			
Pangong Transpressional Zone (P.T.Z.)				
W11/67				
W11/69	✓	✓	✓	✓
W11/71				
W11/63	✓	✓		✓
W11/61				
W11/60	✓	✓		✓
W11/78	✓	✓		
W11/73	✓	✓	✓	✓
W11/74				
W10/27		✓		✓
W10/26	✓			
Muglib Dome (M.D.) 15.1±0.6 (Phillips et al., 2013)				
W10/24				
W10/21				
W10/11	✓	✓	✓	

Table 6.2 Examples of samples showing CPO characteristics described in Section 6.2.3.3.

Many of the samples in the data set have weak/indiscernable quartz CPO. In these samples, most/all of the areas of the pole figures have a close to uniform distribution (M.U.D. ~1, e.g. samples W11/45 and W11/47), indicating a highly disordered (close to random) set of orientations. Other samples show several weak maxima dotted across each pole figure but lack

an overall preferred orientation (e.g. samples W11/116, W11/74 and W11/71). Although these maxima show slightly higher MUD values, their distribution is inconsistent with formation during operation of known quartz crystal slip systems. As such they are interpreted to result from individual, or a few, large grains that were measured many times during EBSD analysis; each large grain contributing an individual maximum. This effect is particularly pronounced in coarse-grained granitoids (e.g. W11/116) where a smaller number of larger grains are analysed compared to finer grained samples.

6.3 Quartz Crystal Preferred Orientation as a Strain Proxy

6.3.1 Controls on CPO development

From an initially random distribution of crystal orientations, CPO strength generally increases with increasing strain (Figure 6.6, Section 6.2.3.1) and may provide therefore a proxy for the relative finite strain accommodated by a rock. This effect is demonstrated by quartz CPO development in Taylor-Bishop-Hill analysis (Lister and Hobbs, 1980), visco-plastic self-consistency modelling (Figure 6.6; Morales et al., 2011), deformation experiments (Heilbronner and Tullis, 2006; Dell'Angelo and Tullis, 1989) and natural examples (e.g. Law et al., 2010; Toy et al., 2008), as well as CPO development in other minerals such as olivine (Hansen et al., 2014; Kaminski and Ribe; 2001; Bystricky et al., 2000) and calcite (Barnhoorn et al., 2004). In order for CPO strength to be used as a strain proxy, other factors that may influence CPO development need to be shown to have been ineffectual. Such factors include variations in lithology, the presence of pre-existing CPO (Toy et al., 2008), and changes in deformation temperature (Jessell and Lister, 1990), deformation mechanism (Kilian et al., 2011), strain-rate (Tullis et al., 1973), 3D strain type (Lister and Hobbs, 1980) and the action of fluids (Jung and Karato, 2001).

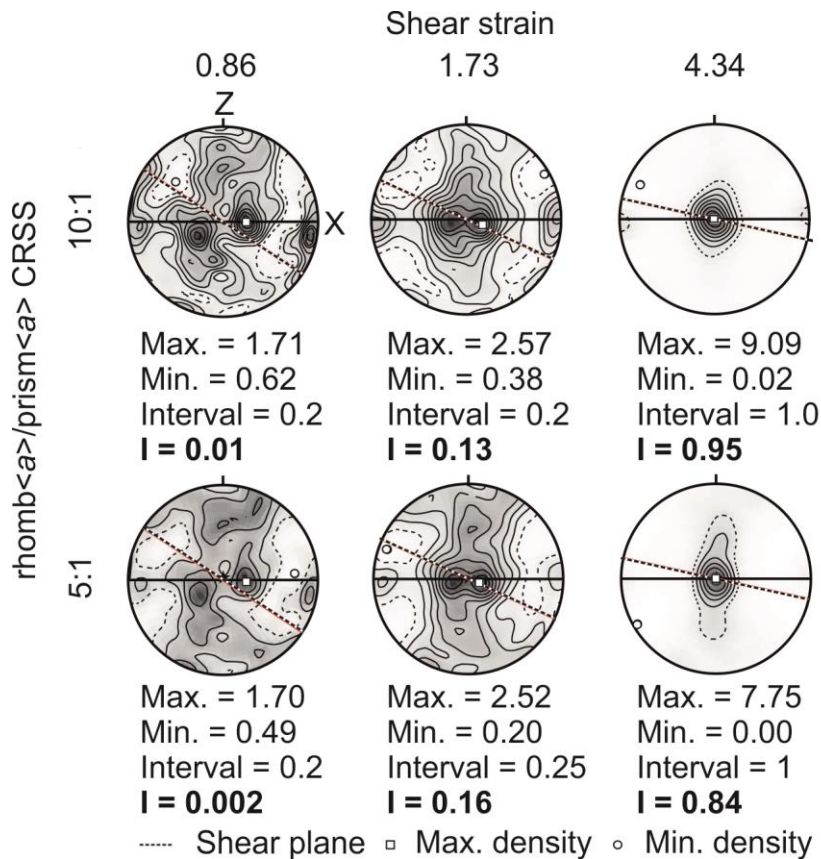


Figure 6.6 Examples of variation in quartz *c*-axes CPO intensity with increasing simple shear strain from viscoplastic self-consistency modelling. Rhomb *a*/prism *a* CRSS is the ratio of critical resolved shear stress for the rhomb *a* and prism *a* slip systems, i.e. increasing deformation temperature. (*c*-axes maxima parallel to the Y kinematic direction become pronounced by shear strains of 1.73 and are well defined by shear strains of 4.34. Increased activity of the rhomb *a* slip system (rhomb *a*/prism *a* = 5:1) results in the (*c*-axes Y maximum extending towards the Z kinematic direction at higher strains. Contouring is multiples of uniform distribution. From Morales et al. (in review). Also given are CPO intensities calculated according to Eqn.1. For additional details of the VPSC method see Morales et al. (2011).

Samples of the main Miocene leucogranitic plutons (Nubra-Siachen leucogranite, Tangtse-Darbuk leucogranite, South Tangtse granite and Muglib dome), taken furthest from the adjacent fault strands at their margins, show a lack of CPO development (Figure 6.4), suggesting that these intrusions had no CPO prior to deformation within the KFZ. This is not necessarily the case for the older lithologies which may have experienced pre-KFZ deformation. However, these make up a smaller proportion of the dataset (6/46 samples) and their microstructure, CPOs and structural

position are consistent with their CPOs being dominated by KFZ deformation.

The short duration of ductile KFZ deformation and limited range of temperatures indicated by both optical quartz microstructures and CPOs (Sections 5.2.2 and 5.2.3.3) indicate that the main phase of ductile KFZ deformation occurred within a relatively restricted range of temperatures (c. 500-550°C) and that changes in deformation temperature (potentially resulting in changes in active slip system) did not cause significant changes in quartz CPO geometry. There is some experimental evidence from quartz c-axis opening angles that higher strain rate has a similar effect to lower temperature on CPO development (Law, 2014; Kruhl, 1998; Gleason et al., 1993; Tullis et al., 1973). If changes in temperature or strain rate were to affect CPO development within the KFZ mylonites then these effects should both be most pronounced in the shear zone centres where strain rates and down-temperature overprinting would be expected to be greatest. This is especially true because higher strain rate and lower temperature act in the same sense on quartz CPO. As argued above however, the relative uniformity of CPO topology within the mylonites indicates that even the combined effects of any reduced temperature and increased strain rate within the shear zone were insufficient to result in CPO transitions.

Changes in deformation mechanism can also influence CPO development (e.g. Kilian et al., 2011). The quartz deformation mechanisms within the KFZ are however well constrained as being dislocation creep and dynamic recrystallisation with a component of fluid assisted diffusive mass transfer throughout the deformed zones (Section 6.2.2, Chapter 3). Grain boundary sliding, which is capable of dramatically modifying CPO (Kilian et al., 2011; Fliervoet et al., 1997), is probably precluded by the highly irregular and interlocked nature of the quartz grain boundaries.

The strain geometry within the KFZ is difficult to quantify precisely due to the absence of markers of known initial geometry. Nonetheless the predominance of S-L tectonites within deformed zones throughout the KFZ (Chapters 2 and 3) suggests approximately plane strain deformation. The shear is assumed therefore to be primarily simple shear, broadly consistent

with the dominantly strike-slip faulting regime. As foliations are typically stronger than lineations within the fault rocks (i.e. S>L tectonites), there may also be a subordinate component of flattening strain resulting from pure shear or general shear deformation, as may be expected in a zone of transpression such as the Pangong Transpressional Zone. This effect may also be due however to the general paucity of elongate minerals within the granitoids, such that lineations are not strongly recorded. It is also worth noting that it is not possible to estimate the average strain across the ductile shear zones of the KFZ from offset markers because the finite offset has been accommodated not only by mylonitic deformation but also by lower temperature deformation mechanisms as the exposed structural level was exhumed (Chapter 3). The amount of offset accrued during early ductile deformation cannot be back-calculated because the slip-rate may have changed during the history of the KFZ.

Fluid inclusions in quartz are common and widespread across the KFZ (Mukherjee et al., 2012), and it is therefore assumed that quartz within all samples was affected by some degree of hydrolytic weakening (Holyoke and Kronenberg., 2013; Kronenberg and Tullis, 1984). Hydrolytic weakening has been reported to promote prism (c) slip over prism <a> slip (Morgan and Law, 2004), although the general absence of CPOs resulting from prism (c) suggests that this was either not the case or was insignificant within the KFZ.

Quartz CPO may be expected to develop differently in lithologies with significantly different mineralogies and mineral distributions. The quartz CPO in the KFZ dataset are all measured on granitoids with the exception of one quartzite (Table 6.1). In these samples quartz occurs as a volumetrically significant phase (typically 20-35% in the granitoids) and typically occurs in similar distributions (i.e. polycrystalline blebs, ribbons and/or bands depending on degree of deformation) throughout the sample set. Other quartz-bearing lithologies with significantly different mineral proportions/distributions (primarily metapelites, Chapter 3) were excluded from the CPO strength analysis. The effects of excluding these lithologies on the results are discussed below (Section 6.4.2). The above considerations

support the assumption that variation in finite strain is the only significant control on CPO intensity within the sample set.

6.3.2 Quantifying Quartz CPO strength

Several measures of CPO strength have been proposed in the literature. The most commonly used parameter is the ‘J-index’ of Bunge (1982), which can be used to quantify the strength of bulk CPO (J) or individual components/directions (pfJ) based on the 3D orientation distribution function. Skemer et al. (2005) noted several drawbacks of the J-index and proposed a measure of bulk CPO strength based on the distribution of uncorrelated (random-pair) misorientation angles, termed the ‘M-index’ (M).

An alternative approach is to use eigenvector-based analyses.

Eigenvectors/eigenvalues can be used to describe spherical distributions for a range of geological purposes (Woodcock, 1977) based on the orientation tensor of the measurements in question (Scheidegger, 1965). The magnitudes of the three principle eigenvectors are the eigenvalues (E_{1-3} , $E_1 \geq E_2 \geq E_3$) and describe a distribution as follows (Woodcock, 1977). E_1 is an estimate of the mean of the distribution, E_3 is an estimate of the pole to the best fit girdle of the distribution and E_2 is mutually perpendicular to E_1 and E_3 . Three distinct eigenvalue-based methods for quantifying the strength of distributions have been proposed; the ‘strength parameter’ (C; Woodcock, 1977), the ‘intensity parameter’ (I; Lisle, 1985) and the ‘random parameter’ (R; Vollmer, 1990) or similarly 1-R (Barth et al., 2010). The derivations of these three measures from the three orthogonal normalised principle eigenvalues, and their ranges, are summarised in Table 6.3.

Parameter	Reference	Equation number	Equation	Range (weak to strong CPO)
Strength (C)	Woodcock (1977)	(6)	$C = \ln(E_1/E_3)$	0 - ∞
Intensity (I)	Lisle (1985)	(7)	$I = 7.5(E_1^2 + E_2^2 + E_3^2 - 1/3)$	0 - 5
Random (R)	Vollmer (1990)	(8)	$R = 3E_3$	1-0
1-R	Barth et al. (2010)	(9)	$1-R=1-3E_3$	0-1

Table 6.3 Summary of eigenvalue-based CPO strength parameters.

As quartz CPO are characterised by complicating effects of symmetrical multiplicity for all directions other than {0001}, measures that can be applied to individual crystal directions (pfJ and eigenvalue-based methods) are preferred over measures of bulk CPO (J and M). For instance, the trigonal symmetry of quartz results in three positive *a*-axes, (2-1-10), (-1-120) and (-12-10), for each crystal. As such, two samples may have the same *c*-axis CPO but different *a*-axis CPO, giving different bulk CPO strengths and also different strengths for the *c*-axis and *a*-axis CPO components within each sample. The strength of CPO for any direction other than {0001} will always be lower than for {0001} due to the symmetrical multiplicity of other directions. In order to simplify the comparison between samples, and to maximise the range of the calculated strength parameters, *c*-axis CPO were used to calculate C, I, 1-R and pfJ (Table 6.3) for the 46 samples from two transects across the KFZ in the Nubra and Tangtse regions (Table 6.4, Figures 5.2 and 5.10).

For unit axis $\pm\mathbf{h}$ in the pole figure $P(\mathbf{h}, \circ)$, pfJ is defined as

$$pfJ = \int |P(\mathbf{h}, \mathbf{r})|^2 d\mathbf{r} \quad \text{Equation 10}$$

with

$$d\mathbf{r} = \sin \alpha \, d\alpha \, d\beta / 4\pi \quad \text{Equation 11}$$

being a rotationally invariant infinitesimal surface element described by the polar angle (α) and azimuthal angle (β) in the ranges 0-180° and 0-360° respectively (Mainprice et al., in press; Bunge, 1982).

Sample	Ref. fault strand	Distance from ref. strand (m, NE +ve)	E ₁	E ₂	E ₃	I	C	1-R	pfJ
NUBRA TRANSECT									
Tirit Granite (T.G.)									
W11/45	Nubra	-4550	0.41	0.31	0.28	0.07	0.38	0.16	1.23
Nubra-Siachen Leucogranite									
W11/29	Nubra	0	0.64	0.25	0.11	1.16	1.77	0.67	2.47
W11/25	Nubra	35	0.51	0.29	0.20	0.37	0.91	0.39	1.41
W11/20	Nubra	70	0.58	0.25	0.17	0.73	1.26	0.50	2.11
W11/44	Nubra	750	0.53	0.32	0.15	0.56	1.28	0.56	1.66
W11/42	Nubra	1450	0.50	0.30	0.20	0.34	0.91	0.40	1.49
W11/41	Nubra	1890	0.43	0.32	0.26	0.11	0.51	0.23	1.27
W11/58	Nubra	5070	0.43	0.34	0.24	0.13	0.57	0.28	1.32
W11/54	Nubra	5150	0.54	0.24	0.21	0.50	0.94	0.36	1.69

Sample	Ref. fault strand	Distance from ref. strand (m, NE +ve)	E ₁	E ₂	E ₃	I	C	1-R	pfJ
Arganglas Diorite (A.D.)									
W11/47	Nubra	6200	0.45	0.29	0.25	0.17	0.58	0.24	1.13
TANGTSE TRANSECT									
Taruk Leucogranite (T.Lgr.)									
W11/129	Tangtse	-2510	0.53	0.25	0.22	0.45	0.90	0.16	1.54
W11/123	Tangtse	-2330	0.49	0.35	0.17	0.38	1.06	0.67	1.80
Taruk Amphibolite									
W11/121	Tangtse	-2330	0.47	0.34	0.19	0.30	0.92	0.39	1.40
South Tangtse Granite									
W11/120	Tangtse	-2330	0.47	0.34	0.19	0.28	0.88	0.50	1.44
W11/122	Tangtse	-2330	0.44	0.36	0.20	0.21	0.76	0.56	1.31
W11/124	Tangtse	-2330	0.49	0.32	0.19	0.35	0.97	0.40	2.46
W11/119	Tangtse	-2230	0.44	0.36	0.20	0.22	0.79	0.23	1.77
W11/116	Tangtse	-1940	0.50	0.26	0.23	0.33	0.77	0.28	2.56
W11/127	Tangtse	-1710	0.48	0.35	0.17	0.38	1.07	0.36	1.72
W11/126	Tangtse	-1690	0.50	0.29	0.21	0.33	0.84	0.24	1.71
W11/115	Tangtse	-1540	0.43	0.34	0.23	0.14	0.60	1.00	1.90
W11/114	Tangtse	-990	0.38	0.37	0.25	0.09	0.43	0.35	1.80
W11/113	Tangtse	-840	0.48	0.35	0.17	0.35	1.02	0.49	1.97
W11/112	Tangtse	-560	0.47	0.32	0.21	0.24	0.79	0.44	1.51
W11/125	Tangtse	-250	0.48	0.35	0.17	0.37	1.06	0.42	2.13
W11/83	Tangtse	-140	0.60	0.25	0.16	0.82	1.34	0.39	2.43
W11/110	Tangtse	0	0.66	0.21	0.14	1.19	1.56	0.44	2.32
Tangtse-Darbuk Leucogranite (T.D.L.)									
W11/91	Tangtse	50	0.65	0.27	0.07	1.30	2.17	0.40	2.76
W11/101	Tangtse	180	0.67	0.26	0.07	1.41	2.28	0.30	3.02
W11/109	Tangtse	390	0.68	0.22	0.09	1.43	1.98	0.50	2.86
W11/102	Tangtse	690	0.67	0.21	0.12	1.33	1.75	0.36	2.68
W11/66	Tangtse	1420	0.51	0.31	0.18	0.42	1.05	0.30	1.92
Pangong Transpressional Zone									
W11/67	Tangtse	1770	0.41	0.31	0.29	0.06	0.35	0.25	1.08
W11/69	Tangtse	2220	0.71	0.16	0.13	1.60	1.73	0.48	2.81
W11/71	Tangtse	2490	0.42	0.34	0.25	0.11	0.52	0.37	1.75
W11/63	Tangtse	3280	0.70	0.18	0.12	1.51	1.76	0.50	3.52
W11/61	Tangtse	3580	0.52	0.25	0.23	0.38	0.82	0.53	3.01
W11/60	Tangtse	3820	0.56	0.27	0.17	0.62	1.20	0.58	1.73
W11/78	Tangtse	4490	0.53	0.26	0.21	0.44	0.94	0.78	1.60
W11/73	Tangtse	4900	0.64	0.21	0.14	1.11	1.51	0.79	4.42
W11/74	Tangtse	4900	0.39	0.34	0.27	0.06	0.37	0.72	1.39
W10/27	Tangtse	5470	0.46	0.29	0.25	0.19	0.63	0.65	1.35
W10/26	Tangtse	5630	0.45	0.29	0.26	0.15	0.55	0.46	1.28
Muglib Dome (M.D.)									
W10/24	Tangtse (Pangong)	6210 (-990)	0.38	0.35	0.27	0.05	0.34	0.14	1.31
W10/21	Tangtse (Pangong)	6650 (-600)	0.38	0.34	0.28	0.04	0.30	0.62	1.18
W10/11	Tangtse (Pangong)	7020 (-10)	0.50	0.29	0.20	0.35	0.90	0.26	1.46

Table 6.4 Reference fault strands, profile distances, normalised quartz (*c*)-axes eigenvalues and the I, C, 1-R and pfJ values used to construct Figures 5.10 and 5.11.

Figure 6.7 shows how C, I, 1-R and pfJ describe the variations in quartz *c*-axis CPO strength across the KFZ. The small range of 1-R (Table 6.3) makes it less suitable for emphasising variations in CPO strength than the other three parameters (Figure 6.7). pfJ on the other hand is highly sensitive to localised maxima within the orientation distribution function, causing it to overestimate the strength of weak CPOs defined by fewer larger grains, such as in the relatively undeformed granitoids (e.g. samples W11/114 and W11/115, Figures 5.5 and 5.10, Table 6.4, Section 6.2.3.3). The eigenvalue-based approaches are less sensitive to this problem as they essentially smooth the distribution. The intensity parameter (I) has an advantage over the strength parameter (C) in that it is less biased towards certain distribution shapes (e.g. point or girdle) than the alternative eigenvalue-based 'strength' parameter (Lisle, 1985; Woodcock, 1977). The intensity parameter is chosen therefore as providing the best representation of variations in the degree quartz *c*-axis CPO development.

The intensity parameter (Lisle, 1985) is based on Mardia's uniformity statistic (Mardia, 1972) and is calculated from the normalised magnitudes of the three principle eigenvectors of a distribution (Equation 7, Table 6.3). Intensity ranges from zero ($E_{1-3}=1/3$, uniform distribution) to 5.00 ($E_1=1$, $E_{2,3}=0$, unimodal cluster). Assuming a random initial distribution of quartz crystal orientations, low CPO intensities are interpreted to indicate an undeformed or low strain sample, whereas higher intensities indicate more deformed samples. Importantly, samples that lack significant quartz deformation microstructures in thin section (e.g Figure 6.2) all have quartz *c*-axes CPO intensities of <0.2 , whereas samples that do show significant deformation microstructures all have intensities >0.2 . Consequently, $I=0.2$ is taken as a practical threshold between undeformed ($I<0.2$) and deformed ($I>0.2$) granitoid samples for these lithologies in this setting and deformation conditions (Figure 6.8).

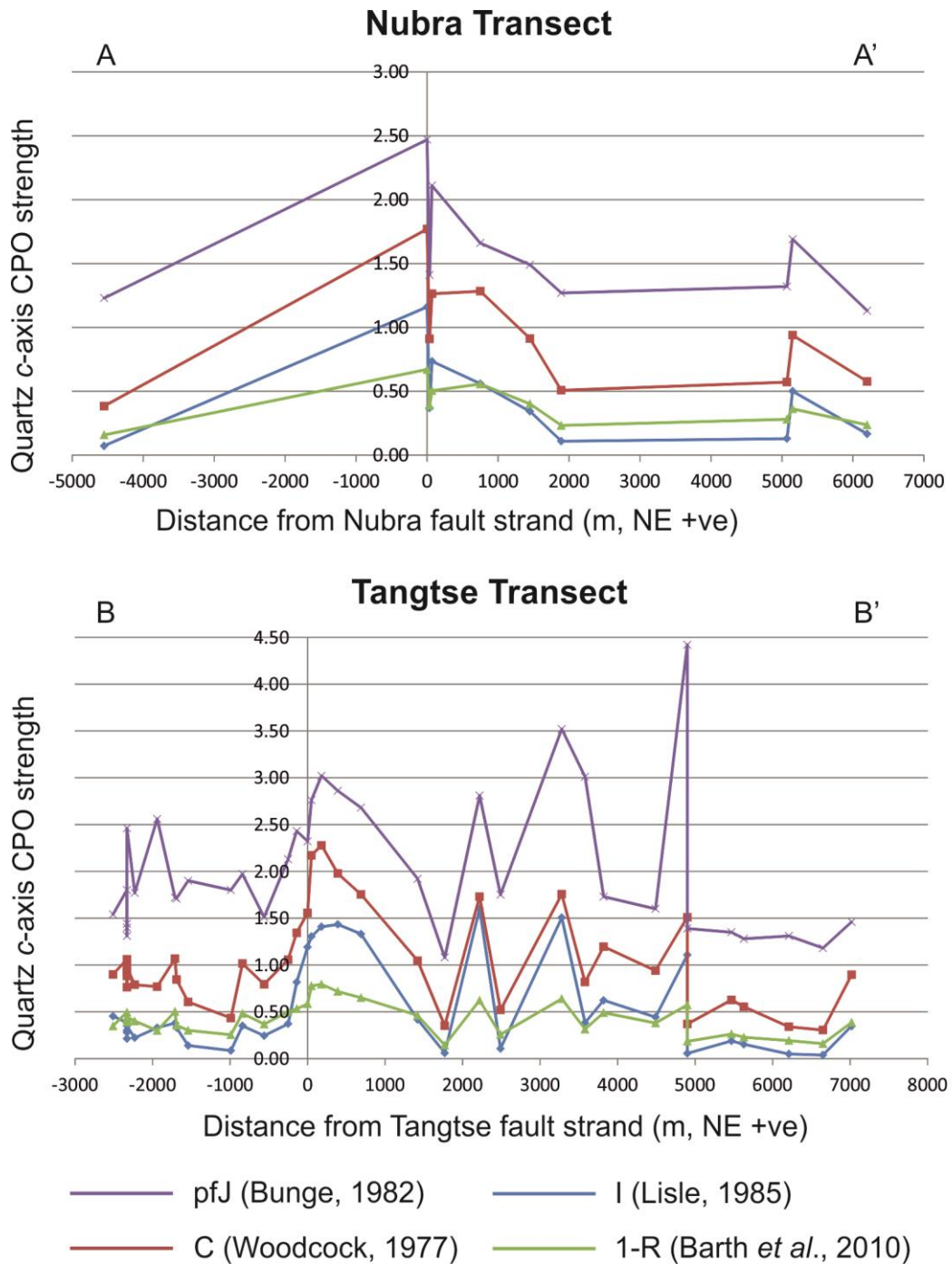


Figure 6.7 Comparison of different measures of quartz *c*-axis CPO strength for profiles A-A' and B-B' in the Nubra and Tangtse areas respectively (Figure 6.1).

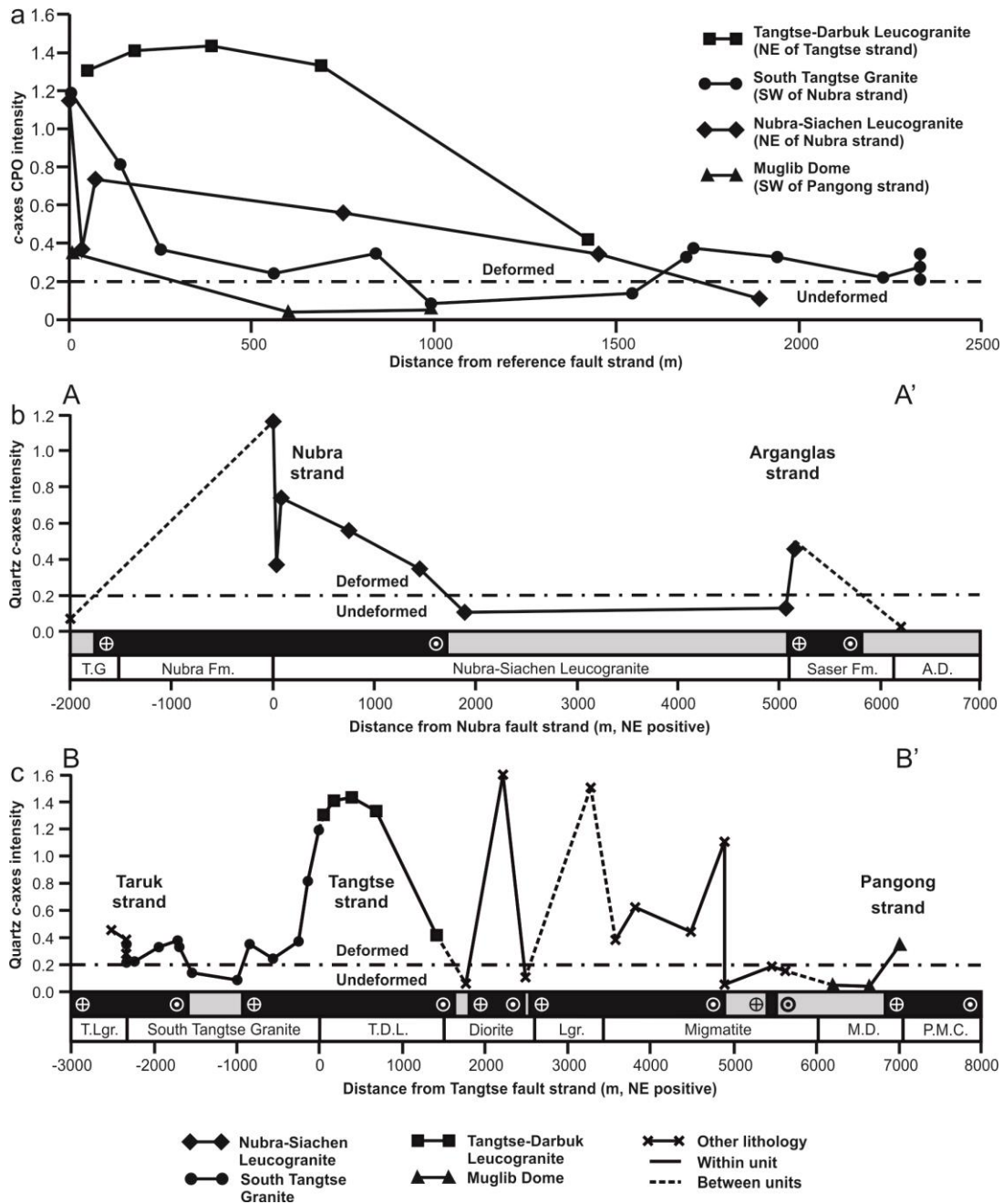


Figure 6.8 Variation in quartz *c*-axes CPO intensity (I, Lisle, 1985) as a proxy for strain. a) 15.1-18.5 Ma plutons. Adjacent to their nearest fault strands the plutons have high CPO intensities reflecting high strain. Decreasing CPO intensity over c. 300-1700 m from the fault strands indicates a decrease in strain. Away from the fault strands three plutons reach an undeformed state. The Tangtse-Darbuk leucogranite would be expected to reach an undeformed state if was 100 m wider in this section. The South Tangtse granite is undeformed in its central portion (c. 900-1600 m) with deformation confined to two fault strands (Tangtse and Taruk) at its margins. b) Nubra transect. c) Tangtse transect. P.M.C-Pangong Metamorphic Complex. Deformed regions are marked black and undeformed regions marked grey. Also shown is a simplified section of lithological units. Unit abbreviations in b) and c) according to Table 6.4.

6.4 Ductile Strain Distribution Within the Karakoram Fault Zone

The CPO intensity data are considered first in terms of the Miocene granitoids only and second in terms of the whole sample set. Separate consideration of the Miocene granitoids is important in order to provide a CPO-based determination of the age relationship between the KFZ and the intrusions. In doing so, further constraints can subsequently be placed on the depth of deformation (Section 6.5). Consideration of the whole dataset provides a proxy for the strain distribution across the KFZ.

6.4.1 Strain Distribution Across Miocene Intrusions

The four main Miocene plutons (Nubra-Siachen leucogranite, Tangtse-Darbuk leucogranite, South Tangtse granite and Muglib dome) all show strong strain gradients towards the adjacent KFZ fault strands (Figure 6.8a). CPOs within the fault strands show development of *c*-axes maxima sub-parallel to Y and *a*-axes in approximately XZ girdles with weak maxima sub-parallel to X, typical of prism-*a* slip (Figures 6.4 and 6.8). Several samples show slight elongation of the *c*-axes Y maxima towards the Z direction (Figure 6.4 and 6.8), indicating activity of the rhomb-*a* slip system. These CPO are typical of lower amphibolite grade deformation (Toy et al., 2008) and corroborate the microstructural temperature estimates of 500-550°C (Section 6.2.2; chapters 3 and 4; Wallis et al., 2013). No evidence for prism-*c* slip (i.e. *c*-axes maxima parallel to X), which occurs at near solidus temperatures (Toy et al., 2008; Mainprice et al., 1986), was found in these units, even in samples where lower amphibolite grade overprinting is absent (Figures 6.4 and 6.8). The presence of distinct strain gradients (Figure 6.8a) linking undeformed regions to regions deformed by prism-*a* slip, together with the absence of near-solidus prism-*c* slip (Figures 6.4 and 6.9), demonstrates that the granitoids were not emplaced within an active shear zone(s) and cooled to ambient lower amphibolite grade temperatures (500-550°C) prior to deformation within the KFZ. The Miocene leucogranites are therefore pre-kinematic with respect to the KFZ, which must have initiated after *c.* 15.6 Ma, contradicting suggestions that it initiated as early as 19-32 Ma (e.g. Boutonnet et al., 2012). These findings support the notion that the

strain distribution recorded by crystal plastic deformation of quartz across the KFZ formed within a relatively restricted time interval between c. 15.7-13.7 Ma (Phillips et al., 2004). This limits a problem that would be present in many other fault zones of having to decipher a strain distribution accrued over a more protracted evolution with potentially multiple phases of activity/reactivation.

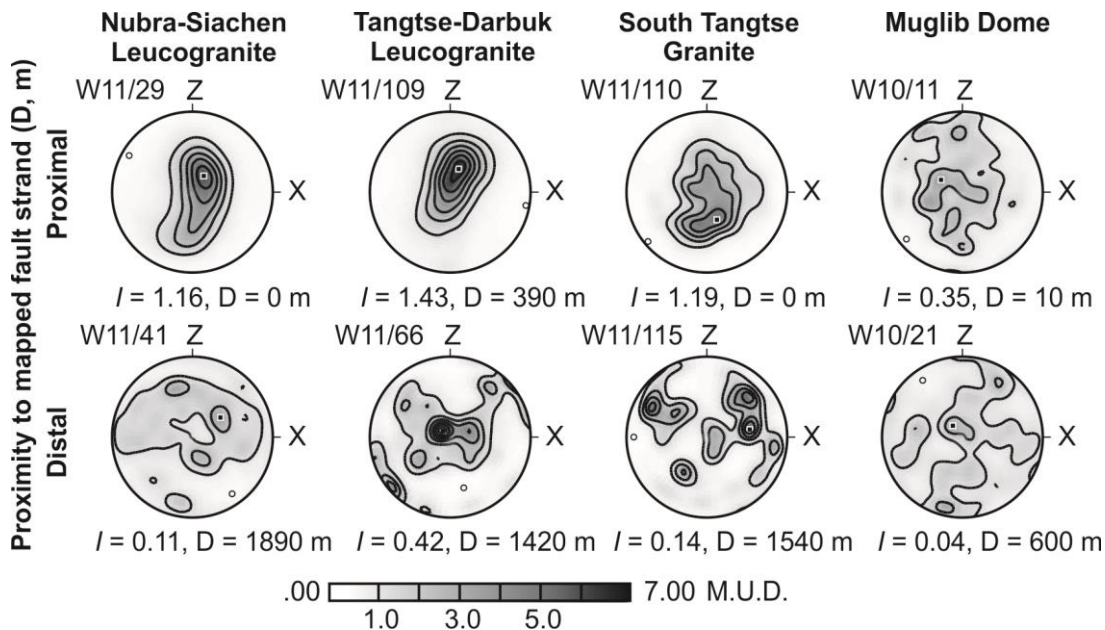


Figure 6.9 Quartz *c*-axis (0001) pole figures from four granitoids deformed by KFZ shear zone strands plotted in the kinematic reference frame (X = lineation, Z = pole to foliation). For each granitoid, a sample close to, and far from, the present day trace of KFZ fault strands is shown. Samples close to fault strands have high CPO *intensity* (*I*), whereas those furthest away have lower *intensity*. Contours in multiples of uniform distribution (M.U.D.).

6.4.2 Strain Distribution Across the Karakoram Fault Zone

The distribution of CPO intensity across the KFZ provides a proxy for the strain distribution formed at 500-550°C (Figure 6.8). It should be emphasised that these strain distributions record the early phase of quartz crystal plastic deformation in the mylonites constrained to c. 15.7-13.7 Ma (Phillips et al., 2004) and largely prior to the onset of deformation by frictional sliding on micaceous foliae in the most deformed samples (Chapter 3). The locations of high CPO intensity regions show a close correlation to the mapped distribution of shear zones across the KFZ (Figure 6.1, Phillips 2008). However, the CPO intensity profiles (Figure 6.8) provide new information on

the widths of the deformed zones, the relative deformation intensity in each strand and the internal deformation gradients.

In order to 'calibrate' quartz *c*-axis CPO intensity as a fully quantitative strain proxy, strain must be determined by an independent method. There are three possible approaches applicable to the deformed granitoids, as follows.

- 1) Finite strain could be estimated from the change in geometry of deformed quartz blebs and ribbons in the same samples from which the CPO measurements were taken (e.g. Menegon et al., 2008). This would require sectioning of the specimens in known orientations relative to the deformation kinematics, which would be potentially problematic for low strain samples where foliation and lineation are weakly recorded. It would also require statistically relevant sample sets of quartz regions, which would require large sample volumes, particularly for coarse grained low strain samples. It would have however the advantage of providing a relatively direct measure of the component of bulk rock strain that specifically affected the quartz.
- 2) Rock deformation experiments could be used in theory to deform samples to known shear strains and the quartz *c*-axis CPO intensity could then be determined. There are however several draw backs to this approach. The behaviour of quartz during deformation of polymineralic rocks is likely to be sensitive to rock type/mineral content (e.g. Menegon et al., 2008). The experiments to calibrate this dataset should therefore ideally be performed on samples of the same lithology and any subsequent new datasets should be calibrated per lithology. Given the coarse grain size of the granitic protoliths (e.g. <2 cm feldspar megacrysts) it is also unlikely that sufficient volume of material could be deformed in experimental apparatus to reproduce the range of local (grain scale) conditions experienced by quartz during natural deformation that contribute to the bulk measured CPO. In addition, recent re-analysis of comparisons between natural and experimental quartz deformation microstructures suggests that deformation experiments are unable to achieve deformation by subgrain rotation and grain boundary migration dynamic

recrystallisation as seen in natural fault rocks (Law, 2014; Stipp et al., 2010). It seems unlikely therefore that it would be possible to replicate the KFZ quartz deformation in rock deformation experiments.

- 3) An alternative approach is to model the quartz CPO response to imposed deformations up to known strains. One method would be to use visco-plastic self-consistency (VPSC) modelling, which is capable of simulating a range of strain geometries and magnitudes with the effects of temperature incorporated by varying the relative CRSS of each slip system (e.g. Figure 6.6; Morales et al., 2011, in review). VPSC modelling may also be used to simulate deformation of polyphase aggregates (e.g. Wenk et al., 1991), including quartz-muscovite mixtures (Canova et al., 1992). VPSC analysis of quartz is however still at a developmental stage (e.g. Morales et al., 2011, in review), cannot incorporate the effects of dynamic recrystallisation and would require rigorous testing against well constrained experimental and/or natural fault rocks.

These possible approaches demonstrate that there is potential for quartz CPO intensity to be fully calibrated for finite strain. However, each approach has drawbacks that place it beyond the scope of the present study. As such the CPO intensity profiles provide an indicative measure of the relative strain across the KFZ.

An important caveat to this analysis and Figure 6.8 is the potential for strain partitioning into the metasedimentary lithologies of the Eastern Karakoram Metamorphic Complex which form the central portions of each fault strand (Chapters 2 and 3). Localisation of the KFZ fault strands along these bands of metamorphics suggests that such strain partitioning has indeed occurred (Chapter 3). These lithologies are not amenable to the same analysis for direct comparison to the deformed granitoids due to the potential for quartz to have behaved differently within the metasediments (Chapter 3). The abundant mica in the metapelites has pinned the quartz grain boundaries and prevented grain growth. The quartz distribution within the metapelites also differs from the granitoids in that it is distributed throughout a mixture of feldspar and micas rather than occurring in distinct bands or pods as it does

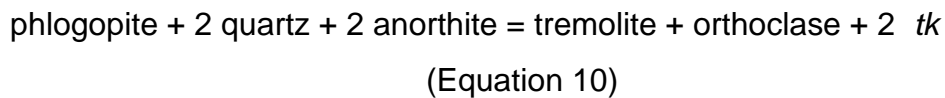
in the granitoids. In particular, a significant amount of deformation may have been accommodated by the micas in the metapelites, whereas quartz was the weakest volumetrically significant phase in the granitoids, at least prior to the formation of interconnected micaceous layers (Chapter 3). It can be assumed therefore that significant strain was also accommodated within the metasedimentary lithologies, potentially more so than in the granitoids. However, this behaviour remains poorly constrained. Nonetheless, the strain distributions presented in Section 6.4 give a unique insight into the distribution of deformation within the granitic lithologies of the KFZ.

6.5 Constraints on the Depth of Deformation

Section 6.4.1 demonstrated that emplacement of the main Miocene intrusions was pre-kinematic with respect to the KFZ. As the region has only been exhumed since their emplacement (Boutonnet et al., 2012; Mukherjee et al., 2012; Dunlap et al., 1998), the emplacement depths of the intrusions also provide maximum depths for the KFZ deformation affecting them. It is theoretically possible to determine emplacement depths for peraluminous garnet 2-mica leucogranites (i.e. the Nubra-Siachen, Tangtse-Darbuk and Muglib dome leucogranites) using garnet-biotite-muscovite-plagioclase or muscovite-biotite-alkali feldspar-quartz geobarometry (Anderson, 1996). The low proportions of garnet, biotite and muscovite present in the leucogranites mean however that it is not easily possible to find suitable quantities of the necessary minerals in close proximity to gather the required quantity of compositional data. The hornblende-bearing STG allows an alternative approach based on Al-in-hornblende geobarometry (e.g. Anderson and Smith, 1995; Schmidt, 1992).

Al-in-hornblende geobarometry is based on the empirical increase in total Al content of hornblende (Al^{tot}) with increasing pressure (Hammarstrom and Zen, 1986). Schmidt (1992) outlined the theoretical basis of Al-in-hornblende geobarometry based on the phase rule as follows. Amphibole-bearing intermediate igneous rocks can be described by the ten component system $SiO_2 - TiO_2 - Al_2O_3 - Fe_2O_3 - FeO - MgO - CaO - Na_2O - K_2O - H_2O$. Therefore a nine-phase tonalite, composed of hornblende + biotite + plagioclase + orthoclase + quartz + titanite + Fe-Ti-oxide + melt + fluid, is a

trivariant system. The three intensive variables, oxygen fugacity, temperature and pressure, can be taken as the three degrees of freedom. Pressure is left as the only unconstrained variable when temperature is close to the nearly isothermal solidus (Hollister et al., 1987) and oxygen fugacity is buffered by a second Fe-Ti-oxide or epidote. Al^{tot} variation is controlled primarily by *tschermak* exchange (*tk*) which may be buffered by the reaction



(Schmidt, 1992; Hammarstron and Zen, 1986). The Al-in-hornblende geobarometer of Schmidt (1992) is calibrated for the above mineral assemblage under water-saturated conditions in the temperature range 655-700°C and pressures of 250-1300 MPa. The relationship between pressure (P) and Al^{tot} under these conditions can be described by the equation

$$P (\pm 60 \text{ MPa}) = 4.76 Al^{tot} - 3.01 \quad (r^2 = 0.99) \quad (\text{Equation 11}).$$

Major element data were gathered from five hornblende grains in sample P141 of the South Tangtse Granite using the Jeol 8230 electron microprobe at the University of Leeds for pressure estimation using the calibration of Schmidt (1992) (Table A.2). Operating conditions were 15kV accelerating voltage, 15 nA probe current, focussed beam with peak and baseline count times of 20 s and 10 s respectively. Sample P141 comes from the SW margin in the Tangtse fault strand. Deformation within the sample has been accommodated by dynamic recrystallization of quartz and feldspar at temperatures insufficient for recrystallization of hornblende, which remains intact and euhedral. The major element chemistry of the hornblendes is therefore inferred not to have been modified during deformation. Analyses were made on transects across five amphibole grains (Figure 6.10) and rim points adjacent to a range of minerals. Results show moderate non-systematic variation in Al content in the grain transects (Figure 6.10). Hornblende rim compositions in equilibrium with the last phase to crystallise (i.e. quartz) are most likely to record final pressure during emplacement (Reichardt and Weinberg, 2012; Johnson and Rutherford, 1989). Thus, only

analyses of hornblende rims adjacent to quartz (Table A.2) were used to estimate the emplacement pressure. The compositional data were recalculated to give cations per 23 O (i.e. excluding volatiles) to be consistent with the calibration of the Al-in-hornblende geobarometer (Schmidt, 1992). Al-contents of amphibole rims adjacent to quartz are 1.58 ± 0.17 (2σ) Al per 23 oxygens. Previous studies on the generation of Miocene hornblende bearing granitoids within the Pangong Transpressional Zone (PTZ) indicate that they were generated by water fluxed melting at low temperatures of $<700^\circ\text{C}$ (Reichardt et al., 2010). This suggestion is supported by amphibole-plagioclase thermobarometry of a migmatite restite (W11/73) in the PTZ, showing that anatexis occurred at $688 \pm 44^\circ\text{C}$ and 522 ± 91 MPa. The PTZ migmatites are interpreted to be representative of the source region for the larger Miocene plutons (Reichardt and Weinberg, 2012; Reichardt et al., 2010). As such, the STG melts are assumed never to have reached temperatures of more than a few 10s of degrees above their wet solidus, consistent with the $645\text{-}700^\circ\text{C}$ calibration of the Schmidt (1992) geobarometer. The effect of temperature on the Al content of hornblende is not considered therefore in this study (consistent with previous geobarometry on granitic bodies in the region, Reichardt and Weinberg, 2012).

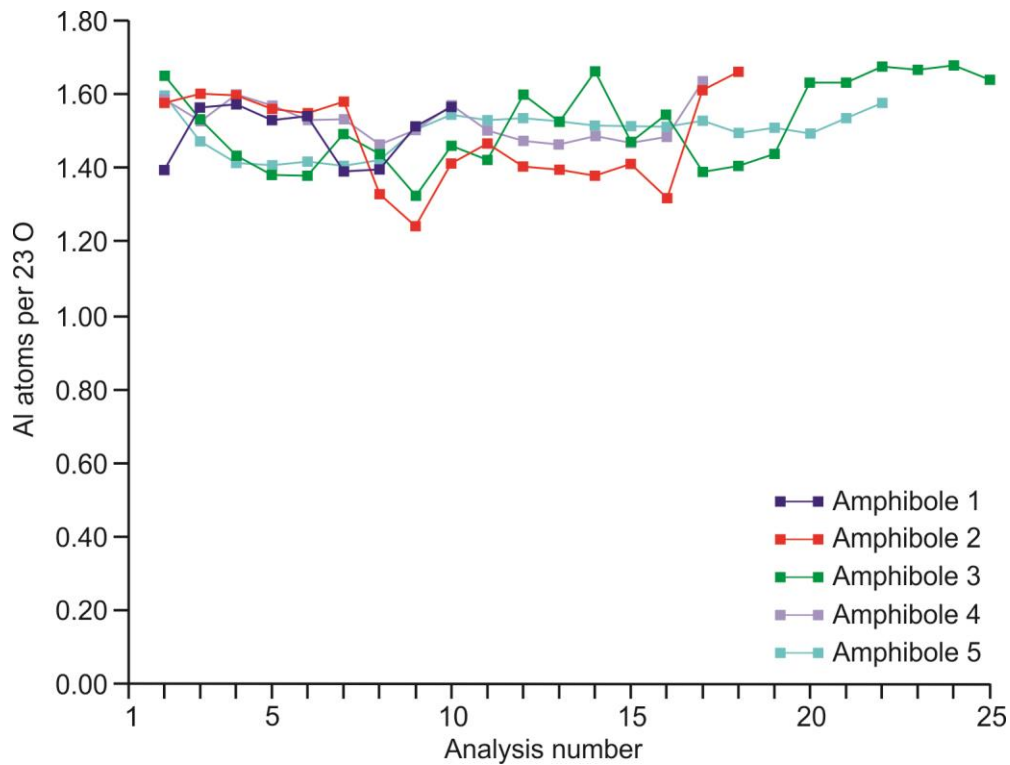


Figure 6.10 Al-content in electron microprobe transects across 5 amphibole grains in sample P141 of the South Tangtse granite.

Al-in-hornblende geobarometry (Schmidt, 1992) on hornblende rims adjacent to quartz within the STG yields a mean crystallisation pressure of 448 ± 100 MPa (quadratic error of ± 60 MPa calibration error and ± 80 MPa two standard deviations of individual measurements). Assuming a crustal density of 2.75 g/cm^3 and that the amphibole rims crystallised at or near the final emplacement depth, this pressure constrains STG emplacement to 16.6 ± 3.7 km depth. This is therefore the maximum depth for STG deformation exhibited at the exposed structural level. As the STG was emplaced at 16.6 ± 3.7 km depth at 17.12 ± 0.06 Ma (Phillips, 2004) the average exhumation rate since that time is 1.0 ± 0.2 km/Myr. Thus, the exposed structural level would have been at depths of c. 15 km when the ductile KFZ deformation initiated between 15.6-13.7 Ma (Phillips et al., 2004). Deformation temperatures of 500-550°C at this depth indicate a geothermal gradient of approximately 33-37°C/km during the mid-Miocene. This geothermal gradient estimate is consistent with the estimate from amphibole-plagioclase thermobarometry of migmatite restite W11/73 of $36 \pm 7^\circ\text{C/km}$ (Section 4.4.1).

6.6 Discussion

6.6.1 Implications for the Age, Thermal Regime and Strain Rate of the KFZ Shear Zone

6.6.1.1 Age of the KFZ

As discussed previously (Chapters 1-4), considerable debate has taken place regarding the timing of initiation of the KFZ (e.g. Wang et al., 2009, 2011, 2014; Phillips et al., 2004, 2013; Boutonnet et al., 2012; Leloup et al., 2011; Searle et al., 2011; Zhang et al., 2011; Valli et al., 2008; Phillips and Searle, 2007; Lacassin et al., 2004; Searle, 1998). The results presented in this chapter provide the following crucial evidence demonstrating that the major c. 22-15 Ma leucogranitic intrusions (Nubra-Siachen leucogranite, Tangtse-Darbuk leucogranite, South Tangtse granite and Muglib dome) were not emplaced within an active shear zone and that the KFZ initiated after their full crystallisation and cooling to ambient lower amphibolite grade conditions.

The four main Miocene plutons show strong strain gradients from their margins ($I=0.35-1.43$) to portions more distal to the KFZ shear zones ($I=0.04-0.42$), with the Nubra-Siachen leucogranite, South Tangtse granite and Muglib dome containing undeformed portions ($I=0.04-0.14$). This fulfils a key criterion for the identification of pre-kinematic granitoids that have solidified prior to shear zone initiation by localised solid-state deformation (Phillips and Searle, 2007; Paterson and Tobisch, 1988; Oliver and Wall, 1987; Lamouroux et al., 1980).

CPOs within the deformed zones are dominated by (c)-axes close to Y and, in some instances, extending towards Z. This indicates that the strain profiles formed predominantly by prism $\langle a \rangle$ slip with subordinate rhomb $\langle a \rangle$ slip, under conditions close to the greenschist-amphibolite facies transition (c. 500-550°C). The deformation recorded by the granitoids therefore occurred in the solid state at temperatures identical to those in the wall rocks (e.g. Chapter 3; Wallis et al., 2013; Phillips and Searle, 2007).

The major plutons show an absence of (c)-axes parallel to the X kinematic direction indicative of deformation by prism (c) slip, even in portions unaffected by lower temperature solid state deformation. In these regions

there is no potential for near-solidus deformation to have been obscured by lower temperature overprinting. They were therefore not pervasively deformed in a partially molten or near-solidus solid state where prism (c) slip is active (Blumenfeld et al., 1986; Mainprice et al., 1986). These units also lack a continuous transition between widespread (sub)magmatic deformation to localised solid state deformation, which is an important criterion for recognition of synkinematic granitoids (Phillips et al., 2007; Paterson et al., 1989, 1998; Pe-Piper et al., 1998).

U-Pb zircon ages show that the larger of the plutons took up to c. 6 Myrs to construct (e.g. c. 22-16 Ma for the Tangtse-Darbuk leucogranite, Phillips et al., 2004, 2013; Boutonnet et al., 2012; Searle et al., 1998). It is unlikely that the KFZ could have been temporarily inactive during this time, given the long-term consistency of kinematic boundary conditions in the region (Copley et al., 2010). It is therefore highly unlikely that the intrusions have failed to document near-solidus deformation due to temporary inactivity of a longer-lived KFZ shear zone.

These findings are consistent with the interpretations put forward in Chapters 3 and 4, based on granitoid deformation microstructures and andalusite porphyroblast microstructures respectively, that the KFZ initiated after emplacement, solidification and cooling of the main Miocene plutons. Such lines of evidence support the findings of Phillips et al. (2004) that the Nubra and Tangtse strands initiated after solidification of the 15.9 ± 0.1 Ma Nubra-Siachen leucogranite and 15.6 ± 0.7 Ma Tangtse-Darbuk leucogranite respectively. Similarly, the CPO data support the interpretations that the Pangong strand crosscuts the 15.1 ± 0.6 Ma Muglib dome and that the Arganglas strand crosscuts the NE margin of the 15.9 ± 0.1 Ma Nubra-Siachen leucogranite and therefore initiated after these times (Phillips et al., 2013). These findings militate against previous suggestions that the KFZ initiated as early as 19-34 Ma as a long-lived and stable structure of the India-Asia collision zone (Sen et al., 2014; Boutonnet et al., 2012; Leloup et al. 2011; Valli et al., 2007, 2008; Lacassin et al., 2004).

6.6.1.2 Strain Rate Within the KFZ Shear Zone

The distribution of deformation across the KFZ revealed by CPO intensity (Figure 6.8) has important implications for the “quartz-strain-rate-metry” (QSR) approach to determining shear zone strain rates and the degree of strain localisation within the continental crust, recently proposed by Boutonnet et al. (2013). The QSR approach aims to infer the strain-rate of quartz deformation by the following workflow:

- 1) Interpret the dominant recrystallisation mechanism,
- 2) estimate deformation temperature,
- 3) measure the recrystallised grain size distribution,
- 4) choose a palaeopiezometer-flow law combination from the 22 possible pairs available by choosing the pair that gives the closest match to the independently estimated strain-rate of the Ailao Shan-Red River shear zone (piezometer of Shimizu, 2008, and flow law of Hirth et al., 2001),
- 5) estimate the flow stress from the recrystallised grain size using the piezometer,
- 6) estimate the strain rate from the deformation temperature and flow stress using the flow law.

The Ailao Shan-Red River shear zone was chosen to ‘calibrate’ the QSR approach because it has independent strain-rate estimates for certain outcrops (Sassier et al., 2009), potentially allowing selection of a palaeopiezometer-flow law combination that reproduces these strain-rates. The applicability of the chosen pairing to other outcrops or shear zones is however highly uncertain due to potential variations in the physical and chemical conditions of deformation. Two further general problems with the QSR approach are that (1) Ti-in-quartz geothermometry used by Boutonnet et al. (2013) is still at a developmental stage, with significant doubts remaining about its applicability to temperatures below 500°C where Ti diffusion is slow (Law, 2014; Morgan et al., 2013; Grujic et al., 2011) and (2) no attempt seems to have been made to constrain the extent to which strain-rates affecting quartz relate to those independently known for the bulk shear zone in the original calibration. The latter point means that the choice of flow law-palaeopiezometer pair may be highly unreliable as the quartz may have

experienced a higher or lower strain rate than the bulk shear zone if quartz was deforming respectively more quickly or slowly than other mineral phases in the rock. Despite the considerable uncertainties introduced at each step, Boutonnet et al. (2013) apply the QRS approach to attempt to estimate the strain rates inside and outside the Ailao Shan-Red River and KFZ shear zones (Figure 6.11). Using these strain rates and their estimates of the shear zone widths they calculate estimates for the shear zone shear-rates (c. 11 mm/yr for the KFZ). By comparing the shear zone strain-rates ($>1 \times 10^{-13} \text{ s}^{-1}$) with those in the adjacent wall rocks ($<1 \times 10^{-15} \text{ s}^{-1}$) they also infer a high degree of strain localisation within the shear zones (Figure 6.11).

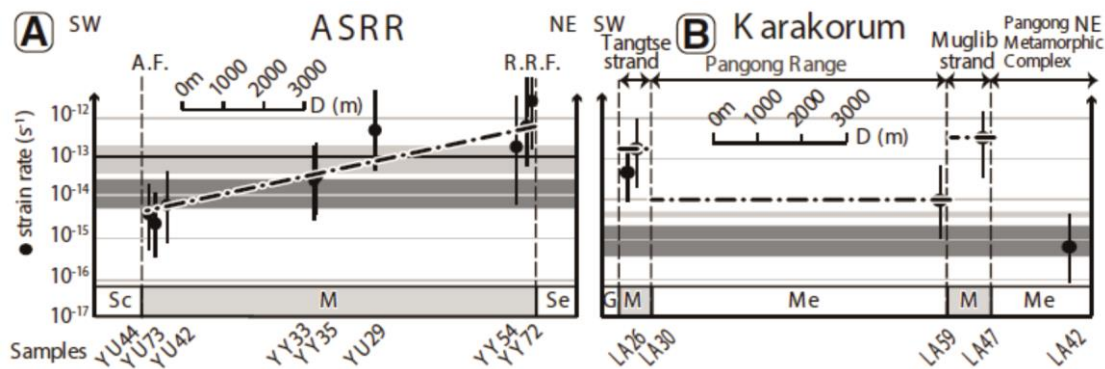


Figure 6.11 Quartz-strain-rate-metry results after Boutonnet et al., 2013, Figure 5. Dot-dashed lines indicate shear rate profiles used for the calculation of integrated shear rates. (A) Ailao Shan-Red River shear zone: light and dark grey horizontal bands indicate bulk strain rates calculated for a 10 km wide shear zone, respectively for fast fault slip rates between 2.8 and 5.3 cm/yr, or slow ones between 0.5 and 1.4 cm/yr. (B) Karakoram shear zone: light and dark grey horizontal bands indicate bulk strain rates calculated for an 8 km wide shear zone, respectively for fast fault slip rates between 0.7 and 1.1 cm/yr, or slow ones between 0.1 and 0.5 cm/yr. Sc-schist, M-mylonites, Se-sediments, G-undeformed granite, Me-metamorphic.

The KFZ analysis of Boutonnet et al. (2013) is based however on measurements from only five samples and estimates of the widths of the Tangtse and Pangong strands. Even if the QSR method is taken at “face value”, the CPO-derived strain profile for the Tangtse area (Figure 6.8c) shows several fundamental flaws in the QSR analysis, relating to the shear zone strain distribution, as follows.

- 1) The estimated widths of the fault strands are inaccurate: the Tangtse strand is actually c. 2.5 km wide rather than c. 0.8 km; the Pangong

strand deforms a c. 0.2 km width of granitic material rather than c. 1 km)

- 2) The degree of deformation, and therefore most likely also strain-rate, within individual fault strands is highly variable and gradational (best exemplified by the Tangtse strand). The 1-2 samples per fault strand used by Boutonnet et al. (2013) are therefore insufficient to determine the integrated strain-rate within an individual strand.
- 3) Deformation in the section is partitioned across 5-6 main strands of the KFZ shear zone, each of varying width and deformation intensity. The two strands used by Boutonnet et al. (2013) are therefore insufficient to determine the integrated strain-rate across the entire KFZ shear zone.

In summary, the complexity of deformation revealed by variations in CPO intensity shows that the 'quartz-strain-rate-metry' approach of Boutonnet et al. (2013), based on only 5 samples, cannot provide an accurate integrated strain rate across the KFZ, or comparable shear zones. If the analysis is to work at all it needs considerably larger datasets.

6.6.1.3 Thermal Regime During KFZ Deformation

As discussed previously in Chapters 3 and 4, the metamorphic petrology and thermobarometry results of Rolland and Pêcher (2001) and Rolland et al. (2009) appear to suggest apparent geothermal gradients of >40 °C/km, 38-52 °C/km and 24-37 °C/km respectively for granulite, amphibolite and greenschist facies metamorphism within the PTZ. The authors interpret these results to indicate high geothermal gradients resulting from shear heating and synkinematic magma advection within the KFZ. However, as shown in Chapter 4, upper amphibolite grade metamorphism, anatexis and leucogranite emplacement pre-date the KFZ and, as shown in Chapter 3, KFZ deformation occurred during exhumation, cooling and retrograde metamorphism. Amphibole-plagioclase thermobarometry on a c. 17 Ma migmatite restite (W11/73) indicates an apparent geothermal gradient of $36 \pm 7^\circ\text{C}$ (Chapter 4) shortly prior to KFZ initiation at c. 15 Ma. The deformation temperature estimates and barometric depth constraint for the KFZ deformation (Section 6.5) suggest that the KFZ deformation occurred under a geothermal gradient of approximately 33-37°C/km between 15.7-

13.7 Ma (Phillips et al., 2004). Whilst the latter estimate should be treated with caution due to the uncertainties associated with both the temperature and depth estimates, this result is consistent with the migmatite thermobarometric estimate and the estimate for greenschist facies metamorphism of Rolland et al., 2009. These results also suggest however, that higher geothermal gradients estimated for amphibolite and granulite facies metamorphism by Rolland and Pêcher (2001) and Rolland et al. (2009) either a) represent pre-KFZ metamorphic events, b) over estimate the temperature or under estimate the pressure or c) a combination of both a) and b). The results presented in chapters 4 and 5 suggest that the latter is the case.

6.6.2 Relationship to Other Faults and Implications for Fault Modelling

6.6.2.1 Comparison to Other Faults

In the Eastern Karakoram, partial melting was occurring throughout the early to mid-Miocene at temperatures of $<700^{\circ}\text{C}$ (Phillips et al., 2013; Reichardt et al., 2010), equivalent to <20 km depth, and deformation was widespread throughout this low viscosity crustal layer (Phillips et al., 2013). Meanwhile, simultaneous melting occurred at c. 850°C and somewhat greater depths of >25 km in the central Karakoram (Searle et al., 2010), showing that Miocene crustal melting in the Eastern Karakoram was not a localised phenomenon. The strain profiles presented in this study (Figure 6.8) represent therefore the deformation that occurred in an important structural transition zone between more localised deformation within the shallower frictional-viscous transition zone and the deeper pervasively deforming, partially molten mid-crust (c. 20 km depth). A range of geophysical and geological observations indicate that a weak, partially molten layer is present at similar depths beneath at least some parts of Tibet today (e.g. Wang et al., 2012; Klemperer, 2006). Wang et al. (2012) reported 1.5-9.0 Ma peraluminous rhyolites from the vicinity of the Kunlun Fault in northern Tibet and interpreted them to indicate the presence of a partially molten mid-lower crustal layer beneath northern Tibet. This raises the possibility that the crustal viscosity structure of the Eastern Karakoram and the exhumed

structure of the KFZ may be highly analogous to other major strike-slip faults in northern Tibet, such as the Kunlun, Altyn Tagh, Karakax and Longmu-Goza Co faults, all of which are seismically active (Wang and Wright, 2012; Wang et al., 2012).

Having occurred at 500-550°C on a relatively high geothermal gradient of c. 35°C/km, the measured distribution of KFZ ductile deformation that occurred at c. 15 km depth could be comparable to that at greater depths of 20-22 km in regions with a lower geothermal gradient of 25°C/km. However, regions outside orogenic plateaus, with thinner crust and lower geothermal gradients, likely lack a partially molten mid-lower crustal layer. It remains unclear how the absence of an underlying partially molten layer of distributed deformation would structurally affect shallower portions of a shear zone. The implications of the findings presented in Chapters 3-5 for understanding of strike-slip faults in Tibet and other settings are explored further in Chapter 6.

Comparable systematic studies of shear zone strain distributions with good depth constraints from other tectonic settings are rare. Systematic CPO analysis of mylonites exhumed by the transpressive plate boundary Alpine Fault, New Zealand, do appear to have a simpler, more localised structure (Figure 6.12a; Toy et al., 2008). CPOs within the hanging wall of the Alpine Fault indicate prism <a> slip (i.e. deformation conditions broadly comparable to the KFZ mylonites) in a zone of only c. 300 m structural thickness (Figure 6.12a; Toy et al., 2008), significantly more localised than even a single strand of the KFZ (Figure 6.8). However, the significant component of reverse slip on the Alpine fault may have resulted in asymmetry and/or truncation of the exposed strain profile.

The strike-slip Kuckaus mylonite zone, Namibia, formed under similar retrograde amphibolite-greenschist conditions and is 1-1.5 km in width (Figure 6.12b; Rennie et al., 2013). Kuckaus mylonite zone strain profiles based on qualitative assessment of proto- to ultra-mylonitic deformation fabrics (Figure 6.12b) display a similar, albeit more condensed, distribution to the KFZ profiles (Figure 6.8) with strain distributed across multiple anastomosing strands of varying intensity (Rennie et al., 2013).

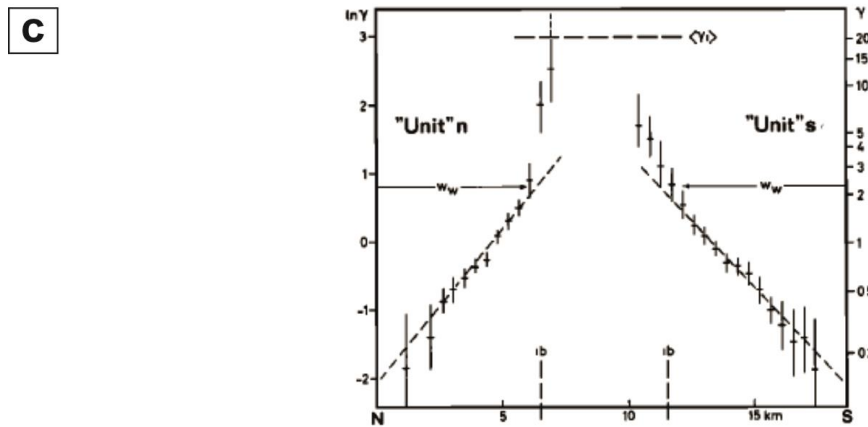
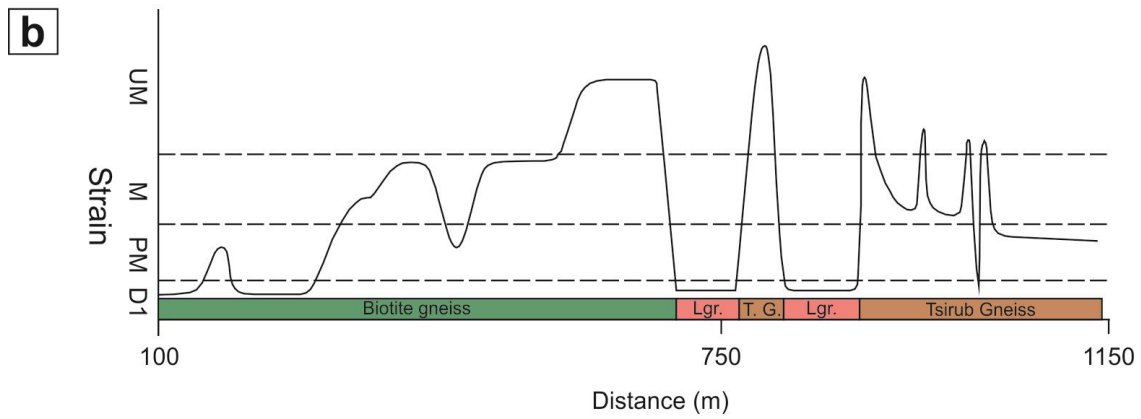
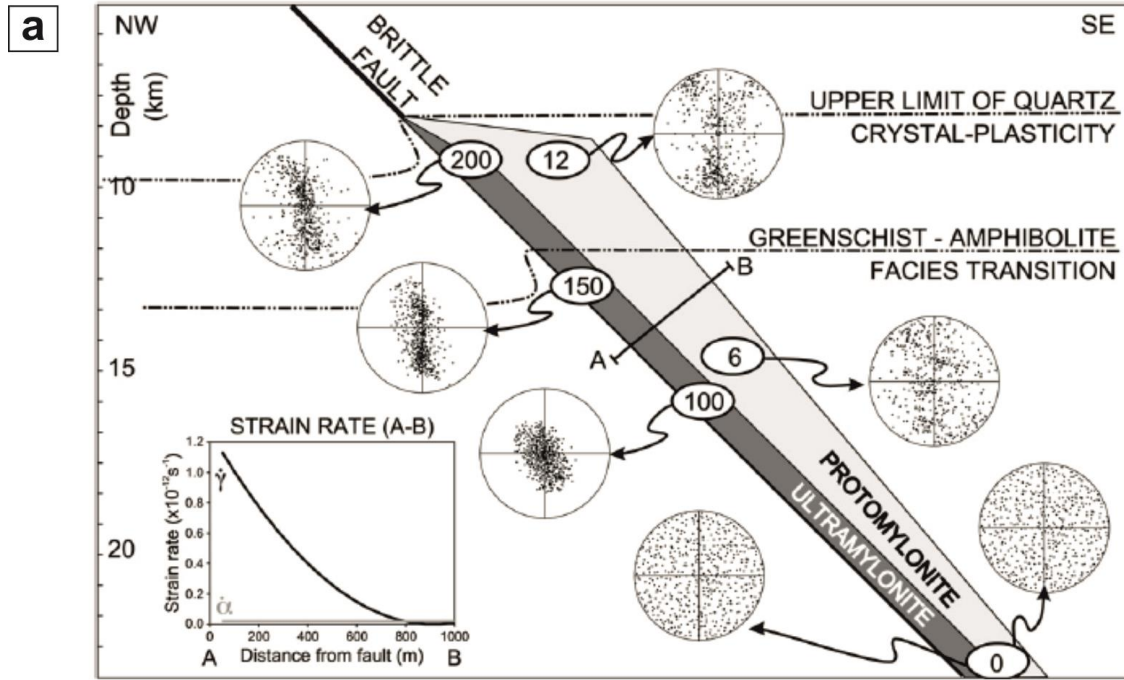


Figure 6.12 Published strain profiles across predominantly strike-slip shear zones discussed in the text. a) Cartoon illustrating strain and CPO development during exhumation and cooling within the Alpine Fault, New Zealand from Toy et al. (2008). Finite strain estimates in white ellipses and inset strain rate graph are from Norris and Cooper (2003). Pole figures show contrasting quartz c-axis CPO development in protomylonites and ultramylonites. b) Qualitative strain profile across the Kuckaus mylonite zone, Namibia, from Rennie et al., 2013, based on the distribution of protomylonitic (PM), mylonitic (M) and ultramylonitic (UM) reworking of pre-existing fabrics (D1). c) Quantitative strain profile across the Nordre Strømfjord, Greenland, based on rotated strike lines (Sørensen, 1983). lb-inner boundary. Ww-width of strain weakening zone.

Strain has been quantified in the crustal-scale Nordre Strømfjord (Sørensen, 1983) and Ikertôk (Grocott and Watterson, 1980) shear zones in Greenland that were deformed at conditions close to the amphibolite-granulite transition. These are approximately 20-45 km in width and wider than the 10-12 km total width of the KFZ. The Nordre Strømfjord shear zone has an offset of 120 km, comparable to the KFZ and reaches shear strains up to 20 in its inner portion (Figure 6.12c; Sørensen, 1983). However the method of measuring deflected strike lines from aerial photographs (Sørensen, 1983) lacks the resolution to distinguish individual strands comparable to Figure 6.8.

Based on the cross-sectional strain profile of the Nordre Strømfjord shear zone, which shows an internal high strain plateau region, Sørensen (1983) proposed a model of shear zone growth whereby strain hardening within the shear zone and weakening at its margins promotes widening of the shear zone by preferential deformation of marginal material (Figure 6.12c). The well-defined curve of strain intensity over the Tangtse strand of the KFZ (Figure 6.8c) precludes application of this model to the Tangtse strand. This difference may be due to the lower deformation temperature of the KFZ and the onset of weakening within the KFZ (Chapter 3). The Ikertôk shear zone has an offset of 48 km and shows an heterogeneous strain distribution revealed by changes in fold interlimb angles and axes plunges (Grocott and Watterson, 1980). Multiple high strain strands of the shear zone reach shear strains of between 5 and 14.5 (Grocott and Watterson, 1980).

Clearly, significant variations in fault zone structure exist, not only with changing deformation depth, but also between shear zones formed at similar

metamorphic grades. A variety of factors other than the pressure-temperature conditions of deformation can affect fault zone evolution and structural development, including the role of fluids, metamorphic processes, lithological factors and pre-existing tectonic fabrics (Chapter 3; Rutter et al., 2001). Future geological investigations should aim therefore to characterise shear zone strain distributions by the most quantitative methods applicable, coupled with constraining the controls on shear zone structure and evolution.

6.6.2.2 Implications for Fault Modelling

The crustal structure of the eastern Karakoram portion of the KFZ, with a brittle upper-crustal fault rooting into a zone of distributed deformation in a partially molten weak layer, lends support to models of earthquake cycle deformation in Tibet that include a mid-crustal weak layer (DeVries and Meade, 2013). Such models have been successful in reproducing surface deformation before and after the 1997 Manyi and 2001 Kokoxili earthquakes in Northern Tibet (DeVries and Meade, 2013). However, as such models demonstrate the sensitivity of surface deformation to the deep structure and viscosity of fault zones (see also Yamasaki and Houseman, 2012), improved results may potentially be achieved by incorporating geological constraints on the complexity of shear zone structure.

The KFZ strain distribution (Figure 6.8) shows that models of fault mechanics that assume a single localised shear zone beneath active faults may be oversimplified. Fault zone processes are typically modelled using a single planar discontinuity representing the brittle upper crustal fault, with or without using a rectangular/cuboid low viscosity region representing the underlying shear zone (Section 6.1). This simplified approach allows such models to provide insights into fundamental fault zone processes, such as stress transfer, earthquake nucleation/cyclicity and fault creep, using conceptually simple and computationally less demanding geometries (Cowie et al., 2013; Yamasaki and Houseman, 2012; Ellis et al., 2006; Malservisi et al., 2003). It is likely to be the case however that the complex models required to allow truly predictive interpretations of fault behaviour will require more rigorous, complex and well-constrained geological inputs, such as the KFZ deformation distribution investigated here (Figure 6.8).

6.7 Conclusions

Quartz deformation microstructures and crystallographic preferred orientations (CPO) preserve a record of the deformation conditions and distribution within the Karakoram Fault Zone (KFZ). These provide valuable information on the fault zone structure and may be used to constrain models of processes operating in active strike-slip faults. Quartz deformation microstructures and CPOs indicate that quartz deformation occurred predominantly by grain boundary migration dynamic recrystallisation and prism $\langle a \rangle$ slip with subordinate contributions from subgrain rotation dynamic recrystallisation and rhomb $\langle a \rangle$ slip. These combined deformation mechanisms suggest deformation temperatures of *c.* 500-550°C (i.e. close to the lower amphibolite-upper greenschist grade transition). The deformation temperatures are consistent with considerations based on deformation depth, Miocene geothermal gradient, timing of deformation and long term average exhumation rate.

Quartz (*c*)-axes CPO intensity can be used as a proxy for the magnitude of KFZ finite strain that affected Miocene granitoids and potentially older quartz-bearing lithologies. The distribution of quartz (*c*)-axes CPO intensity across the KFZ reveals that strain is heterogeneously distributed across multiple fault strands up to *c.* 3 km in width. Strong strain gradients across Miocene intrusions demonstrate the cross-cutting nature of the KFZ and that the fault initiated after their *c.* 15.7 Ma emplacement ages. Geobarometric determination of the 16.6 ± 3.7 km emplacement depth of the pre-kinematic 17.12 ± 0.06 Ma South Tangtse granite constrains the exhumation rate since the mid-Miocene to 1.0 ± 0.2 km/Myr and the formation of the strain profiles to *c.* 15 km depth. Overall, the results presented in this chapter have the following general implications.

- 1) The Miocene geothermal gradient during KFZ deformation was *c.* 36°C/km. Previous interpretations that shear heating elevated geothermal gradients to $>40^\circ\text{C}/\text{km}$ within the KFZ (Rolland et al., 2009; Rolland and Pêcher, 2001) are not supported by the observations and analysis in this study.

- 2) The “quartz-strain-rate-metry” (QSR) approach suggested by Boutonnet et al., (2013) must be applied to datasets large enough to characterise the complex and heterogeneous strain distribution across large scale shear zones in order to achieve potentially meaningful integrated shear-rate estimates. The five samples used by Boutonnet et al., for the KFZ are inadequate to characterise the deformation.
- 3) Models of fault zone processes that consider only a single uniform shear zone beneath active faults do not reflect the geological complexity of deformation at c. 500°C in faults similar to the KFZ. Such models may potentially be improved by incorporating more complex and realistic geological constraints.

7. The structure, strength and significance of continental strike-slip faults

Abstract

Synthesis of the results presented in previous chapters constrains the key characteristics of the Karakoram Fault Zone (KFZ) and allows its macroscopic architecture to be reconstructed from the exposed fault rock distributions. The KFZ is then used as an analogue for the mid-crustal portions of several major active strike-slip faults to provide insights to questions regarding their structure and deformation mechanisms, including seismogenic processes.

The KFZ initiated between 15.7 and 13.7 Ma. Older peak metamorphic assemblages, including migmatites, and leucogranite bodies are not the result of shear heating within the fault and it cannot have channelled leucogranite magmas before this time. The KFZ has subsequently deformed with an average strike-slip slip-rate of c. 8 mm/yr, resulting in an offset of c. 120 km in its central portion. The fault is therefore a relatively recent structure and can have accommodated only a limited amount of eastward extrusion of Tibet. The architecture of the KFZ is characterised by localised fault cores (<10 m thick) surrounded by broad damage zones (up to 2 km thick) within and above the frictional-viscous transition zone. At greater depths the fault rapidly broadens and branches downwards as ductile shear zones, each up to c. 3 km across at c. 15 km depth. The shear zones are inferred to merge into a broad (>10 km wide) zone within partially molten crust at c. 20 km depth.

Comparisons with the Altyn Tagh and Kunlun faults in Tibet suggest that the KFZ provides an analogue for the mid-crustal portions of seismogenic strike-slip faults in northern Tibet that are typically poorly resolved in magnetotelluric and seismic surveys. Evidence from the KFZ also supports hypotheses regarding the downward continuation of the San Andreas Fault into low friction gouge or phyllonite at <10 km depth and suggestions arising

from the Alpine Fault, New Zealand, that the seismic behaviour of such fault rocks is subject to a complex interplay of multiple controls.

7.1 Introduction

The aim of this thesis has been to investigate the structure, strength and tectonic significance of major continental strike-slip faults through the example of the Karakoram Fault Zone (KFZ) in Ladakh, NW India. The previous three chapters presented new results regarding the operative deformation mechanisms, shear strength and strain distribution within the fault zone and the relationships between faulting, metamorphism and magmatism in the region. This chapter provides a discussion of the implications and significance of these findings and, by using the KFZ as an exhumed analogue, explores questions arising from the study of other major strike-slip faults.

First, the role of the KFZ in accommodating deformation within the India-Asia collision zone is assessed based on the new evidence from this study. This constrains the key characteristics of the fault (e.g. age, offset, slip-rate, thermal state, depth extent) that are later required in to draw comparisons with other fault zones. Secondly, the macroscopic structure of the KFZ is synthesised from the evidence presented in previous chapters and considered in relation to its shear strength and deformation mechanisms. These features of the KFZ are then compared to other major strike-slip faults and used to address questions regarding their structure and seismogenic processes.

7.2 Characterising the Karakoram Fault Zone and its role in the India-Asia collision zone

The role of the KFZ in accommodating deformation in the India-Asia collision zone depends primarily on its age, offset, slip-rate and architecture (i.e. depth extent and deep structure). If the fault has been active for much of the time since the initial India-Asia collision (c. 52 Ma, Rowley, 1996) and has a large offset (e.g. >250 km) and rapid slip-rate (e.g. >10 mm/yr) then it could have accommodated several hundreds of kilometres lateral extrusion of

Tibet (Boutonnet et al., 2012; Valli et al., 2008; Lacassin et al., 2004; Leloup et al., 1999). If however the fault is a relatively recent (e.g. <16 Ma) structure of the collision zone and/or has had only a low slip-rate (e.g. <10 mm/yr) and offset (<150 km) then plate-like extrusion of Tibet cannot be a significant mechanism for accommodating India-Asia convergence (Wang et al., 2011, 2012; Phillips and Searle, 2007; Phillips et al., 2004; Searle et al., 1998). The results presented in Chapters 3-5 have a bearing on the age of the fault, the offset across it (and therefore its slip-rate) and whether or not it has generated significant shear heating (a prediction of models assuming localised deformation at high slip-rates, e.g. Leloup et al., 1999).

Two new lines of evidence presented in this thesis indicate that the KFZ initiated in, or propagated through, its central portion in Ladakh after the emplacement of several 22-16 Ma leucogranite plutons (Phillips et al., 2013). In Chapter 4 it was shown that andalusite porphyroblasts within the Nubra Formation result from contact metamorphism during emplacement of the adjacent 15.87 ± 0.08 Ma Nubra-Siachen leucogranite (Phillips et al., 2004). These porphyroblasts contain randomly oriented biotite inclusions or inclusion fabrics discordant to the matrix KFZ foliation. Such microstructural relationships indicate that any deformation resulting in biotite grain alignment prior to andalusite growth was not continuous with the KFZ deformation that affected the andalusites after their growth (e.g. Passchier and Trouw, 2005).

A complementary line of evidence is provided by the CPO intensity profiles presented in Chapter 6. Strong quartz CPOs within shear zones at the leucogranite margins decrease in intensity towards the pluton centres where near random CPOs are preserved and significant deformation microstructures are lacking. In addition, evidence of near-solidus deformation in quartz, such as “chessboard” extinction and/or prism (c) slip, are lacking, even outside the regions affected by lower temperature deformation.

The evidence provided by andalusite porphyroblast microstructures and CPO intensity profiles across the leucogranites indicates that KFZ deformation was not occurring at the time that the leucogranites were emplaced (e.g. Passchier and Trouw, 2005; Paterson and Tobisch, 1988;

Blumenfeld et al., 1986; Lamouroux et al., 1980). Thus, the KFZ was active either before leucogranite emplacement but transiently inactive whilst they were emplaced, or it initiated after emplacement of the main leucogranite plutons. As the kinematic boundary conditions (i.e. rate and orientation of India-Asia convergence) have remained relatively constant since at least c. 30 Ma (Copley et al., 2010), and leucogranite pluton emplacement occurred over a protracted c. 7 Myr period (Phillips et al., 2013), it is improbable that the leucogranites and associated contact metamorphism could have failed to record KFZ deformation due to a >7 Myr hiatus of activity. These lines of evidence support the hypothesis that the KFZ initiated after emplacement and solidification of the leucogranites since c. 15.7 Ma.

The maximum KFZ age constraint is provided by the Nubra-Siachen and Tangtse-Darbuk leucogranites, which give a maximum KFZ age of 15.68 ± 0.52 Ma (Phillips et al., 2004). The South Tangtse granite adds no further age constraint as it is older than these leucogranites (18.8-17.1 Ma; Boutonnet et al., 2012; Phillips, 2004). The Muglib dome on the other hand is potentially younger (15.1 ± 0.6 Ma; Phillips et al., 2013) but its age overlaps with the Nubra-Siachen and Tangtse-Darbuk leucogranites within error. In any case, the Pangong strand of the KFZ, which cross-cuts the Muglib dome, may have initiated after the Tangtse strand, which cross-cuts the Tangtse-Darbuk leucogranite, so again no further maximum age constraint is provided. A minimum age constraint for initiation of the KFZ is provided by discordant leucogranite dykes emplaced at 13.73 ± 0.28 Ma that cross-cut the KFZ mylonitic foliation (Phillips et al., 2004). Thus, having initiated at c. 14-15 Ma, the KFZ must be a relatively recent structure in the >50 Myr collision of India and Eurasia.

In Chapter 4, petrological, microstructural and thermobarometric results from each sub-unit of the Eastern Karakoram Metamorphic Complex were used to demonstrate that the late Mesozoic-Cenozoic poly-metamorphic/magmatic evolution of the Eastern Karakoram correlates with that of the central Karakoram in the Hunza and Baltoro regions. These results agree with those of Streule et al. (2009) from the Pangong Metamorphic Complex. The evolution of the Eastern Karakoram does not correlate however with the antiformal metasediments/mélange of the central-northern Qiangtang

terrane and the northern Karakoram terrane in the Pamir, both of which record primarily early Mesozoic tectono-metamorphic events (Pullen et al., 2011). These metamorphic considerations support a correlation between the Shyok and Bangong-Nujiang suture zones, which are offset by c. 120 km across the KFZ (Figure 2.1; Phillips et al., 2004). Concomitantly, they preclude correlation of the Rushan-Pshart and Bangong-Nujiang sutures and of the Shyok and Shiquanhe sutures (Figure 2.1; Valli et al., 2008; Lacassin et al., 2004), militating against the possibility of offsets in the range 250-1000 km (Valli et al., 2008; Lacassin et al., 2004; Peltzer and Tapponnier, 1988). These findings support the hypothesis that the KFZ can only have accommodated limited lateral extrusion of the Tibetan plateau (<150 km) in response to the India-Asia collision (Searle et al., 1998, 2011; Phillips et al., 2004).

The c. 15 Myr age of, and c. 120 km offset across the KFZ in Ladakh suggest an average slip-rate of c. 8 mm/yr in this central portion of the fault (Phillips et al., 2004; Searle et al., 1998). Such a slip-rate is considerably lower than the 20 mm/yr predicted by the analogue modelling of McCaffrey and Nabelek (1998) and the Quaternary slip-rate of 32 ± 8 mm/yr calculated by Liu (1993), which was inferred by Avouac and Tapponnier (1993) to support plate-like extrusion of the Tibetan plateau. The latter slip-rate was based on dating of a glacial moraine, but this was later shown to be incorrect by Brown et al. (2002), who revised the Quaternary KFZ slip-rate estimate to 4 mm/yr. The low long-term average slip-rate of c. 8 mm/yr in the central portion of the KFZ, indicates that the fault accommodates only a small proportion of the c. 40 mm/yr India-Asia convergence (Copley et al., 2010). Thus, lateral extrusion of the Tibetan plateau on the KFZ (e.g. Avouac and Tapponnier, 1993; Peltzer and Tapponnier, 1988) is not a major mechanism for allowing northward motion of India.

The related issues of the depth of penetration of the KFZ and whether or not it generates significant shear heating are also important factors for characterising the fault and its role in the India-Asia collision zone. Leloup et al. (1999) used finite difference steady-state thermomechanical modelling of a lithospheric-scale strike-slip fault to determine the maximum possible shear heating. For stiff lithosphere entirely cut by a fault with a friction

coefficient of 0.6 and in which all mechanical energy is dissipated as heat in both the frictional and viscous layers, they calculated that a temperature increase of 475°C could occur at 20 km depth. Rolland and Pêcher (2001) and Rolland et al. (2009) suggested that shear heating has resulted in upper amphibolite-granulite facies metamorphism within the KFZ and may have aided leucogranite melt generation. Several factors indicate however that this extreme case does not apply to the KFZ and that shear heating is not an important process within this fault zone.

The microstructural observations and mechanical inferences presented in Chapter 3 suggest that much of the fault rock has potential to have deformed with reduced friction coefficients (typically <0.4), thereby reducing the potential for frictional heat production. The modelling of Leloup et al. (1999) suggests that a friction coefficient of 0.3 would permit shear heating of only 180°C at 20 km depth, and even this would require a slip rate of 30 mm/yr, i.e. considerably faster than the c. 8 mm/yr of the KFZ (e.g. Searle *et al.*, 1998). Similarly, the observations emphasised in Chapters 3 and 5 that quartz and feldspar initially deformed by dynamic recrystallisation, indicates that a significant proportion of the mechanical energy in the viscous layer is stored as increased grain boundary surface area, rather than being dissipated as heat. The assumption of a stiff lithosphere is also challenged by the presence of migmatites that were shown in Chapter 4 to have formed at mid-crustal depths as shallow as c. 20 km.

The presence of migmatites at c. 20 km depths also raises questions about the maximum possible depth extent of the KFZ. Klemperer et al. (2013) used $^3\text{He}/^4\text{He}$ ratios in hydrothermal spring waters, which appear to spike across both the southern and central portions of the KFZ, to argue that the KFZ provides a conduit for fluids with a Tibetan mantle helium isotopic signature and that the KFZ must therefore cut the entire c. 70 km crustal thickness. Cross-sections based on shortening estimates across the NW Himalaya-Karakoram indicate that much of the KFZ must be underlain by underthrust Indian lithosphere, suggesting that the KFZ may be restricted to within the Asian crust (Searle et al., 2010). Klemperer et al. (2013) argue that only *actively* subducting Indian *lower* lithosphere beneath the KFZ would preclude the fault from accessing Tibetan mantle, and that Indian crust may

be stranded beneath western Tibet and cut by the KFZ down to Tibetan mantle beneath. The geodynamic feasibility of such a configuration remains poorly constrained. Vauchez and Tomassi (2003) argue, based on a review of exhumed lower-crustal shear zones, that strain localisation in partially molten material does occur. The presence of migmatites at 20 km depth beneath the trace of the KFZ, and elsewhere across the Karakoram, raises the possibility however that localised upper-crustal strike-slip deformation may be dissipated into a layer of broadly distributed deformation at mid-crustal depths. The lithospheric-scale fault used in shear heating models by Leloup et al. (1999) therefore may not be representative of the KFZ and this aspect of the fault architecture remains an important research goal.

Two other lines of evidence presented in this study indicate that the KFZ has not generated appreciable shear heating, at least not in quantities sufficient to result in prograde metamorphism or leucogranite generation. Firstly, evidence for synkinematic metamorphism presented in Chapters 3 and 5 shows that KFZ deformation was associated with retrogressive sericitisation and phyllonitisation rather than a prograde event. Secondly, new metamorphic and structural evidence presented in Chapters 4 and 5 indicates that the KFZ postdates emplacement of the main Miocene leucogranite plutons (see above). The main phase of leucogranite magmatism pre-dates therefore the initiation of the KFZ and cannot be the result of shear heating within it (Phillips et al., 2013). Neither can the vertical ascent of leucogranite magmas have been assisted by the fault zone, as suggested by Leech (2008), prior to c. 15.7 Ma (Parrish, 2009; Searle and Phillips, 2009).

In summary, this thesis presents several new geological constraints on age (i.e. leucogranite strain profiles, andalusite microstructures), offset (i.e. correlation of metamorphism in the eastern and central Karakoram) and thermal regime (i.e. thermobarometry) of the KFZ, thus allowing discrimination between differing interpretations of the role of the fault in the India-Asia collision zone. The KFZ has been active since c. 15 Ma with a long-term average slip-rate of c. 8 mm/yr and maximum offset of 150 km in its central portion. The depth extent of the fault is uncertain and may be >70 km or restricted to the upper-middle crust only, with the latter scenario

preferred. Shear heating has not had a significant impact on deformation processes within the KFZ. These findings support previous suggestions that the KFZ can have only facilitated a limited amount of eastward extrusion of the Tibetan plateau in response to the India-Asia collision (Wallis et al., 2014b; Phillips et al., 2004; Brown et al., 2002; Murphy et al., 2000; Searle et al., 1998).

7.3 Fault zone structure and strain accommodation

7.3.1 Structure and strength of the Karakoram Fault Zone

The central KFZ consists of a wide range of fault rocks inferred to have formed at 15 km to near surface depths (Chapters 2-6). The distribution of these fault rock types are described in detail in Chapters 2 and 3, Phillips and Searle (2007) and Rutter et al. (2007). In each fault strand, all deformation fabrics strike approximately parallel to the regional trend of the KFZ (140°). On the Nubra strand, protomylonitic-mylonitic textures are distributed over several hundred metres in the Nubra Formation and approximately 1.5 km into the Nubra-Siachen leucogranite (Chapters 3, 5 and 6), reaching a maximum intensity at the contact between the two (Chapter 6). These mylonitic fabrics are sequentially overprinted by bands of phyllonite and cataclasite approaching the contact (Chapter 5). Similar relationships are present on the Tangtse and Arganglas strands, although phyllonites have not been recognised on these strands and cataclasites are more limited. On the Pangong strand, granioids of the PTZ and marbles and schists of the PMC are mylonitised for several hundred metres across the contact of these units (Chapter 6; Phillips and Searle, 2007; Rutter et al., 2007). Again, the mylonites are overprinted by sequential down-temperature gouge and cataclasites (Chapter 3; Rutter et al. 2007).

The areal distribution of KFZ fault rocks and the general down-temperature overprinting nature of the suite (i.e. broad zones of mylonitic series overprinted by narrower phyllonites, cataclasites and gouges towards the active traces of the fault strands) indicate that they record ongoing deformation at a range of crustal depths (Chapters 2, 3, 5 and 6) during 1.0 ± 0.2 mm/yr regional denudation and exhumation (Chapter 6).

Geothermobarometry results from across the Eastern Karakoram Metamorphic Complex suggest an increase in peak metamorphic conditions from $622\pm 41^{\circ}\text{C}$ and $>650\text{ MPa}$ in the Nubra Formation in the NW to $736\pm 47^{\circ}\text{C}$ and $1059\pm 219\text{ MPa}$ in the PMC in the SE (Chapter 4). However, this metamorphism and associated deformation predates the KFZ (Chapter 4) and therefore regional differential exhumation may have occurred prior to KFZ initiation. More local differential exhumation associated with the KFZ is evidenced by the juxtaposition of Miocene upper amphibolite grade migmatites in the PTZ against older amphibolites of broadly similar grade in the adjacent PMC (Chapter 4). This increased exhumation, localised adjacent to the major step-over in the KFZ, is likely to be the result of transpressional fault motion. However, the highest temperature deformation microstructures unequivocally attributable to the KFZ are ubiquitously lower amphibolite grade (Chapter 3) and, further, thermochronology results across the region suggests a relatively uniform pattern of exhumation across the central KFZ since the mid-Miocene (Boutonnet et al., 2012; Bhutani et al., 2003; Dunlap et al., 1998). These considerations suggest that whilst regional scale differential exhumation may have occurred across the eastern Karakoram prior to KFZ initiation, exhumation during motion on the KFZ has been relatively uniform, with the exception of slightly increased rates within the PTZ. Exhumation across the central KFZ region is therefore inferred to be dominated by erosion rather than tectonic denudation. This interpretation is supported by detrital material, attributable to a source in the Karakoram by Nd and Pb isotope analysis, in the bedload of the Indus river, into which the Shyok river flows from the eastern Karakoram (Clift et al., 2002). The exhumation rate of $1.0\pm 0.2\text{ mm/yr}$ (Chapter 6) and geothermal gradient of $36\pm 7^{\circ}\text{C/km}$ are consistent with the cooling rates of $30\text{-}40^{\circ}\text{C/Ma}$ across the Tangtse-Pangong region inferred by Boutonnet et al. (2012).

Several lines of evidence suggest that the KFZ is a near vertical structure. Measurements of the the KFZ foliations are steeply NE and SW dipping, suggesting that the KFZ is vertical on average and that local deviations are caused by complexities of its 3D architecture (see Chapter 2 and especially Figure 2.11). Regional scale mapping of the KFZ shows that individual fault strands are approximately linear in plan view (Phillips, 2008) and that even

the extreme topography of the region does not emphasise an overall dipping geometry. Also, the most intensely deformed fault rocks of each type are typically located close to the active fault traces, consistent with a vertical strike-slip fault zone being passively exhumed by erosion. The fault rocks exposed at the surface today record therefore deformation processes currently operating approximately directly beneath the exposed fault rocks, albeit translated along strike (Chapter 3). This configuration makes it possible to construct interpretive vertical cross-sections of the generalised KFZ structure at depth by extrapolating the exposed fault rock distributions vertically down to the depths at which they are inferred to have formed (Figures 6.1 and 6.2). As such, it provides a rare insight into fault zone structure throughout the upper-middle crust. The structure of the KFZ at various depths is synthesised from information presented in previous chapters and summarised below by considering portions deformed above, within and below the frictional-viscous transition zone (FVTZ). It should be noted however that there are overlaps and gradual transitions between these portions of the KFZ (Chapter 3). Quoted depth ranges are calculated from deformation temperatures and assume a geothermal gradient of 35°C/km (Chapters 3 and 4).

The shallowest portion of the KFZ is characterised by fault rocks, such as cataclasites, dominated by frictional deformation mechanisms (e.g. Figures 3.4h, 3.6c, 3.6e and 3.7d; Rutter et al., 2007) and broadly corresponds to <250°C and <7 km depth (Figures 6.1 and 6.2). At these depths the fault structure loosely corresponds to a fault core+damage zone model (Caine et al., 1996; Chester et al., 1993). This structure is best demonstrated by the Nubra strand where intense fracturing and a metre-scale zone of cataclasite at the contact between the Nubra-Siachen leucogranite and the Nubra Formation form a well-developed fault core (Section 3.2). The Arganglas strand also contains localised zones of intensely brecciated marble, whilst marble cataclasites are present within the Tangtse and Pangong strands (Section 3.2; Rutter et al., 2007).

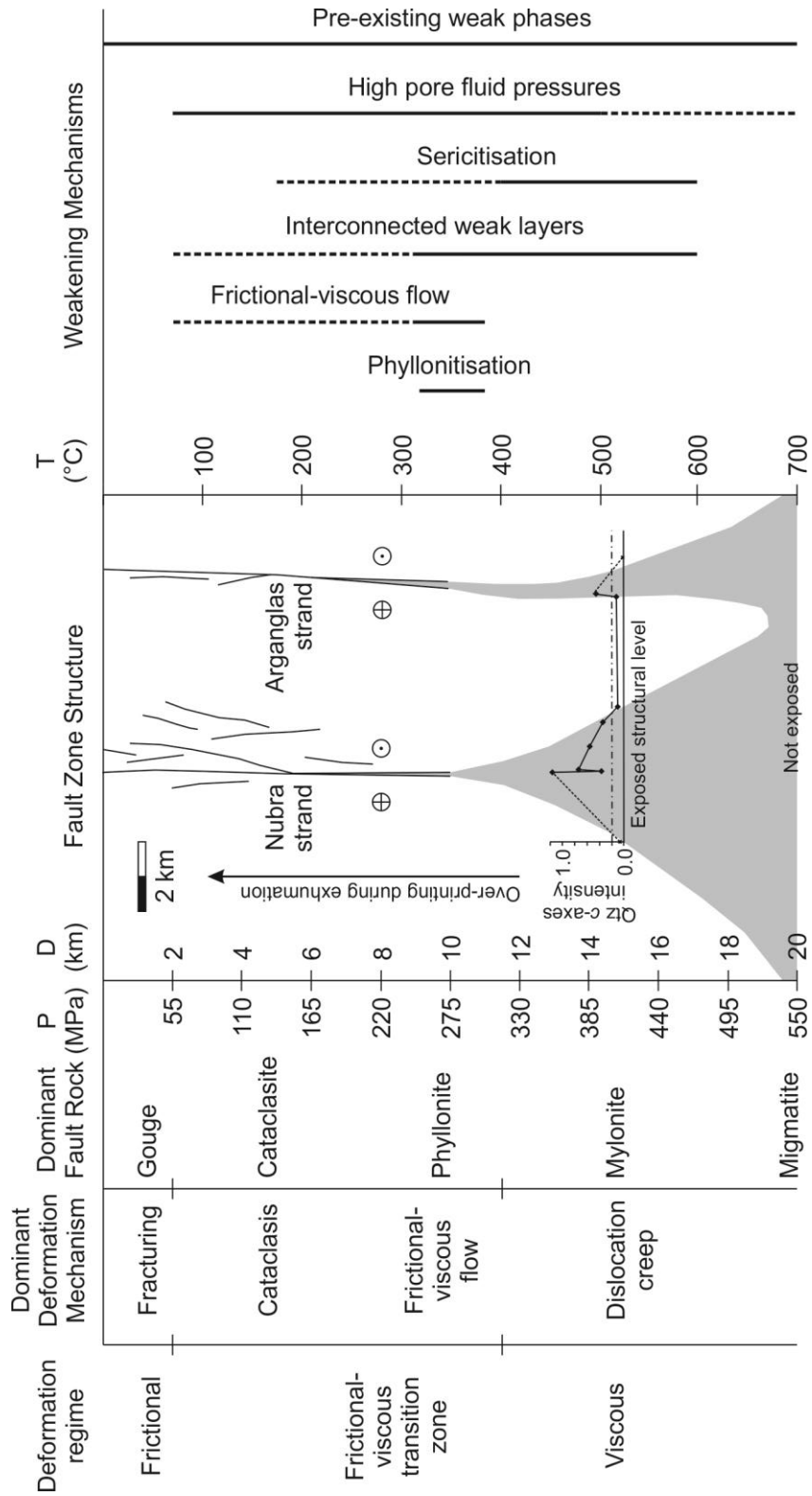


Figure 7.1 Summary schematic cross-section of the structure of the KFZ in the Nubra area, also showing changes in deformation mechanisms, dominant fault rock and fault weakening mechanisms with depth. The CPO intensity profile from the Nubra transect (Chapter 6) is used to constrain the width of the shear zone at 15 km depth. The rocks presently exposed in the Nubra area record overprinting by the deformation process and structures formed at shallower depths as the section was exhumed.

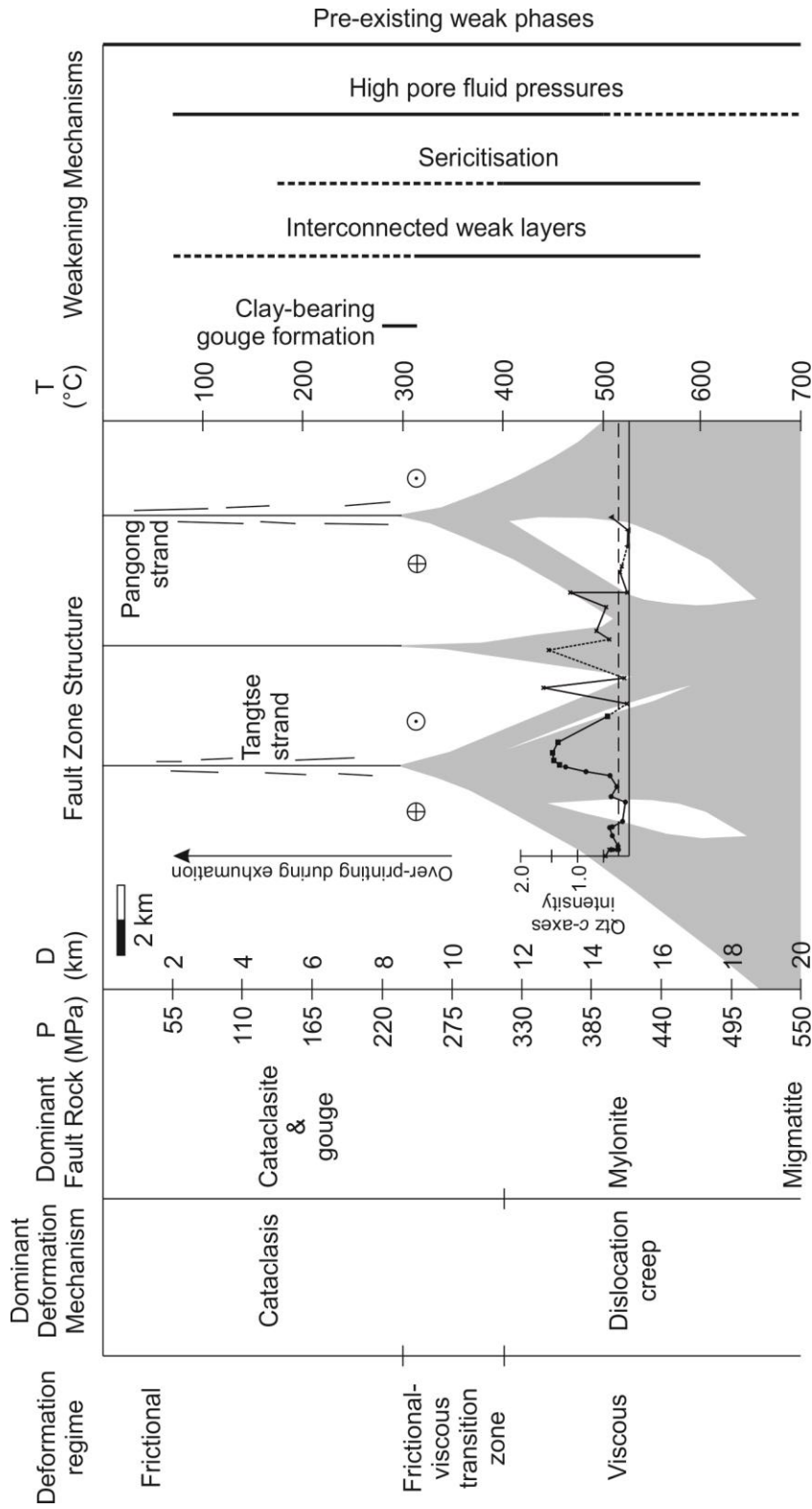


Figure 7.2 Summary schematic cross-section of the structure of the KFZ in the Tangtse area, also showing changes in deformation mechanisms, dominant fault rock and fault weakening mechanisms with depth. The CPO intensity profile from the Tangtse transect (Chapter 6) is used to constrain the width of the shear zone at 15 km depth. The rocks presently exposed in the Tangtse area record overprinting by the deformation process and structures formed at shallower depths as the section was exhumed.

More minor and distributed deformation is present also across the majority of the KFZ, representing the damage zone, and takes three main forms. Firstly, minor faults of cataclasite or gouge up to a few 10s of cm thickness occur with variable orientations but are particularly common in granitoids and marbles within <2 km of the major fault strands (Chapter 3). Secondly, tourmaline±quartz veins occur within a few hundred metres of the Nubra and Tangtse fault strands and represent episodic fluid overpressure and hydrofracturing (Section 3.2). Thirdly, discrete planar fractures with slickensides but lacking comminuted fault rocks are present in granitoids, particularly along the Nubra fault strand.

The shallow (<7 km depth) structure of the KFZ is characterised therefore by highly localised cataclasite and breccia fault cores less than a few metres thick surrounded by wide (up to c. 2 km) damage zones of variable deformation styles (Figures 6.1 and 6.2). At these depths the majority of strike-slip displacement is inferred to have been accommodated in the through-going fault cores, whilst the less well connected and more variably oriented damage zone structures resulted from more incipient or transient faulting. Due to the exhumation history of the KFZ, it is clear that the damage zone structures formed several million years after the initiation of the KFZ (e.g. Figure 3.8), because the presently exposed section was in the ductile regime at the time of fault initiation. The damage zone structures are not therefore the result of distributed deformation at the propagating fault tip (e.g. Kim et al., 2004). Instead, they represent a variety of “wall damage zone” structures in the sense of Kim et al. (2004) that form during build-up of displacement and/or due to geometrical irregularities of the fault core.

Within the FVTZ, loosely corresponding to 250-400°C or 7-11 km depth (Figures 3.8, 6.1 and 6.2), fault rocks can again be classified as localised or more distributed. Phyllonite and gouge fault cores that formed within this depth range are present in the Nubra and Pangong strands respectively and are <10 m thick (Chapters 3 and 5; Phillips and Searle, 2007; Rutter et al., 2007). More widespread deformation microstructures formed at these depths are present for a few hundred metres in marbles across each main fault strand and include twins and bulging/subgrain rotation dynamic recrystallisation microstructures (Chapter 3; Rutter et al., 2007). Deformation

in the leucogranites at similar depths was dominated by frictional slip on micaceous interconnected weak layers along with fluid-assisted diffusive mass transfer (Chapter 3). Evidence for this style of deformation is similarly distributed over a few hundred metres within the leucogranites (Chapter 3). The onset of these deformation mechanisms during exhumation may explain the absence of bulging dynamic recrystallisation and basal $\langle a \rangle$ slip in quartz (e.g. Chapters 3 and 5) that might otherwise be expected to occur under these conditions (e.g. Toy et al., 2008; Stipp et al., 2002). Within the FVTZ, strain is considered to be highly localised within the narrow phyllonite and gouge zones. Deformation fabrics formed under similar conditions in the surrounding lithologies (e.g. marbles, pelites and granitoids) are considerably less intense but more extensive, suggesting that these units accommodated much lower strains.

Beneath the FVTZ, under conditions where deformation is dominated by viscous mechanisms (i.e. $>400^{\circ}\text{C}$ and >11 km depth), the structure of the KFZ changes dramatically. At 500°C and c. 15 km depth, mylonitic fault rocks are distributed across shear zones ranging from a few hundred metres up to c. 3 km width. The high strain zones, which are <10 m wide in and above the FVTZ, are inferred to broaden rapidly downwards. Concomitantly, it is likely that the deformation intensity contrast between the high strain zones and surrounding lower strain rocks evident in the FVTZ decreases with depth due to reduction in their strength contrasts. In the Tangtse area, multiple shear zones visibly wrap around less deformed lenses in both plan view and cross-section (Figures 2.2 and 6.2). The shear zone structure in this region likely reflects the greater pre-existing lithological complexity in the Tangtse area compared to the Nubra area, where the simpler structure of two shear zones was likely influenced by the lack of rheological contrasts/weaknesses within the bulk of the homogenous Nubra-Siachen leucogranite. In the Tangtse transect, shear zones closest to the centre of the fault zone have the strongest CPO intensities (Figures 5.10c and 6.2) suggesting that they record higher strain than the more marginal strands. Extrapolation of the broadening trend to greater depths suggests that the shear zones may merge into a single zone of deformation at >18 km depth (Figures 6.1 and 6.2). This depth is broadly coincident with the depth at

which migmatization/anatexis was occurring, supporting the suggestion that deformation was widely distributed in a partially molten crust.

As discussed in Section 7.2, the continuation of the KFZ to depths greater than c. 20 km is uncertain. It must extend to at least these depths in order to have exhumed migmatites from the anatexis zone. It is not clear from the available geological evidence however whether the fault penetrates this zone as a coherent structure or whether it dissipates into it.

The fault rocks formed at various depths within the KFZ and now exposed at the surface contain evidence for having deformed with a range of shear strengths (Chapter 3). This suggests that the strength of the rocks that constitute the exposed structural level evolved as they were exhumed through progressively shallower levels of the KFZ, and allows the approximate strength profile of the KFZ to be reconstructed from strengths and depths at which various fault rocks formed (Figure 3.8). Recrystallised grain size palaeopiezometry indicates that initial deformation occurred at shear stresses of 24-64 MPa for quartz deformed at c. 500°C (Boutonnet et al., 2013). This deformation resulted however in the rapid (<2 Myr) development of weaker interconnected micaceous foliae and enhanced diffusive mass transfer. The switch in deformation mechanisms would have been promoted by hardening of quartz crystal plasticity as the rocks were exhumed and cooled, especially as the quartz CPOs that developed due to prism $\langle a \rangle$ and rhomb $\langle a \rangle$ slip would result in quartz orientations that were unfavourable for basal $\langle a \rangle$ at lower temperatures (Toy et al., 2008). This weakening resulted in narrowing of the active shear zones from <3 km to a few hundred metres thickness (see above). Further weakening occurred as the rocks were exhumed and cooled to c. 350°C (Chapter 5), at which point phyllonitisation of the Nubra Formation occurred (Section 3.3.1, Chapter 5). The phyllonite deformed by frictional-viscous flow with a modelled maximum shear strength of c. 28 MPa (Chapter 5). As the rocks were further exhumed, the lower temperature reduced the efficiency of diffusive processes in the phyllonite and granitoids. Concomitantly, the lower confining pressure (and hence normal stress) facilitated frictional and dilational deformation mechanisms that resulted in both distributed fracturing and more localised cataclasis. Widespread veins suggest that this process

was further enhanced by cyclic pore fluid pressure fluctuations during crack-seal events. A similar sequence of progressive weakening and strain localisation during exhumation is preserved within the marbles of the Pangong strand (Section 3.3.4). These deformed by dynamic recrystallisation at flow stresses of 40-110 MPa at 300-375°C, and twinning under differential stresses of 160-250 MPa at c. 300°C, at which point deformation switched to a <10 m wide zone of frictionally weak phyllosilicate-rich gouge (Section 3.3.4; Rutter et al., 2007).

In summary the structure of the KFZ consists of two main sub-parallel strands that accommodate the majority of shallow (<7 km) brittle deformation in narrow (a few metres thick) fault cores. These widen slightly downwards into the FVTZ but, at <10 m thick, they remain highly localised to depths of c. 11 km. Throughout this depth range, low intensity deformation occurs across a wider zone, several 100 m to a few km across. Deformation in the fault cores and surrounding regions occurs by a complex variety of deformation mechanisms. Beneath the FVTZ the fault strands broaden rapidly and branch downwards into shear zones up to c. 3 km thick at 15 km depth where deformation occurs primarily by intra-crystalline plasticity and dynamic recrystallisation. The shear zones likely continue to broaden with depth into a wide zone of deformation (>10 km across) in partially molten crust at c. 19-20 km depth. This structure is controlled by evolution to progressively weaker fault rocks and associated strain localisation during synchronous exhumation and strike-slip deformation.

7.3.2 Implications for the structure and deformation processes of large scale strike-slip faults

7.3.2.1 Implications for the structure of strike-slip faults in the Tibetan plateau

The exhumed fault rocks of the KFZ provide a rare opportunity to directly examine deep deformation processes operating within a strike-slip fault of the Tibetan plateau. Lower exhumation rates in the central and northern plateau regions mean that mid-crustal portions of major strike-slip faults in these areas are typically not exposed. These regions are however more politically and geographically amenable to geophysical surveys and present

therefore an opportunity to compare the exhumed structure of the KFZ to observations of other faults at depth within a comparable tectonic setting. One such fault is the Altyn Tagh Fault (ATF), termed the Karakax Fault in its western portion (Figure 2.1), which forms a >2000 km long sinistral strike-slip system delineating the northern margin of the Tibetan plateau between the Tarim basin in the west and the Qilian Shan in the East (Figure 7.3; Searle et al., 2011). As the Tarim basin consists of a relatively rigid lithospheric body (Neil and Houseman, 1997), the ATF acts as a plate boundary fault in this region. The ATF cuts primarily through Proterozoic-Palaeozoic rocks and Jurassic non-marine sediments, and contains exposures of fault rocks formed predominantly at shallow crustal levels, including a 200 m thick gouge zone (Searle et al., 2011; Ritts and Biffi, 2000). The fault is considered to have initiated either at c. 23 Ma or earlier at 49 Ma (Yue et al., 2003; Yin et al., 2002), has total geological offsets in the range 350-470±70 km (Yin et al., 2002; Zhang et al., 2001) and average long-term slip-rate estimates that range widely between <9-45 mm/yr (Searle et al., 2011; Chen et al., 2002; Yin et al., 2002). Recent slip-rate estimates that attempt to reconcile geodetic, millennial and geological constraints tend to favour lower slip-rates of c. 9 mm/yr (He et al., 2013; Cowgill et al., 2009).

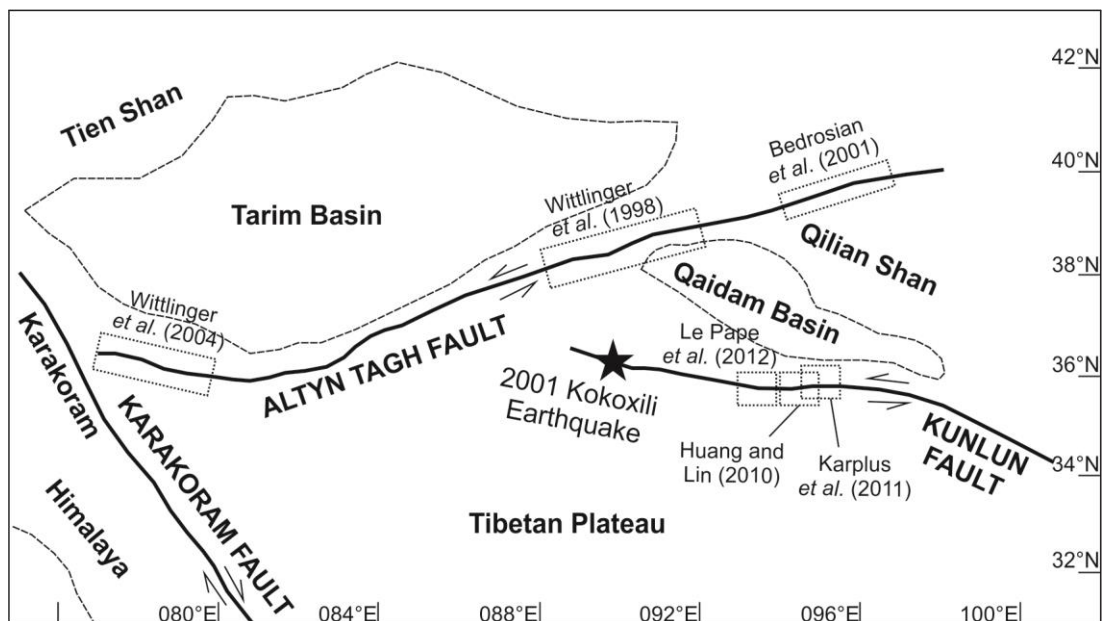


Figure 7.3 Sketch map of the tectonic features of the north Tibet region showing the major faults and localities discussed in the text.

The structure of the ATF at depth has been investigated using magnetotelluric and seismic surveys. Bedrosian et al. (2001) obtained magnetotelluric measurements from four transects between 094-097°E (Figure 7.3). The measurements extended to 8 km depth. In each transect a dramatic change in resistivity, typically <100 to $>1000 \Omega\text{m}$, occurred directly beneath the ATF across a zone <5 km wide and extending to >8 km depth. This change in resistivity was interpreted to result from juxtaposition of low and high resistivity lithologies on opposing sides of the fault. These observations indicate that the shallow structure of the ATF is characterised by a narrow zone of high strain comparable in width to the shallow portion of the KFZ (e.g. the separation of brittle fault rocks in the Nubra and Arganglas strands; Figure 7.1). The majority of strain in the ATF at these shallow depths may actually be accommodated in a much narrower zone that is difficult to resolve using magnetotellurics but comparable to a single strand of the KFZ.

Xiao et al. (2011) provide magnetotelluric results across the ATF that extend to greater depths of 100 km. These show the downward continuation of shallow structure imaged by Bedrosian et al. (2001) to depths of 30 km. Down to this depth, the resistivity contrasts continue to occur within a narrow zone <10 km in width. In one profile, close to 094°E, Xiao et al. (2011) interpret the ATF to broaden or branch downwards in a zone up to c. 20 km wide between 30-50 km depth. This structure at 0-50 km depth in the ATF is highly comparable to the exhumed structure of the KFZ formed at 0-15 km depth (Figures 6.1 and 6.2). The magnetotellurics do not detect resistivity contrasts across the ATF at depths greater than 50 km.

Detection of the ATF at greater depths is provided by seismic investigations. Teleseismic receiver functions appear to show an abrupt Moho offset directly beneath the ATF at 077°E (Figure 7.3), from 90 km depth under Tibet to 60 km under the Tarim basin (Wittlinger et al., 2004). This offset occurs across a vertical zone no more than c. 20 km in width (Wittlinger et al., 2004). Similarly, Wittlinger et al. (1998) used P-wave tomography to image a negative velocity anomaly ($<8\%$) <40 km in width extending to >100 km depth beneath the ATF at 090°E (Figure 7.3). The ATF appears to follow a Silurian-Devonian suture zone along much of its length (Sobel and Arnaud,

1999), which could have potentially provided pre-existing rheological contrast throughout much of the crust/lithosphere and facilitated the great depth extent of the ATF. This contrasts markedly with the KFZ, which cross-cuts at least two suture zones (Phillips et al., 2004) and appears to have been controlled primarily by the Neogene kinematics of the India-Asia collision without significant influence by older structures or fabrics.

Another comparable fault within the Tibetan plateau is the Kunlun Fault. This is a c. 1500 km long sinistral strike-slip fault that reactivates the Ordovician-Silurian Kunlun suture zone (Bian et al., 2001) and separates the Songpan-Ganzi and Kunlun-Qaidam terranes in NE Tibet. The fault has a Quaternary slip-rate of 10-12 mm/yr along much of its length, decreasing to <2 mm/yr within 150 km of its eastern tip (Kirby et al., 2007). The finite offset and initiation age of the Kunlun Fault are uncertain, although Fu and Awata (2007) suggest that it has a total offset of 100 ± 20 km and, assuming an average slip-rate of 10 mm/yr, suggest that it initiated at 10 ± 2 Ma. At least five M_w 6.4-7.8 earthquakes have occurred on the fault since 1937 (Kirby et al., 2007).

Although the shear strength of the Kunlun Fault is not well constrained, Huang and Lin (2010) suggest that the fault at c. 094°E (Figure 7.3) may be exceptionally weak (shear strength <1 MPa) at shallow depths (< 1 km) on the basis of fault-related fold orientations and borehole measurements. Wang et al. (2009) conducted seismic refraction profiling shortly after the M_w 7.8 2001 Kokoxili earthquake (Figure 7.3) and used trapped waves to estimate the fault zone width to be 300 m at <5 km depth. They also observed S-wave velocities 30-45% lower in the fault zone than in the wall rocks, which they interpreted to indicate high pore fluid pressures to depths of at least 1-2 km within the fault. These observations, although limited, suggest that the shallow structure of the Kunlun Fault may be characterised by localised brittle deformation, high pore fluid pressures and low shear strength, similar to that of the KFZ (Chapter 3, Section 7.3.1).

As with the ATF, the deep structure of the Kunlun Fault has been investigated using a combination of magnetotelluric and seismic experiments (Le Pape et al., 2012; Karplus et al., 2011). Le Pape et al. (2012) report a

NE-SW magnetotelluric profile across the Kunlun Fault at 094°E (Figure 7.3) and extending to 150 km depth. An extensive low resistivity layer ($<10 \Omega\text{m}$) at 20-45 km depth beneath the Songpan-Ganzi terrane to the SW of the Kunlun Fault was interpreted as a partially molten layer. This layer was imaged to extend northeast at 30-40 km depth beneath the north and south strands of the Kunlun Fault (separated by *c.* 10 km), and to extend another 20 km northeast beneath the Kunlun Shan. The layer was interpreted to mechanically decouple the upper and lower crust and to suggest that a major tectonic division is not present at >30 km depth beneath the trace of the Kunlun Fault. A complementary active source seismic profile at 95°E (Figure 7.3) also detected a low velocity layer at 20-40 km depth beneath the fault (Karplus et al., 2011). In addition, this study confirmed that there is no offset of the Moho beneath either strand of the Kunlun Fault in this region, suggesting that the fault does not cut the full 70 km crustal thickness (Karplus et al., 2011). Furthermore, viscoelastic modelling of pre- and post-seismic displacements related to the M_w 7.8 Kokoxili earthquake showed that the displacements could be reproduced by models with a ≤ 20 km thick low viscosity ($\leq 10^{18.5}$ Pas) mid-crustal layer, without the need for multiple relaxation times required by classic two-layer models (DeVries and Meade, 2013), adding independent support for a mid-crustal low viscosity layer beneath the Kunlun Fault.

The above observations of the Kunlun Fault are highly comparable to the exhumed structure of the KFZ, where migmatites indicate a former partially molten layer at >19 km depth (Chapter 4 and Section 7.3.1) and cross sections suggest that the KFZ may be restricted to the upper-middle crust (Searle et al., 2010). The structure of the Kunlun Fault from 5-20 km depth is not well constrained by geophysical observations. The aforementioned similarities between the Kunlun Fault and KFZ however suggest that the exhumed structure of the KFZ (Section 7.3.1) could be highly analogous to the structure of the Kunlun Fault in this depth range. In this sense, structural observations of the KFZ are significant for interpreting the structure and deformation processes operating at depth within the Kunlun Fault and potentially other strike-slip faults in northern Tibet.

Although the Altyn Tagh and Kunlun faults both reactivate Palaeozoic sutures in northern Tibet, their deep structures appear to differ dramatically. The former apparently remains relatively localised (<20-40 km width) to depths of >90 km where it cuts the Moho, whereas the latter appears to extend no deeper than 30-40 km where it likely roots into a low viscosity partially molten layer. The structures of these faults are clearly strongly influenced by the rheology of mid-lower crustal materials. The abundance of migmatites and crustal melt-derived granitoids emplaced throughout the Miocene across the Karakoram (Phillips et al., 2013) suggests that the deep structure of the KFZ was, at that time at least, similar to the Kunlun Fault and lends support to the hypothesis that the KFZ is restricted to the upper-middle crust (Searle et al., 2010).

7.3.2.2 Implications for the behaviour of seismogenic strike-slip faults

An ongoing challenge in the study of fault zone processes is to better understand controls on the varied styles of seismological behaviour through integrating constraints from fault structure, microstructure and mechanics (e.g. Barth et al., 2013; Noda and Lapusta, 2013; Segall, 2012). In recent years this field has been greatly advanced by detailed geological and experimental investigations of active faults with well constrained seismological and palaeoseismological records (e.g. Barth et al., 2013; Berryman et al., 2012; Carpenter et al., 2012; Holdsworth et al., 2011; Murray and Langbein, 2006). This is particularly true of the strike-slip San Andreas Fault (SAF), California, and the transpressional Alpine Fault (AF), New Zealand, through which boreholes have been drilled to directly investigate the properties of these faults at c. 3200-3300 m and c. 90-130 m depth respectively (Sutherland et al., 2012; Holdsworth et al., 2011; Zoback et al., 2010; Townend et al., 2009). Whilst these and related investigations have revealed a wealth of information on shallow fault structure, microstructure, mineralogy, deformation/weakening mechanisms, mechanics, stress states and the role of fluids (e.g. Townend et al., 2013; Carpenter et al., 2012; Hadizadeh et al., 2012; Sutherland et al., 2012; Holdsworth et al., 2011; Lockner et al., 2011; Solum et al., 2006; Hickman and Zoback, 2004), it remains unclear how such properties/processes may be representative of, or relate to, those in the deeper portions of fault zones

at and/or below 5-15 km depth where most large earthquakes nucleate (Schleicher et al., 2012; Holdsworth et al., 2011; Sibson, 1986).

Investigations of exhumed fault zones such as the KFZ, that contain a near continuous record of fault rocks formed across a range of crustal depths, can play an important role therefore in evaluating the applicability and relationships of shallow processes to those at greater depths.

The SAF is a c. 800 km long dextral transform fault forming the boundary between the Pacific and North American plates. It has been active since c. 27 Ma (Sharman et al., 2013), has an offset of c. 315 km in its central portion (Revenaugh and Reasoner, 1997) and has a present day slip-rate of c. 35 mm/yr (Lisowski et al., 1991). The San Andreas Fault Observatory at Depth (SAFOD) borehole near Parkfield, California, allowed direct sampling of fault core material across two zones at 3196.5-3197.1 m and 3296.52-3299 m depth that were revealed by distortion of the borehole casing to be actively deforming (Holdsworth et al., 2011; Zoback et al., 2011). Microstructural analysis of the host rocks and currently inactive gouges/cataclasites revealed that cataclastic deformation was accompanied by pressure solution, precipitation of calcite, smectite and anhydrite veins and development of networks of smectitic clays (Hadizadeh et al., 2012; Holdsworth et al., 2011). The active gouges were found to lack significant veining but were dominated by Mg-rich smectite (saponite) that was interpreted to have chemically interacted with entrained serpentinite clasts (Holdsworth et al., 2011). The active gouge was interpreted to have deformed also by a combination of frictional sliding and fluid-assisted diffusive mass transfer (Hadizadeh et al., 2012; Holdsworth et al., 2011). The saponite-rich gouges were found to be frictionally weak (friction coefficient, 0.15), velocity strengthening and associated with nanocrystalline illite-smectite and chlorite-smectite coatings on slip surfaces (Schleicher et al., 2010, 2012; Lockner et al., 2011).

Whilst the above findings offer explanations for the frictional weakness and microseismic creeping behaviour of the Parkfield segment of the SAF at shallow crustal depths, the extent to which they characterise processes at depths greater than c. 4 km remains unclear. Schleicher et al. (2012) proposed that Mg-rich chlorite-smectite present in the borehole could be

stable to depths >8 km within the SAF, potentially extending the applicability of the SAFOD findings to much of the upper crust. This suggestion is supported by similar evidence from the Pangong strand of the KFZ, where Rutter et al. (2007) identified a <10 m thick gouge zone formed at $300\pm 30^{\circ}\text{C}$ and containing chlorite, illite and saponite. The geothermal gradient of c. $35^{\circ}\text{C}/\text{km}$ (Chapters 4 and 5), although determined from metamorphic assemblages c. 6 Myrs older than the gouge, suggests that the gouge formed at 8-9 km depth. As discussed in Chapter 3, the Pangong strand gouge has comparable mineralogy to Alpine Fault gouges which have experimentally determined friction coefficients of 0.28-0.37 (Boulton et al., 2012; Barth et al., 2013). Whilst slightly stronger than the shallower gouges from the SAFOD borehole, the exhumed gouges of the Pangong strand suggest that the presence of low friction phyllosilicate-rich gouges can weaken major strike-slip faults down to the depths suggested by Schleicher et al. (2012).

Holdsworth et al. (2011) provide an alternative, but possibly complementary, suggestion that at depths >5 km the relative importance of solution-precipitation creep may increase due to higher temperatures, leading to the onset of frictional-viscous flow, as discussed in Chapter 3 (e.g. Jefferies et al., 2006a, 2006b; Bos and Spiers 2000, 2002). The exhumed section of the Nubra strand of the KFZ strongly supports this suggestion. Within the Nubra strand, mylonitic lithologies are overprinted by both phyllonites formed at $351\pm 34^{\circ}\text{C}$ (9-11 km depth), and cataclasites inferred to have formed at $<300^{\circ}\text{C}$ (<8 km depth, Figures 3.8 and 6.1, Section 3.3.1). The phyllonite contains deformation microstructures, such as interconnected muscovite foliae and sutured and indented plagioclase clasts, indicative of frictional-viscous flow (Chapters 3 and 5). These fault rocks demonstrate that frictional cataclastic deformation at shallow depths gives way to multi-mechanism frictional-viscous deformation within the frictional-viscous transition zone in suitably phyllosilicate-rich lithologies such as the KFZ Nubra Formation metapelites (Section 3.3.1) or potentially the predominantly pelitic Great Valley Block in the SAF (Holdsworth et al., 2011). As discussed in Chapter 5, frictional-viscous flow potentially occurs in strike-slip, normal and thrust faults, a wide range of fault rocks (e.g. schists, phyllonites,

foliated cataclasites and gouges) and under conditions ranging from 200-500°C and *c.* 5-15 km depth. As such, frictional-viscous flow likely plays an important role in controlling the shear strength and rheology of presently active faults, including the SAF, at mid-crustal depths. Evidence of extensive veining within the KFZ, as in the SAF, shows that pore fluids play an integral role in promoting fracturing and fluid-assisted diffusive mass transfer processes under a wide range of conditions (Chapters 3 and 5).

The KFZ contains both fault gouges formed at $300\pm 30^\circ\text{C}$ in the Pangong strand (Rutter et al., 2007) and phyllonites formed under broadly similar conditions within the Nubra strand (Chapter 3, Phillips and Searle, 2007). These show that the fault rocks and associated deformation processes proposed by both Schleicher et al. (2012) (dominantly frictional sliding in clay-rich gouges) and Holdsworth et al. (2011) (dominantly frictional-viscous flow in foliated cataclasites/phyllonites) could potentially occur at depth within the SAF and similar faults. Evidence from the fault rock distribution within the KFZ suggests that protolith lithology exerts a first order control on dominant fault rock type and deformation processes operating at these mid-crustal depths. Where the KFZ cuts the Pangong Metamorphic Complex (dominantly marbles with subordinate amphibolites and metapelitic schists), the relative abundance of stronger minerals (e.g. calcite, quartz, feldspar) in the protoliths has promoted cataclastic deformation and formation of gouge, within which clays and chlorite grew. Where the KFZ cuts the Nubra Formation (dominantly metapelites with subordinate metavolcanics and marble) the relative abundance of phyllosilicates (e.g. biotite, muscovite and chlorite) in the protoliths has promoted phyllonitisation and frictional-viscous flow. These observations suggest that constraining protolith lithology is crucial to predicting deformation mechanisms and fault rock rheology in the mid-crust.

Evidence from the exhumed section of the KFZ can also be used to test questions arising from investigations into the seismic characteristics of fault rocks within the Alpine Fault, New Zealand. The Alpine fault runs along the NW margin of South Island, New Zealand, where it accommodates *c.* 70% of the relative motion of the Pacific and Australian plates (Norris and Cooper, 2001). Present day slip-rates on the fault are estimated at 27 ± 5 mm/yr strike-

slip and 8-10 mm/yr reverse components (Norris and Copper, 2001; Bull and Cooper, 1986).

The AF has been investigated in both borehole studies (Townend et al., 2013; Sutherland et al., 2012) and extensively in outcrop, where transpressional slip has exhumed gouges, cataclasites, pseudotachylytes and mylonites from up to c. 25 km depth (Barth et al., 2013; Boulton et al., 2012; De Pascale and Langridge, 2012; Toy et al., 2008; Cooper and Norris, 1994; White and White, 1983). Recent experimental investigations have aimed to characterise the frictional properties of fault gouges from the central (Boulton et al., 2012) and southern (Barth et al., 2013) portions of the AF and relate them to the seismic behaviour of the fault. Illite-chlorite and saponite-chlorite-lizardite gouges from three localities along the southern Alpine Fault (Barth et al., 2013) were found to be frictionally weak (steady state friction coefficients 0.12-0.37), velocity strengthening and impermeable ($K = 10^{-20}$ to 10^{-22} m²). Fault gouges from the central AF are broadly similar and are associated with frictionally stronger hanging wall cataclasites (steady state friction coefficients 0.51-0.57, Boulton et al., 2012). The gouges at both localities showed little or no frictional healing (i.e. the difference in peak friction following a hold relative to the steady state sliding friction) and were inferred on mechanical and microstructural grounds to have deformed by stable aseismic creep at low strain rates (Barth et al., 2013; Boulton et al., 2012). A range of geological, seismological and palaeoseismological evidence from both these portions of the fault indicates however that the AF typically generates $M_w > 7.0$ earthquakes that accommodate the majority of its displacement over Holocene or greater time-scales (Berryman et al. 2012; Beavan et al., 2010; Sutherland et al., 2007). In the central portion, earthquake ruptures may have preferentially deformed the pre-existing gouge (Boulton et al., 2012).

A similar, apparently paradoxical, situation is present along the KFZ. Phyllosilicate-rich fault gouges in the Pangong strand are inferred to be frictionally weak and likely velocity-strengthening, whilst phyllonites in the Nubra strand are inferred to have deformed by aseismic frictional-viscous creep (Chapter 3). Both the gouge and phyllonite are considered to have accommodated the majority of the deformation within the depth ranges

where they formed (c. 7-11 km depth) and in which the majority of large earthquakes are expected to nucleate (Sibson, 1986). Both fault strands are associated however with Quaternary palaeoseismic evidence for repeated M_w 6-8 earthquakes, including syn-sedimentary lacustrine seismites and offset debris flows, alluvial fans and fluvio-lacustrine strata (Phartiyal and Sharma, 2009; Phartiyal et al., 2005; Upadhyay, 2001, 2003; Brown et al., 2002).

Barth et al. (2013) suggested several reasons why large earthquakes could occur on faults where exposed fault rocks are otherwise indicative of aseismic creep. These include variations in normal stress due to fault roughness (e.g. Dieterich and Smith, 2009), fluctuations in pore fluid pressure (e.g. Hillers and Miller, 2007), competition between frictional sliding and temperature, strain rate and grain-size sensitive deformation mechanisms (Gratier et al., 2011; Bos and Spiers, 2002) and changes in rock friction rate parameters (i.e. from velocity strengthening to weakening) with increasing temperature (e.g. den Hartog et al., 2012; Tembe et al., 2009; Blanpied et al., 1995). Geological evidence from the exhumed fault rocks of the KFZ suggests that several of these do indeed have potential to impact seismicity within the fault across the depth ranges of the gouge and phyllonite. The KFZ architecture is characterised by geometric irregularities across a wide range of depths and scales (Figures 6.1 and 6.2; Chapter 6; Phillips and Searle, 2007). These would create regions of locally elevated or reduced normal stress and shear stress around irregularities, variably promoting or inhibiting frictional slip relative to normal stress insensitive deformation mechanisms (e.g. crystal plasticity or fluid-assisted diffusive mass transfer). Fluctuating pore fluid pressures are evidenced by widespread quartz, calcite and tourmaline veins within mylonites, phyllonites and cataclasites (Chapter 3). Multiple generations of quartz and tourmaline veins associated with cataclasite within the Nubra-Siachen leucogranite demonstrate that fluid pressures promoted repeated fracture events (Chapter 3). Competition between deformation mechanisms is also inferred on the basis of contrasting deformation microstructures in adjacent lithologies at broadly equivalent depths. This is the case for adjacent lithologies (e.g. cataclasis in marbles/leucogranites and frictional-viscous

flow in phyllonites/metapelites) within individual fault strands (Chapter 3) and also for along-strike changes in fault rock type (e.g. phyllonite in the Nubra strand to gouge in the Pangong strand, see above). Changes in fault rock friction rate parameters with temperature are difficult to assess based on field/microstructural evidence alone. Several experimental studies on a variety of gouge compositions have demonstrated however a change from velocity strengthening to velocity weakening behaviour with increasing temperature in the range 100-400°C (e.g. den Hartog et al., 2012, Tembe et al., 2009; Blanpied et al., 1995). For example, Tembe et al. (2009) tested the frictional properties of illite-rich gouge from SAFOD over the temperature range 96-431°C. They found that the gouge is velocity weakening between 266-349°C (i.e. spanning the temperature of KFZ illite-rich gouge formation), but velocity strengthening at both lower and higher temperatures. Thus, as Barth et al. (2013) acknowledge, such results suggest that the velocity strengthening behaviour observed by Boulton et al. (2012) and Barth et al. (2013) at room temperature may not be representative of behaviour under the conditions at which large earthquakes nucleate.

Another potential explanation for the seismic behaviour of such faults comes from the observations of the Carboneras Fault, Spain, by Faulkner et al. (2003). The Carboneras Fault, exhumed from 1.5-4 km depth, is dominated by 100s m thick phyllosilicate-rich gouge zones containing large blocks of dolomite. Faulkner et al. (2003) inferred that velocity weakening behaviour in locked blocks of dolomite had initiated seismic ruptures that propagated through otherwise velocity strengthening and creeping gouge. This suggestion is supported by recent experimental results demonstrating that many geological materials with velocity strengthening characteristics at low slip-rates change to velocity weakening at higher slip-rates ($> 1 \mu\text{m/s}$, Niemeijer and Spiers, 2007; Wibberley et al., 2008). Such findings suggest that earthquake ruptures that initiate within velocity weakening materials, such as marbles or granites in the KFZ or cataclased mylonites in the AF, could propagate through, and potentially even localise within, the frictionally weaker phyllosilicate-rich gouges or phyllonites (e.g. Wibberley et al., 2008; Faulkner et al., 2003). As suggested by Barth et al. (2013), a combination of the above factors may facilitate earthquake rupture initiation and propagation

within faults such as the AF and KFZ. Thus, the structure and behaviour of the whole fault zone system must be considered in order to draw conclusions on the (a)seismic behaviour of both active and ancient exhumed fault zones.

7.3.2.3 Summary

In summary, the documented structure and deformation processes in the well exposed and deeply exhumed Karakoram Fault Zone, provide an analogue for less well exposed and/or less deeply exhumed active seismogenic fault zones such as the Altyn Tagh and Kunlun faults within the Tibetan plateau and the San Andreas and Alpine faults in other tectonic settings. As such, the KFZ can be used to test questions/hypotheses regarding fault structure and seismic behaviour arising from studies of these faults. The structure of the KFZ (Figures 6.1 and 6.2) provides an analogue for the mid-crustal sections of strike-slip faults in Tibet (e.g. ATF and Kunlun Fault), which are typically poorly resolved in geophysical surveys. The broadening and downwards branching structure of the KFZ provides a link between the narrow shallow structures and broader deep structures imaged in such faults using magnetotellurics or seismics. Their continuation to greater depths may be dependent however on the regional crustal structure and rheology (e.g. presence of pre-existing weak suture zones or mid-crustal melt). Evidence from the KFZ suggests that the SAF could plausibly continue downwards into frictionally weak fault rocks of either phyllosilicate-rich gouge, phyllonite or potentially both, dependent primarily on protolith lithologies. As another example, hypotheses put forward to explain seismogenic behaviour on apparently velocity strengthening fault segments of the AF appear to be highly applicable to the KFZ also. Such considerations suggest that detailed analyses of the interactions between different portions of structures with different rheologies are required to better understand seismogenesis in complex fault zone systems.

8. Conclusions and Future Work

8.1 Conclusions

8.1.1 Architecture of the Central Karakoram Fault Zone

Field and microstructural studies of the varied fault rocks exposed within the Karakoram Fault Zone (KFZ), Ladakh, NW India, indicate that they record progressive deformation during exhumation (Chapters 2 and 3) and can be used to reconstruct the fault zone architecture throughout the upper- to mid-crust (Chapter 7). Whilst changes in fault zone structure and deformation processes are likely to be complex and gradational, observations of the KFZ suggest that it may be broadly characterised by three portions, respectively above, within and below the frictional-viscous transition zone (FVTZ, Chapters 3 and 7).

At shallow depths of less than c. 8 km (c. 280°C), the structure of the fault zone is characterised by cataclasite-filled fault cores ranging from a few centimetres up to 2 m in thickness. These cores are most obviously developed within the Nubra, Pangong and Arganglas fault strands. Similar but more minor faults are widely distributed across damage zones up to c. 2 km thick adjacent to the main fault strands, and are associated with both open planar fractures and quartz±tourmaline veins. Deformation within this depth range occurred predominantly by frictional mechanisms, including fracturing, frictional sliding, dilation, comminution and cataclasis.

Fault core thickness increases with depth into the FVTZ, where phyllonites and foliated gouges up to 10 m thick formed at 8-11 km depth (c. 280-380°C). Lower intensity deformation fabrics (e.g. minor phyllonite/gouge zones), formed at such depths are distributed over zones a few hundred metres across and represent the downward continuation of the shallower damage zone structures. Deformation within this depth range occurred predominantly by a complex interplay of frictional and viscous deformation mechanisms, including fracturing, frictional sliding and fluid-assisted diffusive mass transfer processes.

Below the FVTZ, at depths of c. 15 km (c. 500-550°C), the fault zone structure changes dramatically. Variations in quartz crystal preferred orientation (CPO) intensity indicate that at such depths, multiple shear zones, up to c. 3 km across, accommodate varying strain magnitudes (CPO intensities up to 1.60) and separate less deformed lenses (CPO intensities <0.20, Chapter 6). This deformation initially occurred predominantly by quartz crystal plasticity involving dislocation creep on the prism <a> and rhomb <a> slip systems during grain boundary migration and subgrain rotation dynamic recrystallisation. Associated syn-kinematic breakdown of feldspars to phyllosilicates however led to the onset of frictional-sliding and fluid-assisted diffusive mechanisms (Figure 3.4, Sections 3.2.2 ad 3.2.4). The fault cores present within the FVTZ must broaden dramatically downwards into these shear zones. This widening trend is inferred to continue down dip into a broad region (>10 km across) of relatively low viscosity migmatite at depths of c. 19-20 km (688±44°C, 522±91 MPa, Chapters 4 and 7).

8.1.2 Rheology of the Central Karakoram Fault Zone

Detailed microstructural analysis provides the first assessment of the shear strength of the KFZ throughout the upper- to mid-crust and reveals a wide range of fault weakening mechanisms that operated within each fault rock type (Chapters 3 and 5). Throughout the depths of formation of the exhumed fault rocks, multiple generations of veins and extensive hydrous retrograde metamorphic assemblages indicate that pore fluids reduced the effective shear strength of the fault zone. This behaviour occurred through mechanisms such as lowering of effective frictional shear strength, reaction softening, and facilitation of fluid-assisted diffusive mass transfer. Concomitantly, the resultant phyllosilicate-rich fault rocks deformed by frictional or frictional-viscous deformation characterised by low friction coefficients (typically 0.3-0.4). The effective shear strength of portions of the KFZ deforming in such a manner is likely no more than a few 10s MPa (e.g. < 20 MPa for the Nubra strand phyllonites, Chapters 3 and 5).

Despite extensive evidence for fault rocks and deformation mechanisms associated with low friction, strain softening, velocity strengthening behaviour (indicative of stable and largely aseismic creep), the central KFZ

has generated *c.* M_w 6-8 earthquakes during the Quaternary (e.g. Brown et al., 2002, Chapters 3, 5 and 7). This is likely due to the structural and lithological complexity of the fault zone and velocity weakening behaviour of the fault rocks at high sliding velocities (e.g. Niemeijer and Spiers, 2005). As such, earthquake ruptures nucleating in locally unstable portions of the fault zone are not significantly impeded by the otherwise creeping fault core lithologies, allowing large rupture surfaces to form (Chapters 5 and 7).

8.1.3 Evolution of the Karakoram Fault Zone

The KFZ represents the most recent phase of deformation of the eastern Karakoram terrane, which has experienced protracted polyphase mid-upper amphibolite facies deformation and metamorphism (Chapter 4).

Metamorphism peaked at 677-736°C and 875-1059 MPa and culminated in migmatization at 688±44°C and 522±91 MPa during regional deformation prior to the initiation of the KFZ (Chapter 4). The age of the KFZ is constrained by its relationship to adjacent leucogranite plutons that solidified at *c.* 15.7 Ma (Phillips et al., 2004). Profiles of strain distribution across the leucogranites, along with microstructures in their contact metamorphic aureoles indicate that the KFZ initiated after leucogranite emplacement (Chapters 4 and 6) and corroborate the field and microstructural evidence of Phillips et al. (2004) and Phillips and Searle (2007). Since that time the fault has accrued a maximum dextral strike-slip displacement of *c.* 120 km in its central portion. The maximum average slip-rate over the duration of fault activity is therefore *c.* 8 mm/yr. During KFZ activity, exhumation resulted in cooling and retrograde metamorphism (Chapter 3), rather than the shear heating and magmatic heat advection invoked by Rolland and Pêcher (2001) and Rolland et al. (2009). The limited offset and low slip rate of the KFZ militate against the fault having accommodated several hundred kilometres of plate-like lateral extrusion of the Tibetan plateau (e.g. Lacassin et al., 2004a; Peltzer and Tapponnier, 1988; Tapponnier et al., 1982). Instead geological evidence from the KFZ lends support to models of continental deformation in which distributed viscous crustal thickening and flow are the principle mechanisms for accommodating shortening during collision (e.g. Searle et al. 2011; England and Houseman, 1986, 1988; Molnar, 1988).

8.2 Future Work

8.2.1 Calibration of Crystal Preferred Orientation Strain Profiles

As discussed in Chapter 6, there is potential for crystal preferred orientation intensity to be calibrated for the magnitude of finite strain. This may be possible using approaches based on rock deformation experiments, theoretical modelling or from deformed microstructural features. Whilst each approach is subject to drawbacks, limitations and assumptions, such issues may begin to be overcome by commencing such studies on simple monomineralic lithologies, before developing towards application to more complex polymineralic fault rocks. A combination of such approaches should prove most informative. Development of CPO intensity as a finite strain proxy could potentially yield a widely applicable tool for lithologies otherwise devoid of strain markers.

8.2.2 Petrofabric-Derived Seismic Modelling of Strike-Slip Fault Zones

The deep structure of large continental strike-slip faults is often ambiguous (e.g. Section 7.3.2.1). Seismic surveys that investigate such lower crustal deformation attempt to constrain variations in seismic velocities and anisotropies throughout the crust. Both seismic velocities and anisotropies can be estimated from EBSD datasets of crystal orientations in samples exhumed from the regions of interest (e.g. Mainprice et al. 2011; Mainprice, 1990) and used to constrain and/or augment interpretations of regional seismic surveys (e.g. Erdman et al. 2013; Brownlee et al., 2011). This approach, known as *petrofabric-derived seismic* properties, is potentially most powerful when combined with seismic ray-tracing modelling (e.g. Lloyd et al. 2011; Lloyd and Kendall, 2005) to predict the macroscopic seismic response to micro-scale deformation processes. Petrofabric-derived seismic properties have potential to help answer questions such as the debated depth extent of the KFZ (Klemperer et al., 2013; Searle et al., 2010) and the deep structure of other large strike-slip faults where deep fault rocks are exhumed (e.g. North Anatolian Fault, Turkey).

8.2.3 Characterisation of Deformation Mechanisms by Misorientation and Schmid Factor Analyses

The varied fault rocks exposed within the KFZ are likely typical of many large continental fault zones. As such, further fault rock characterisation would benefit understanding not only of the evolution of the KFZ system but also of continental crustal deformation more generally. Ongoing advances based on electron backscattered diffraction map analysis provide a means to further develop the analyses presented in this study. These include misorientation (e.g. Wheeler et al. 2001; Lloyd et al., 1997) and Schmid factor analysis capabilities provided by Oxford Instruments' Channel 5 Tango module and other EBSD data processing software, such as the MTEX toolbox for MATLAB (Hielscher and Schaeber, 2008). Misorientation and Schmid factor analyses provide alternative but complementary means to constrain deformation characteristics, such as active slip systems, twinning, and recrystallisation mechanisms. This can be achieved by investigating the relative orientations of portions of the microstructure (e.g. grains, subgrains, twins) by misorientation analysis or of the microstructure and hypothetical/inferred stress orientations by Schmid factor analysis. Such approaches will provide further insights into the micro-geodynamics of continental deformation.

List of References

- Absar, A. et al. 1991. A Preliminary Conceptual Model of Nubra Valley Geothermal System, Ladakh, J and K, India. *Journal of the Geological Society of India*, **37**, pp.533-545.
- Anderson, J.L. 1996. Status of thermobarometry in granitic batholiths. *Transactions of the Royal Society of Edinburgh*, **87**, pp.125-138.
- Anderson, J.L. and Smith, D.R. 1995. The effects of temperature and f_{O_2} on the Al-in-hornblende barometer. *American Mineralogist*, **80**, pp.549-559.
- Anderson, J.L. et al. 1983. Cataclastic rocks of the San Gabriel Fault-an expression of deformation at deeper crustal levels in the San Andreas Fault Zone. *Tectonophysics*, **98**, pp.209-251.
- Avouac, J.-P. and Tapponnier, P. 1993. Kinematic model of active deformation in Central Asia. *Geophysical Research Letters*, **20**, pp.895-898.
- Banerjee, P. and Bürgmann, R. 2002. Convergence across the NW Himalaya from GPS measurements. *Geophysical Research Letters*, **29**, pp.30.1-30.4.
- Barnhoorn, A. et al. 2004. The role of recrystallisation on the deformation behaviour of calcite rocks: large strain torsion experiments on Carrara marble. *Journal of Structural Geology*, **26**, pp.885-903.
- Barth, N.C. et al. 2010. Strain within the ultrahigh-pressure Western Gneiss region of Norway recorded by quartz CPOs. In: Law, R.D. et al. eds. *Continental Tectonics and Mountain Building: The Legacy of Peach and Horne*. Bath: Geological Society, London, Special Publications, **335**, pp.663-685.
- Barth, N.C. et al. 2013. Slip localisation on the southern Alpine Fault, New Zealand. *Tectonics*, **32**, pp.620-640.
- Beavan, J. et al. 2010. Distribution of present day vertical deformation across the Southern Alps, New Zealand, from 10 years of GPS data. *Geophysical Research Letters*, **37**, L16305.

- Bedrosian, P.A. et al. 2001. Structure of the Altyn Tagh Fault and Daxue Shan from magnetotelluric surveys: Implications for faulting associated with the rise of the Tibetan Plateau. *Tectonics*, **20**, pp.474-486.
- Behnsen, J. and Faulkner, D.R. 2012. The effect of mineralogy and effective normal stress on frictional strength of sheet silicates. *Journal of Structural Geology*, **42**, pp.49-61.
- Berryman, K.R. et al. 2012. Major earthquakes occur regularly on an isolated plate boundary fault. *Science*, **336**, pp.1690-1693.
- Berthe, D. et al. 1979. Orthogneiss, mylonites and non coaxial deformation of granites – example of the south-Armorican-shear-zone. *Journal of Structural Geology*, **1**, pp.31-42.
- Bhadra, S. and Bhattacharya, A. 2007. The barometer tremolite + tschmakite + 2 albite = 2 pargasite + 8 quartz: Constraints from experimental data at unit silica activity, with application to garnet-free natural assemblages. *American Mineralogist*, **92**, pp.491-502.
- Bhutani, R. et al. 2003. Age of the Karakoram fault activation: $^{40}\text{Ar}/^{39}\text{Ar}$ geochronological study of Shyok suture zone in northern Ladakh, India. *Current Science*, **84**, pp.1454-1458.
- Bian, Q. et al. 2001. A Study of the Kunlun-Qilian-Qinling Suture System. *Acta Petrologica Sinica*, **75**, pp.364-374.
- Blacic, J.D., and J.M. Christie 1984. Plasticity and Hydrolytic Weakening of Quartz Single Crystals. *Journal of Geophysical Research*, **89**, pp.4223-4239.
- Blanpied, M.L. et al. 1995. Frictional slip of granite at hydrothermal conditions. *Journal of Geophysical Research-Solid Earth*, **100**, pp.13045-13064.
- Blumenfeld, P. et al. 1986. C-slip in quartz from subsolidus deformed granite. *Tectonophysics* **127**, pp.97-115.
- Bos, B. and Spiers, C.J. 2001. Experimental investigation into the microstructural and mechanical evolution of phyllosilicate-bearing fault rock under conditions favouring pressure solution. *Journal of Structural Geology*, **23**, pp.1187-1202.

Bos, B. and Spiers, C.J. 2002. Frictional-viscous flow of phyllosilicate-bearing fault rock: microphysical models and implications for crustal strength profiles. *Journal of Geophysical Research*, **107**, doi:10.1029/2001JB000301.

Bos, B. et al. 2000. Frictional-viscous flow of simulated fault gouge caused by the combined effects of phyllosilicates and pressure solution. *Tectonophysics*, **327**, pp.173-194.

Boulton, C. et al. 2012. Physical properties of surface outcrop cataclastic fault rocks, Alpine Fault, New Zealand. *Geochemistry Geophysics Geosystems*, **13**, Q01018.

Bourdelle, F. et al. 2013. A new chlorite geothermometer for diagenetic to low-grade metamorphic conditions. *Contributions to Mineralogy and Petrology*, **165**, pp.723-735.

Boutonnet, E. et al. 2012. Synkinematic magmatism, heterogeneous deformation, and progressive strain localisation in a strike-slip shear zone: The case of the right-lateral Karakorum fault. *Tectonics*, **31**, TC4012.

Boutonnet, E. et al. 2013. Ductile strain rate measurements document long-term strain localisation in the continental crust. *Geology*, **41**, pp.819-822.

Braathen, A. and Osmundsen, P.T. 2004. Dynamic development of fault rocks in a crustal-scale detachment: An example from western Norway. *Tectonics*, **23**, TC4010.

Brace, W.F. and Byerlee, J. 1966. Stick-Slip as a Mechanism for Earthquakes. *Science*, **153**, pp.990-992.

Brantut N. et al. 2013. Time-dependent cracking and brittle creep in crustal rocks: A review. *Journal of Structural Geology*, **52**, pp.17-43.

Brock, W.G. and Engelder, T. 1977. Deformation associated with the movement of the Muddy Mountain overthrust in the Buffington window, southeastern Nevada. *Geological Society of America Bulletin*, **88**, pp.1667-1677.

Brodie, K.H. and Rutter, E.H. 1985. On the relationship between deformation and metamorphism, with special reference to the behaviour of basic rocks.

In: Thompson, A.B. and Rubie, D. eds. *Kinetics, Textures and Deformation*. New York: Springer, Advances in Physical Geochemistry, **4**, pp.138-179.

Brown, E.T. et al. 2002. Slip rates of the Karakorum fault, Ladakh, India, determined using cosmic ray exposure dating of debris flows and moraines. *Journal of Geophysical Research*, **107**, B92192.

Brown, E.T. et al. 2005. Comment on "Slip-rate measurements on the Karakorum Fault may imply secular variations in fault motion". *Science*, **309**, p.1326.

Brownlee, S.J. et al. 2011. Predicted velocity and density structure of the exhuming Papua New Guinea ultrahigh-pressure terrane. *Journal of Geophysical Research*, **116**, B08206.

Bull, W.B. and Cooper, A.F. 1986. Uplifted marine terraces along the Alpine Fault, New Zealand. *Science*, **234**, pp.1225-1228.

Bunge, H.J. 1982. *Texture analysis in materials science: mathematical methods*. London: Butterworths.

Bürgmann, R. and Dresen, G. 2008. Rheology of the Lower Crust and Upper Mantle: Evidence from Rock Mechanics, Geodesy, and Field Observations. *Annual Review of Earth and Planetary Sciences*, **36**, pp.531-567.

Bürgmann, R. et al. 2000. Earthquake Potential Along the Northern Hayward Fault, California. *Science*, **289**, pp.1178-1182.

Burkhard, M. 1993. Calcite twins, their geometry, appearance and significance as stress-strain markers and indicators of tectonic regime: a review. *Journal of Structural Geology*, **15**, pp.351-368.

Burov, E.B. 2011. Rheology and strength of the lithosphere, Marine and Petroleum. *Geology*, **28**, pp.1402-1443.

Burov, E.B. and Diament, M. 1995. The effective elastic thickness (T_e) of continental lithosphere: What does it really mean? *Journal of Geophysical Research*, **100**, pp.3905-3928.

Burov, E.B. and Watts, A.B. 2006. The long-term strength of continental lithosphere: "jelly sandwich" or "crème brûlée"? *GSA Today*, **12**, pp.4-10.

- Butler, C.A. et al. 1995. Evidence for Caledonian sinistral strike-slip motion and associated fault zone weakening, Outer Hebrides Fault Zone, NW Scotland. *Journal of the Geological Society*, **152**, 743-746.
- Byerlee, J. 1978. Friction of Rocks. *Pure and Applied Geophysics*, **116**, pp.615-626.
- Byerlee, J. 1990. Friction, overpressure and fault normal compression. *Geophysical Research Letters*, **17**, pp.2109-2112.
- Byerlee, J. and Brace, W.F. 1968. Stick Slip, Stable Sliding, and Earthquakes-Effect of Rock Type, Pressure, Strain Rate, and Stiffness. *Journal of Geophysical Research*, **73**, pp.6031-6037.
- Bystricky, M. et al. 2000. High Shear Strain of Olivine Aggregates: Rheological and Seismic Consequences. *Science*, **290**, pp.1564-1567.
- Caine, J.S. et al. 1996. Fault zone architecture and permeability structure. *Geology*, **24**, pp.1025-1028.
- Canova, G.R. et al. 1992. Deformation modelling of multi-phase polycrystals: case of a quartz-mica aggregate. *Acta Metallurgica et Materialia*, **40**, pp.1519-1530.
- Carpenter, B.M. 2012. Frictional properties and sliding stability of the San Andreas fault from deep drill core. *Geology*, **40**, pp.759-762.
- Carpenter, B.M. et al. 2011. Weakness of the San Andreas Fault Revealed by samples from the active fault zone. *Nature Geoscience*, **4**, pp.251-254.
- Cathelineau, M. 1988. Cation site occupancy in chlorites and illites as a function of temperature. *Clay Minerals*, **23**, pp.471-485.
- Cathelineau, M. and Nieva, D. 1985. A chlorite solid solution geothermometer: The Los Azufres (Mexico) geothermal system. *Contributions to Mineralogy and Petrology*, **91**, pp.235-244.
- Chen, W.-P. and Molnar, P. 1983. Focal depths of intra-continental and intra-plate earthquakes and their implications for the thermal and mechanical properties of the lithosphere. *Journal of Geophysical Research*, **88**, pp.4183-4214.

- Chen Y. et al. 2002. New paleomagnetic constraints on central Asian kinematics: Displacement along the Altyn Tagh fault and rotation of the Qaidam Basin. *Tectonics*, **21**, 1042.
- Chen, W.P. et al. 2012. Rheology of the continental lithosphere: Progress and new perspectives. *Gondwana Research*, **21**, pp.4-18.
- Chester, F.M. 1995. A rheologic model for wet crust applied to strike-slip faults. *Journal of Geophysical Research*, **100**, pp.13033-13044.
- Chester, F.M., and Chester, J.S. 1998. Ultracataclasite structure and friction processes of the Punchbowl fault, San Andreas system, California. *Tectonophysics*, **295**, pp.199-221.
- Chester, F.M. and Higgs, N.G. 1992. Multimechanism friction constitutive model for ultrafine quartz gouge at hypocentral conditions. *Journal of Geophysical Research*, **97**, pp.1859-1870.
- Chester, F.M., and Logan J.M. 1986. Implications for mechanical properties of brittle faults from observations of the Punchbowl Fault, California. *Pure and Applied Geophysics*, **124**, pp.79-106.
- Chester, F.M. et al. 1993. Internal structure and weakening mechanisms of the San-Andreas Fault. *Journal of Geophysical Research-Solid Earth*, **98**, pp.771-786.
- Chevalier, M.-L. et al. 2005. Slip-Rate Measurements on the Karakorum Fault May Imply Secular Variations in Fault Motion. *Science*, **307**, pp.411-414.
- Chevalier, M.-L., et al. 2012. Spatially constant slip rate along the southern segment of the Karakorum fault since 200 Ka. *Tectonophysics*, **530**, pp.152-179.
- Clift, P.D., et al. 2002. Nd and Pb isotope variability in the Indus River System: implications for sediment provenance and crustal heterogeneity in the Western Himalaya. *Earth and Planetary Science Letters*, **200**, pp.91-106.
- Cole J. et al. 2007. Localized ductile shear below the seismogenic zone: Structural analysis of an exhumed strike-slip fault, Austrian Alps. *Journal of Geophysical Research-Solid Earth*, **112**, B12304.

- Collettini, C. and Holdsworth, R.E. 2004. Fault zone weakening and character of slip along low-angle normal faults: insights from the Zuccale fault, Elba, Italy. *Journal of the Geological Society, London*, **161**, pp.1039-1051.
- Collettini, C. et al. 2006. The development and behaviour of low-angle normal faults during Cenozoic asymmetric extension in the Northern Apennines, Italy. *Journal of Structural Geology*, **28**, pp.333-352.
- Collettini, C. et al. 2009a. Fault zone fabric and fault weakness. *Nature*, **462**, pp.907-910.
- Collettini, C. et al. 2009b. Development of interconnected talc networks and weakening of continental low-angle normal faults. *Geology*, **37**, pp.567-570.
- Collettini, C. et al. 2011. Fault structure, frictional properties and mixed-mode fault slip behavior. *Earth and Planetary Science Letters*, **311**, pp.316-327.
- Cook, K.L. and Royden L.H. 2008. The role of crustal strength variations in shaping orogenic plateaus, with application to Tibet. *Journal of Geophysical Research: Solid Earth*, **113**, B08407.
- Cooper, A.F. and Norris, R.J. 1994. Anatomy, structural evolution, and slip-rate of a plate-boundary thrust – the Alpine Fault at Gaunt Creek, Westland, New-Zealand. *Geological Society of America Bulletin*, **106**, pp.627-633.
- Copley, A. et al. 2010. India-Asia collision and the Cenozoic slowdown of the Indian plate: Implications for the forces driving plate motions. *Journal of Geophysical Research-Solid Earth*, **115**, B03410.
- Corsini M. et al. 1996. Ductile duplexing at a bend of a continental-scale strike-slip shear zone: Example from NE Brazil. *Journal of Structural Geology*, **18**, pp.385-394.
- Corteel, C. and De Paepe, P. 2003. Boron metasomatism in the Brabant Massif (Belgium): Geochemical and petrographical evidence of Devonian tourmalinite pebbles. *Netherlands Journal of Geosciences-Geologie En Mijnbouw*, **82**, pp.197-208.

- Cowgill, E. et al. 2009. Low Quaternary slip-rate reconciles geodetic and geologic rates along the Altyn Tagh fault, northwestern Tibet. *Geology*, **37**, pp.647-650.
- Cowie, P.A. et al. 2013. Viscous roots of active seismogenic faults revealed by geologic slip rate variations. *Nature Geoscience*, **6**, pp.1036-1040.
- De Bresser, J.H.P. and Spiers, C.J. 1997. Strength characteristics of the *r*, *f*, and *c* slip systems in calcite. *Tectonophysics*, **272**, pp.1-23.
- De Bresser, J.H.P. et al. 2001. Grain size reduction by dynamic recrystallisation: can it result in major rheological weakening? *International Journal of Earth Sciences*, **90**, pp.28-45.
- De Caritat P. et al. 1993. Chlorite Geothermometry: a review. *Clays and Clay Minerals*, **41**, pp.219-239.
- Dell'Angelo, L.N. and Tullis, J. 1989. Fabric development in experimentally sheared quartzites. *Tectonophysics*, **169**, p.1-21.
- Dempsey, E.D. et al. 2011. Mica-controlled anisotropy within mid-to-upper crustal mylonites: an EBSD study of mica fabrics in the Alpine Fault Zone, New Zealand. *Geological Society, London, Special Publications*, **360**, pp.33-47.
- den Hartog, S.A.M. et al. 2012. New constraints on megathrust slip stability under subduction zone P-T conditions. *Earth and Planetary Science Letters*, **353-354**, 240-252.
- den Hartog, S.A.M. et al. 2013. Friction on subduction megathrust faults: Beyond the illite-muscovite transition. *Earth and Planetary Science Letters*, **373**, pp.8-19.
- De Pascale, G.P. and Langridge, R.M. 2012. New on-fault evidence for a great earthquake in AD 1717, central Alpine fault, New Zealand. *Geology*, **40**, pp.791-794.
- DeVries, P.M.R. and Meade, B.J. 2013. Earthquake cycle deformation in the Tibetan plateau with a weak mid-crustal layer. *Journal of Geophysical Research: Solid Earth*, **118**, pp.3101-3111.

Dewers, T. and Ortoleva P. 1991. Influences of clay minerals on sandstone cementation and pressure solution. *Geology*, **19**, pp.1045-1048.

Dieterich, J.H. and Smith, D.E. 2009. Nonplanar faults: Mechanics of slip and off-fault damage. *Pure and Applied Geophysics*, **166**, pp.1799-1815.

Di Toro, G. et al. 2011. Fault lubrication during earthquakes. *Nature*, **471**, pp.494-498.

Dunlap, W.J. and Wysoczanski, R. 2002. Thermal evidence for early Cretaceous metamorphism in the Shyok suture zone and age of the Khardung volcanic rocks, Ladakh, India. *Journal of Asian Earth Sciences*, **20**, pp.481-490.

Dunlap, W.J. et al. 1998. Karakoram fault zone rocks cool in two phases. *Journal of the Geological Society*, **155**, pp.903-912.

Eberl, D.D. et al. 1987. Sericite from the Silverton caldera, CO: Correlation among structure, composition, origin, and particle thickness. *American Mineralogist*, **72**, pp.914-935.

Ellis S. et al. 2006. Simplified models of the Alpine Fault seismic cycle: stress transfer in the mid-crust. *Geophysical Journal International*, **166**, pp.386-402.

England, P.C. and Houseman, G.A. 1986. Finite strain calculations of continental deformation, 2, Comparison with the India-Asia collision. *Journal of Geophysical Research*, **91**, pp.3664-3676.

England, P.C. and Houseman, G.A. 1988. The mechanics of the Tibetan Plateau. *Philosophical Transactions of the Royal Society of London, A*, **326**, pp.301-319.

England, P.C. and Jackson, J.A. 2011. Uncharted seismic risk. *Nature Geoscience*, **4**, pp.348-349.

England, P.C. and McKenzie, D. 1982. A thin viscous sheet model for continental deformation. *Geophysical Journal of the Royal Astronomical Society*, **70**, pp.295-321.

- England, P.C. and McKenzie, D. 1983. Correction to: A thin viscous sheet model for continental deformation. *Geophysical Journal of the Royal Astronomical Society*, **73**, pp.523-532.
- England, P. and Molnar, P. 1990. Right-lateral shear and rotation as the explanation for strike-slip faulting in east Tibet. *Nature*, **344**, pp.140-142.
- England, P. and Molnar, P. 1997. The field of crustal velocity in Asia calculated from Quaternary rates of slip on faults. *Geophysical Journal International*, **130**, pp.551-582.
- England, P. and Molnar, P. 2005. Late Quaternary to decadal velocity fields in Asia. *Journal of Geophysical Research-Solid Earth*, **110**, B12401.
- Erdman, M.E. et al. 2013. Seismic anisotropy of the crust: electron-backscatter diffraction measurements from the Basin and Range. *Geophysical Journal International*, **195**, 1211-1229.
- Éric, S. et al. 2009. Ti-in-biotite geothermometry in non-graphitic, peraluminous metapelites from Crni vrh and Resavski humovi (Central Serbia). *Geologica Carpathica*, **60**, 3-14.
- Faulkner, D.R. et al. 2003. On the internal structure and mechanics of large strike-slip fault zones: field observations of the Carboneras fault in southeastern Spain. *Tectonophysics*, **367**, pp.235-251.
- Faulkner, D.R. et al. 2008. On the structure and mechanical properties of large strike-slip faults. *Geological Society, London, Special Publications*, **299**, pp.139-150.
- Fliervoet, T.F. et al. 1997. Evidence for dominant grain-boundary sliding deformation in greenschist- and amphibolite-grade polymineralic ultramylonites from the Redbank Deformed Zone, Central Australia. *Journal of Structural Geology*, **19**, pp.1495-1520.
- Foster, G. et al. 2004. The generation of prograde *P-T-t* points and paths; a textural, compositional and chronological study of metamorphic monazite. *Earth and Planetary Science Letters*, **228**, pp.125-142.

- Fraser, J.E. et al. 2001. Chronology of deformation, metamorphism and magmatism in the southern Karakoram mountains. *Geological Society of America Bulletin*, **113**, pp.1443-1455.
- Frost, E. et al. 2009. Progressive strain localisation in a major strike-slip fault exhumed from mid-seismogenic depths: Structural observations from the Salzach-Ennstal-Mariazell-Puchberg fault system, Austria. *Journal of Geophysical Research-Solid Earth*, **114**, B04406.
- Frost, E. et al. 2011. Direct observation of fault zone structure at the brittle-ductile transition along the Salzach-Ennstal-Mariazell-Puchberg fault system, Austrian Alps. *Journal of Geophysical Research-Solid Earth*, **116**, B02411.
- Fryer, P. et al. 1999. Mariana blueschist mud volcanism: Implications for conditions within the subduction zone. *Geology*, **27**, pp.103-106.
- Fu, B.H. and Awata, Y. 2007. Displacement and timing of left-lateral faulting in the Kunlun Fault Zone, northern Tibet, inferred from geologic and geomorphic features. *Journal of Asian Earth Sciences*, **29**, pp.253-265.
- Gaudemer, Y. et al. 1989. River offsets across active strike-slip faults. *Ann. Tectonicae*, **3**, pp.55-76.
- Gleason, G.C. et al. 1993. The role of dynamic recrystallization in the development of lattice preferred orientations in experimentally deformed quartz aggregates. *Journal of Structural Geology*, **15**, pp.1145-1168.
- Godard, G. and van Roermund, H.L.M. 1993. Deformation-induced clinopyroxene fabrics from eclogites. *Journal of Structural Geology*, **17**, pp.1425-1443.
- Goldsby, D.L. and Tullis, T.E. 2011. Flash heating leads to low frictional strength of crustal rocks at earthquake slip rates. *Science*, **334**, pp.216-218.
- Gratier, J.-P. et al. 2011. Aseismic sliding of active faults by pressure solution creep: Evidence from the San Andreas Fault Observatory at Depth. *Geology*, **39**, pp.1131-1134.
- Gratier, J.-P. et al. 2013. The Role of Pressure Solution Creep in the Ductility of the Earth's Upper Crust. In: Dmowska R. (ed.) *Advances in Geophysics*, **54**, pp.47-179.

Grocott, J. and Watterson, J. 1980. Strain profile of a boundary within a large ductile shear zone. *Journal of Structural Geology*, **2**, pp.111-117.

Grujic, D. et al. 2011. Thermometry of quartz mylonites: importance of dynamic recrystallisation on Ti-in-quartz reequilibration. *Geochemistry Geophysics Geosystems*, **12**, Q06012.

Hadizadeh, J. et al. 2012. A microstructural study of fault rocks from the SAFOD: Implications for the deformation mechanisms and strength of the creeping segment of the San Andreas Fault. *Journal of Structural Geology*, **42**, pp.246-260.

Halfpenny, A. et al. 2012. Electron backscatter diffraction analysis to determine the mechanisms that operated during dynamic recrystallisation of quartz-rich rocks. *Journal of Structural Geology*, **36**, pp.2-15.

Hammarstrom, J.M. and Zen, E.-an. 1986. Aluminium in hornblende: an empirical igneous geobarometer. *American Mineralogist*, **71**, pp.1297-1313.

Han, R. et al. 2011. Granular nanoparticles lubricate faults during seismic slip. *Geology*, **39**, pp.599-602.

Handy, M.R. 1990. Solid State Flow of Polymineralic Rocks. *Journal of Geophysical Research*, **95**, pp.8647-8661.

Handy, M.R. et al. 1999. Frictional-viscous flow in mylonite with varied biminerale composition and its effect on lithospheric strength. *Tectonophysics*, **303**, 175-191.

Handy, M.R. et al. 2005. Continental fault structure and rheology from the frictional-viscous transition downward. In: Handy M.R. et al. eds. *Tectonic Faults: Agents of Change on a Dynamic Earth*. Cambridge, Massachusetts: MIT Press, pp.139-181.

Hanmer, S. 1988. Great Slave Lake shear zone, Canadian shield: reconstructed vertical profile of a crustal-scale shear zone. *Tectonophysics*, **149**, pp.245-64.

Hansen, L.N. et al. 2014. Protracted fabric evolution in olivine: Implications for the relationship among strain, crystallographic fabric, and seismic anisotropy. *Earth and Planetary Science Letters*, **387**, pp.157-168.

Harrison, T.M. et al. 1985. Diffusion of ^{40}Ar in biotite: Temperature, pressure and compositional effects. *Geochimica and Cosmochimica Acta*, **49**, pp.2461-2468.

He, J., and Chéry J. 2008. Slip rates of the Altyn Tagh, Kunlun and Karakorum faults (Tibet) from 3D mechanical modelling. *Earth and Planetary Science Letters*, **274**, pp.50-58.

He, J.K. et al. 2013. Nailing down the slip-rate of the Altyn Tagh fault. *Geophysical Research Letters*, **40**, pp.5382-5386.

Heilbronner, R. and Tullis, J. 2006. Evolution of c axis pole figures and grain size during dynamic recrystallisation: Results from experimentally sheared quartzite. *Journal of Geophysical Research-Solid Earth*, **111**, B10202.

Henry, D.J. and Guidotti, C.V. 2002. Titanium in biotite from metapelitic rocks: Temperature effects, crystal-chemical controls, and petrologic applications. *American Mineralogist*, **87**, pp.375-382.

Henry, D. J. et al. 2005. The Ti-saturation surface for low-to-medium pressure metapelitic biotite: Implications for Geothermometry and Ti-substitution Mechanisms. *American Mineralogist*, **90**, 316-328.

Hey, M.H. 1954. A new review of chlorites. *Mineralogical Magazine*, **30**, pp.277-292.

Hickman, S. and Evans, B. 1995. Kinetics of pressure solution at halite-silica interfaces and intergranular clay films. *Journal of Geophysical Research*, **100**, pp.13113-13132.

Hickman, S. and Zoback, M. 2004. Stress orientations and magnitudes in the SAFOD pilot hole. *Geophysical Research Letters*, **31**, L15S12.

Hielscher, R., and Schaeben, H., 2008. A novel pole figure inversion method: specification of the MTEX algorithm. *Journal of Applied Crystallography*, **41**, pp.1024-1037.

Hillers, G. and Miller, S.A. 2007. Dilatancy controlled spatiotemporal slip evolution of a sealed fault with spatial variations of the pore pressure. *Geophysical Journal International*, **168**, pp.431-445.

- Hippertt, J.F.M. 1994. Grain boundary microstructures in micaceous quartzite: Significance for fluid movement and deformation processes in low metamorphic grade shear zones. *Geology*, **102**, pp.331-348.
- Hirth, G. and Kohlstedt, D.L. 2003. Rheology of the upper mantle and the mantle wedge: a view from the experimentalists. In: Eiler, J., (ed.) *Inside the subduction factory*. Washington D.C.: American Geophysical Society, Geophysical Monograph, **138**, pp.83-105.
- Hirth, G., and Tullis J. 1994. The brittle-plastic transition in experimentally deformed quartz aggregates. *Journal of Geophysical Research*, **99**, pp.11731-11747.
- Hirth, G. et al. 2001. An evaluation of quartzite flow laws based on comparisons between experimentally and naturally deformed rocks. *International Journal of Earth Sciences*, **90**, pp.77-87.
- Holdaway, M.J. 1971. Stability of andalusite and aluminium silicate phase diagram. *American Journal of Science*, **271**, pp.97-131.
- Holdaway, M.J. and Mukhopadhyay, B. 1993. A re-evaluation of the stability relations of andalusite; Thermochemical data and phase diagram for the aluminum silicates. *American Mineralogist*, **78**, pp.298–315.
- Holdsworth, R.E. 2004. Weak faults—Rotten cores. *Science*, **303**, pp.181-182.
- Holdsworth, R.E. et al. 2001. The structure and rheological evolution of reactivated continental fault zones: a review and case study. In: Miller J.A. et al. (eds.) *Continental Reactivation and Reworking*. Bath: Geological Society, London, Special Publications, 184, pp.115-137.
- Holdsworth, R.E. et al. 2011. Fault rocks from the SAFOD core samples: Implications for weakening at shallow depths along the San Andreas Fault, California. *Journal of Structural Geology*, **33**, pp.132-144.
- Holland, T. and Blundy, J. 1994. Non-ideal interactions in calcic amphiboles and their bearing on amphibole-plagioclase thermometry. *Contributions to Mineralogy and Petrology*, **116**, pp.433-447.

Holland, T. and Powell, R. 1998. An internally consistent thermodynamic data set for phases of petrological interest. *Journal of Metamorphic Geology*, **16**, pp.309-343.

Hollister, L.S. et al. 1987. Confirmation of the empirical correlation of Al in hornblende with pressure of solidification of calc-alkaline plutons. *American Mineralogist*, **72**, 231-239.

Holt W.E. et al. 2000. Velocity field in Asia inferred from Quaternary fault slip rates and Global Positioning System observations. *Journal of Geophysical Research*, **105**, pp.19185-19209.

Holyoke, C.W. and Kronenberg, A.K. 2013. Reversible water weakening of quartz. *Earth and Planetary Science Letters*, **374**, pp.185-190.

Houlié, N. and Phillips, R.J. 2013. Quaternary rupture behavior of the Karakoram Fault and its relation to the dynamics of the continental lithosphere, NW Himalaya–western Tibet. *Tectonophysics*, **599**, pp.1-7.

Houseknecht, D.W. 1988. Intergranular pressure solution in four quartzose sandstones. *Journal of Sedimentary Petrology*, **58**, pp.228-246.

Huang, W. and Lin, A. 2010. Weakness of the Intracontinental Strike-Slip Kunlun Fault and Implications for Tibetan Tectonics. *The Open Geology Journal*, **4**, pp.62-66.

Ikari, M.J. et al. 2011. On the relation between fault strength and frictional stability. *Geology*, **39**, 83-86.

Imber, J. et al. 1997. Fault-zone weakening processes along the reactivated Outer Hebrides Fault Zone, Scotland. *Journal of the Geological Society, London*, **154**, pp.105-109.

Imber, J. et al. 2001. A reappraisal of the Sibson-Scholz fault zone model: The nature of the frictional to viscous ("brittle-ductile") transition along a long-lived, crustal-scale fault, Outer Hebrides, Scotland. *Tectonics*, **20**, pp.601-624.

Imber, J. et al. 2008. Frictional-viscous flow, seismicity and the geology of weak faults: a review and future directions. In: Wibberley C.A.J. et al. eds.

Internal Structure of Fault Zones: Implications for Mechanical and Fluid-flow Properties. Bath: Geological Society Special Publication, **299**, pp.151-173.

Jackson, J. 2001. Living with earthquakes: Know your faults. *Journal of Earthquake Engineering*, **5**, pp.5-123.

Jackson, J. 2002. Strength of the continental lithosphere: time to abandon the jelly sandwich? *GSA Today*, **12**, pp.4-9.

Jackson, J. et al. 2008. New views on the structure and rheology of the lithosphere. *Journal of the Geological Society*, **165**, pp.453-465.

Jade, S. et al. 2004. GPS measurements from the Ladakh Himalaya, India: Preliminary tests of plate-like or continuous deformation in Tibet. *Geological Society of America Bulletin*, **116**, pp.1385-1391.

Jefferies, S.P. et al. 2006a. Origin and mechanical significance of foliated cataclastic rocks in the cores of crustal scale faults: Examples from the Median Tectonic Line, Japan. *Journal of Geophysical Research*, **111**, B12303.

Jefferies S.P. et al. 2006b. The nature and importance of phyllonite development in crustal-scale fault cores: an example from the Median Tectonic Line, Japan. *Journal of Structural Geology*, **28**, pp.220-235.

Jessell, M.W., and Lister, G.S., 1990. A simulation of the temperature dependence of quartz fabrics. In: Knipe, R.J. and Rutter, E.H. eds. *Deformation Mechanisms, Rheology and Tectonics*. Bath: Geological Society Special Publication, **54**, pp.353-362.

Jiang, W.T. et al. 1994. Chlorite geothermometry? – contamination and apparent octahedral vacancies. *Clays and Clay Minerals*, **42**, pp.593-605.

Johnson, M.C. and Rutherford, M.J. 1989. Experimental calibration of the aluminium-in-hornblende geobarometer with application of Long Valley caldera (California) volcanic rocks. *Geology*, **17**, pp.837-841.

Jung, H., and Karato, S., 2001. Water-Induced Fabric Transitions in Olivine. *Science*, **293**, pp.1460-1463.

Kaminski, É., and Ribe, N.M., 2001. A kinematic model for recrystallisation and texture development in olivine polycrystals. *Earth and Planetary Science Letters*, **189**, pp.253-267.

Kanamori, H. and Brodski, E.E. 2004. The physics of Earthquakes. *Reports on Progress in Physics*, **67**, pp.1429-1496.

Kapp, P. et al. 2003. Tectonic evolution of the early Mesozoic blueschist-bearing Qiangtang metamorphic belt, central Tibet. *Tectonics*, **22**, 1043.

Karplus, M.S. et al. 2011. Injection of Tibetan crust beneath the south Qaidam Basin: Evidence from INDEPTH IV wide-angle seismic data. *Journal of Geophysical Research-Solid Earth*, **116**, B07301.

Kilian, R. et al. 2011. Quartz grain size reduction in a granitoid rock and the transition from dislocation to diffusion creep. *Journal of Structural Geology*, **33**, pp.1265-1284.

Kim, Y.-S. et al. 2004. Fault damage zones. *Journal of Structural Geology*, **26**, pp.503-517.

Kirby, E. et al. 2007. Slip-rate gradients along the eastern Kunlun fault. *Tectonics*, **26**, TC2010.

Kirkpatrick, J.D. et al. 2013. Silica gel formation during fault slip: Evidence from the rock record. *Geology*, **41**, pp.1015-1018.

Kirstein, L.A. et al. 2009. Cenozoic unroofing history of the Ladakh Batholith, western Himalaya, constrained by thermochronology and numerical modelling. *Journal of the Geological Society, London*, **166**, pp.667-678.

Klein, E.L. and Koppe, J.C. 2000. Chlorite geothermometry and physicochemical conditions of gold mineralization in the Paleoproterozoic Caxias deposit, São Luís craton, northern Brazil. *Geochimica Brasiliensis*, **14**, pp.219-232.

Klemperer, S.L. 2006. Crustal flow in Tibet: geophysical evidence for the physical state of Tibetan lithosphere, and inferred patterns of active flow. In: Law, R.D. et al. eds. *Channels Flow, Ductile Extrusion and Exhumation in Continental Collision Zones*. Bath: Geological Society Special Publication, **268**, pp.39-70.

Klemperer, S.L. et al. 2013. Mantle fluids in the Karakoram fault: Helium isotope evidence. *Earth and Planetary Science Letters*, **366**, pp.59-70.

Knipe, R.J. 1989. Deformation mechanisms – recognition from natural tectonites. *Journal of Structural Geology*, **11**, pp.127-146.

Kranidiotis, P. and MacLean, W.H. 1987. Systematics of Chlorite Alteration at the Phelps Dodge Massive Sulfide Deposit, Matagami, Quebec. *Economic Geology*, **82**, pp.1898-1911.

Kronenberg, A.K. and Tullis, J. 1984. Flow strengths of quartz aggregates – grain-size and pressure effects due to hydrolytic weakening. *Journal of Geophysical Research*, **89**, pp.4281-4297.

Kronenberg, A.K. et al. 1990. Basal slip and mechanical anisotropy of biotite. *Journal of Geophysical Research*, **85**, pp.19257-19278.

Kruhl, J.H. 1998. Reply: Prism- and basal-plane parallel subgrain boundaries in quartz: a potential microstructural geothermobarometer. *Journal of Metamorphic Geology*, **16**, pp.142-146.

Kruse, R. and Stünitz, H. 1999. Deformation mechanisms and phase distribution in mafic high-temperature mylonites from the Jotun Nappe, Southern Norway. *Tectonophysics*, **303**, pp.223-249.

Lacassin, R. et al. 2004a. Large-scale geometry, offset and kinematic evolution of the Karakoram Fault, Tibet. *Earth and Planetary Science Letters*, **219**, pp.255-269.

Lacassin, R. et al. 2004b. Reply to Comment on “Large-scale geometry, offset and kinematic evolution of the Karakoram fault, Tibet”. *Earth and Planetary Science Letters*, **229**, pp.159-163.

Lamouroux, C. et al. 1980. Shear zones in the granodioritic massifs of the central Pyrenees and the behaviour of these massifs during Alpine orogenesis. *Journal of Structural Geology*, **2**, pp.49-53.

Lanari, P. et al. 2014. A thermodynamic model for di-trioctahedral chlorite from experimental and natural data in the system MgO-FeO-Al₂O₃-SiO₂-H₂O: applications to P-T sections and geothermometry. *Contributions to Mineralogy and Petrology*, **167**, 968.

Law, R.D. 2014. Deformation thermometry based on quartz c-axis fabrics and recrystallization microstructures: a review. *Journal of Structural Geology*, **66**, 129-161.

Law, R.D. et al. 2010. Moine Thrust zone mylonites at the stack of Glencoul: I – microstructures, strain and influence of recrystallization on quartz crystal fabric development. In: Law, R.D. et al. eds. *Continental Tectonics and Mountain Building: The Legacy of Peach and Horne*. Bath: Geological Society, London, Special Publications, **335**, pp.543-577.

Lee, E.P. et al. 2012. Strain partitioning in the mid-crust of a transpressional shear zone system: Insights from the Homestake and Slide Lake shear zones, central Colorado. *Journal of Structural Geology*, **39**, pp.237-252.

Leech, M.L. 2008. Does the Karakoram fault interrupt mid-crustal channel flow in the western Himalaya? *Earth and Planetary Science Letters*, **276**, pp.314-322.

Leech, M.L. 2009. Reply to comment by M.P. Searle and R.J. Phillips (2009) and R.R. Parrish (2009) on: “Does the Karakoram fault interrupt mid-crustal channel flow in the western Himalaya?” by Mary L. Leech, *Earth and Planetary Science Letters* 276 (2008) 314-322. *Earth and Planetary Science Letters*, **286**, pp.592-595.

Leloup P.H. et al. 1995. The Ailao Shan-Red River shear zone (Yunnan, China), Tertiary transform boundary of Indochina. *Tectonophysics*, **251**, pp.3-10.

Leloup, P.H. et al. 1999. Shear heating in continental strike-slip shear zones: model and field examples. *Geophysical Journal International*, **136**, pp.19-40.

Leloup P.H. et al. 2011. Long-lasting intra-continental strike-slip faulting: New evidence from the Karakoram shear zone in the Himalayas. *Terra Nova*, **23**, pp.92-99.

Leloup, P.H. et al. 2013. Comment on “Displacement along the Karakoram fault, NW Himalaya, estimated from LA-ICP-MS U Pb dating of offset geologic markers” published by Shifeng Wang et al. in *EPSL*, 2012. *Earth and Planetary Science Letters*, **363**, pp.242-245.

Le Pape, F. et al. 2012. Penetration of crustal melt beyond the Kunlun Fault into northern Tibet. *Nature Geoscience*, **5**, pp.330-335.

Lisle, R.J. 1985. The use of the orientation tensor for the description and statistical testing of fabrics. *Journal of Structural Geology*, **7**, pp.115-117.

Lisowski, M. et al. 1991. The velocity-field along the San-Andreas fault in central and southern California. *Journal of Geophysical Research-Solid Earth and Planets*, **96**, pp.8369-8389.

Lister, G.S. and Hobbs, B.E. 1980. The simulation of fabric development during plastic deformation and its application to quartzite: the influence of deformation history. *Journal of Structural Geology*, **2**, pp.355-370.

Liu, Q. 1993. *Paléoclimat et contraintes chronologiques sur les mouvements récent dans l'Ouest du Tibet: Failles du Karakorum et de Longmu Co-Gozha Co, lacs en pull-apart de Longmu Co et de Sumxi Co*. Ph.D thesis, Université Paris VII.

Lloyd, G. 1987. Atomic number and crystallographic contrast images with the SEM: a review of backscattered electron techniques. *Mineralogical Magazine*, **51**, pp.3-19.

Lloyd, G.E. and Kendall, J.M. 2005. Petrofabric-derived seismic properties of a mylonitic quartz simple shear zone: implications for seismic reflection profiling. In: Harvey, P.K. et al. eds. *Petrophysical Properties of Crystalline Rocks*. Bath: Geological Society, London, Special Publications, **240**, pp.75-94.

Lloyd, G.E. et al. 1997. Misorientation analysis and the formation and orientation of subgrain and grain boundaries. *Tectonophysics*, **279**, pp.55-78.

Lloyd, G.E. et al. 2011. From crystal to crustal: petrofabric derived seismic modelling of regional tectonics. In: Prior D.J. et al. eds. *Deformation Mechanisms, Rheology and Tectonics: Microstructures, Mechanics and Anisotropy*. Bath: Geological Society, London, Special Publication, **360**, pp.7-32.

Lockner, D.A. et al. 2011. Low strength of deep San Andreas fault gouge from SAFOD core. *Nature*, **472**, pp.82-85.

Lyons, S. and Sandwell, D. 2003. Fault creep along the southern San Andreas from interferometric synthetic aperture radar, permanent scatterers, and stacking. *Journal of Geophysical Research*, **108**, B12047.

Mainprice, D. 1990. An efficient Fortran program to calculate seismic anisotropy from the lattice preferred orientation of minerals. *Computers and Geosciences*, 16, pp.385-393.

Mainprice, D. et al. 1986. Dominant c-slip in naturally deformed quartz: implications for dramatic plastic softening at high temperature. *Geology*, **14**, pp.819-822.

Malservisi, R. et al. 2003. Numerical modeling of strike-slip creeping faults and implications for the Hayward fault, California. *Tectonophysics*, **361**, pp.121-137.

Mainprice, D. et al. 2011. Calculating anisotropic physical properties from texture data using the MTEX open-source package. In: Prior, D.J. et al. eds. *Deformation Mechanisms, Rheology and Tectonics: Microstructures, Mechanics and Anisotropy*. Geological Society, London, Special Publications, **360**, pp.175-192.

Mainprice, D. et al. in press. Descriptive tools for the analysis of texture projects with large datasets using MTEX – strength, symmetry, and components. In: Faulkner, D.R. et al. eds. *Rock Deformation from Field, Experiments and Theory: A Volume in Honour of Ernie Rutter*. Bath: Geological Society, London, Special Publications.

Manatschal, G. 1999. Fluid- and reaction-assisted low-angle normal faulting: evidence from rift-related brittle fault rocks in the Alps (Err Nappe, eastern Switzerland). *Journal of Structural Geology*, 21, pp.777-793.

Mancktelow, N.S. 1987. Quartz textures from the Simplon Fault Zone, southwest Switzerland and north Italy. *Tectonophysics*, **135**, pp.133-153.

Mardia, K., 1972. *Statistics of Directional Data*. London: Academic Press, pp.357.

Marone, C. and Scholz, C.H. 1988. The depth of seismic faulting and the upper transition from stable to unstable slip regimes. *Geophysical Research Letters*, **15**, pp.621-624.

Marsh, J.H. et al. 2009. Coupling of deformation and reactions during mid-crustal shear zone development: an *in situ* frictional-viscous transition. *Journal of Metamorphic Geology*, **27**, pp.531-553.

McCaffrey, R. and Nabelek, J. 1998. Role of oblique convergence in the active deformation of the Himalayas and southern Tibet plateau. *Geology*, **26**, pp.691-694.

McCarthy, M.R. and Weinberg, R.F. 2010. Structural complexity resulting from pervasive ductile deformation in the Karakoram Shear Zone, Ladakh, NW India. *Tectonics*, **29**, TC3004.

McClay, K.R. 1977. Pressure solution and Coble creep in rocks and minerals: a review. *Journal of the Geological Society of London*, **134**, pp.57-70.

Meade, B.J. 2007. Present-day kinematics at the India-Asia collision zone. *Geology*, **35**, pp.81-84.

Menegon, L. et al. 2008. Evolution of quartz microstructure and c-axis crystallographic preferred orientation within ductilely deformed granitoids (Arolla unit, Western Alps). *Journal of Structural Geology*, **30**, pp.1332-1347.

Mitra, G. 1978. Ductile deformation zones and mylonites: the mechanical processes involved in the deformation of crystalline basement rocks. *American Journal of Science*, **278**, pp.1057-1084.

Mizuno, T. et al. 2008. Spatial Variations in Fault-Zone Structure along the Nojima Fault, Central Japan, as Inferred from Borehole Observations of Fault-Zone Trapped Waves. *Bulletin of the Seismological Society of America*, **98**, pp.558-570.

Molnar, P. 1988. Continental tectonics in the aftermath of plate tectonics. *Nature*, **335**, pp.131-137.

Molnar, P. and Lyon-Caen H. 1989. Fault plane solutions of earthquakes and active tectonics of the Tibetan Plateau and its margins. *Geophysical Journal International*, **99**, pp.123-153.

Morales, L.F.G. et al. in review. Fabric transitions in quartz via viscoplastic self-consistency modelling Part I: axial compression and simple shear under constant strain: *Tectonophysics*.

Morales, L.F.G. et al. 2011. Crystal fabric development and slip systems in a quartz mylonite: an approach via transmission electron microscopy and viscoplastic self-consistent modelling. In: Prior, D.J. et al. eds. *Microstructures, Mechanics, and Anisotropy*. Bath: Geological Society, London, Special Publications, **360**, pp.151-174.

Morgan, D.J., Jollands, M.C., Lloyd, G.E., Banks, D.A. 2013. Using titanium-in-quartz geothermometry and geospeedometry to recover temperatures in the aureole of the Ballachullish Igneous Complex, NW Scotland. In: Llana-Funez, S. et al. eds. *Deformation Structures and Processes within the Continental Crust*. Bath: Geological Society, London, Special Publications, **394**.

Morgan, S.S. and Law, R.D. 2004. Unusual transition in quartzite dislocation creep regimes and crystal slip systems in the aureole of the EJB pluton, California: a case for anhydrous conditions created by decarbonation of adjacent marbles. *Tectonophysics*, **384**, pp.209-231.

Morrow, C.A. et al. 2000. The effect of mineral bond strength and adsorbed water on fault gouge frictional strength. *Geophysical Research Letters*, **27**, pp.815-818.

Mukherjee, B.K. et al. 2012. Exhumation history of the Karakoram fault zone mylonites: New constraints from microstructures, fluid inclusions, and $^{40}\text{Ar}/^{39}\text{Ar}$ analyses. *Lithosphere*, **4**, pp.230-241.

Murphy, M.A. et al. 2000. Southward propagation of the Karakoram fault system, southwest Tibet: Timing and magnitude of slip. *Geology*, **28**, pp.451-454.

Murphy, M.A. et al. 2002. Structural evolution of the Gurla Mandhata detachment system, south-west Tibet: implications for the eastward extent of the Karakoram fault system. *Geological Society of America Bulletin*, **114**, pp.428-447.

- Murphy, M.A. et al. 2014. Limit of strain partitioning in the Himalaya marked by large earthquakes in western Nepal. *Nature Geoscience*, **7**, 38-42.
- Murray, J. and Langbein, J. 2006. Slip on the San Andreas fault at Parkfield, California, over two earthquake cycles, and the implications for seismic hazard. *Bulletin of the Seismological Society of America*, **96**, S283-S303.
- Neall, F.B. and Phillips, G.N. 1987. Fluid-wall interaction in an Archean hydrothermal gold deposit: a thermodynamic model for the Hunt Mine, Kambalda. *Economic Geology*, **82**, pp.1679-1694.
- Neil, E.A. and Houseman, G.A. 1997. Geodynamics of the Tarim Basin and the Tien Shan in central Asia. *Tectonics*, **16**, pp.571-584.
- Niemeijer, A.R. and Spiers C.J. 2005. Influence of phyllosilicates on fault strength in the brittle-ductile transition: insights from rock analogue experiments. In: Bruhn, D. and Burlini, L. eds. *High Strain Zones: Structure and Physical Properties*. Bath: Geological Society, London, Special Publications, **245**, pp.303-327,
- Niemeijer, A.R. and Spiers, C.J. 2006. Velocity dependence of strength and healing behavior in simulated phyllosilicate-bearing fault gouge. *Tectonophysics*, **427**, pp.231-253.
- Niemeijer, A.R. and Spiers, C.J. 2007. A microphysical model for strong velocity weakening in phyllosilicate-bearing fault gouges. *Journal of Geophysical Research-Solid Earth*, **112**, B10405.
- Noda, H. and Lapusta, N. 2013. Stable creeping fault segments can become destructive as a result of dynamic weakening. *Nature*, **493**, pp.518-521.
- Norris, R.J. and Cooper, A.F. 2001. Late Quaternary slip-rates and slip-partitioning on the Alpine Fault, New Zealand. *Journal of Structural Geology*, **23**, pp.507-520.
- Norris, R.J. and Cooper, A.F. 2003. Very high strains recorded in mylonites along the Alpine Fault, New Zealand: implications for the deep structure of plate boundary faults. *Journal of Structural Geology*, **25**, pp.2141-2157.
- Oskin, M. et al. 2008. Elevated shear zone loading rate during an earthquake cluster in eastern California. *Geology*, **36**, pp.507-510.

Otten, M.T. 1984. The origin of brown amphibole in the Artfjället gabbro and dolerites. *Contributions to Mineralogy and Petrology*, **86**, pp.189-199.

Palin, R.M. et al. 2012. Combined thermobarometry and geochronology of peraluminous metapelites from the Karakoram metamorphic complex, North Pakistan: New insights into the tectonothermal evolution of the Baltoro and Hunza Valley regions. *Journal of Metamorphic Geology*, **30**, pp.793-820.

Park, R.G. 2010. Structure and evolution of the Lewisian Gairloch shear zone: variable movement directions in a strike-slip regime. *Scottish Journal of Geology*, **46**, pp.31-44.

Parrish, R.R. 2009. Comment on: "Does the Karakoram fault interrupt mid-crustal channel flow in the western Himalaya?" by Mary L. Leech, *Earth and Planetary Science Letters* 276 (2008) 314-322. *Earth and Planetary Science Letters*, **286**, pp.586-588.

Parry, W.T. et al. 1988. Pore-fluid chemistry and chemical-reactions on the Wasatch normal-fault, Utah. *Geochimica et Cosmochimica Acta*, **52**, pp.2053-2063.

Passchier, C.W. and Trouw, R.A.J. 2005. *Microtectonics*. 2nd ed. Berlin: Springer, pp.366.

Paterson, S.R. and Tobisch, O.T. 1988. Using pluton ages to date regional deformations: Problems with commonly used criteria. *Geology*, **16**, pp.1108-1111.

Paterson, S.R. et al. 1989. A review of criteria for the identification of magmatic and tectonic foliations in granitoids. *Journal of Structural Geology*, **11**, pp.349-363.

Paterson, S.R. et al. 1998. Interpreting magmatic fabric patterns in plutons. *Lithos*, **44**, pp.53-82.

Pearce, M.A. et al. 2011. Relative strength of mafic and felsic rocks during amphibolite facies metamorphism and deformation. *Journal of Structural Geology*, **33**, pp.662-675.

Peltzer, G. and Saucier, F. 1996. Present-day kinematics of Asia derived from geologic fault rates. *Journal of Geophysical Research-Solid Earth*, **101**, pp.27943-27956.

Peltzer, G. and Tapponnier, P. 1988. Formation and evolution of strike-slip faults, rifts, and basins during the India-Asia collision: An experimental approach. *Journal of Geophysical Research*, **93**, pp.15085-15117.

Pe-Piper, G. et al. 1998. Synkinematic granite emplacement in a shear zone: The Pleasant Hills pluton, Canadian Appalachians. *Geological Society of America Bulletin*, **110**, pp.523-536.

Phartiyal, B. and Sharma, A. 2009. Soft-sediment deformation structures in the Late Quaternary sediments of Ladakh: Evidence for multiple phases of seismic tremors in the North western Himalayan Region. *Journal of Asian Earth Sciences*, **34**, pp.761-770.

Phartiyal, B. et al. 2005. Quaternary geology, tectonics and distribution of palaeo- and present fluvio/glacio lacustrine deposits in Ladakh, NW Indian Himalaya-a study based on field observations. *Geomorphology*, **65**, pp.214-256.

Phillips, R.J. 2004. *Macro- and Micro-structural Evolution of the Karakoram Fault*. D.Phil thesis, University of Oxford.

Phillips, R.J. 2008. Geological map of the Karakoram Fault zone, Eastern Karakoram, Ladakh, NW Himalaya. *Journal of Maps*, **2008**, pp.38-49.

Phillips, R.J. and Searle M.P. 2007. Macrostructural and microstructural architecture of the Karakoram fault: Relationship between magmatism and strike-slip faulting. *Tectonics*, **26**, TC3017.

Phillips, R.J. et al. 2004. Age constraints on ductile deformation and long-term slip rates along the Karakoram fault zone, Ladakh. *Earth and Planetary Science Letters*, **226**, pp.305-319.

Phillips, R.J. et al. 2013. The geochemical and temporal evolution of the continental lithosphere and its relationship to continental-scale faulting: The Karakoram Fault, eastern Karakoram, NW Himalayas. *Geochemistry, Geophysics, Geosystems*, **14**, pp.583-603.

Platt, J.P. and Behr, W.M. 2011. Deep structure of lithospheric fault zones. *Geophysical Research Letters*, **38**, L24308.

Platt, J.P. and Behr, W.M. 2012. Lithospheric shear zones as constant stress experiments. *Geology*, **39**, pp.127-130.

Prior, D.J. et al. 1999. The application of Electron Backscatter Diffraction and Orientation Contrast Imaging in the SEM to textural problems in rocks. *American Mineralogist*, **84**, pp.1741-1759.

Pullen, A. et al. 2011. Metamorphic rocks in central Tibet: Lateral variations and implications for crustal structure. *Geological Society of America Bulletin*, **123**, pp.585-600.

Que, M. and Allen A.R. 1996. Sericitization of plagioclase in the Rosses Granite Complex, Co. Donegal, Ireland. *Mineralogical Magazine*, **60**, pp.927-936.

Reichardt, H. and Weinberg, R.F. 2012. Hornblende Chemistry in Meta- and Diatexites and its Retention in the Source of Leucogranites: an Example from the Karakoram Shear Zone, NW India. *Journal of Petrology*, **53**, pp.1287-1318.

Reichardt, H. et al. 2010. Hybridization of granitic magmas in the source: The origin of the Karakoram Batholith, Ladakh, NW India. *Lithos*, **116**, pp.249-272.

Rennie, S.F. et al. 2013. Strain distribution within a km-scale, mid-crustal shear zone: The Kuckaus Mylonite Zone, Namibia. *Journal of Structural Geology*, **56**, pp.57-69.

Revenaugh, J. and Reasoner, C. 1997. Cumulative offset of the San Andreas fault in central California: A seismic approach. *Geology*, **25**, pp.123-126.

Ritts, B.D. and Biffi, U. 2000. Magnitude of post-Middle Jurassic (Bajocian) displacement on the central Altyn Tagh fault system, northwest China. *Geological Society of America Bulletin*, **112**, pp.61-74.

Robinson, A.C. 2009a. Geologic offsets across the northern Karakorum fault: Implications for its role and terrane correlations in the western

Himalayan-Tibetan orogen. *Earth and Planetary Science Letters*, **279**, pp.123-130.

Robinson, A.C. 2009b. Evidence against Quaternary slip on the northern Karakorum Fault suggests kinematic reorganization at the western end of the Himalayan-Tibetan orogen. *Earth and Planetary Science Letters*, **286**, pp.158-170.

Rolland, Y. and Pêcher, A. 2001. The Pangong Granulites of the Karakoram Fault (Western Tibet): vertical extrusion within a lithosphere-scale fault? *Earth and Planetary Sciences*, **332**, pp.363-370.

Rolland Y. et al. 2009. Syn-kinematic emplacement of the Pangong metamorphic and magmatic complex along the Karakorum Fault (N Ladakh). *Journal of Asian Earth Sciences*; **34**, pp.10-25.

Rowley, D.B. 1996. Age of initiation of collision between India and Asia: A review of stratigraphic data. *Earth and Planetary Science Letters*, **145**, pp.1-13.

Ruina, A. 1983. Slip instability and state variable friction laws. *Journal of Geophysical Research*, **88**, pp.10359-10370.

Rutter, E.H. 1976. The kinetics of rock deformation by pressure solution. *Philosophical Transactions of the Royal Society of London Series A*, **283**, pp.203-219.

Rutter, E.H. 1983. Pressure solution in nature, theory and experiment. *Journal of the Geological Society, London*, **140**, pp.725-740.

Rutter, E.H. 1986. On the nomenclature of mode of failure transitions in rocks. *Tectonophysics*, **122**, pp.381-387.

Rutter, E.H. et al. 2007. Rock deformation processes in the Karakoram fault zone, Eastern Karakoram, Ladakh, NW India. *Journal of Structural Geology*, **29**, pp.1315-1326.

Rutter, E.H. et al. 2001. The nature and tectonics significance of fault-zone weakening: an introduction. In: Holdsworth R.E. et al. eds. *The Nature and Tectonic Significance of Fault Zone Weakening*. Bath: Geological Society, London, Special Publications, 186, pp.1-11.

- Rutter, E.H. et al. 2013. Reduction of friction on geological faults by weak-phase smearing. *Journal of Structural Geology*, 51, pp.52-60.
- Saffer, D.M. and Marone, C. 2003. Comparison of smectite- and illite-rich gouge frictional properties: application to the updip limit of the seismogenic zone along subduction megathrusts. *Earth and Planetary Science Letters*, **215**, pp.219-235.
- Saffer, D.M. et al. 2001. Laboratory results indicating complex and potentially unstable frictional behaviour of smectite clay. *Geophysical Research Letters*, **28**, pp.2297-2300.
- Sanders, C.O. 1990. Earthquake Depths and the Relation to Strain Accumulation and Stress Near Strike-Slip Faults in Southern California. *Journal of Geophysical Research*, **95**, pp.4751-4762.
- Sartini-Rideout, C. et al. 2006. Geology and timing of dextral strike-slip shear zones in Danmarkshavn, North-East Greenland Caledonides. *Geological Magazine*, **143**, pp.431-446.
- Sassier, C. et al. 2009. Direct measurement of strain rates in ductile shear zones: A new method based on syntectonic dikes. *Journal of Geophysical Research*, **114**, 01406.
- Scheidegger, A.E. 1965. On the statistics of the orientation of bedding planes, grain axes, and similar sedimentological data. *U.S. Geological Survey Professional Paper*, **525-C**, pp.164-167.
- Schiffman, P. and Fridleifsson, G.O. 1991. The smectite-chlorite transition in drillhole NJ=15, Nesjavellir geothermal field, Iceland: XRD, BSE and electron microprobe investigations. *Journal of Metamorphic Geology*, 9, pp.679-696.
- Schleicher, A.M. et al. 2010. Nanocoatings of clay and creep of the San Andreas fault at Parkfield, California. *Geology*, **38**, pp.667-670.
- Schleicher, A.M. et al. 2012. Chlorite-smectite clay minerals and fault behaviour: New evidence from the San Andreas Fault Observatory at Depth (SAFOD) core. *Lithosphere*, **4**, pp.209-220.
- Schmid, S.M. and Casey, M. 1986. Complete fabric analysis of some commonly observed quartz *c*-axis patterns. In: Hobbs, B.E. and Heard, H.C.

eds. *Mineral and Rock Deformation Laboratory Studies: The Paterson Volume*. Washington D.C.: American Geophysical Union, Geophysical Monograph, **36**, pp.263-286.

Schmid, S.M. and Handy, M.R. 1991. Towards a genetic classification of fault rocks: Geological usage and tectonophysical implications. In: Muller, D.W. et al. eds. *Controversies in Modern Geology: Evolution of Geological Theories in Sedimentology, Earth History and Tectonics*. San Diego: Academic. pp.339-361.

Schmidt, M.W. 1992. Amphibole composition in tonalite as a function of pressure: an experimental calibration of the Al-in-hornblende barometer. *Contributions to Mineralogy and Petrology*, **110**, pp.304-310.

Scholz, C.H. 1988. The brittle-plastic transition and the depth of seismic faulting. *Geologische Rundschau*, **77**, pp.319-328.

Scholz, C.H. 1989. Mechanics of Faulting. *Annual Reviews of Earth and Planetary Sciences*, **17**, pp.309-334.

Scholz, C.H. 1998. Earthquakes and friction laws. *Nature*, **391**, pp.37-42.

Scruggs, V.J. and Tullis T.E. 1998. Correlation between velocity dependence of friction and strain localization in large displacement experiments on feldspar, muscovite and biotite gouge. *Tectonophysics*, **295**, pp.15-40.

Searle, M.P. 1996. Geological evidence against large-scale pre-Holocene offsets along the Karakoram fault: Implications for the limited extrusion of the Tibetan Plateau. *Tectonics*, **15**, pp.171-186.

Searle, M.P. 2013. Crustal melting, ductile flow, and deformation in mountain belts: Cause and effect relationships. *Lithosphere*, **5**, pp.547-554.

Searle, M.P. and Phillips, R.J. 2004. A comment on "Large-scale geometry, offset, and kinematic evolution of the Karakoram fault, Tibet" by R. Lacassin et al. (Earth Planet. Sci. Lett. 219 (2004) 255–69). *Earth and Planetary Science Letters*, **229**, pp.255-269.

Searle, M.P. and Phillips, R.J. 2007. Relationships between right-lateral shear along the Karakoram fault and metamorphism, magmatism,

exhumation and uplift: evidence from the K2-Gasherbrum-Pangong ranges, north Pakistan and Ladakh. *Journal of the Geological Society, London*, **164**, pp.439-450.

Searle, M.P. et al. 1990. Age of crystallisation and cooling of the K2 gneiss in the Baltoro Karakoram. *Journal of Geological Society, London*, **147**, pp.603-606.

Searle, M.P. et al. 1998. Transpressional tectonics along the Karakoram fault zone, northern Ladakh: constraints on Tibetan extrusion. In: Holdsworth, R.E. eds. *Continental Transpressional and Transtensional Tectonics*. Bath: Geological Society, London, Special Publications, **35**, 307-326.

Searle, M.P. et al. 2010. Anatomy, age and evolution of a collisional mountain belt: the Baltoro granite batholith and Karakoram Metamorphic Complex, Pakistani Karakoram. *Journal of the Geological Society, London*, **167**, pp.183-202.

Searle M.P. et al. 2011. Crustal-lithospheric and continental extrusion of Tibet. *Journal of the Geological Society, London*, **168**, pp.633-672.

Segall, P. 2012. Understanding earthquakes. *Science*, 336, pp.676-677.

Sen, K. et al. 2014. Interplay of deformation and magmatism in the Pangong transpressional Zone, eastern Ladakh, India: Implications for remobilisation of the trans-Himalayan magmatic arc and initiation of the Karakoram Fault. *Journal of Structural Geology*, **62**, pp.13-24.

Sharman, G.R. et al. 2013. A reappraisal of the early slip history of the San Andreas fault, central California, USA. *Geology*, 41, pp.727-730.

Shearer, P.M. 2002. Parallel fault strands at 9-km depth Resolved on the Imperial Fault, Southern California. *Geophysical Research Letters*, **29**, 1674.

Shigematsu, N. et al. 2012. Internal structure of the Median Tectonic Line fault zone, SW Japan, revealed by borehole analysis. *Tectonophysics*, 532, pp.103-118.

- Shimizu, I., 2008. Theories and applicability of grain size piezometers, the role of dynamic recrystallization mechanisms. *Journal of Structural Geology*, **30**, pp.899-917.
- Sibson, R. 1977. Fault rocks and fault mechanisms. *Journal of the Geological Society, London*, **133**, pp.191-213.
- Sibson, R. 1980. Transient discontinuities in ductile shear zones. *Journal of Structural Geology*, **2**, pp.165-171.
- Sibson, R. 1982. Fault zone models, heat flow, and the depth distribution of earthquakes in the continental crust of the United States. *Bulletin of the Seismological Society of America*, **72**, pp.151-163.
- Sibson, R. 1983. Continental Fault Structure and the Shallow Earthquake Source. *Journal of the Geological Society*, **140**, pp.741-767.
- Sibson, R. 1986. Earthquakes and Rock Deformation in Crustal Fault Zones. *Annual Review of Earth and Planetary Sciences*, **14**, pp.149-175.
- Sibson, R. 2003. Thickness of the seismic slip zone. *Bulletin of the Seismological Society of America*, **93**, pp.1169-1178.
- Singleton, J.S. and Mosher, S. 2012. Mylonitization in the lower plate of the Buckskin-Rawhide detachment fault, west-central Arizona: Implications for the geometric evolution of metamorphic core complexes. *Journal of Structural Geology*, **39**, pp.180-198.
- Skemer, P. et al. 2005. The misorientation index: Development of a new method for calculating the strength of lattice-preferred orientation. *Tectonophysics*, **411**, pp.157-167.
- Sloan, R.A. et al. 2011. Earthquake depth distributions in central Asia, and their relations with lithosphere thickness, shortening and extension. *Geophysical Journal International*, **185**, pp.1-29.
- Smith, S.A.F. et al. 2008. Recognizing the seismic cycle along ancient faults: CO₂-induced fluidization of breccias in the footwall of a sealing low-angle normal fault. *Journal of Structural Geology*, **30**, pp.1034-1046.
- Sobel, E.R. and Arnaud, N. 1999. A possible middle Paleozoic suture in the Altyn Tagh, NW China. *Tectonics*, **18**, pp.64-74.

Solum, J.G. et al. 2006. Mineralogical characterization of protolith and fault rocks from the SAFOD Main Hole. *Geophysical Research Letters*, **33**, L21314.

Sørensen, K. 1983. Growth and Dynamics of the Nordre Strømfjord Shear Zone. *Journal of Geophysical Research*, **88**, pp.3419-3437.

Southerland, R. et al. 2012. Drilling reveals fluid control on architecture and rupture of the Alpine fault New Zealand. *Geology*, **40**, pp.1143-1146.

Srimal, N. 1986. India-Asia collision: Implications from the Geology of the eastern Karakoram. *Geology*, **14**, pp.523-527.

Steffen, K. et al. 2001. Episodic weakening and strengthening during synmetamorphic deformation in a deep-crustal shear zone in the Alps. In: Holdsworth R.E. et al. eds. *The Nature and Tectonic Significance of Fault Zone Weakening*. Bath: Geological Society, London, Special Publications, **186**, 141-156.

Stewart M. et al. 1999. The structure and early kinematic history of the Great Glen Fault Zone, Scotland. *Tectonics*, **18**, pp.326-342.

Stewart, M. et al. 2000. Deformation processes and weakening mechanisms within the frictional-viscous transition zone of major crustal-scale faults: insights from the Great Glen Fault Zone, Scotland. *Journal of Structural Geology*, **22**, pp.543-560.

Stipp, M. and Tullis, J. 2003. The recrystallized grain size piezometer for quartz. *Geophysical Research Letters*, **30**, 2088.

Stipp, M. et al. 2002. Dynamic recrystallisation of quartz: Correlation between natural and experimental conditions. In: De Meer, S. et al. eds. *Deformation Mechanisms, Rheology and Tectonics: Current Status and Future Perspectives*. Geological Society, London, Special Publications, **20**, pp.171-190.

Stipp, M. et al. 2010. A new perspective on paleopiezometry: Dynamically recrystallised grain size distributions indicate mechanism changes. *Geology*, **38**, pp.759-762.

Strecker M.R. et al.1995. Quaternary deformation in the eastern Pamirs, Tajikistan and Kyrgyzstan. *Tectonics*, **14**, pp.1061-1079.

Streule, M.J. et al. 2009. Evolution and chronology of the Pangong Metamorphic Complex adjacent to the Karakoram Fault, Ladakh: constraints from thermobarometry, metamorphic modelling and U Pb geochronology. *Journal of the Geological Society*, **166**, pp.919-932.

Tapponnier, P. and Molnar, P.J. 1976. Slip-line field theory and large-scale continental tectonics. *Nature*, **264**, pp.319-324.

Tapponnier, P. et al. 1982. Propagating extrusion tectonics in Asia: New insights from simple experiments with plasticine. *Geology*, **10**, pp.611-616.

Tembe, S. et al. 2009. Constraints on the stress state of the San Andreas Fault with analysis based on core and cuttings from the San Andreas Fault Observatory at Depth (SAFOD) drilling phases 1 and 2. *Journal of Geophysical Research*, **114**, B11401.

Thakur, V.C. 1981. Regional framework and geodynamic evolution of the Indus-Tsangpo suture zone in the Ladakh Himalayas. *Transactions of the Royal Society of Edinburgh Earth Sciences*, **72**, pp.89-97.

Thakur, V.C. and Misra, D.K. 1984. Tectonic framework of the Indus and Shyok Suture Zones in eastern Ladakh, Northwest Himalaya. *Tectonophysics*, **101**, pp.207-220.

Thakur, V.C. et al. 1981. A Note on the Geology of Nubra-Shyok Area of Ladakh, Kashmir, Himalaya. *Journal of the Geological Society of India*, **22**, pp.46-50.

Thanh, N.X. et al. 2011. Multiple garnet growth in garnet–kyanite–staurolite gneiss, Pangong metamorphic complex, Ladakh Himalaya: New constraints on tectonic setting. *Lithos*, **127**, pp.552-563.

Thatcher, W. 2007. Microplate model for the present day deformation of Tibet. *Journal of Geophysical Research*, **112**, B01401.

Thatcher, W. 2009. How the Continental Deform: The Evidence From Tectonic Geodesy. *Annual Review of Earth and Planetary Science*, **37**, pp.237-262.

Townend, J. and Zoback M.D. 2000. How faulting keeps the crust strong. *Geology*, **28**, pp.399-402.

Townend, J. et al. 2009. Deep Fault Drilling Project-Alpine Fault, New Zealand. *Scientific Drilling*, **8**, pp.75-82.

Townend, J. et al. 2013. Late-interseismic state of a continental plate-bounding fault: Petrophysical results from DFDP-1 wireline logging and core analysis, Alpine Fault, New Zealand. *Geochemistry Geophysics Geosystems*, **14**, pp.3801-3820.

Toy, V.G. et al. 2008. Quartz fabrics in the Alpine fault mylonites, Influence of pre-existing preferred orientations on fabric development during progressive uplift. *Journal of Structural Geology*, **30**, pp.602-621.

Tullis, J. and Yund, R.A. 1977. Experimental deformation of dry Westerly Granite. *Journal of Geophysical Research*, **82**, pp.5705-5718.

Tullis, J., and Yund, R.A. 1980. Hydrolytic weakening of experimentally deformed Westerly granite and Hale albite rock. *Journal of Structural Geology*, **2**, pp.439-451.

Tullis, J. and Yund, R.A. 1985. Dynamic recrystallization of feldspar: A mechanism for ductile shear zone formation. *Geology*, **13**, pp.238-241.

Tullis, J.A. et al. 1973. Microstructures and preferred orientations of experimentally deformed quartzites. *Geological Society of America Bulletin*, **84**, pp.297-314.

Tullis, T.E. et al. 1991. Flow Laws of Polyphase Aggregates from End-Member Flow Laws. *Journal of Geophysical Research*, **96**, pp.8081-8096.

Twiss, R.J. 1977. Theory and Applicability of a Recrystallized Grain-size Paleopiezometer. *Pure and Applied Geophysics*, **115**, pp.227-244.

Upadhyay, R. 2001. Seismically-induced soft-sediment deformational structures around Khalsar in the Shyok Valley, northern Ladakh and eastern Karakoram, India. *Current Science*, **81**, pp.600-604.

Upadhyay, R. 2003. Earthquake-induced soft-sediment deformation in the lower Shyok river valley, northern Ladakh, India. *Journal of Asian Earth Sciences*, **21**, pp.413-421.

Valli, F. et al. 2007. Twenty million years of continuous deformation along the Karakorum fault, western Tibet: A thermochronological analysis.

Tectonics, **26**, TC4004.

Valli, F. et al. 2008. New U-Th/Pb constraints on timing of shearing and long-term slip-rate on the Karakorum fault. *Tectonics*, **27**, TC5007.

Vauchez, A. and Tomassi, A. 2003. Wrench faults down to the asphenosphere: geological and geophysical evidence and thermomechanical effects. In: Storti, F. et al. eds. *Intraplate Strike-Slip Deformation Belts*. London: Geological Society, London, Special Publications, **210**, pp.15-34.

Villa, I.M. et al. 1996. Late Miocene to Early Pliocene tectonometamorphism and cooling in south-central Karakorum and Indua-Tsangpo suture, Chogo Lungma area (NE Pakistan). *Tectonophysics*, **260**, pp.201-214.

Voll, G. 1976. Recrystallisation of quartz, biotite and feldspars from Erstfeld to the Levantina Nappe, Swiss Alps, and its geological significance.

Schweizer Mineralogische und Petrographische Mitteilungen, **56**, pp.641-647.

Vollmer, F.W. 1990. An application of eigenvalue methods to structural domain analysis. *Geological Society of America Bulletin*, **102**, pp.786-791.

Walker R.J. et al. 2012. Fault-zone evolution in layered basalt sequences: A case study from the Faroe Islands, NE Atlantic margin. *Geological Society of America Bulletin*, **124**, pp.1382-1393.

Wallis, D. et al. 2013. Fault weakening across the frictional-viscous transition zone, Karakoram Fault Zone, NW Himalaya. *Tectonics*, **32**, pp.1227-1246.

Wallis, D. et al. in 2014a. Evolution of the Eastern Karakoram Metamorphic Complex, Ladakh, NW India, and its relationship to magmatism and regional tectonics. *Tectonophysics*, **626**, pp.41-52.

Wallis, D. et al. 2014b. Comment on "Interplay of deformation and magmatism in the Pangong Transpressional Zone, Eastern Ladakh, India: Implications for remobilization of the trans-Himalayan magmatic arc and initiation of the Karakoram Fault" by K. Sen, B.K. Mukherjee and A.S.

Collins, Journal of Structural Geology 62 (2014) 13-24. *Journal of Structural Geology*, **65**, pp.117-119.

Wang, H., and Wright T.J. 2012. Satellite geodetic imaging reveals internal deformation of western Tibet. *Geophysical Research Letters*, **39**, L07303.

Wang, Q. et al. 2012. Crustal Melting and Flow beneath Northern Tibet: Evidence from Mid-Miocene to Quaternary Strongly Peraluminous Rhyolites in the Southern Kunlun Range. *Journal of Petrology*, **53**, pp.2523-2566.

Wang, S. et al. 2009. New radiometric dating constrains the time for initiation of the Karakorum fault zone (KFZ), SW Tibet. *Tectonophysics*, **475**, pp.503-513.

Wang, S. et al. 2011. U-Pb SHRIMP and $^{40}\text{Ar}/^{39}\text{Ar}$ ages constrain the deformation history of the Karakoram fault zone (KFZ), SW Tibet. *Tectonophysics*, **509**, pp.208-217.

Wang, S. et al. 2012. Displacement along the Karakoram fault, NW Himalaya, estimated from LA-ICP-MS U-Pb dating of offset geologic markers. *Earth and Planetary Science Letters*, **337-338**, pp.156-163.

Wang, S. et al. 2013. Reply to Comment on "Displacement along the Karakoram fault, NW Himalaya, estimated from LA-ICPMS U-Pb dating of offset geologic markers" by Leloup et al. in EPSL, 2012. *Earth and Planetary Science Letters*, **363**, pp.246-248.

Wang, S. et al. 2014. Karakoram fault activity defined by temporal constraints on the Aji Shan detachment, SW Tibet. *International Geology Review*, **56**, pp.15-28.

Watkins, H.E. 2011. Composition and origin of exotic fault-related intrusions, Karakoram fault, Ladakh, NW Himalaya. MSc thesis, University of Leeds.

Weinberg, R.F. and Dunlap, W.J. 2000. Growth and Deformation of the Ladakh Batholith, Northwest Himalayas: Implications for Timing of Continental Collision and Origin of Calc-Alkaline Batholiths. *The Journal of Geology*, **108**, pp.303-320.

- Weinberg, R.F. and Mark G. 2008. Magma migration, folding, and disaggregation of migmatites in the Karakoram Shear Zone, Ladakh, NW India. *Geological Society of America Bulletin*, **120**, pp.994-1009.
- Weinberg, R.F. and Searle, M.P. 1998. The Pangong Injection Complex, Indian Karakoram: a case of pervasive granite flow through hot viscous crust. *Journal of the Geological Society, London*, **155**, pp.883-891.
- Weinberg, R.F. et al. 2000. New field, structural and geochronological data from the Shyok and Nubra valleys, northern Ladakh: linking Kohistan to Tibet. In: Khan M.A. et al. eds. *Tectonics of the Nanga Parbat Syntaxis and the Western Himalaya*. Bath: Geological Society, London, Special Publications, **170**, pp.253-275.
- Weller, O.M. et al. 2013. Quantifying Barrovian metamorphism in the Danba Structural Culmination of eastern Tibet. *Journal of Metamorphic Geology*, **31**, pp.909-935.
- Wells, D.L. and Coppersmith, K.J. 1994. New Empirical Relationships among Magnitude, Rupture Length, Rupture Area and Surface Displacement. *Bulletin of the Seismological Society of America*, **84**, pp.974-1002.
- Wenk, H.-R. and Christie, J.M., 1991. Comments on the interpretation of deformation textures in rocks. *Journal of Structural Geology*, **13**, pp.1091-1110.
- Wenk, H.-R. et al 1991. Modelling plastic-deformation of peridotite with the self-consistent theory. *Journal of Geophysical Research-Solid Earth and Planets*, **96**, pp.8337-8349.
- Wheeler, J. et al. 2001. The petrological significance of misorientation between grains. *Contributions to Mineralogy and Petrology*, **141**, pp.109-124.
- White, J.C. and White S.H. 1983. Semi-brittle deformation within the Alpine fault zone, New Zealand. *Journal of Structural Geology*, **5**, pp.579-589.
- White, S.H. et al. 1980. On mylonites in ductile shear zones. *Journal of Structural Geology*, **2**, pp.175-187.

White, S.R. 2001. Textural and microstructural evidence for semi-brittle flow in natural fault rocks with varied mica contents. *International Journal of Earth Sciences*, 90, pp.14-27.

Wibberley, C.A.J. 2005. Initiation of basement thrust detachments by fault-zone reaction weakening. In: Bruhn, D. and Burlini, L. eds. *High Strain Zones: Structure and Physical Properties*. Bath: Geological Society, London, Special Publications, 245, pp.347-372.

Wibberley, C.A.J. and Shimamoto T. 2005. Earthquake slip weakening and asperities explained by thermal pressurization. *Nature*, **436**, pp.689-692.

Wibberley, C.A.J. et al. 2008. Recent advances in the understanding of fault zone internal structure: a review. In: Wibberley, C.A.J. et al. eds. *The Internal Structure of Fault Zones: Implications for Mechanical and Fluid-Flow Properties*. Bath: Geological Society, London, Special Publications, 299, pp.5-33.

Wilkinson, A.J. and Hirsch, P.B. 1997. Electron diffraction based techniques in scanning electron microscopy of bulk materials. *Micron*, **28**, pp.279-308.

Wilson, J.E. et al. 2003. Microfracture analysis of fault growth and wear processes, Punchbowl Fault, San Andreas system, California. *Journal of Structural Geology*, **25**, pp.1855-1873.

Wintsch, R.P. et al. 1995. Fluid-rock Reaction Weakening of Fault Zones. *Journal of Geophysical Research-Solid Earth*, **100**, pp.13021-13032.

Wittlinger, G. et al. 1998. Tomographic Evidence for Localized Lithospheric Shear Along the Altyn Tagh Fault. *Science*, 282, pp.74-76.

Wittlinger, G. et al. 2004. Teleseismic imaging of subducting lithosphere and Moho offsets beneath western Tibet. *Earth and Planetary Science Letters*, 221, pp.117-130.

Woodcock, N.H. 1977. Specification of fabric shapes using an eigenvalue method. *Geological Society of America Bulletin*, **88**, pp.1231-1236.

Wright, T.J. 2004. InSAR observations of low slip rates on the major faults of western Tibet. *Science*, **305**, pp.236-239.

Wyllie, P.J. 1977. Crustal anatexis: an experimental review. *Tectonophysics*, **43**, pp.41-71.

Xiao, Q. et al. 2011. Electrical resistivity structure at the northern margin of the Tibetan Plateau and tectonic implications. *Journal of Geophysical Research*, **116**, B12401.

Yamasaki, T. and Houseman, G.A. 2012. The signature of depth-dependent viscosity structure in post-seismic deformation. *Geophysical Journal International*, **190**, pp.769-784.

Yamasaki, T. et al. 2014. Weak ductile shear zone beneath a major strike-slip fault: inferences from earthquake cycle model constrained by geodetic observations of the western North Anatolian Fault Zone. *Journal of Geophysical Research-Solid Earth*, **119**, pp.3678-3699.

Yin, A. et al. 2002. Tectonic history of the Altyn Tagh fault system in northern Tibet inferred from Cenozoic sedimentation. *Geological Society of America Bulletin*, **114**, pp.1257-1295.

Yue, Y. et al. 2003. Slowing extrusion tectonics: lowered estimate of post-Early Miocene slip-rate for the Altyn Tagh fault. *Earth and Planetary Science Letters*, **217**, pp.111-122.

Zang, W. and Fyfe, W.S. 1995. Chloritization of the hydrothermally altered bedrock at the Igarapé Bahia gold deposit, Carajás, Brazil. *Mineralium Deposita*, **30**, pp.30-38.

Zhang, J. et al. 2001. Petrology and geochronology of eclogites from the western segment of the Altyn Tagh, northwest China. *Lithos*, **56**, pp.187-206.

Zhang, K.-J. et al. 2006. Eclogites from central Qiangtang, northern Tibet (China) and tectonic implications. *Earth and Planetary Science Letters*, **245**, pp.722-729.

Zhang P.Z. et al. 2004. Continuous deformation of the Tibetan Plateau from global positioning system data. *Geology*, **32**, pp.809-812.

Zhang R. et al. 2011. Late Eocene crustal thickening followed by Early-Late Oligocene extension along the India-Asia suture zone: Evidence for cyclicity in the Himalayan orogen. *Geosphere*, **7**, pp.1249-1268.

Zoback, M.D. and Harjes, H.-P. 1997. Injection-induced earthquakes and crustal stress at 9 km depth at the KTB deep drilling site, Germany. *Journal of Geophysical Research*, **102**, pp.18477-18491.

Zoback, M.D. et al. 2010. Scientific drilling into the San Andreas fault zone. *Eos: Transactions of the American Geophysical Union*, **91**, pp.197-199.

Zoback, M.D. et al. 2011. Scientific drilling into the San Andreas Fault zone – an overview of SAFOD's first five years. *Scientific Drilling*, **11**, pp.14-28.

List of Abbreviations

- Ab – Albite
- Act - Actinolite
- AD – Arganglas Diorite
- AF – Alpine Fault
- Am(p) – Amphibolite
- ATF – Altyn Tagh Fault
- BGL – Bulging dynamic recrystallisation
- BNS – Bangong-Nujiang Suture
- Bt – Biotite
- C – ‘strength’ parameter
- Cal - Calcite
- Cat - Cataclasite
- Chl - Chlorite
- CMT - Centroid moment tensor
- CPO – Crystal preferred orientation
- Cpx – Clinopyroxene
- CRSS – Critical resolved shear stress
- Czo – Clinozoisite
- D0-3 Deformation events
- E_{1-3} - Eigenvalues
- EBSD – Electron backscattered diffraction
- EDX – Energy dispersive X-ray spectroscopy
- EKMC – Eastern Karakoram Metamorphic Complex
- Ep – Epidote
- Fsp – Feldspar
- FVF – Frictional-viscous flow
- FVTZ – Frictional-viscous transition zone

GBM – Grain boundary migration dynamic recrystallisation
Gr(t) – Granite
Grt - Garnet
Hbl – Hornblende
I - Intensity
ICWL – Interconnected weak layers
ID-TIMS Isotope dilution thermo-ionisation mass spectrometry
J – J-index
KF – Karakoram Fault
Kfs – K-feldspar
KFZ – Karakoram Fault Zone
L - lineation
Leu - Leucosome
Lgr – Leucogranite
M – M-index
M0-4 – Metamorphic events
MD – Muglib Dome
Mel – Melanosome
MS – Muscovite
MUD – Multiples of uniform distribution
 M_w – Moment magnitude
N – Number of Analyses
NF – Nubra Formation
NSL – Nubra-Siachen Leucogranite
Opx – Orthopyroxene
pfJ – Pole Figure J-index
Phg - Phengite
Pl – Plagioclase
Pl Rx – Recrystallised plagioclase

PM - Protomylonitic

PMC – Pangong Metamorphic Complex

PTZ – Pangong Transpressional Zone

QSR – Quartz strain-rate-metry

Qtz – Quartz

R – 'random' parameter

R1 – Riedel shear

Rt - Rutile

S - Foliation

SAF – San Andreas Fault

SAFOD – San Andreas Fault Observatory at Depth

Ser - Sericite

SF- Saser Formation

SGR – subgrain rotation dynamic recrystallisation

SHRIMP – Sensitive high resolution ion microprobe

Si – Inclusion foliation

Sm – Matrix foliation

SS – Shyok Suture

STG – South Tangtse Granite

TDL – Tangtse-Darbuk Leucogranite

TG – Tirit Granite

TL(gr) – Taruk Leucogranite

Ttn - Titanite

Tra- Travertine

TSZ – Taruk shear zone

Tur – Tourmaline

UM - Ultramylonitic

Appendix A Summary of Electron Microprobe Compositional Data

A.1 Summary of Amphibole Compositional Data

Sample	W11/73		W11/121		P59		P121	
Lithology	Migmatite		Amphibolite		Amphibolite		Amphibolite	
Unit	PTZ		PTZ		PMC		PMC	
N	35		32		15		15	
	Mean	2 σ	Mean	2 σ	Mean	2 σ	Mean	2 σ
SiO ₂	44.65	1.25	42.99	2.30	45.05	0.92	42.98	2.91
TiO ₂	0.91	0.17	0.55	0.22	0.70	0.08	0.39	0.19
Al ₂ O ₃	10.13	0.87	10.73	1.51	13.03	1.20	14.82	3.69
Cr ₂ O ₃	0.05	0.09	0.03	0.05	0.06	0.08	0.07	0.17
Fe ₂ O ₃	2.87	0.75	4.24	1.19	2.33	0.55	3.70	0.75
FeO	12.15	1.17	15.36	1.49	11.72	0.50	12.20	1.12
MnO	0.46	0.07	0.74	0.08	0.32	0.06	0.31	0.11
MgO	12.19	0.82	9.15	1.65	11.79	0.46	10.48	1.91
CaO	11.93	0.22	11.89	0.20	11.45	0.22	11.26	0.56
Na ₂ O	1.35	0.16	1.23	0.17	1.45	0.15	1.88	0.52
K ₂ O	1.18	0.24	1.20	0.29	0.27	0.06	0.22	0.15
H ₂ O	1.98	0.05	1.90	0.05	2.03	0.06	2.03	0.04
F	0.08	0.09	0.13	0.13	0.06	0.11	0.03	0.07
Cl	0.03	0.02	0.09	0.06	0.01	0.01	0.01	0.01
Total	99.97	0.45	100.24	0.64	100.26	0.56	100.38	0.60
O=F	0.04	0.04	0.05	0.05	0.03	0.05	0.01	0.03
O=Cl	0.01	0.00	0.02	0.01	0.00	0.00	0.00	0.00
Total	99.93	0.45	100.17	0.64	100.24	0.58	100.36	0.60
Fe=FeO	14.73	0.86	19.18	2.17	13.82	0.42	15.53	1.12
Si	6.61	0.14	6.49	0.26	6.54	0.12	6.29	0.39
Ti	0.10	0.02	0.06	0.02	0.08	0.01	0.04	0.02
Al	1.77	0.16	1.91	0.29	2.23	0.21	2.56	0.65
Cr	0.01	0.01	0.00	0.01	0.01	0.01	0.01	0.02
Fe ³⁺	0.32	0.08	0.48	0.14	0.25	0.06	0.41	0.08
Fe ²⁺	1.50	0.16	1.94	0.21	1.42	0.06	1.49	0.15
Mn	0.06	0.01	0.10	0.01	0.04	0.01	0.04	0.01
Mg	2.69	0.16	2.06	0.34	2.55	0.10	2.29	0.40
Ca	1.89	0.03	1.92	0.02	1.78	0.04	1.77	0.09
Na	0.39	0.05	0.36	0.05	0.41	0.04	0.53	0.15
K	0.22	0.05	0.23	0.06	0.05	0.01	0.04	0.03
Total	15.55	0.09	15.55	0.11	15.36	0.05	15.47	0.13
Al ^{VI}	0.37	0.04	0.40	0.05	0.77	0.10	0.85	0.27
Mg/(Mg+Fe)	0.64	0.04	0.51	0.07	0.64	0.02	0.60	0.06
Modal class.	Edenite		Magnesio-hastingsite		Magnesio-hornblende		Tschermakite	

Table A.1 Summary of amphibole electron microprobe compositional data used for amphibole-plagioclase geothermobarometry (Chapter 4) given as oxide wt.% and cations per 23 oxygen formula unit. Also given are the number of analyses (N), octahedral Al (Al^{VI}) content and magnesium number (Mg/(Mg+Fe)). PTZ-Pangong Transpressional Zone, PMC-Pangong Metamorphic Complex.

Sample	P141	
Lithology	Am+Bt monzogranite	
Unit	STG	
N	31	
	Mean	2σ
SiO₂	44.36	1.17
TiO₂	0.45	0.35
Al₂O₃	8.82	0.92
Cr₂O₃	0.02	0.03
Fe₂O₃	4.23	0.90
FeO	15.30	0.85
MnO	0.64	0.05
MgO	10.48	0.67
CaO	11.60	0.17
Na₂O	1.77	0.20
K₂O	1.11	0.19
Total	98.77	0.95
Fe=FeO	19.11	0.92
Si	6.71	0.14
Ti	0.05	0.04
Al	1.57	0.17
Cr	0.00	0.00
Fe³⁺	0.00	0.00
Fe²⁺	2.42	0.12
Mn	0.08	0.01
Mg	2.36	0.14
Ca	1.88	0.02
Na	0.52	0.06
K	0.21	0.04
Total	15.82	0.10
Al^{VI}	0.20	0.05
Mg/(Mg+Fe)	0.55	0.03
Modal class.	Edenite	

Table A.2 Summary of amphibole electron microprobe compositional data used for Al-in-amphibole geobarometry (Chapter 6) given as oxide wt.% and cations per 23 oxygen formula unit. Also given are the number of analyses (N), octahedral Al (Al^{VI}) content and magnesium number (Mg/(Mg+Fe)). STG-South Tangtse Granite.

A.2 Summary of Plagioclase Compositional Data

Sample	W11/73		W11/121		P59		P121	
Lithology	Migmatite		Amphibolite		Amphibolite		Amphibolite	
Unit	PTZ		PTZ		PMC		PMC	
N	35		32		15		15	
	Mean	2 σ	Mean	2 σ	Mean	2 σ	Mean	2 σ
SiO ₂	61.46	0.73	59.50	1.83	57.37	1.95	62.09	1.75
TiO ₂	0.01	0.02	0.01	0.02	0.01	0.02	0.01	0.02
Al ₂ O ₃	24.68	0.43	25.98	1.15	27.71	1.34	24.59	1.18
Fe ₂ O ₃	0.23	0.10	0.21	0.12	0.26	0.10	0.20	0.13
MnO	0.01	0.02	0.01	0.04	0.01	0.03	0.01	0.02
MgO	0.01	0.03	0.01	0.02	0.01	0.02	0.01	0.03
CaO	6.14	0.44	7.64	1.32	9.21	1.58	5.50	1.34
Na ₂ O	8.26	0.28	7.43	0.83	6.72	1.00	8.92	0.89
K ₂ O	0.26	0.09	0.15	0.06	0.04	0.02	0.06	0.02
BaO	0.03	0.08	0.03	0.08	0.02	0.05	0.02	0.07
Total	101.09	0.49	100.98	0.63	101.36	0.48	101.41	0.43
Si	2.71	0.02	2.63	0.07	2.54	0.07	2.72	0.06
Ti	0.00	0.00	0.00	0.00	0.00	0.00	0.00	0.00
Al	1.28	0.02	1.36	0.07	1.45	0.08	1.27	0.07
Fe ³⁺	0.01	0.00	0.01	0.00	0.01	0.00	0.01	0.00
Mn	0.00	0.00	0.00	0.00	0.00	0.00	0.00	0.00
Mg	0.00	0.00	0.00	0.00	0.00	0.00	0.00	0.00
Ca	0.29	0.02	0.36	0.06	0.44	0.08	0.26	0.06
Na	0.71	0.02	0.64	0.07	0.58	0.08	0.76	0.07
K	0.01	0.01	0.01	0.00	0.00	0.00	0.00	0.00
Ba	0.00	0.00	0.00	0.00	0.00	0.00	0.00	0.00
Total	5.01	0.01	5.01	0.01	5.02	0.01	5.02	0.01
An	28.82	2.11	36.16	6.60	44.29	7.78	26.32	6.64
Modal Class.	Oligoclase		Andesine		Andesine		Oligoclase	

Table A.3 Summary of plagioclase electron microprobe compositional data used for amphibole-plagioclase geothermobarometry (Chapter 4) given as oxide wt.% and cations per 8 oxygen formula unit. Also given are the number of analyses (N), and anorthite number (An). PTZ-Pangong Transpressional Zone, PMC-Pangong Metamorphic Complex.

A.3 Summary of Biotite Compositional Data

Sample	P85		P146	
Lithology	Ky+Gt metapelite		Metapelite	
Unit	Nubra Fm.		Saser Fm.	
N	79		41	
	Mean	2 σ	Mean	2 σ
SiO ₂	34.87	1.04	35.00	0.70
TiO ₂	2.09	0.73	2.77	0.57
Al ₂ O ₃	20.57	3.12	18.17	0.81
Cr ₂ O ₃	0.07	0.10	0.01	0.03
FeO	20.03	2.30	21.92	1.01
MnO	0.20	0.06	0.38	0.08
MgO	7.99	1.15	7.45	0.53
CaO	0.05	0.14	0.02	0.04
Na ₂ O	0.25	0.08	0.17	0.11
K ₂ O	8.54	1.03	9.42	0.19
H ₂ O	3.92	0.09	3.88	0.04
Total	98.57	1.70	99.20	0.79
Fe=FeO	20.03	2.30	21.92	1.01
Si	5.33	0.12	5.41	0.08
Ti	0.24	0.09	0.32	0.07
Al	1.04	0.47	0.72	0.11
Cr	0.01	0.01	0.00	0.00
Fe ²⁺	2.56	0.32	2.84	0.15
Mn	0.03	0.01	0.05	0.01
Mg	1.82	0.27	1.72	0.12
Ca	0.01	0.02	0.00	0.01
Na	0.07	0.02	0.05	0.03
K	1.67	0.21	1.86	0.04
OH	4.00	0.00	4.00	0.00
Total	19.44	0.30	19.56	0.10
Mg/(Mg+Fe)	0.42	0.03	0.38	0.02
Modal Class.	Annite		Annite	

Table A.4 Summary of biotite electron microprobe compositional data used for Ti-in-biotite geothermometry (Chapter 4) given as oxide wt.% and cations per 22 oxygen formula unit. Also given are the number of analyses (N) and magnesium number (Mg/(Mg+Fe)).

A.4 Summary of Chlorite Compositional Data

Sample	W11/2	
Lithology	Phyllonite	
Unit	Nubra Fm.	
N	148	
	Mean	2σ
SiO₂	23.80	1.55
TiO₂	0.07	0.07
Al₂O₃	21.60	1.23
Cr₂O₃	0.01	0.05
FeO	28.16	1.75
MnO	0.40	0.12
MgO	11.11	0.89
CaO	0.04	0.06
Na₂O	0.02	0.06
K₂O	0.05	0.37
Total	85.27	1.85
Si	5.27	0.22
Ti	0.01	0.01
Al	5.64	0.20
Cr	0.00	0.01
Fe	5.22	0.39
Mn	0.08	0.02
Mg	3.67	0.34
Ca	0.01	0.01
Na	0.01	0.03
K	0.02	0.10
Total	19.91	1.33
Al^{IV}	2.73	0.22
Al^{IV}_c	3.14	0.22
Fe/(Fe+Mg)	0.59	0.02
Modal Class.	Ripidolite	

Table A.5 Summary of chlorite electron microprobe compositional data used for chlorite geothermometry (Chapter 5) given as oxide wt.% and cations per 28 oxygen formula unit. Also given are the number of analyses (N), tetrahedral Al (Al^{IV}) and corrected tetrahedral Al (Al^{IV}_c, Kranidiotis and MacLean, 1987) contents and iron number (Fe/(Fe+Mg)).